2015

Mechanical Control of Sensory Hair-Bundle Function

Joshua D. Salvi

MECHANICAL CONTROL OF SENSORY HAIR-BUNDLE FUNCTION

A Thesis Presented to the Faculty of

The Rockefeller University

in Partial Fulfillment of the Requirements for

the degree of Doctor of Philosophy

by

Joshua D. Salvi

June 2015

MECHANICAL CONTROL OF SENSORY HAIR-BUNDLE FUNCTION

Joshua D. Salvi, Ph.D.
The Rockefeller University 2015

Hair bundles detect sound in the auditory system, head position and rotation in the vestibular system, and fluid flow in the lateral-line system. To do so, bundles respond to periodic, static, and hydrodynamic forces contingent upon the receptor organs in which they are situated. As the mechanosensory function of a hair bundle varies, so too do the mechanical properties of the bundle and its microenvironment. Hair bundles range in height from 1 μm to 100 μm and in stiffness from 100 $\mu N \cdot m^{-1}$ to 10,000 $\mu N \cdot m^{-1}$. They are composed of actin-filled, hypertrophic microvilli—stereocilia—that number from fewer than 20 through more than 300 per bundle. In addition, bundles may or may not possess one true cilium, the kinocilium. Hair bundles differ in shape across organs and organisms: they may be isodiametric, fan-shaped, or V-shaped. Depending on the organ in which they occur, bundles may be free-standing or they may be coupled to a tectorial membrane, otolithic membrane, cupula, or sallet. Because all hair bundles are comprised of similar molecular components, their distinct mechanosensory functions may instead be regulated by their mechanical loads.

Dynamical-systems analysis provides mathematical predictions of hair-bundle behavior. One such model captures the effects of mechanical loading on bundle function in a state diagram. A mechanical-load clamp permits exploration of this state diagram by robustly controlling the loads—constant force, load stiffness, virtual drag, and virtual

mass—imposed on a hair bundle. Upon changes in these mechanical parameters, the bundle's response characteristics alter. Subjected to particular control parameters, a bundle may oscillate spontaneously or remain quiescent. It may respond nonlinearly to periodic stimuli with high sensitivity, sharp frequency tuning, and easy entrainment; or it may respond linearly with low sensitivity, broad tuning, and reluctant entrainment. The bundle's response to a force pulse may resemble that of an edge-detection system or a low-pass filter. Finally, a bundle from an amphibian vestibular organ can operate in a manner qualitatively similar to that from a mammalian auditory organ, implying an essential similarity between hair bundles.

The bifurcation near which a bundle's operating point resides controls its function: the state diagram provides a functional map of mechanosensory modalities. Auditory function is best tuned near a supercritical Hopf bifurcation, whereas vestibular function is captured by a subcritical Hopf bifurcation and a cusp bifurcation. Within the proposed region vestibular responsiveness, a hair bundle exhibits mechanical excitability analogous to the electrical excitability of neurons. This behavior implies for the first time a direct relationship between the mechanical behaviors of sensory organelles and the electrical behaviors of afferent neurons.

Man-made detectors function in limited capacities, each designed for a unique purpose. A single hair bundle, on the other hand, evolved to serve multiple purposes with the requirement of only two functional traits: adaptation and nonlinear channel gating. The remarkable conservation of these capabilities thus provides unique insight into the evolution of sensory systems.

To my devoted parents, Damian and Diane, whose steadfast support maintained my spirit.

To my grandfathers, Ernest and Gaetano, who taught me the meaning of compassion and perseverance.

To my best friend and beloved, Annie, whose insight and encouragement propelled me forward.

To my paragon of a mentor, Jim, whose guidance and cultivation actuated my scientific ambition.

ACKNOWLEDGMENTS

Nothing in this work would be possible without the unending support of my family. My parents, Damian and Diane, promoted a culture of curiosity at home and nurtured my interest in science. My sister and her partner, Rachel and Austin, grounded me throughout my years in the program. My grandmothers, Cecilia and Marcella, supplied me with unconditional encouragement. I owe a special debt of gratitude to my grandfathers, Ernest and Gaetano, whose lessons in perseverance, inquisitiveness, and dedication to one's family will reside in me for a lifetime.

My entrance into an MD-PhD program would not have been possible without the guidance of my undergraduate advisors and mentors. After a challenging freshman year at another university, I was welcomed with open arms by Karl Martz at Penn State, and I remain indebted to him. Peter Butler welcomed me into a biomaterials research program over the course of a summer at the Hershey Medical Center. Because of this, I was able to work in the laboratory of Henry Donahue, who served as my undergraduate thesis advisor for the next two-and-a-half years. With their guidance and the support of Christian Brady and Will Hancock, I successfully matriculated into the Schreyer Honors College after two difficult years. While there, Keefe Manning and Margaret Slattery motivated me to pursue a career in research. I owe all of them and my undergraduate institution my sincere gratitude.

I am lucky to have worked with and learned from the members of the Hudspeth Laboratory. During my rotation, Jon Fisher and Fumiaki Nin supported me through a brief study of the chinchilla's basilar membrane. Jon and I continue to work together in

an astrovisualization outreach program, *Neurodome*. Suchit Patel shared many lessons regarding his time in the MD-PhD program that remain with me today. I worked closely with Eliot Dow on one of his projects, a time that reminded both of us the benefits of sleep. Eliot was additionally crucial in my application for a fellowship from the National Institutes of Health. Other members of the laboratory—Aaron Steiner, Kate Leitch, Julien Azimzadeh, Corstiaen Versteegh, Tobias Bartsch, Adrian Jacobo, Taeryn Kim, Tobias Reichenbach, and Kim Siletti—shared countless conversations with me that both helped me in this project and kept me grounded. I must in particular thank Beth Dougherty. When I needed anything, whether it was advice or a reimbursement, she made it happen. Beth made any transitions smooth and my time in the lab more enjoyable.

Special thanks goes out to those who were crucial throughout the duration of this project. Without Brian Fabella, much of the success in these experiments would not be possible. He dedicated countless hours to programming the mechanical-load clamp, calibrating parts of the experimental setup, and customizing the LabVIEW system for our specific needs. Mélanie Tobin worked closely with me for nearly a year during the early stages of this project. Our work together not only got the project off the ground, but we converted the struggles of the project into a fun experience. Dáibhid Ó Maoiléidigh developed the theory that motivated this work, and his insight was crucial throughout the project. He designed the classification scheme and performed all of the simulations in *Chapter 6*. Dáibhid served as a second mentor for me throughout my time in the laboratory, and much of my knowledge in dynamical-systems theory arose from our conversations.

I am fortunate to have learned from the members of my faculty advisory committee: David Christini, Tarun Kapoor, and Stan Leibler. Our discussions motivated me to explore new and challenging topics, and their enthusiasm kept my spirits high. I must also thank Charles Peskin for serving as my external examiner of the thesis committee.

Olaf Andersen, Ruth Gotian, and the administrators of the MD-PhD office have been crucial to my progress in the program. Additionally, Sid Strickland, Emily Harms, Kristen Cullen, Cris Rosario, and Marta Delgado have made my time at Rockefeller enjoyable and my transitions smooth. Together, these people have been crucial in my personal and professional development.

After I first spoke with Jim regarding a possible rotation in 2011, I left with an enthusiasm for science I had never felt before. Over the course of my time in the laboratory, Jim shared with me a scientific curiosity and desire to teach that soon became a part of me. He has been and always will be one of my greatest scientific role models. I aspire to share at least a small fraction of his scientific prowess and ability to teach. I am thankful to have had the opportunity to work with and learn from Jim over these years.

Finally, I must thank Annie Handler for her unwavering support during my time in graduate school. She tempered my stress and anxiety. She motivated me to try new things. She challenged me in conversation and action. While writing this thesis, she maintained my sanity. Because of Annie, I'll strive to not just be a better scientist, but also a better friend and family member.

TABLE OF CONTENTS

LIST OF FIGURES AND ILLUSTRATIONS

FIGURE NUMBER AND TITLE **PAGE**

LIST OF TABLES

List of Abbreviations

BAPTA	*1,2-bis(o-aminophenoxy)ethane-N,N,N′,N′-tetraacetic acid*
BM	*Basilar membrane*
BT	*Bogdanov-Takens (bifurcation)*
CF	*Characteristic frequency*
DPOAE	*Distortion-product otoacoustic emission*
EEOAE	*Electrically-evoked otoacoustic emission*
FDT	*Fluctuation-dissipation theorem*
IHC	*Inner hair cell*
NOMP	*No mechanoreceptor potential*
OAE	*Otoacoustic emission*
OHC	*Outer hair cell*
OM	*Otolithic membrane*
PID	*Proportional-integral-derivative*
PIP_2	*Phosphatidylinositol-4,5-bisphosphate*
PKA	*Protein kinase A*
PKC	*Protein kinase C*
PMCA	*Plasma membrane Ca^{2+}-ATPase*
RM	*Reissner's membrane*
RMS	*Root-mean-square*
SHC	*Short hair cell (avian)*
SM	*Scala media*
SNIC	*Saddle-node on invariant cycle (bifurcation)*
SNIPER	*Saddle-node infinite period (bifurcation)*
SNLC	*Saddle-node of limit cycles (bifurcation)*
SOAE	*Spontaneous otoacoustic emission*
SPL	*Sound pressure level*
ST	*Scala tympani*
SV	*Scala vestibuli*
TEOAE	*Transient-evoked otoacoustic emission*
THC	*Tall hair cell (avian)*
TM	*Tectorial membrane*
TMC	*Transmembrane channel-like*
TRP	*Transient receptor potential*

CHAPTER 1

The Mechanics of Hearing

Human audition is a paragon of biophysics, bestowing finely tuned perception of complex biological and environmental stimuli. The auditory input from numerous sources comprises multiple frequencies that change rapidly from one moment to another. The human ear can nonetheless distinguish these varied signals. To accomplish this, the auditory system evolved to incorporate features permitting impressive temporal resolution in signal detection. The ear can respond to stimuli with periods as small as 45 μs (1). Additionally, the robust temporal responsiveness of audioception permits observers to detect interaural time differences as small as 6-10 μs (2). Trained musicians can distinguish frequencies that differ by as little as 0.2%, or about 3% of a semitone (3), resulting in an inner-ear filter that encompasses a bandwidth of only 1.2% of its center frequency (4). Sound-pressure stimuli varying over a millionfold in amplitude and a trillionfold in power can be tolerated and are compressed into only a few orders of magnitude in response (5). Finally, the human ear possesses a hearing threshold whose energy approximates that of thermal fluctuations (6), corresponding to subatomic displacements of 10-100 pm within the cochlea (7). Such traits imply that this system adds work through multiple active mechanisms to enhance signal detection.

This chapter deals with the aforementioned phenomena, commencing with a review of human audition and concluding with a narrative on the sensory cells that provide the ear with its remarkable traits.

SECTION 1.1: *Human Audition: From Pressure to Perception*

Auditory sensation in jawed vertebrates commences at the external and middle ears, which collect and transform longitudinal pressure vibrations. In humans, the pinna, concha, and external acoustic meatus of the outer ear first amass sound energy and apply a transfer function dictated by the frequency and location of the source (8-10). This filtered wave impinges on the tympanum, corresponding to tympanic movements as small as 1 pm near the threshold of hearing (11). Fluctuation of the tympanum induces motion of three middle-ear ossicles: the malleus, incus, and stapes. The lever action of these bones provides a second transformation that applies a frequency-dependent gain of more than 20 dB for frequencies below a resonant frequency of 1 kHz and a reduction in gain of about -8 dB/octave for higher frequencies (12). Coupled to the stapes is the oval window of the cochlea, and a piston-like motion of the stapes induces vibrations within the cochlea's fluid-filled chambers. Taken together, the air-filled middle ear seeks to match the impedance of airborne vibrations of sound with that of the fluid vibrations of the cochlea.

The spiral-shaped cochlea (from Greek *κοχλίας*, meaning *snail*) is the auditory component of the inner ear. Within the cochlea are three partitions: the scala vestibuli and scala tympani, each containing perilymph, and the scala media containing endolymph (Figure 1.1a) (13). Reissner's membrane separates the scala vestibuli from the scala media, whereas the basilar membrane segregates the scala media from the scala tympani. The cochlea makes approximately 2.5 turns around a central conical modiolus, with the scala vestibuli and scala tympani meeting at the apical helicotrema (Figure 1.1b)

(14). Motion of the stapes transmits vibrations directly to the scala vestibuli through the oval window (Figure 1.1c). A round window that adjoins the scala tympani relieves intracochlear pressure. This motion induces transverse waves along the length of the cochlea and in particular a traveling wave along the basilar membrane (15). However, the cochlear traveling wave is not uniform (Figure 1.1d). Like an ocean wave, the traveling wave increases in amplitude until it reaches a peak at a characteristic place along the length of the cochlear duct, after which it collapses. This characteristic place depends on the frequency of the wave, with high frequencies peaking near the base and low frequencies near the apex of the cochlea. The passive mechanical properties of the basilar membrane permit this behavior. Unlike the strings of a guitar, this membrane wields gradients in stiffness, mass, and dimensions along its length. For example, the basilar membrane achieves its greatest stiffness and smallest width (<0.16 mm) near the base and its smallest stiffness and greatest width (>0.42 mm) near the apex (16). Thus, a spatial arrangement of frequencies exists along the basilar membrane, creating a tonotopic organization.

Sitting atop the basilar membrane within the scala media is the organ of Corti (Figure 1.2). Within the organ of Corti are the sensory hair cells of the inner ear, so named for the mechanosensitive hair bundles that project from their apical surfaces. Each 8 μm section comprises one row of inner hair cells that primarily receive afferent innervation and three rows of outer hair cells that accept mostly efferent innervation. Lying above the hair cells is a gelatinous tectorial membrane. Like those of the basilar membrane, the mechanical properties of the tectorial membrane vary tonotopically. The

tectorial membrane achieves a maximum cross-sectional area near the apex and a minimal area near the base, corresponding to a mass load of approximately 100 ng per hair-cell row at the apical turn and 35 ng per row at the basal turn (17). Although outer hair cell bundles are directly attached to the tectorial membrane, inner hair cell bundles are unattached. Instead, viscous fluid flow between the tectorial membrane and the inner hair cells yields indirect coupling. Waves along the basilar membrane induce a shearing motion between hair cells and the overlying tectorial membrane, causing a deflection of the bundles of both inner and outer hair cells (Figure 1.3). At the threshold of hearing, this deflection can be as small as 0.3 nm. If a hair bundle were the height of the Burj Khalifa—the world's tallest building—this would correspond to a movement of only 9 cm at its tip (2, 18). Deflection of a bundle increases inward K^+ and Ca^{2+} currents into the cell through mechanotransduction channels at the tip of each actin-filled stereocilium, depolarizing the hair cell below. This depolarization provokes synaptic transmission between the basolateral surface of the hair cell and an afferent neuron.

Signals along afferent neurons propagate along the auditory nerve, cranial nerve VIII, to the cochlear nucleus of the medulla (41.3) (19). From the cochlear nucleus, some neurons project to the ipsilateral superior olivary complex in the pons and others to the contralateral superior olivary complex through the trapezoid body. Neurons in the superior olivary complex then project to the inferior colliculus of the tectum. An alternate pathway from the cochlear nucleus is a direct projection to the inferior colliculus through the lateral lemniscus. Signals proceed from the inferior colliculus to the medial geniculate nucleus of the thalamus and finally to the primary auditory cortex

within the temporal lobe of the brain (Brodmann areas 41 and 42) (13, 19). Throughout the central auditory pathway, the tonotopic mapping generated at the cochlea is preserved (19, 20). It remains to be elucidated how neural circuits within the cortex eventually filter and process complex environmental and biological sound stimuli allowing for meaningful sensory perception.

Figure 1.1. Schematic cross-section of the human cochlea. (a) A transverse section of the cochlea presents its three partitions. The scala vestibuli and scala tympani, containing perilymph, lie respectively superior and inferior to an endolymph-filled scala media. A Reissner's membrane (RM, *red*) separates the scala vestibuli from the scala media, and the basilar membrane (BM, *blue*) separates the scala media from the scala tympani. (b) Unwinding the 2.5 turns of the cochlea and viewing it in a longitudinal section depicts the same partitions in (a). At the cochlear apex, the scala vestibuli and scala tympani adjoin at the helicotrema (HT). Abutting the scala vestibuli is an oval window (OW) that couples directly to the stapes footplate of the middle ear. The scala tympani joins a round window (RW) at the cochlear base. (c) Pressure-induced vibrations of the oval window (green) produce transverse motion of the cochlear duct. The round window (orange) relieves pressure within the scala tympani. (d) Here Reissner's membrane and the basilar membrane are collapsed onto one another for illustrative purposes (purple). In the human cochlea, a traveling wave peaks at a frequency-dependent characteristic place along the basilar membrane. High frequencies peak near the base (red), and low frequencies peak near the apex (blue). Like an inverse piano, this behavior represents each frequency of vibrational input at a unique location along the length of the cochlear partition.

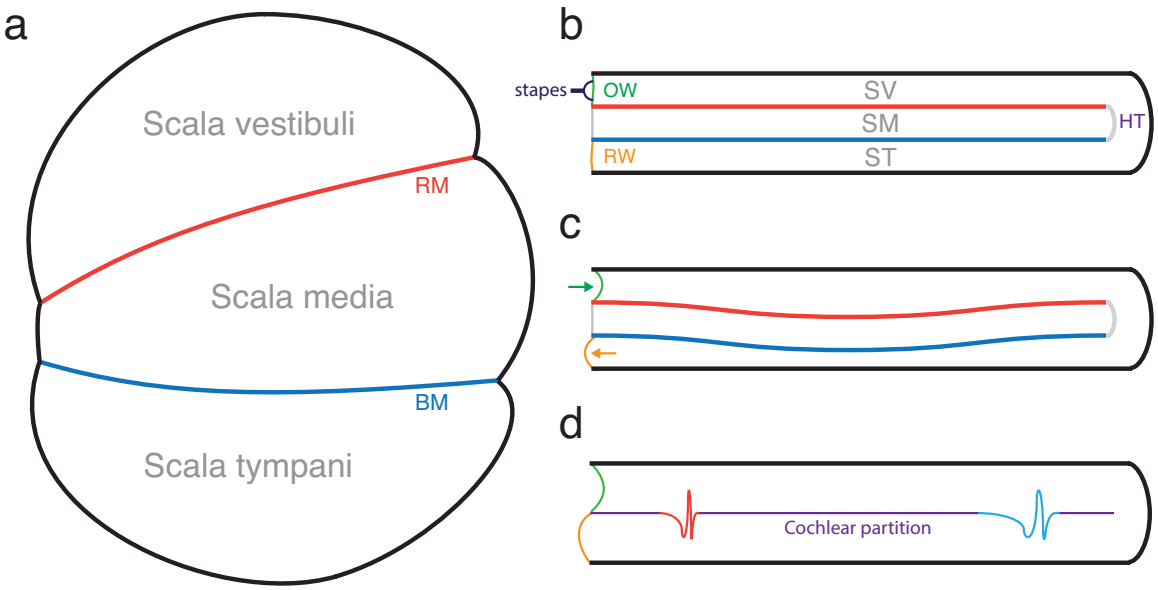
a
Scala vestibuli
RM
Scala media
BM
Scala tympani
b
stapes
OW
SV
SM
ST
HT
RW
c
d
Cochlear partition

Figure 1.2. The organ of Corti. The organ of Corti dwells on the basilar membrane within the scala media of the cochlea. Lying along the most lateral (right) side of the organ are the cells of Claudius (purple) and the cells of Hensen (green). Three rows of outer hair cells (OHC, *red*) are supported by cells of Deiters (dark blue). Pillar cells (light blue) lie medial to the outer hair cells and enclose the triangular tunnel of Corti across which nerve fibers pass. One row of inner hair cells (IHC, *orange*) lies medial to the tunnel of Corti. Residing medial to the inner hair cells are the inner-sulcus cells (brown) and interdental cells (green). The reticular lamina represents the apical surface of the organ of Corti from a portion medial to the inner hair cells through the most medial cells of Hensen. Extending from the central modiolus is a tectorial membrane that provides a canopy over the hair cells. The hair bundles of outer hair cells embed themselves within the tectorial membrane, whereas those of inner hair cells remain unattached (21).

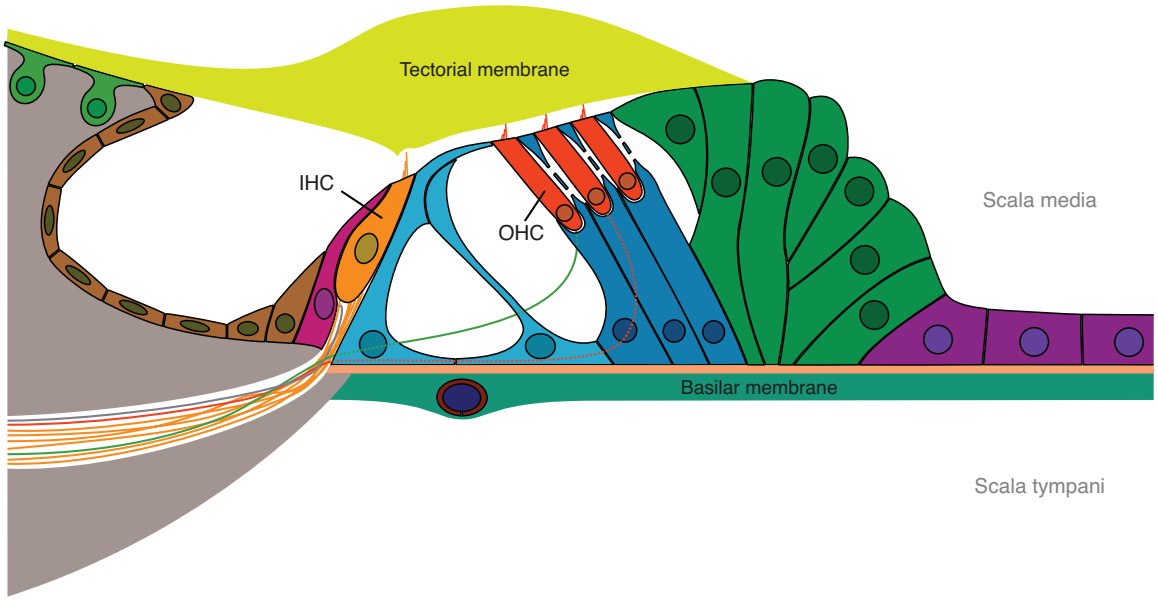
Tectorial membrane
IHC
OHC
Scala media
Basilar membrane
Scala tympani

Figure 1.3. Pressure-induced motion of the organ of Corti. (a) A schematic diagram of the organ of Corti portrays the basilar membrane (green), tectorial membrane (yellow), and all combined cellular components (blue). The hair bundles of outer hair cells (red) project into the tectorial membrane, whereas those of inner hair cells (orange) are coupled to the tectorial membrane by viscous drag. (b) Upon stimulation of the cochlear partition, vertical motion of the basilar membrane (purple arrow) induces a shearing motion between hair cells and the overlying tectorial membrane, deflecting the hair bundles (blue arrow). Hair-bundle deflection causes an influx of cationic current, depolarizing the hair cell and initiating auditory-signal transduction.

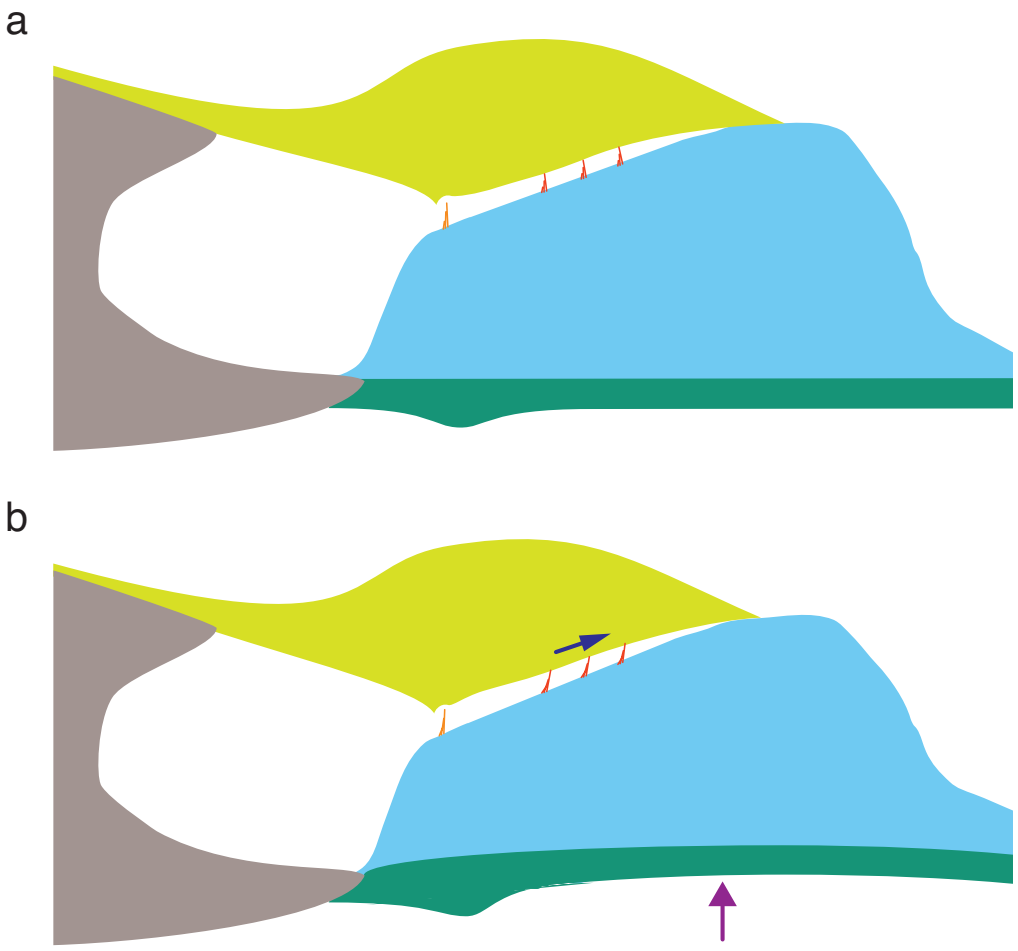
a
b

Figure 1.4. The central auditory pathway. Neurons along cranial nerve VIII project from the cochlea to the dorsal and ventral cochlear nuclei in the medulla. Projections from the ventral cochlear nucleus synapse onto neurons in either the dorsal cochlear nucleus or the contralateral superior olivary complex, whereas those from the dorsal cochlear nucleus continue to the ipsilateral superior olivary complex or the contralateral inferior colliculus. Each inferior colliculus receives inputs from the ipsilateral superior olivary complex, the contralateral dorsal cochlear nucleus, and the contralateral inferior colliculus. Neurons from the inferior colliculus then project to the ipsilateral medial geniculate body of the thalamus. Finally, thalamic neurons project to the primary auditory cortex within the temporal lobe. Each stage of transmission outlined here preserves the tonotopic map generated by the cochlea.

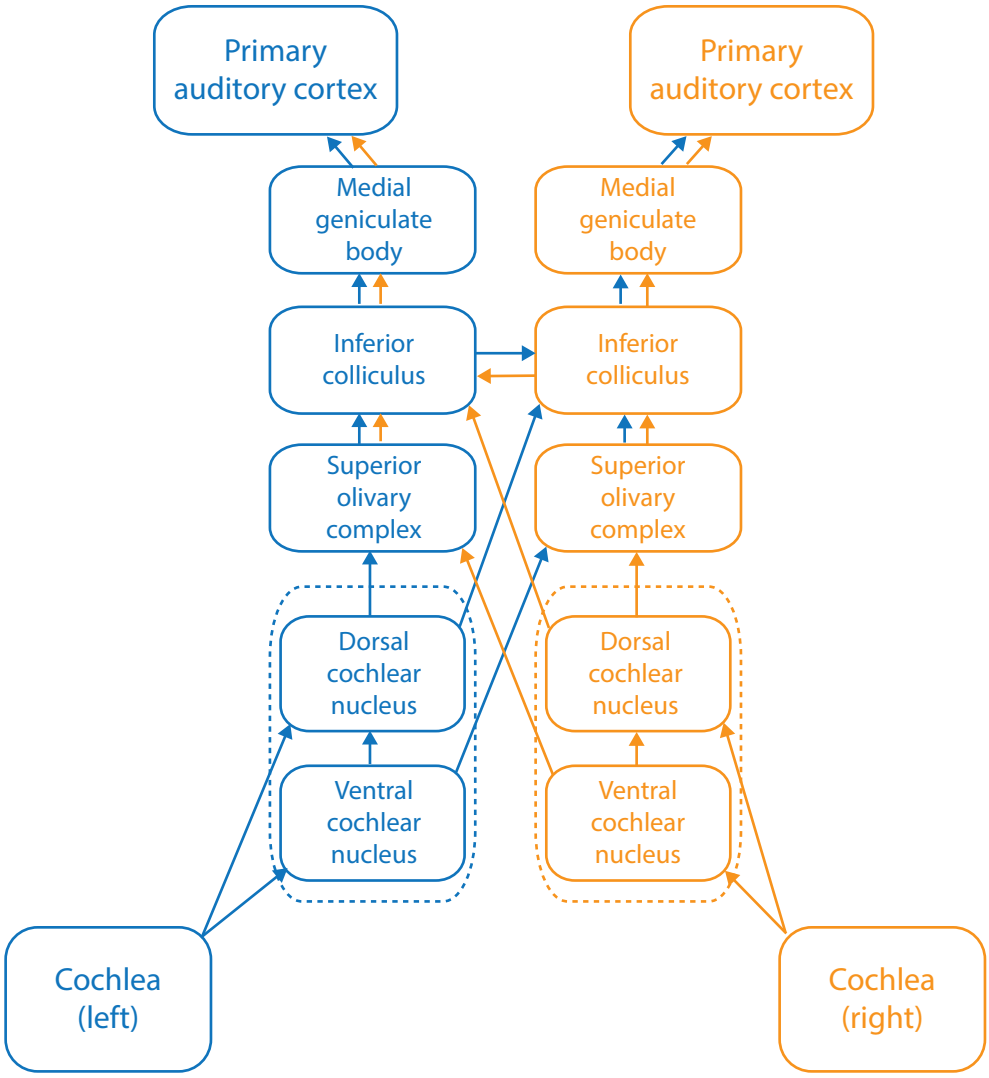
Primary auditory cortex
Primary auditory cortex
Medial geniculate body
Medial geniculate body
Inferior colliculus
Inferior colliculus
Superior olivary complex
Superior olivary complex
Dorsal cochlear nucleus
Dorsal cochlear nucleus
Ventral cochlear nucleus
Ventral cochlear nucleus
Cochlea (left)
Cochlea (right)

SECTION 1.2: *An Active Process in the Cochlea*

In his pioneering work on the cochlear traveling wave, von Békésy concluded that a sensory hair cell responds with a displacement smaller than the diameter of a hydrogen atom (15). Later, in 1948, Thomas Gold suggested that the cochlea cannot simply be a passive detector; it must amplify signals through a positive feedback mechanism (22). Indeed, this hypothesis was confirmed 35 years later (23). Such feedback in mammals arises from bidirectional transduction in outer hair cells that couples mechanical and electrical responses, causing electrically coupled mechanical length changes of their somata (24, 25). This electromotility arises a motor protein called prestin that lines the basolateral membrane of each outer hair cell (26). Prestin directly adjusts the mechanical impedance of the cochlear partition and can overcome viscous losses within the cochlea. Additionally, prestin's function endows the system with nonlinear amplification (27), so that blockade of prestin suppresses active amplification of the cochlear traveling wave (28). Taken together, it seems apparent that efferent innervation of outer hair cells provides active work to augment incoming auditory signals.

The auditory and vestibular hair cells of frogs, lizards, and birds are less specialized than those found in their mammalian counterparts. Their cells do not contain prestin and thus cannot exhibit electromotility. These species must nevertheless overcome viscous losses in order to achieve their remarkable sensitivity. The auditory organs in nonmammalian vertebrates may instead augment incoming signals through active hair-bundle motility (*see* Chapter 2) and the electrical resonance of hair-cell basolateral membranes (29, 30). It is evident that active-process phenomena arise not just

from one mechanism, but instead from the coalescence of multiple feedback and feedforward processes.

Initial and direct evidence of an active process in humans arose from the work of David Kemp, who recorded what he called "echoes" from healthy human ears (31). These "Kemp echoes" are a type of otoacoustic emission (OAE) called transient-evoked otoacoustic emissions (TEOAE). Kemp soon demonstrated that TEOAEs were not simply echoes and were instead sounds actively generated from the ear (32). Otoacoustic emissions have since been used as a tool in basic and clinical auditory research. Different varieties of OAEs include electrically evoked OAEs (EEOAE), spontaneous OAEs (SOAE), and distortion-product OAEs (DPOAEs). Strikingly, these emissions have been found in nonmammalian vertebrates, implying an active process that does not depend on electromotility in these species and may instead depend on critical oscillations of hair bundles (33).

Taken together, hearing organs are endowed with an active process that serves to augment incoming auditory signals. The active process is in fact a collection of multiple cellular mechanisms that coalesce to inject energy so as to compensate for viscous losses. Active-process phenomena can be seen in the active amplification of auditory inputs, sharp frequency tuning of sensory cells and their nerve fibers, compressive nonlinearity over a broad dynamic range, and the epiphenomenon of otoacoustic emissions. The cellular mechanisms that give rise to these behaviors include a species-dependent combination of hair-cell electromotility, electrical resonance of hair-cell basolateral membranes, and electromechanical hair-bundle motility (34). In mammals the interplay

of all these mechanisms probably gives rise to active-process phenomena, whereas in nonmammals a select few can yield qualitatively similar results (33).

SECTION 1.3: *Auditory Nonlinearities*

The cochlea performs its function through nonlinear processes that become essential in the dynamical-systems theory that lays the foundation for studies described in this work (7, 35). Nonlinear systems yield combined responses to combinations of stimuli that are not simple algebraic sums of individual responses. The method by which this behavior is achieved depends on the mechanics of a particular system. One method by which a system can achieve nonlinearity is to a clip signal above some limit. This generates a waveform distortion, a behavior readily seen in any amplifier driven beyond its maximum power rating (36). An alternative approach is automatic gain control, achieved by a closed-loop circuit that regulates the proportional gain imposed on a signal to reduce the dynamic range required of a device (37). Automatic gain controls have been employed in amplitude-modulated radio receivers and hearing aids (37, 38). The benefit of the latter technique is a reduction in the degree and prevalence of waveform distortions. Finally, critical oscillators poised near the boundary of self-oscillation can produce the same compressive nonlinearity (39). As will be seen, evolution has endowed the auditory system with the capacity to compress signals over a large dynamic range without requiring the system to reach its saturating limit.

When two tones at frequencies f_1 and f_2 are delivered to the ear, sounds at arithmetic combinations $f_2 - f_1$, $2f_2 - f_1$, $2f_1 - f_2$, and others are perceived. These distortion products were discovered and utilized by the Italian baroque composer and violinist Giuseppe Tartini (40). More than two centuries later, Goldstein assessed the most prominent $2f_2 - f_1$ distortion product in psychoacoustical experiments on human subjects (41). As he decreased the amplitude of the stimulus tones, the amplitude of the distortion product diminished to a nearly equal extent. He called this phenomenon an *essential nonlinearity*, in contrast with passive nonlinearities that are achieved only at saturating limits. A Taylor expansion for a nonlinear system provided with small-amplitude signals reveals that odd-ordered distortion products (e.g. the cubic $2f_2 - f_1$) are of higher amplitude than even-ordered ones (e.g. the quadratic $f_2 - f_1$), and this feature has been demonstrated experimentally (42).

Auditory nonlinearities can arise from multiple physiological mechanisms. Outer hair cells in the mammal control the impedance of the cochlear partition, as was demonstrated by stiffness changes of the partition with OHC bundle disruption (43). Additionally, the cochlear partition can generate pressure waves in a sealed canal, and distortion products created by the cochlear partition emerge as DPOAEs that have undergone a middle-ear transformation (44). Taken together, these results indicate that the activity of outer hair cells generate the principal nonlinearities of the cochlea.

Critical oscillators poised near the edge of an oscillatory instability display the ability to produce these nonlinear phenomena. Specifically, a Hopf bifurcation (*see* Chapter 3) is a generic phenomenon that can reproduce all active-process and nonlinear

behaviors (39, 45). Self-oscillations persist on one side of this bifurcation as a result of negative damping, whereas the system remains stable and quiescent on the positively damped side of the bifurcation. Driving a Hopf cochlea poised very near this border of activity yields responses with sharp frequency tuning, high amplification, compressive responses, and cubic nonlinearities.

In the outer hair cells of mammals, the physiological mechanisms that can give rise to auditory active processes and nonlinearities include mechanoelectrical transduction-channel gating, force generation by stereociliary hair bundles, and somatic electromotility. In nonmammals, electromotility is mostly absent (46), and the active motility of hair bundles presumably fills the role of nonlinear force generation (30).

CHAPTER 2

The Mechanics of Hair Bundles

Hair bundles are mechanosensitive sensory antennae that protrude from the apical surfaces of hair cells. In addition to their responsiveness to periodic stimuli in the auditory system, hair bundles detect linear and angular acceleration in the vestibular system and hydrodynamic forces in the lateral-line system. In each instance, mechanical deflection of a hair bundle induces an electrical response in the hair cell below. Mechanoelectrical transduction is remarkable for its fast timescale, capable of detecting stimuli exceeding 100 kHz in some auditory organs (47). Additionally, hair bundles are not simply passive detectors: they employ an active process to overcome viscous damping and augment stimuli. Hair bundles wield the capacity to detect stimuli as small as 0.3 nm in amplitude at the threshold of hearing (6, 19). Thanks to their adaptation process, bundles can distinguish a change in acceleration of 10^{-7} *g* in the presence of 1 *g* constant gravitational acceleration (48).

This chapter introduces mechanoelectrical transduction in hair bundles, delves into an active process in hair bundles that produces the same active-process phenomena appreciated in the cochlea, and compares the anatomical and physiological features of different bundles across organs and organisms.

SECTION 2.1: *Mechanoelectrical Transduction*

A sensory hair bundle comprises tens to hundreds of actin-filled stereocilia (Figure 2.1a). Stereocilia are not true microtubule-filled cilia but are instead enlarged actin-filled microvilli akin to microvilli of the intestinal brush border and leukocytes. Each stereocilium encloses a paracrystalline array of cross-linked actin within its membrane (49). A few tens of these actin filaments extend through a tapered region at the base of each stereocilium and into an actin-based cuticular plate. Within each bundle, stereocilia are arranged in rows of increasing height, and each stereocilium is connected to its taller neighbor by a proteinaceous tip link composed of protocadherin-15 and cadherin-23 (50-52). In some mechanosensory organs, a true cilium termed the kinocilium stands at the tallest edge of each hair bundle (Figure 2.1a). Kinocilia can be found in vestibular hair bundles and bundles from the lateral-line system of fish and amphibians (53, 54).

Positive deflection of a hair bundle—toward its tallest edge—causes each stereocilium to pivot at its base (55-58). This precipitates a shearing motion between stereocilia, increasing the tension in each tip link. Because each tip link is in series with one or two force-sensitive mechanoelectrical transduction channels, an increase in tip-link tension compels the channels to open and cationic current to flow into the cell (Figure 2.1a) (13, 19). Each channel operates with a unitary conductance of approximately 80-300 pS (59, 60), and there exist less than four channels per stereocilium and possibly as few as one (61, 62). The channel passes primarily K^+, and its pore is blocked in the presence of Ca^{2+} (59). Increasing the Ca^{2+} concentration decreases the channel conductance from roughly 200 pS in normal artificial endolymph to

approximately 100 pS in 1 mM Ca^{2+} (62-65). To achieve optimal transduction, a low-Ca^{2+}, high-K^{+} endolymph bathes the apical surfaces of hair cells, and a high-Ca^{2+}, low-K^{+} perilymph bathes their basal surfaces.

To satisfy the high-speed requirements of auditory end organs, mechanoelectrical transduction must be fast. Indeed, mechanoelectrical transduction occurs through direct channel gating without the requirement of second messengers (66). For example, in a study of bullfrog saccular hair bundles, a force pulse delivered to a bundle resulted in only a 25-μs delay in the bundle's response (63). The time constant to ultimately reach a steady-state position depends on both the magnitude of the bundle's displacement and the ambient temperature. This relationship can be approximated by Arrhenius' equation

$$\tau_{ss} = \tau_0 \exp\left\{\frac{\Delta G}{k_B T}\right\}, \tag{2.1}$$

in which τ_0 (≈ 0.17 ps) is the inverse of the bundle's intrinsic frequency, ΔG is a free energy barrier that depends on the magnitude of the stimulus, k_B is Boltzmann's constant, and T is the temperature (67). Equation 2.1 predicts that the time to reach steady state changes with both the amplitude of the force pulse and the temperature of the system. The relationship endures for turtle (62) and frog (63, 66) hair bundles, but mammalian bundles display much faster time constants to allow for transduction at yet higher frequencies (68). For example, turtle papillar hair bundles achieve a time constant of 0.4-0.75 ms (1,333-2,500 s^{-1}) under extreme differences in Ca^{2+} conditions, well above the 1 kHz upper frequency bound for turtle audition (67, 69). Mammalian cochlear hair

bundles, on the other hand, achieve time constants below 50 μs, empowering them to detect stimuli in the kilohertz range (67). Taken together, the kinetics of direct channel gating permit transduction at speeds required for audition, a feature neither required nor possible with other classic sensory modalities.

In series with each mechanoelectrical transduction channel lies an elastic element called a gating spring (Figure 2.2a). The gating spring may comprise the tip link, elastic components in the adaptation motor complex, and other associated proteins and lipids. In the gating-spring model, tension in a series elastic element increases the probability of channel opening (67, 70). This provokes a gating element of the transduction channel to swing open over some distance d. To achieve this, the system must cross a free energy barrier ΔG_{OC} defined by

$$\Delta G_{OC} = G^O - G^C = \Delta\mu - \Delta G_{GS}(X), \tag{2.2}$$

in which G^O is the free energy of the open state of the channel, G^C is the energy of its closed state, $\Delta\mu$ is the free energy difference between the two states in the absence of a gating spring, and $\Delta G_{GS}(X)$ is the energy in the gating spring as a function of the bundle position X (67). Equation 2.2 can be redefined according to the mechanical properties of the gating spring, yielding

$$\Delta G_{OC} = \Delta\mu - K_{GS} d(\gamma X + x_r). \tag{2.3}$$

Here K_{GS} is the stiffness of the gating spring, γ is a geometric factor relating the extension of the gating spring to deflection of the bundle, and x_r is the extension of the gating spring at rest (67). The geometric factor is approximately equal to the mean distance s between each stereocilium at the base divided by the height h at which the

gating spring resides. This factor is roughly 0.14 in the bullfrog's sacculus (71), 0.06 in the turtle's basilar papilla (72), and 0.05 in the mouse's utriculus (73). The geometric factor also manifests a tonotopic change along the length of cochleae, ranging from 0.17 at the high-frequency end to 0.67 at the low-frequency end in the chick (s = 1 μm, h = 1.5-6 μm), 0.06-0.2 in the Tokay gecko (s = 1 μm, h = 5-16 μm), and 0.03-0.88 in the alligator lizard (s = 1 μm, h = 12-30 μm) (74, 75). ΔG_{OC} depends on γ, in which an increase in γ increases the gating force and decreases the free energy barrier (equation 2.3). Thus, a tonotopic decrease in bundle height from low to high frequency yields a larger geometric gain and an easier barrier crossing.

At equilibrium, the probability of channel opening can be approximated by the Boltzmann relation (76)

$$P_O = \frac{1}{1+\exp\{\Delta G_{OC}/k_BT\}} = \frac{1}{1+\exp\{[\Delta\mu - K_{GS}d(\gamma X + x_r)]/k_BT\}}. \tag{2.4}$$

Here the open probability follows a sigmoidal relationship with hair-bundle position X (Figure 2.2b). In other words, a positive increase in bundle deflection increases gating-spring tension that in turn promotes channel opening in a nonlinear fashion. The open probability can also be defined according to the force required to open a channel, $z = \gamma K_{GS} d$, by the following relationship

$$P_O = \frac{1}{1+\exp\{-z(X - X_O)/k_BT\}}, \tag{2.5}$$

in which X_O is the bundle's position for an open probability of 0.5. At rest, an amphibian vestibular hair bundle achieves an open probability of approximately 0.15 (Figure 2.2b)

(76). The model also predicts that the bundle acts as a low-pass filter with a cutoff frequency that depends on the rates of channel opening and closing (77). The gating-spring hypothesis thus provides a unique tool to quantitatively describe the kinetics of direct channel gating in hair bundles.

What is the molecular identity of the mechanoelectrical-transduction channel? The question remains unanswered, but interrogations by many groups may present an answer within the next few years. An early channel candidate was a member of the epithelial sodium channel (ENaC) family, implicated in both arterial baroreception and touch reception in the roundworm *Caenorhabditis elegans* (78, 79). Anti-ENaC antibodies label stereociliary tips (80), and amiloride, a direct inhibitor of the ENaC channel, effectively blocks hair-bundle mechanotransduction (81, 82). However, ENaC channels with a conductance of 10-15 pS cannot account for the large conductance of 80-300 pS observed in hair bundles, nor for the Ca^{2+} permeability of the hair-bundle mechanoelectrical transduction channel (83). Additionally, amiloride displays a higher affinity for the bundle's transduction channel than it does for members of the ENaC family (84). Although *in situ* localization of ENaC demonstrated expression in the cochlear partition, the metaphorical nail in the coffin for the ENaC family arose from its complete absence in hair cells (85, 86).

Promising channel candidates include members of the transient receptor potential (TRP) family. These channels are responsible for the sensation of pain, stretch, hydrodynamic flow, temperature, capsaicin, light, and taste, along with the regulation of divalent-cation homeostasis in various cell types (87-90). The first of these channels to be

identified as part of a mechanoelectrical transduction apparatus was nompC (TRPN1), so called because fruit flies bearing a mutation in the channel exhibited *no* *m*echanoreptor *p*otential in their bristles. Consistent with a role for nompC as a hair-bundle transduction channel, mutant flies exhibited significant hearing defects (91). Although nompC plays a role in hair-cell mechanotransduction in *Xenopus* (92) and *Danio rerio* (93), the TRPN1 gene is absent from mammals and birds. Thus, it cannot mediate mechanotransduction in higher vertebrates (94).

However, the TRP family is large, and more candidates exist within this group of mechanosensitive channels. Another channel contender was TRPA1 (ANKTM1 in *Drosophila*), a cold-sensing channel that resides in nociceptive neurons (95). Although localization and RNAi screening reinforce the hypothesis of TRPA1 as the mechanotransduction channel (96), TRPA1 knockout mice exhibited no auditory defects and featured only a reduced sensitivity to mustard oil (97). Thus, TRPA1 would be an attractive channel candidate only if a second protein could compensate for its loss of function.

A particularly auspicious pair of channel candidates includes the transmembrane channel-like (TMC) protein isoforms 1 and 2 (TMC1 and TMC2). Individual TMC knockouts alter mechanotransduction-channel conductance (98, 99). However, recent work has shown that TMC knockouts exhibit large currents when mammalian hair bundles are displaced in the negative direction (100). The debate accordingly centers around the question of whether these proteins are the pore-forming subunits of the

channel or chaperones that assist in localization of the mechanotransduction channel to each stereociliary tip (99, 101).

Whatever the identity of the mechanoelectrical transduction channel, its kinetic properties remain at the core of hair-bundle dynamics as described here. Nonlinear and rapid gating of high-conductance channels permits the robust responsiveness of hair bundles. However, with a change in environment or stimulus magnitude, a bundle must adapt to both avoid damage and maintain its high sensitivity.

Figure 2.1. Anatomy of a hair bundle. (a) A hair bundle protrudes from the apical surface of a hair cell. Hair bundles are composed of tens to hundreds of cylindrical, actin-filled stereocilia (orange) and may or may not contain one true cilium, the kinocilium (brown) with an associated kinociliary bulb (purple). The hair bundle inserts into the hair cell through an actin-based cuticular plate (green). Positive deflection, toward the bundle's tallest edge, causes a shearing motion between adjacent stereocilia that increases tension on tip links (blue) between each stereocilium and its taller neighbor (*inset*). Increased tip-link tension induces the influx of cationic current, depolarizing the hair cell. This leads to synaptic transmission between the hair cell and an afferent neuron at the basolateral surface of the cell's soma (light brown). In some species (*e.g.* anurans) and classes of hair cells (*e.g.* mammalian outer hair cells), efferent neurons synapse onto hair cells (dark brown). (b) Expanding the tips of two neighboring stereocilia reveals the transduction apparatus. Each stereocilium is tightly packed with an array of actin filaments (light green). A mechanoelectrical-transduction channel (dark green) at the tip of one stereocilium is coupled to the side of a taller neighboring stereocilium through a tip link (blue) composed of a dimer of dimers of cadherin-23 and protocadherin-15. Positive deflection of the hair bundle increases tension in the tip link, opening the transduction channel and allowing an influx of K^+ and Ca^{2+}. A myosin-1c motor complex (purple) permits adaptation by adjusting of tip-link tension.

a

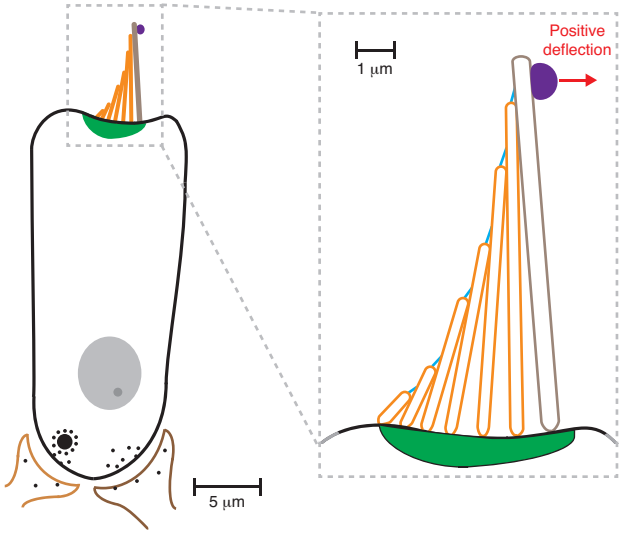

b

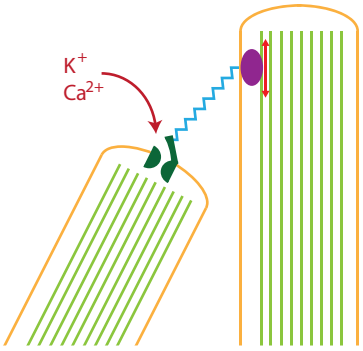

Figure 2.2. The gating-spring model of bundle mechanotransduction. (a) A mechanoelectrical transduction channel (green) is in series with a gating spring (blue) of stiffness K_{GS}. Excitatory stimulation of the bundle in the positive direction along its axis of symmetry increases the tension in the gating spring (red, F_{GS}), which causes the channel to open with a gating swing of length d. (b) The open probability of a channel increases with bundle position according to equation 2.4, in which $\Delta\mu$ = 43 zJ, K_{GS} = 450 $\mu N \cdot m^{-1}$, γ = 0.14, d = 4 nm, x_r = 20 nm, and T = 298 K. The open probability follows a sigmoidal relation from zero to one. At rest (X = 0), the open probability is approximately 0.15 (blue).

a

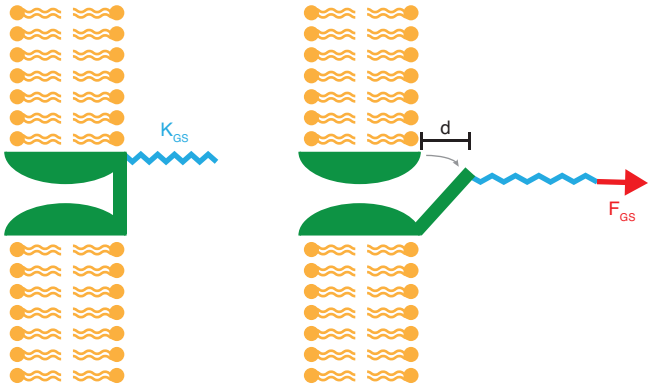
K_{GS}
d
F_{GS}

b

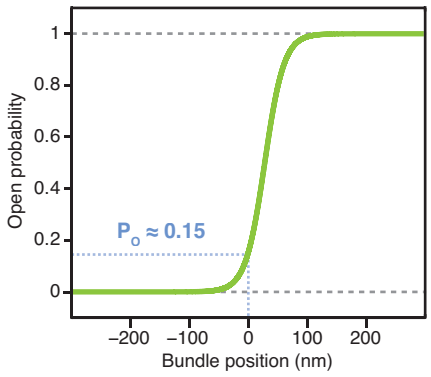
Open probability
1
0.8
0.6
0.4
0.2
0
$P_O \approx 0.15$
−200
−100
0
100
200
Bundle position (nm)

SECTION 2.2: *Hair-Bundle Adaptation*

In response to a persistent mechanical stimulus, the receptor current of a bundle decays over time. This decay is bimodal and comprises two time constants: a fast timescale of a few milliseconds to less than one millisecond and a slow timescale of tens of milliseconds or more (102). These processes, designated fast and slow adaptation, correspond to distinct mechanisms.

Slow adaptation occurs when a bundle gradually moves in the same direction as its stimulus (Figure 2.3). This causes a shift in the operating range of the bundle, permitting it to remain sensitive to additional stimuli (103, 104). This form of adaptation occurs through a mechanism that decreases tension in the gating spring, yielding a corresponding decrease in the magnitude of transduction current (70). A myosin-1c motor complex that decreases or increases gating-spring tension by respectively slipping or climbing along actin filaments achieves this behavior (105). Slipping occurs when Ca^{2+} influx through the mechanoelectrical-transduction channels promotes myosin-1c detachment from actin and gating-spring tension exceeds the stall force of the motor complex. Elimination of Ca^{2+} influx permits myosin-1c attachment to actin and thus allows the motor complex to restore resting tension. This asymmetry is particularly striking in that the rate of motor slipping is dependent on displacement whereas the rate of climbing is fixed (103).

Fast adaptation occurs at a timescale of a few milliseconds at most and is poorly understood. Unlike slow adaptation, fast adaptation is independent of myosin ATPase activity (106). Two proposed models of fast adaptation include the *channel-reclosure*

model and the *release-element model* (102). In the channel-reclosure model, Ca^{2+} directly binds to or near the transduction channel, causing the channel to close (Figure 2.4a). Channel closure increases tension in the gating spring, which causes the bundle to rapidly withdraw in the negative direction. In the release-element model, Ca^{2+} binds to an elastic element with Ca^{2+}-dependent stiffness (Figure 2.4b). Binding causes a reduction in the release element's stiffness, propelling the bundle farther in the positive direction. The channels are then allowed to close, displacing the bundle again in the negative direction and completing a biphasic movement (102). The mechanism of fast adaptation is under rigorous scrutiny and should be elucidated within the next few years.

Figure 2.3. Mechanism of slow adaptation. A hair bundle initially responds to a positive stimulus force pulse with a rapid movement (*a*-*b*). This increases tension in the in tip-link (light blue), inducing a negative peak in transduction current. Because tension on the tip links overcomes the stall force of a myosin-1c motor complex (purple), the motor complex slides downward along the side of the taller stereocilium (*c*), allowing the bundle to displace farther in the positive direction. Since downward sliding of the adaptation-motor complex reduces tip-link tension, the transduction current becomes less negative. At the offset of a force pulse, the bundle first rapidly moves in the negative direction and its transduction current rises (*d*-*e*). Because the position of the adaptation complex has changed relative to its position prior to the onset of stimulation, the transduction current falls below its resting value. With tip-link tension now less than the stall force of the motor complex, adaptation motors climb along the lateral side of the taller stereocilium (*f*). This gradually decreases both the offset and transduction current of the bundle.

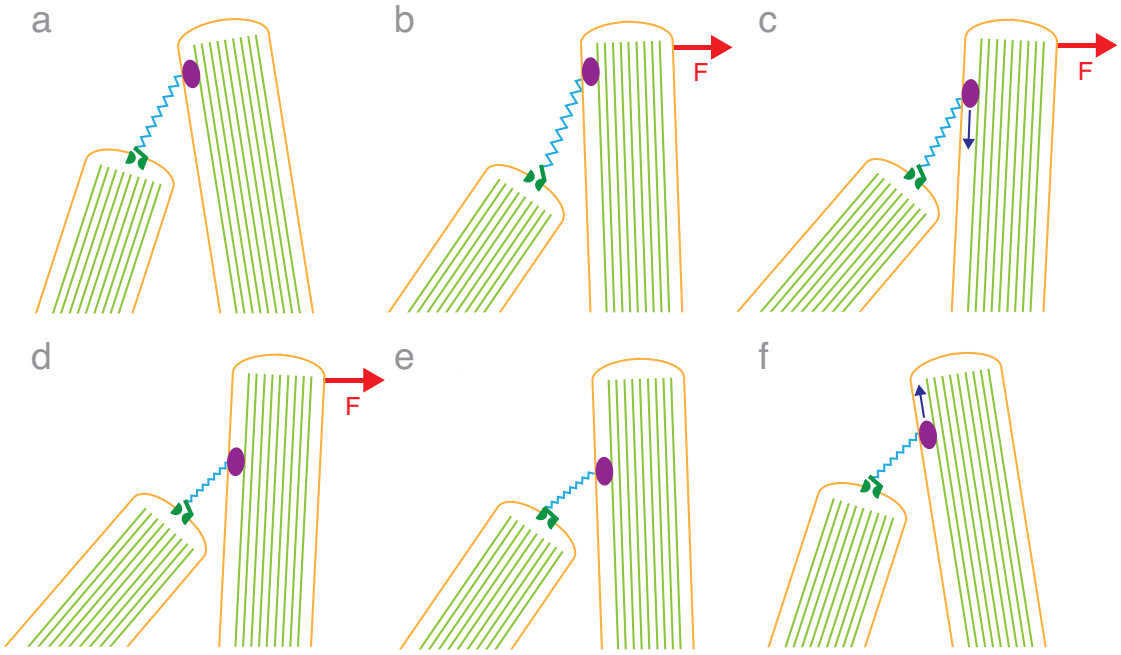
a
b
F
c
F
d
F
e
f

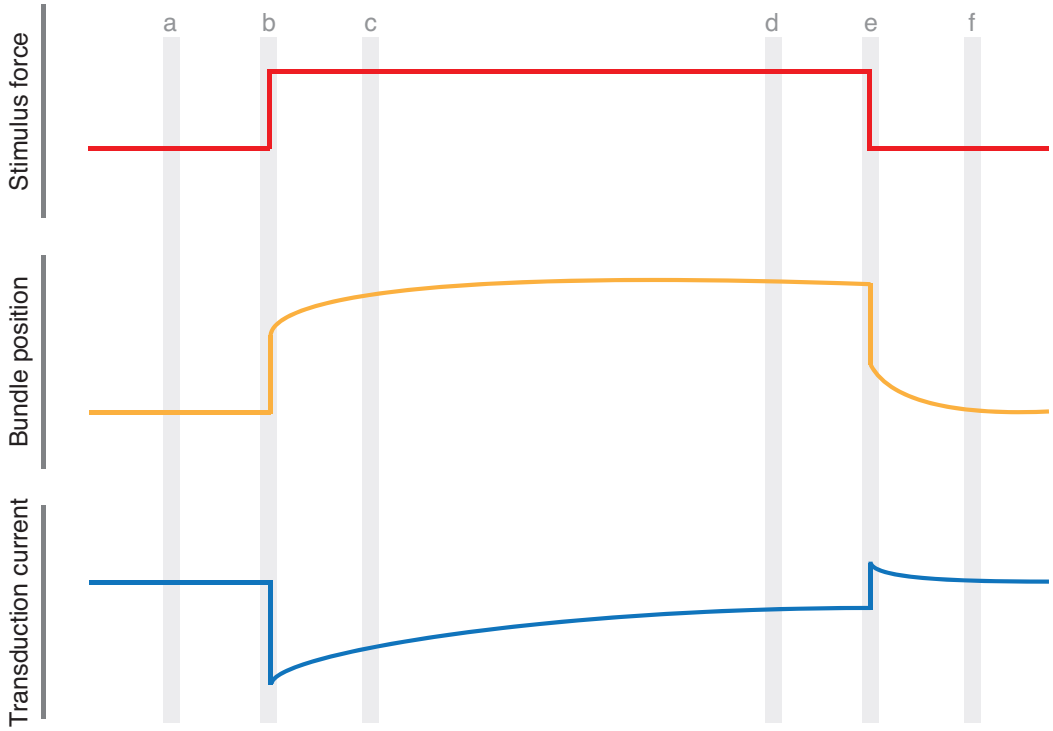
a
b
c
d
e
f
Stimulus force
Bundle position
Transduction current

Figure 2.4. Models of fast adaptation. (a) In the *channel-reclosure* model of fast adaptation, a positive force step increases the open probability of transduction channels. Ca^{2+} (red) binds onto or near the transduction channel (green), inducing a negative movement of the hair bundle. A trace of the bundle's position in response to a force pulse depicts the biphasic motion as a result of passive mechanics, channel reclosure, and slow adaptation (right). (b) In the *release-element* model of fast adaptation, a positive force step again induces Ca^{2+} influx. Here Ca^{2+} binds to an elastic release element (dark blue) in series with the transduction channel. This binding slackens the release element, causing a movement in the positive direction. As with the model in (a), channel closure results in negative bundle movement. A trace of the bundle's position in response to a constant force pulse reveals the same biphasic motion in (a) but with the addition of a release element (right).

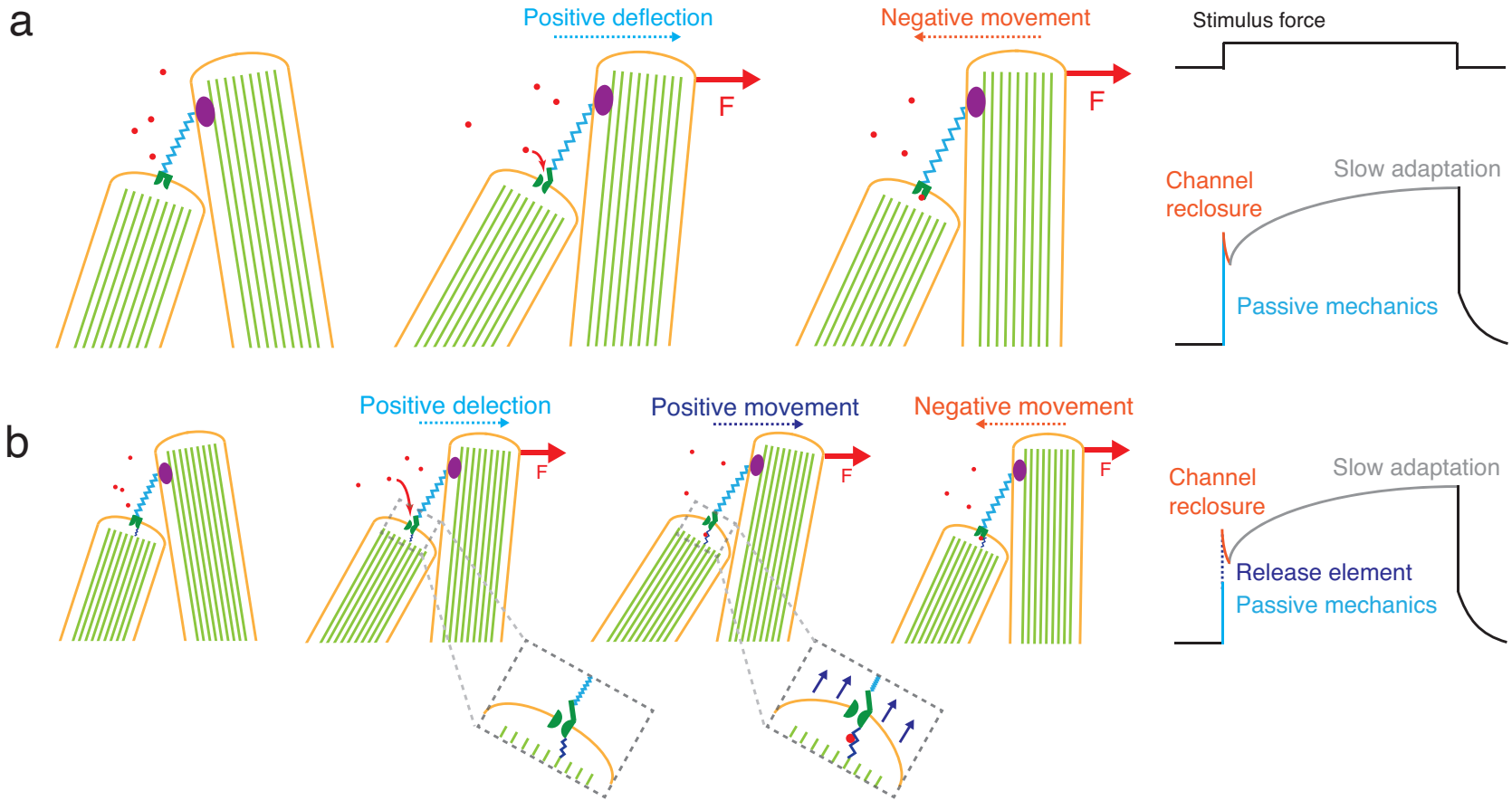
a
Positive deflection
Negative movement
F
F
Stimulus force
Channel reclosure
Slow adaptation
Passive mechanics
b
Positive delection
Positive movement
Negative movement
F
F
F
Channel reclosure
Slow adaptation
Release element
Passive mechanics

SECTION 2.3: *The Force-Displacement Relation*

Like the cochlea itself, hair bundles feature nonlinear behavior (107-110). Within the range of displacements for which channel gating occurs, a bundle exhibits reduced stiffness, a phenomenon termed gating compliance (108). To quantify this behavior, one can deliver forces to a hair bundle with a flexible glass fiber and record the bundle's response. A sudden displacement of the fiber's base causes a bundle coupled to the fiber's tip to move a certain distance. The force delivered by the fiber onto the bundle follows the relation

$$F_{SF} = K_{SF}(\Delta - X), \tag{2.6}$$

in which K_{SF} is the stimulus fiber's stiffness, Δ is the position of the base of the fiber, and X is the bundle's position. By delivering a series of pulses to a bundle and measuring its response rapidly enough to be faster than the time constant of slow adaptation ($\tau_{slow} < 50$ ms) and with a delay longer than the time constant required for the bundle to reach steady state ($\tau_{ss} = 100$ μs in the bullfrog's sacculus (67)), an experimenter can define the relationship between the force delivered to the bundle and its position (108, 111).

This force-displacement relation reveals a bundle's stiffness (Figure 2.5a). At the most positive and negative positions—with all channels either open or closed—the bundle behaves like a linear, Hookean spring. For intermediate positions, however, the curve becomes nonlinear. Nonlinear force-displacement relations have been revealed for hair bundles in amphibians (108, 109), reptiles (112), and mammals (113, 114), implying a preservation of nonlinear channel gating across otherwise divergent organs and

organisms. The gating-spring model affirms a mechanism for reduced bundle stiffness within the range of displacements for which channel gating operates. An increase in the force applied to a bundle increases the open probability of the mechanoelectrical-transduction channel. Channel opening subsequently decreases gating-spring tension and produces a gating force z. On the contrary, an inhibitory (negative) force decreases the transduction channel's open probability and channel closure increases gating-spring tension (108).

For N identical channels, the force exerted on the hair bundle for a displacement X can be approximated by

$$F = K_{\infty}X - NzP_O + F_O, \tag{2.7}$$

in which K_∞ is the bundle's stiffness for an open probability P_O equal to one or zero and is the sum of the gating-spring stiffness plus the combined stiffness of the stereociliary pivots, and $F_O = K_{GS}(x_r + \frac{d}{z})$. Because the open probability P_O is a sigmoidal function of X (Figure 2.2b), the force-displacement relation defined by equation 2.7 is also nonlinear and depends on channel gating. Indeed, blockade of transduction channels with aminoglycoside antibiotics abolishes the nonlinear shape of the force-displacement relation (108, 115).

As mentioned before, a hair bundle manifests increased compliance within the range of displacements for which channel gating can occur. The stiffness of a hair bundle follows the relation

$$K_{HB} = K_{\infty} - \frac{Nz^2}{k_B T} P_O (1 - P_O) . \quad (2.8)$$

Equation 2.8 predicts that a hair bundle's stiffness is minimal when half the transduction channels are open ($P_O = 0.5$) (67). Under appropriate ionic conditions, the stiffness of a bundle can even become *negative* (Figure 2.5a). Negative stiffness occurs when gating compliance surpasses the bundle's overall stiffness through cooperative opening of parallel transduction channels (Figure 2.5b) (116). As a result, an unstable region emerges. The bundle's operating point cannot reside at any position within the negative-stiffness regime because any small fluctuations will propel it onto a position of positive stiffness. Thus, a hair bundle displays one unstable operating point bounded by two stable points. It is this phenomenon combined with adaptation that grants hair bundles with the capacity to generate self-oscillations.

Figure 2.5. Negative stiffness. (a) A hair bundle exhibits *gating compliance* according to equations 2.7 and 2.8. In red, the bundle exhibits reduced stiffness over the region of channel gating. When P_O is zero or one, the bundle behaves as a linear elastic element. When the force of channel gating is doubled, the bundle's stiffness becomes negative within the region of channel gating (blue). Negative stiffness can occur when the gating force exceeds the bundle's passive stiffness $Z > \sqrt{\frac{4k_BTK_\infty}{N}}$ (67). In both cases, $\Delta\mu$ = 43 zJ, K_∞ = 680 μN·m^{-1}, γ = 0.14, d = 4 nm, x_r = 20 nm, N = 60, and T = 298 K. The force of channel gating is either z = 0.7 pN (red) or z = 1.4 pN (blue), and F_O is either 0 pN (red) or 20 pN (blue). (b) Negative stiffness arises from the cooperative opening of parallel transduction channels (116). Here three channels are in parallel with one another. Though each channel typically resides on a different stereocilium, they are shown here on a single membrane for ease of visualization. When a force F is applied to the channels, the bundle first moves a small distance dictated by the stiffness of the gating springs. An increase in gating-spring tension increases the open probability of each channel. When one channel opens, the gating spring in series with that channel slackens, propelling the bundle farther in the positive direction. The force is now distributed across the remaining gating springs. This further increases the open probability of each remaining channel and causes each to open, causing additional positive displacement. Though the force F is constant, the bundle moves farther than predicted for a simple linear spring.

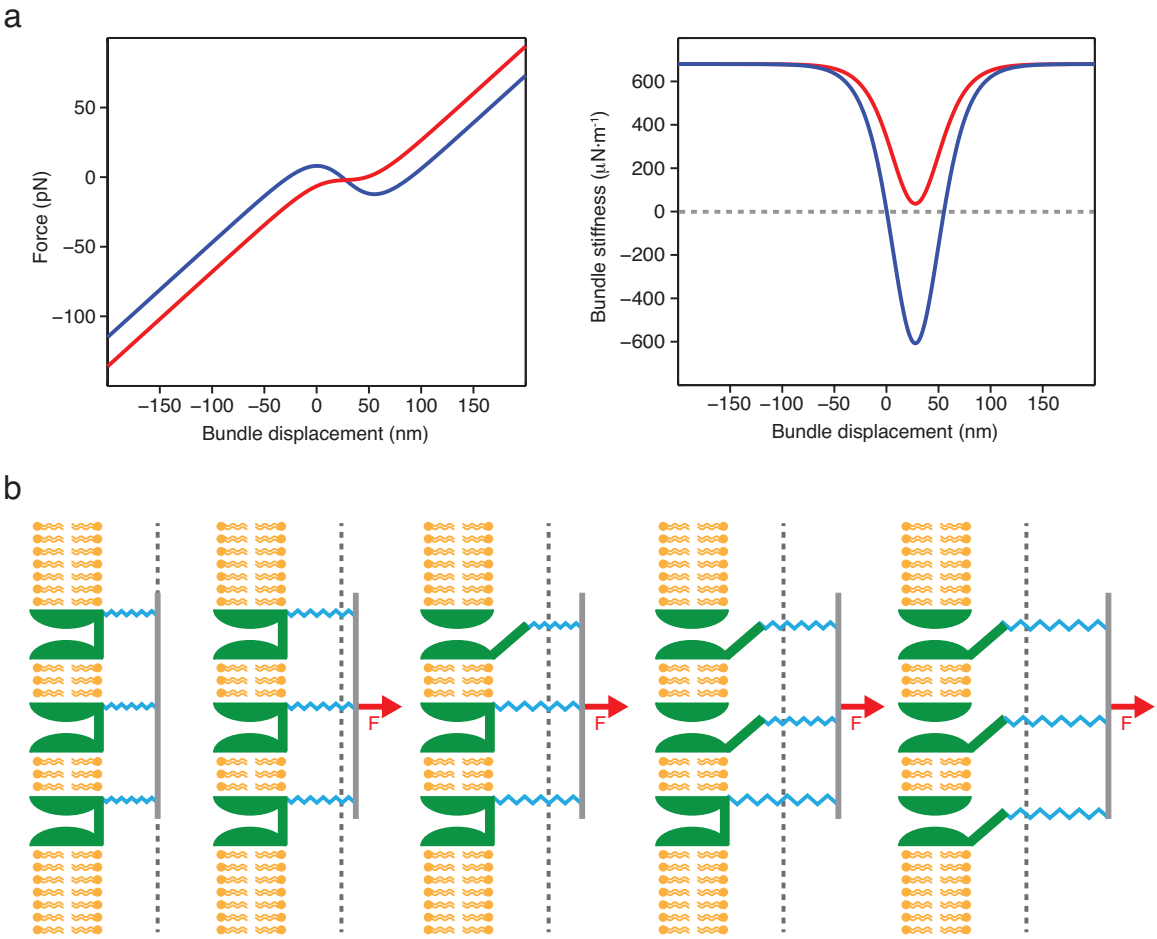
a
Force (pN)
50
0
−50
−100
−150 −100 −50 0 50 100 150
Bundle displacement (nm)
Bundle stiffness (μN·m⁻¹)
600
400
200
0
−200
−400
−600
−150 −100 −50 0 50 100 150
Bundle displacement (nm)
b
F
F
F
F

SECTION 2.4: *An Active Process in Hair Bundles*

Hair bundles respond actively to mechanical signals. Like the cochlea, bundles employ an active process characterized by amplification, frequency tuning, compressive nonlinearity, and spontaneous oscillation. The active process persists across species, but the mechanism by which it is regulated remains poorly understood. The study presented in later chapters directly addresses the problem of active-process control. For now, let us systematically consider each component of a hair bundle's active process.

Sensory hair bundles are active motors, capable of producing work and oscillating spontaneously (117). Spontaneous hair-bundle oscillations have been observed in the hair bundles of fish (118). amphibians (119), and reptiles (120). In the bullfrog's sacculus, these oscillations range in frequency from 5 Hz to 100 Hz and in amplitude to 50 nm or more (67, 115). Interestingly, spontaneous oscillations are non-sinusoidal: they resemble relaxation oscillations (*see* Chapter 3), yielding a bimodal probability distribution also encountered in the spontaneous otoacoustic emissions of frogs (121), lizards (122), and humans (123). Moreover, both the spontaneous oscillations of hair bundles and the spontaneous otoacoustic emissions are controlled by the endolymphatic Ca^{2+} concentration (124-126). The resemblance between self-oscillations of hair bundles and otoacoustic emissions suggests a link between the active process in hearing and active force generation by hair bundles.

The mechanism by which spontaneous oscillations can occur is revealed through an interplay between a domain of negative stiffness and an adaptive shift of the force-displacement relation (Figure 2.6) (127). As mentioned before, a bundle's operating point

cannot reside within the unstable neighborhood of its force-displacement curve. Instead, it must dwell within one of two stable sectors. When no force is applied to the bundle and most transduction channels are open, the bundle moves to a position more positive than that at which the adaptation motor would achieve a steady state. As a result, a myosin-1c motor complex slips down the side of each taller stereocilium to slowly adapt the bundle's position farther in the positive direction. Slow adaptation yields an adaptive shift of the force-displacement relation along a slope defined by the stiffness of the bundle's stereociliary pivots (128). The positive-displacement stable point subsequently vanishes when the relation crosses the abscissa. This causes the bundle to propel itself back across the unstable region to the negative-displacement stable point. Here most transduction channels are closed, fostering slow adaptation in the negative direction. This causes the force-displacement to shift once again, but in the opposite direction. As before, the negative-displacement local maximum ultimately crosses the abscissa, hurling the bundle in the positive direction and onto a positive-displacement stable point. This cycle generates spontaneous relaxation oscillations, with a slow phase corresponding to the rate of slow adaptation and the a phase arising from switching between two stable positions defined by the force-displacement curve.

Spontaneous oscillations of hair bundles are not futile phenomena. By delivering a force at least 3 pN in amplitude, even robust oscillations will phase lock to the stimulus (129). As the force increases, the amplitude and shape of the bundle's response change. This pattern mimics the behavior of auditory nerve fibers in fish (130), amphibians (131), and birds (132), in which the neuronal firing rates do not increase

until a stimulus exceeds a value about 10 dB greater than the threshold of phase locking. Entrainment permits active amplification of small stimuli with fine frequency tuning by hair bundles, yet another crucial component of an auditory active process. An open problem prior to this study is the mechanism by which amplification and tuning can be controlled. Furthermore, can quiescent hair bundles amplify stimuli with at least the same quality as actively oscillating ones?

Finally, hair bundles manifest compressive nonlinearity. Compression permits the auditory system to reduce the range of responses over a broad range of stimulus magnitudes. For stimuli of increasing force near a bundle's frequency of spontaneous oscillation, one can calculate sensitivity as the magnitude of the bundle's linear response function

$$\tilde{\chi}(\omega_S) = \frac{\left\langle \tilde{X}(\omega_S) \right\rangle}{\tilde{\Delta}(\omega_S)(K_{SF} + i\omega_S \xi)}, \tag{2.9}$$

in which $\left\langle \tilde{X}(\omega_S) \right\rangle$ is the expectation value of the bundle's Fourier component at the frequency of driving ω_S, $\tilde{\Delta}(\omega_S)$ is the Fourier component of the stimulus fiber's base at the driving frequency, K_{SF} is the fiber's stiffness, and ξ is the combined viscous force acting on the fiber (129). If the bundle's response grows linearly with the magnitude of the stimulus force, a sensitivity-force relation features a slope of zero. If the bundle's phase-locked response grows less rapidly than the magnitude of the stimulus force ($\left|\left\langle \tilde{X}(\omega_S) \right\rangle\right| \propto F_S^a$ with $a < 1$), the slope becomes negative ($\left|\tilde{\chi}(\omega_S)\right| \propto F_S^b$ with $b < 0$). Indeed, micromechanical stimuli delivered to individual hair bundles from the bullfrog's

sacculus reveal a compressively nonlinear behavior for a range of stimulus forces (129). The relationship between sensitivity and stimulus force follows $\left|\tilde{\chi}(\omega_S)\right| \propto F_S^{-2/3}$, a power law consistent with behavior near a supercritical Hopf bifurcation (*see* Chapters 3 and 4). Taken together, a hair bundle exhibits features of an active process consistent with that present in the cochlea. In part of this study, I show that imposing different mechanical loads on a hair bundle can control each feature of the active process in hair bundles. If active hair-bundle motility relies on these loads, then how do the *in vivo* mechanical properties of hair bundles differ across organs and genera?

Figure 2.6. Mechanism of spontaneous oscillations. A hair bundle's force-displacement relation is shown at the top with the same parameter values as in Figure 2.5 but shifted along a line defined by the stiffness K_{SP} of the bundle's stereociliary pivots (dashed purple line). At position (1), the bundle resides at a positive (excitatory) position with a majority of its transduction channels open. Slipping of myosin-1c motors causes the hair bundle's force-displacement curve to shift in the positive direction (*cyan* to *red*). At point (2), the stable point on the abscissa crosses zero and vanishes. This causes the bundle to leap back to a negative-displacement stable point (3). With the bundle now in the negative (inhibitory) direction, slow adaptation promotes channel opening by shifting the force-displacement relation farther in the negative direction (*red* to *cyan*). Eventually, the local maximum crosses the abscissa (4) and vanishes, vaulting the operating point back onto a positive-displacement stable point (1). A diagram of the bundle's relaxation oscillation illustrates the fast and slow dynamics resulting from the aforementioned model (*from* (109)).

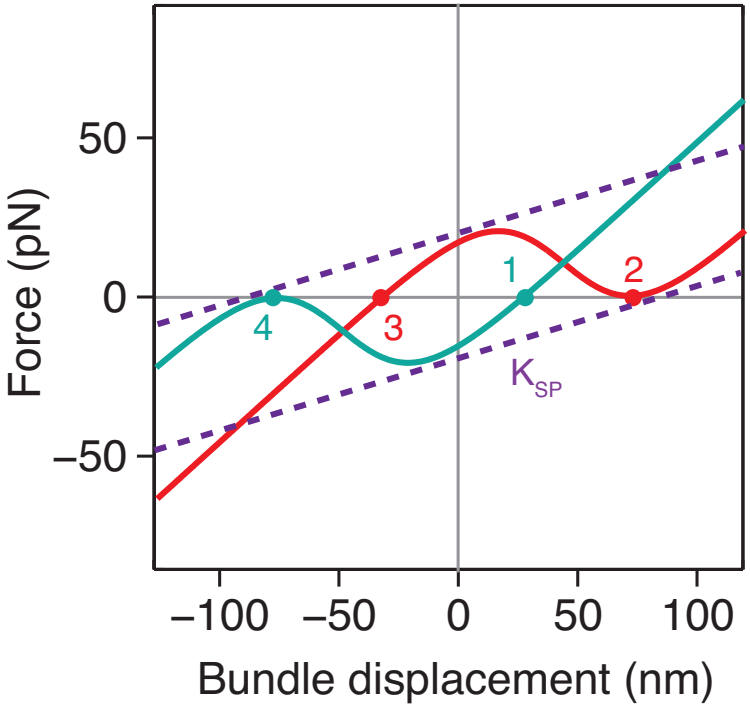
50
0
−50
Force (pN)
−100
−50
0
50
100
Bundle displacement (nm)
1
2
3
4
K_{SP}

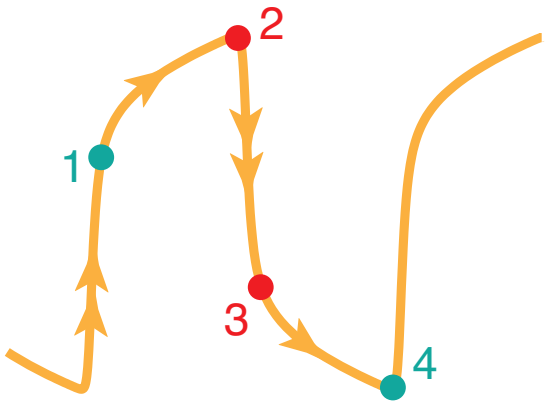
1
2
3
4

SECTION 2.5: *The Mechanical Properties of Hair Bundles*

Hair bundles can detect auditory stimuli in the sensory papillae of frogs, turtles, lizards, and birds, and the organs of Corti in mammals (69). They also sense hydrodynamic forces in the lateral-line systems of fish and accelerational forces in vestibular organs. In the tympanal organ of insects, mechanosensitive cilia respond to periodic forces. Although all hair bundles encompass similar molecular constituents, their mechanical properties differ. Despite these differences, all of these mechanoreceptors employ an active process (33, 67, 114, 133, 134), and a change in a bundle's architecture and its mechanical load correlates with its sensory function. Has evolution provided a mechanism by which to control hair-bundle function by changing a bundle's mechanical properties? To answer this question, let us first consider the morphology of mechanoreceptive organelles in insects, as well as in amphibians, reptiles, birds, and mammals (Table 2.1).

In the tympanal organs of insects, sensory cilia are long, thin, and contain true cilia. In the hair bundles of neuromasts in the fish lateral-line system, hair bundles include short stereocilia but long kinocilia. The auditory and vestibular hair bundles of frogs, turtles, and lizards are isodiametric in cross-section and also incorporate kinocilia. In the basilar papillae of birds, hair bundles again involve kinocilia but the bundles instead appear ovoid or band-shaped. Finally, in the mammalian cochlea, inner hair cell bundles look fan-shaped and outer hair cell bundles assume a V-shaped appearance, with neither incorporating a kinocilium. Along with a change in shape comes a distinct pattern in height. Hair bundles of fish, turtles, and frogs are approximately 5-10 μm in

height (108, 120, 129, 135, 136), whereas those of lizards reach heights of 12-30 μm (137). In avian species, bundles reside on either short hair cells or tall hair cells whose bundles achieve lengths that vary tonotopically from 1.5 μm at the high-frequency end to 5.5 μm at the low-frequency end (138). Mammalian cochlear hair bundles are shorter than their amphibian cousins, and bundle heights also vary tonotopically from less than 1 μm to as great as 5 μm (139, 140).

Differences in hair-bundle height confer expected changes in a bundle's stiffness. In the bullfrog's sacculus, a hair bundle treated with 1,2-bis(o-aminophenoxy)ethane-N,N,N′,N′-tetraacetic acid (BAPTA) exhibits a linear stiffness of approximately 500 $\mu N \cdot m^{-1}$ (115). A bundle within the turtle's basilar papilla displays a stiffness of 600 $\mu N \cdot m^{-1}$, near that of a bullfrog's saccular hair bundle (120). However, hair bundles in other sensory organs manifest larger stiffnesses. The bundle of a short hair cell from the avian basilar papilla shows a stiffness of approximately 1,000 $\mu N \cdot m^{-1}$ (138). In the mammalian cochlea, OHC bundles can be even stiffer, ranging from greater than 4,000 $\mu N \cdot m^{-1}$ near the base to less than 1,000 $\mu N \cdot m^{-1}$ near the apex (114). The tonotopic gradient in stiffness along the cochlea indicates that a hair bundle's mechanical properties tuned to achieve an appropriate resonant frequency. Bundle morphology also bestows a distinct drag coefficient. Vestibular bundles of the bullfrog's sacculus possess drag coefficients of around 200 $nN \cdot s \cdot m^{-1}$ (108), whereas auditory bundles of the mammalian cochlea exhibit a drag coefficient of only 50 $nN \cdot s \cdot m^{-1}$ (141).

Morphological differences between hair bundles beget particular responses to periodic stimuli (Table 2.1). For a damped oscillator, the resonant frequency f_{HB} and quality factor Q_{HB} at resonance are

$$f_{HB} = \sqrt{\frac{K_{HB}}{m_{HB}}}, \tag{2.10}$$

$$Q_{HB} = \sqrt{\frac{m_{HB}K_{HB}}{\xi_{HB}}}, \tag{2.11}$$

in which m_{HB}, ξ_{HB}, and K_{HB} are respectively the bundle's mass, drag coefficient, and stiffness. A hair bundle endowed with a low drag coefficient and high stiffness attains a higher resonant frequency and sharper quality of resonance. On the contrary, more compliant bundles with higher drag coefficients achieve lower frequencies and poorer qualities. Indeed, frog vestibular hair bundles respond to frequencies of 5-150 Hz, but the stiffest mammalian hair bundles can respond to frequencies exceeding 100 kHz (69). In Table 2.1, the quality of resonance is defined as

$$Q_{10dB} = \frac{f_C}{\Delta f_{10dB}}, \tag{2.12}$$

in which f_C is the center frequency and Δf_{10dB} is the bandwidth at an amplitude 10 dB below the resonant peak. Though equations 2.11 and 2.12 employ different definitions of quality, these two operational definitions are roughly proportional. In the bullfrog's sacculus and amphibian papilla, a hair bundle responds to a periodic stimulus with a Q_{10dB} of 0.7-2 (69, 129). As predicted, mammalian auditory hair bundles can achieve a much higher Q_{10dB} of 5.5 (69). Overall, bandwidths of hair-bundle response range from 5-150 Hz in amphibian vestibular organs through 20-100,000 Hz in mammalian auditory

organs (139), and qualities of resonance range from Q_{10dB} = 0.4 in the fish lateral-line system (142) through Q_{10dB} = 5.5 in the mammalian auditory system (69, 143). Although the processes of mechanoelectrical transduction are preserved across genera, hair-bundle responses differ greatly.

The microenvironment in which a hair bundle resides also varies across sensory organs (Table 2.1). Hair cells rest on a basilar membrane in the cochleae of turtles, lizards, birds, and mammals, but the membrane is mechanically tuned only in the mammalian cochlea (69). The basilar membrane is absent in insects, fishes, and amphibians. The apical surfaces of hair bundles couple directly to otolithic membranes in sacculi and utriculi, cupulae in neuromasts and semicircular cristae, tectorial membranes in basilar papillae and the organ of Corti, or sallets in lizard basilar papillae. Additionally, free-standing hair bundles can be observed within the basilar papillae of some lizards or on IHCs in the organ of Corti. Each apical structure imparts a mechanical load on a hair bundle. The otolithic membrane of the bullfrog sacculus displays an elemental stiffness of approximately 1,000 $\mu N \cdot m^{-1}$ (144), and an aggregate of calcium carbonate crystals—otoconia—imparts a mass load of about 5 mg per ear, or of 3-5 μg per bundle if evenly distributed. The mammalian tectorial membrane instead adds a much greater stiffness of 1-100 $mN \cdot m^{-1}$ and a mass load of 35-100 ng per hair-cell row, with each of these parameters possessing a tonotopic gradient (17). As mentioned previously, the mechanical load imparted by the tectorial membrane varies tonotopically. These data suggest that the mechanical load imposed on an individual hair bundle controls its sensory behavior.

Given this information, one might predict that active hair-bundle motility can account for all features of an active process. Although this is true in principle, sensory organs evolved to incorporate additional features not present in lower chordates (Table 2.1). For example, a basilar membrane is absent in frogs and is tuned only in mammals. Additionally, a voltage-dependent somatic length change known as electromotility or somatic motility can be found only in the mammalian cochlea (145). Electromotility may permit hair-cell responsiveness at speeds required for high-frequency auditory sensation (21, 30, 34, 146). Interestingly, mammalian cochlear hair bundles are the only examples listed in Table 2.1 that exclude a kinocilium (69). It is possible that the kinocilium serves a role in hair bundles that was subsequently replaced by prestin in mammals. The role of active hair-bundle motility in mammals may persist, but the bundle's amplificatory function has likely been superseded by somatic motility. Instead, mammalian hair bundles may inject an appropriately tuned nonlinearity that is later amplified by prestin to overcome viscous damping. In other words, somatic motility contributes high-speed amplification and hair-bundle motility tunes the system.

A study of an active process in hair bundles requires that hair-bundle motility be separated from all other potential contributors. Mammalian hair cells incorporate both flavors of motility, rendering them non-ideal. Additionally, the bundles of birds, lizards, and turtles are attached to a basilar membrane (Table 2.1). If a basilar membrane augments amplification, frequency selectivity, or compressive nonlinearity, these sensory organs must also be excluded. The organs that permit appropriate isolation of mechanoreceptor function include those of insects, fish, and frogs. Among these, the

bullfrog's sacculus is the best-studied organ, and it is ideal owing to its dual responsiveness to both periodic seismic or auditory stimuli and static vestibular stimuli. The sacculus also displays relatively low resonant frequencies, which is disadvantageous for statistical reasons but advantageous in technical terms.

Hair bundles manifest extraordinary qualities from the coalescence of only two mechanisms: *direct channel gating* and *adaptation*. Across organs and genera, evolution has preserved these devices. However, hair-bundle function differs widely across these species. It is possible that the mechanical properties of bundles and their accessory structures confer the unique properties that give rise to these occupational differences. To model this behavior and provide a tractable experimental paradigm, we shall employ dynamical-systems theory.

Table 2.1. Hair-bundle properties. Listed are mechanical properties and behaviors of the mechanoreceptors of insects and the hair bundles of selected species. *Modified and expanded from (69).*

	Insect	Fish	Frog			Turtle	Lizard	Bird		Mammal	
Organ	*Tympanal*	*Neuromast*	*Sacculus*	*Amphibian papilla*	*Basilar papilla*	*Basilar papilla*	*Basilar papilla*	*Basilar papilla*		*Organ of Corti*	
Subclass								*SHC*	*THC*	*IHC*	*OHC*
Function	*Auditory*	*Hydrodynamic*	*Vestibular and Seismic*	*Auditory*	*Auditory*	*Auditory*	*Auditory*	*Auditory*		*Auditory*	
Shape	*Long cilia*	*Short hair bundle with long kinocilium*	*Isodiametric*	*Isodiametric*	*Isodiametric*	*Isodiametric*	*Isodiametric*	*Band-shaped or ovoid*		*Fan-shaped*	*V-shaped*
Kinocilium	Yes	Yes	Yes	Yes	Yes	Yes	Yes	Yes		No (Mature)	
Bundle Height (μm)	5	15	5-10	5-10	5-10	5-10	12-30	1.5-5.5		1-5	
Frequency Range (Hz)	1-1,000	<400	5-150	100-1,400	1,000-4,500	70-1,000	400-7,000	200-12,000		20-100,000	
Quality Factor (Q_{10dB})	1.9	0.4	0.7	2	1.4	3	3.5	5		5.5	
Apical Load	*Scolopale cap*	*Cupula*	*Otolithic membrane*	*Tectorial membrane*	*Tectorial membrane*	*Tectorial membrane*	*Tectorial membrane, sallets, or free-standing*	*Tectorial membrane*		*None*	*Tectorial membrane*
Basilar Membrane	No	No	No	No	No	Untuned	Untuned	Untuned		Tuned	
SOAE	?	N/A	No	Yes	?	?	Yes	Yes		Yes	
Electromotility	?	No	No	No	No	?	?	?		Yes	
Innervation	Afferent	Afferent	Both	Both	Afferent	Both	Both	Efferent	Afferent	Afferent	Both
References	(69, 147-149)	(136, 142, 150)	(1, 69, 108, 124, 129, 151)			(69, 120, 152)	(69, 137, 153)	(69, 138, 154)		(69, 139, 143, 145)	

CHAPTER 3

Survey of Dynamical Systems

What follows is a brief overview of concepts central to dynamical-systems theory. While this chapter functions as a guide to the mathematical foundations important in this study, it is not intended to encompass all details of the field. Instead, it supplies the theoretical bedrock for forthcoming hair-bundle models. To introduce these topics, the chapter commences with an introduction to phase portraits, delves into fundamental topics of bifurcation theory, and concludes with an introduction to a select sample of classic mathematical models.

SECTION 3.1: *Phase Portraits, Fixed Points, and Limit Cycles*

A *dynamical system* describes some process that evolves in geometrical space according to a fixed rule. Such an analysis proves particularly vital in complex nonlinear processes, including hair-bundle motility (155). A *phase portrait* captures the trajectory of this process and is thus a vital tool in dynamical-systems analysis.

To understand the geometry of a phase portrait, consider first a simple pendulum displaced from equilibrium (Figure 3.1a). At its most negative displacement, the pendulum displays a velocity of zero. Swinging forward, its velocity increases until it achieves a maximum positive velocity at zero displacement. As the pendulum swings farther in the positive direction, its velocity steadily decreases until it again reaches zero

at its most positive displacement. The pendulum then reverses its motion and achieves a maximum negative velocity at zero displacement. A phase portrait of position and velocity illustrates this motion (Figure 3.1b). When the pendulum is at its most negative and positive positions, the velocity is zero, and the velocity achieves its maximum and minimum at zero position. Hence, the position-velocity phase portrait traces a clockwise circle in phase space. A phase portrait of the real and imaginary parts of the pendulum's motion provides an alternative representation (Figure 3.1c). Here the imaginary component of the pendulum's motion reaches zero at the most negative and positive positions. However, unlike the position-velocity phase portrait, the real-imaginary phase portrait traces a counter-clockwise circle in phase space. Though not presented here, the shapes and instantaneous phases of the two phase-portrait representations depend on the amplitude and frequency of oscillation in different ways. For example, the vertical span of the position-velocity phase portrait roughly corresponds to the frequency of oscillation at a given amplitude, whereas this diameter does not change with frequency in the complex plane.

At zero position and without perturbation, the pendulum will perpetually reside at equilibrium. In the presence of damping, the pendulum's motion after perturbation will decrease in magnitude until it again resides at equilibrium. This is called a *stable equilibrium*, meaning that all trajectories will eventually reach this point (156, 157). In phase space, trajectories may cross maxima and minima that repel and attract nearby flows, respectively. These are called *unstable* and *stable* points. Consider a trajectory that follows $\dot{X} = -X^2 + 1$ (Figure 3.2a). Two fixed points are defined by $\dot{X} = 0$ at X^* = ±1. If

the initial condition resides at either of these points, the system will remain at that point indefinitely unless perturbed. However, flow along the trajectory near the fixed point at -1 departs from this fixed point. For example, at a position of -2, the velocity is -3, and the flow continues toward negative infinity. At a position of -0.5, the velocity is +0.75, and the flow progresses toward the fixed point at +1. Thus, this fixed point is unstable. The fixed point at +1 is stable, meaning that it attracts nearby flows along the trajectory. Small perturbations from a stable fixed point will result in a return to this stable equilibrium. Inverting the trajectory to $\dot{X} = X^2 - 1$ yields the same fixed points, but the stability of each is reversed (Figure 3.2b). Finally, in the case of $\dot{X} = -X^2$, there exists only one fixed point at zero (Figure 3.2c). In this scenario the fixed point attracts some of the flows and repels others. This is called a *saddle point* (158). Like the others, it is also a stationary point, but it is neither a local maximum nor local minimum. In other words, trajectories flow both into and out of a saddle point.

Let us now return to the oscillating pendulum. In the presence of damping, any perturbation to the oscillator results in a decay of its motion to a stable equilibrium. However, consider a scenario in which a motor is that controls both the amplitude and frequency of the pendulum's oscillation. When the motor is activated, the pendulum oscillates. Small perturbations to the pendulum transiently change its behavior, but its motion always returns to that prescribed by the motor. In phase space, the pendulum's trajectory again traces a closed loop, and all nearby flows are attracted to this loop, analogous to the aforementioned stable fixed point. This is called a *stable limit cycle* (159). An *unstable limit cycle* is also an isolated periodic orbit, but it encompasses a local

maximum with flows departing from it, analogous to an unstable fixed point. Limit cycles describe the oscillatory motion across a broad array of dynamical systems. As will be shown, they can also describe the spontaneous motion of active hair bundles.

Figure 3.1. Phase portraits of a simple pendulum. (a) A pendulum displaced from equilibrium oscillates between its most negative (left) and most positive (right) displacements. When the displacement is zero, the velocity is either at its most positive or negative values (red arrows). (b) Phase portraits of the velocity ($\dot{X}$) and position (X) of the pendulum trace clockwise circular trajectories. (c) Phase portraits of the imaginary (Im) and real (Re) components of the pendulum's motion trace counter-clockwise circular trajectories.

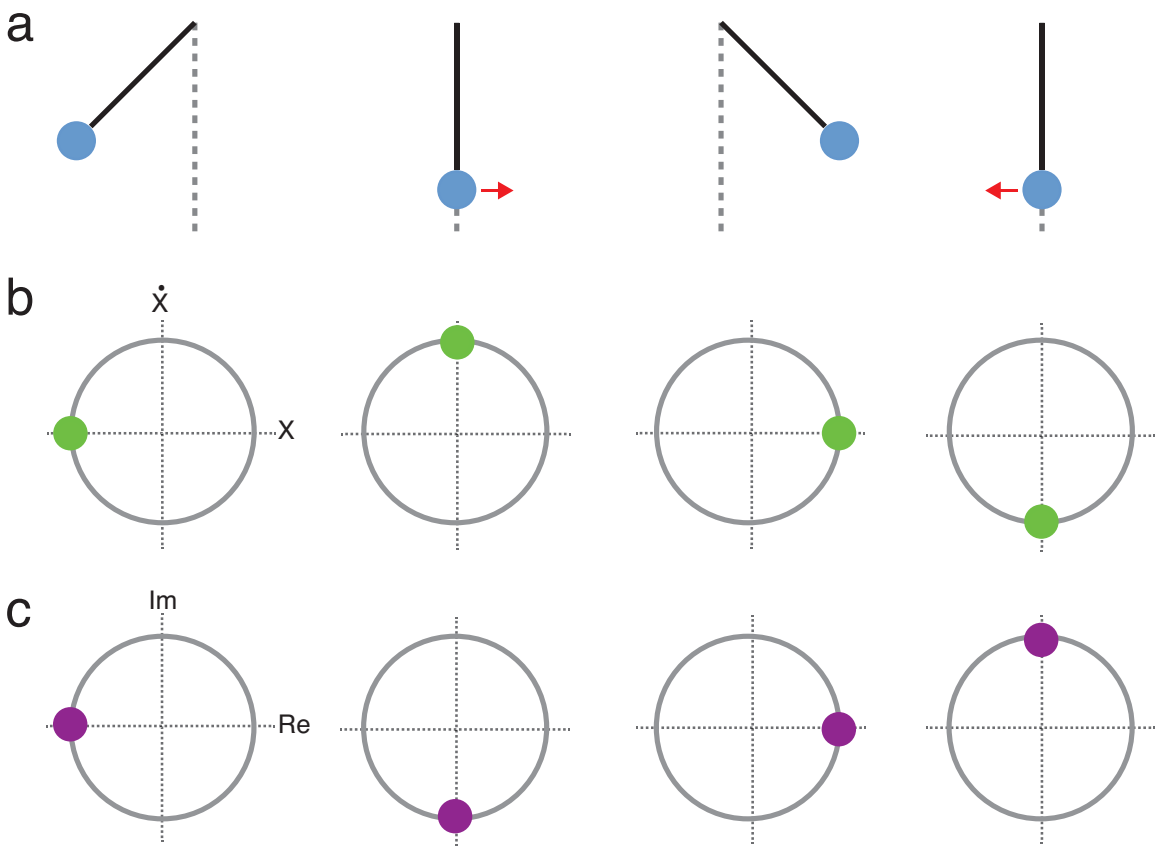
a
b
ẋ
x
c
Im
Re

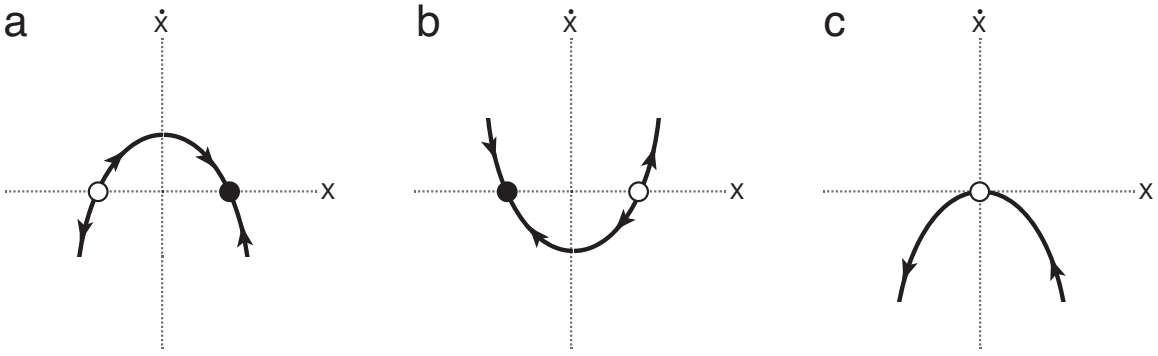

Figure 3.2. Flow along a defined trajectory. (a) The trajectory defined by $\dot{X} = -X^2 + 1$ yields two fixed points at X = ±1. The point at X = -1 is an unstable fixed point (open circle), in which all disturbances from equilibrium grow over time (arrows). The point at X = +1 is a stable fixed point (closed circle), in which small disturbances from equilibrium result in a return to the same point. (b) The trajectory defined by $\dot{X} = X^2 - 1$ also has two fixed points at X = ±1. In this case, the stability of each fixed point is reversed. (c) The trajectory defined by $\dot{X} = -X^2$ has only one fixed point at X = 0 (open circle). This fixed point is a saddle point, in which some flows pass into and others out of it. A saddle point is neither a local maximum not a local minimum.

SECTION 3.2: *Introduction to Bifurcation Theory*

In certain systems, a quantitative change in the value of some parameter—a *control parameter*—results in a striking qualitative change in the system's behavior: a *bifurcation* (157, 160). An example of a bifurcation can be appreciated from the behavior of water. Here the control parameters of temperature and pressure determine the phase of water. A small change to one of these parameters can yield a dramatic change in the physical state of water. For example, decreasing the temperature of liquid water produces a change in its state from a liquid to a solid. This change constitutes a bifurcation. Without knowing the molecular details of this system, one can readily witness a dramatic change in that system's behavior. In a dynamical system, a bifurcation can create, move, and destroy fixed points; birth limit cycles; and change the stability of fixed points and limit cycles. In other words, the bifurcation point of an autonomous system of differential equations divides the control-parameter space into different topologically equivalent regions, each topologically inequivalent with the others (157).

Each bifurcation is defined by a *normal form*, an abridged mathematical description that encompasses its essential features (157, 159). A normal form provides the crucial features of a particular bifurcation type independent of specific models. From this equation, one can then analyze each system for its unique properties and construct maps of the system's behavior in parameter space. Embedded in each normal form is a control parameter that adjusts the distance to a bifurcation. The number of variables that must be adjusted to reach the bifurcation defines the bifurcation's *codimension* (157, 159, 160). For example, codimension-1 bifurcations require that only one control parameter

be varied in order to cross a bifurcation, whereas codimension-2 bifurcations necessitate the adjustment of two control parameters.

Bifurcations may be classified as either *local* or *global* (157, 159). Local bifurcations transpire at the point where an equilibrium point or periodic orbit changes stability. Global bifurcations occur when invariant sets collide with equilibria, for example, when a limit cycle collides with a saddle-node in an infinite-period bifurcation. Although a local bifurcation may be confined to a rather small territory in parameter space, a global bifurcation cannot be restricted to such a small sector.

SECTION 3.3: *Local Bifurcations*

This section explores the details of individual local codimension-1 and codimension-2 bifurcations. These include the saddle-node, transcritical, pitchfork, supercritical Hopf, subcritical Hopf, cusp, Bautin, and Bogdanov-Takens bifurcations (155, 157, 159, 160). The last five bifurcations are particularly important in the analysis of hair-bundle motility.

The simplest example of a local codimension-1 bifurcation is a ***saddle-node bifurcation***. Also called a *fold bifurcation*, a saddle-node bifurcation arises when two equilibria collide with and annihilate one another (157, 161). The normal form of a saddle-node bifurcation follows

$$\dot{X} = r + X^2, \tag{3.1}$$

in which r is a control parameter. For $r < 0$, a stable fixed point resides at $X = -\sqrt{-r}$ and an unstable fixed point resides at $X = \sqrt{-r}$ (Figure 3.3a). When $r = 0$, the two fixed points collide with one another, generating a saddle point. Finally, for $r > 0$, there exist no fixed points. Figure 3.3a also depicts a *bifurcation diagram* that plots the location of stable points in X against the control parameter r. This diagram permits accessible visualization of the behavior of a system near the bifurcation. In the case of a saddle-node bifurcation, two fixed points exist for $r < 0$ that follow $X = \sqrt{-r}$, illustrated by the solid and dashed purple lines. No stable equilibria exist for $r > 0$.

Another local codimension-1 bifurcation is a ***transcritical bifurcation***. A transcritical bifurcation differs from a saddle-node bifurcation in that one or more fixed

points exist for all parameter values (159). The fixed points exchange their stabilities after a critical value of the control parameter is reached. The normal form of a transcritical bifurcation follows

$$\dot{X} = rX - X^2 , \tag{3.2}$$

where r is the control parameter. For $r < 0$, a stable point resides at the origin, and an unstable fixed point dwells at $X = r$ (Figure 3.3b). At $r = 0$, the two fixed points collide to generate a saddle point, analogous to a saddle-node bifurcation. Finally, for $r > 0$, the fixed point at the origin becomes unstable and that at $X = r$ becomes stable. The bifurcation diagram in Figure 3.3b illuminates the *exchange of stabilities* between the two fixed points.

Figure 3.3. Phase portraits and bifurcation diagrams of saddle-node, transcritical, and supercritical pitchfork bifurcations. (a) Phase portraits of a saddle-node bifurcation are shown for three topologically equivalent regions in parameter space. For $r < 0$, two fixed points, one stable and another unstable, exist at $X = \pm\sqrt{-r}$. When $r = 0$, one saddle point resides at the origin. Finally, for $r > 0$, there exist no fixed points. The bifurcation diagram (rightmost panel) illustrates the relationship between stable points in X and the control parameter r. (b) Two fixed points exist for $r < 0$ in the normal form of a transcritical bifurcation, with a stable fixed point at the origin (filled circle) and an unstable fixed point at $X = r$. When $r = 0$, a saddle point resides at the origin. For $r > 0$, the fixed point at the origin becomes unstable, and a stable fixed point appears at $X = r$. The bifurcation diagram (rightmost panel) illustrates this exchange of stabilities. (c) Phase portraits for a supercritical pitchfork bifurcation depict one stable fixed point at the origin for $r \leq 0$. At $r = 0$, the slope of the trajectory becomes zero at the origin, exposing the phenomenon of *critical slowing* near this bifurcation. For $r > 0$, the fixed point at the origin becomes unstable, and two stable fixed points appear at $X = \pm\sqrt{r}$. The bifurcation diagram of a supercritical pitchfork bifurcation represents the change in stability of the fixed point at the origin and the appearance of two stable fixed points for positive values of the control parameter.

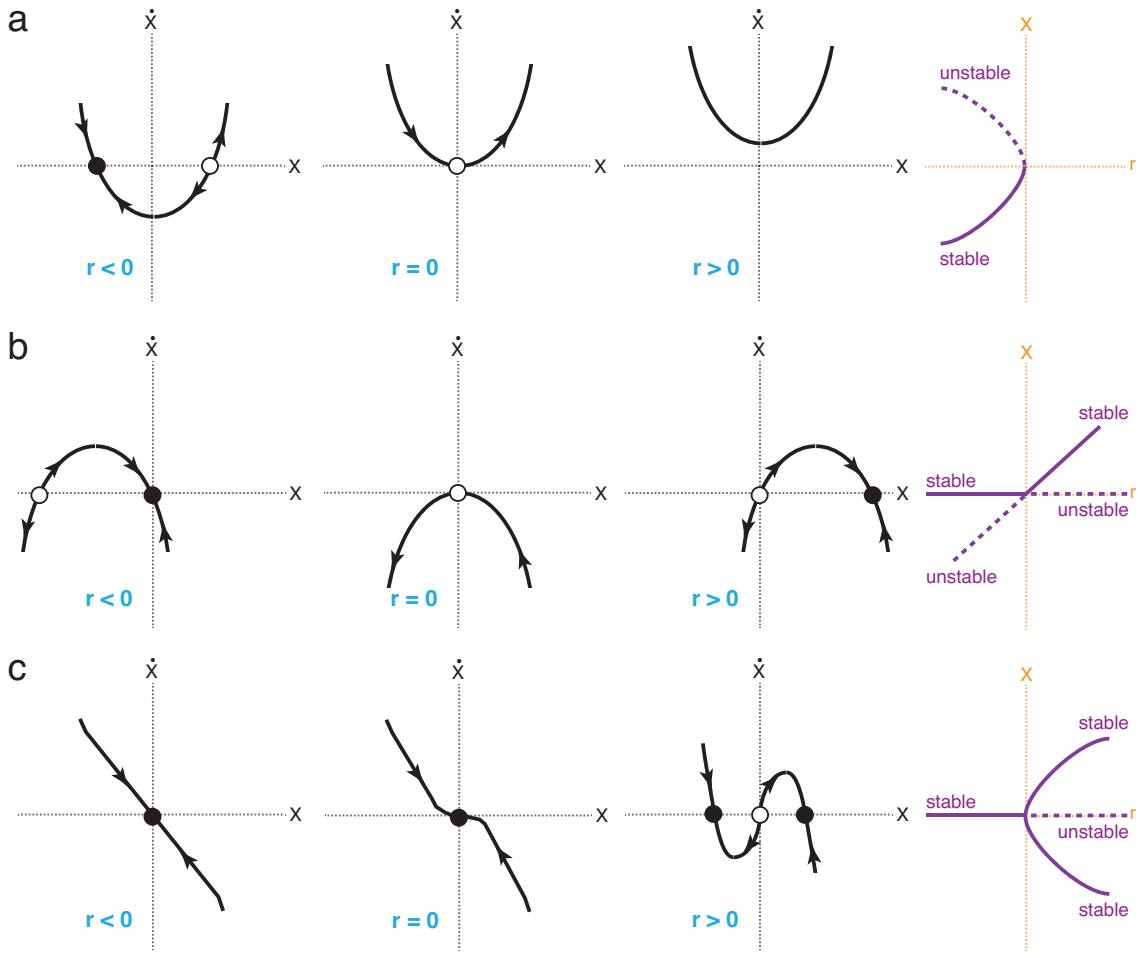
a
ẋ
x
r < 0
ẋ
x
r = 0
ẋ
x
r > 0
X
unstable
r
stable
b
ẋ
x
r < 0
ẋ
x
r = 0
ẋ
x
r > 0
X
stable
stable
r
unstable
unstable
c
ẋ
x
r < 0
ẋ
x
r = 0
ẋ
x
r > 0
X
stable
stable
r
unstable
stable

A ***supercritical pitchfork bifurcation*** is a local codimension-1 bifurcation that transforms the stability of one fixed point while creating two additional fixed points (158, 159). This bifurcation often materializes in systems with symmetry. The nor

mal form of a supercritical bifurcation is

$$\dot{X} = rX - X^3, \tag{3.3}$$

in which r is a control parameter. For $r \leq 0$, the single, stable fixed point lies at the origin. As r increases to zero, the slope of the trajectory around the origin decreases (Figure 3.3c). This causes a decrease in the magnitude of attraction of the fixed point at the origin as the trajectory becomes more nonlinear. Thus, solutions near the fixed point decay more slowly to equilibrium, a phenomenon called *critical slowing* (159). For $r > 0$, the fixed point at the origin becomes unstable and two stable fixed points appear at $X = \pm\sqrt{r}$. The bifurcation diagram in Figure 3.3c exposes the change in stability of the fixed point at the origin and the emergence of two stable fixed points for $r > 0$. Note that the sluggish decay of solutions near the origin—critical slowing—cannot be visualized in the bifurcation diagram.

Another flavor of the pitchfork bifurcation is the ***subcritical pitchfork bifurcation***. The normal form of a subcritical pitchfork bifurcation is

$$\dot{X} = rX + X^3. \tag{3.4}$$

In the normal form of the supercritical pitchfork bifurcation (equation 3.3), the negative cubic term stabilizes the solution (157, 159, 161). In the case of a subcritical pitchfork bifurcation, the cubic term is positive and destabilizes the solution. This causes the stable fixed points previously at $X = \pm\sqrt{r}$ for $r > 0$ in the supercritical pitchfork bifurcation to

become unstable fixed points at $X = \pm\sqrt{-r}$ for $r < 0$ in the subcritical pitchfork bifurcation. The stability of the fixed point at the origin is the same for both bifurcations. This produces an interesting behavior. When the system is perturbed to points exceeding the unstable fixed points for $r > 0$, the cubic term causes $X(t)$ to explode to $\pm\infty$. For $r > 0$, there exist no fixed points, and the cubic term again destabilizes the system, extending its trajectory to infinity. To compensate for this instability, a negative fifth-order term is added to equation 3.4, yielding

$$\dot{X} = rX + X^3 - X^5 . \tag{3.5}$$

The higher-order term now stabilizes the solution in equation 3.5. This system also exhibits *hysteresis* in which multiple stable states can exist for certain values of the control parameter *r*. The stable state at which the system resides depends on how the control parameter is varied (155, 156, 159). Hysteresis causes a lack of reversibility and can be appreciated in many systems and other bifurcations, including the subcritical Hopf bifurcation.

The ***Hopf bifurcation***, also called the *Andronov-Hopf* or *Poincaré-Andronov-Hopf bifurcation*, is a local codimension-1 bifurcation that births a limit cycle from equilibrium (157, 159, 161, 162). Like the pitchfork bifurcation, a Hopf bifurcation may be either supercritical or subcritical. A ***supercritical Hopf bifurcation*** births a stable limit cycle from equilibrium. The normal form of a this bifurcation follows

$$\dot{z} = (\mu + i\omega)z - B|z|^2 z , \tag{3.6}$$

in which z and B are complex numbers with $B > 0$, μ is a control parameter, and ω is the Hopf frequency. The real part of z can be regarded as the real part of the motion of an oscillator. If one considers only the first component, μz, then the system displays exponential growth or decay depending upon the sign of μ. The imaginary component, $i\omega z$, corresponds to a sinusoidal oscillation at the Hopf frequency. With a negative value of μ, the first two terms generate an exponential decay to a stable equilibrium. If instead μ is positive, this results in the exponential growth of a sine wave. The third cubic component, however, constrains the wave's motion and generates a limit cycle (163). Thus, for $\mu < 0$, there exists one stable fixed point (Figure 3.4a). When μ becomes positive, the fixed point changes stability and a limit cycle arises. The limit cycle follows $z(t) = \sqrt{\mu / \mathrm{Re}[B]}e^{i\omega t}$, in which Re[$B$] is the real part of B and is the first Lyapunov coefficient (157, 159, 161). When Re[B] = 1, the amplitude of the limit-cycle oscillation becomes $\sqrt{\mu}$. Figure 3.4a depicts the bifurcation diagram of a supercritical Hopf bifurcation, illustrating the growth of the limit cycle with an increase in μ.

Figure 3.4. Phase portraits and bifurcation diagrams of Hopf bifurcations. (a) A supercritical Hopf bifurcation births a limit cycle for $\mu > 0$. For $\mu < 0$, there exists one stable fixed point. For $\mu > 0$, the fixed point becomes unstable and a limit cycle grows with $\sqrt{\mu}$. The bifurcation diagram (rightmost panel) depicts the behaviors around a supercritical Hopf bifurcation. For $\mu < 0$ (red circle), the system resides at a stable equilibrium. For $\mu > 0$ (orange and blue arrows), the system oscillates with amplitude proportional to $\sqrt{\mu}$. (b) A subcritical Hopf bifurcation also yields in a change in the stability of a fixed point. However, the third-order limit cycle is unstable and birthed for $\mu < 0$ in the case of a subcritical Hopf bifurcation (dashed circle). A fifth-order stable limit cycle stabilizes the system for $\mu > 0$ (solid circle). The bifurcation diagram illustrates this behavior (right panel). For $\mu << 0$ (red point), the system resides at a stable equilibrium. At intermediate values of the control parameter (orange point and arrow), the system may reside on a stable equilibrium or it may oscillate at an amplitude and frequency defined by the higher-order stable limit cycle. This produces hysteresis in the case of a subcritical Hopf bifurcation. Finally, for $\mu > 0$ (blue arrow), the system will oscillate only on the stable limit cycle.

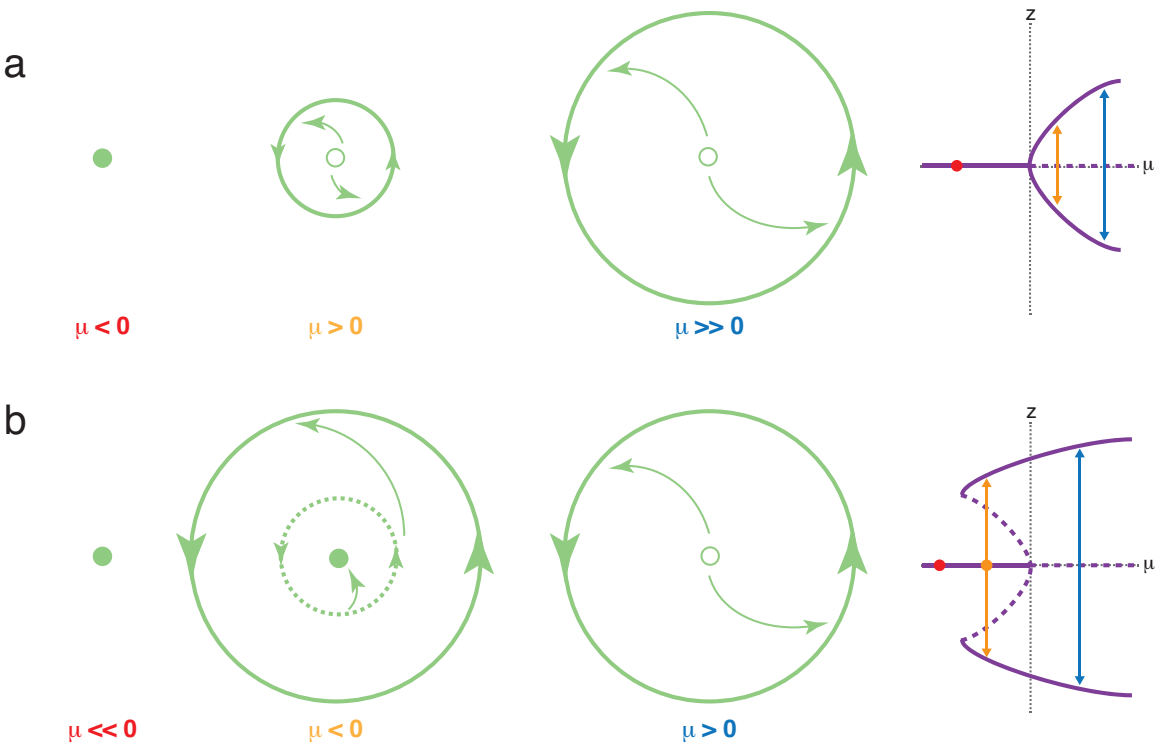
a
μ < 0
μ > 0
μ >> 0
z
μ
b
μ << 0
μ < 0
μ > 0
z
μ

The supercritical Hopf bifurcation also yields convenient behaviors when external forcing is applied. For example, if the system is driven at the Hopf frequency, it responds with large amplification. This amplification diminishes as the driving frequency departs from the Hopf frequency, producing sharp frequency tuning with high amplification. Furthermore, linear changes in the amplitude of forcing yield nonlinear changes in the amplitude of response near a Hopf bifurcation. Specifically, the phase-locked response R follows $R \propto F^{1/3}$, in which F is the amplitude of the driving force. These phenomena characterize the active process of auditory hair bundles, a point to which we will return (164).

A ***subcritical Hopf bifurcation*** also births a limit cycle, but the sign of the third-order term in equation 3.6 becomes positive (159, 161). Thus, the third-order term no longer stabilizes the system and instead destabilizes it, analogous to the subcritical pitchfork bifurcation. The normal form of a subcritical Hopf bifurcation is

$$\dot{z} = (\mu + i\omega)z + B|z|^2 z - C|z|^4 z, \tag{3.7}$$

in which z, B, and C are complex numbers, μ is a control parameter, and ω is the Hopf frequency. As μ crosses zero, the fixed point changes stability in the same way it does for the supercritical Hopf bifurcation (Figure 3.4b). However, the third-order limit cycle occurs for $\mu < 0$ and is now unstable. Without a higher-order term, the system would continue toward positive or negative infinity at all positive values of the control parameter and all perturbations outside the third-order limit cycle at all negative values of the control parameter. To compensate for this, a negative fifth-order term is

incorporated into equation 3.7 to stabilize the system. This causes the system to oscillate at an amplitude and frequency defined by the higher-order term for $\mu > 0$. For $\mu < 0$, the stable fifth-order limit cycle persists until it collides with the unstable third-order limit cycle at a global bifurcation called a *saddle-node of limit cycles (SNLC)* (*see* Section 3.4) (157). For control parameters less than zero and greater than the critical value defined by the SNLC, the system can either remain at a stable fixed point or settle on the higher-order stable limit cycle. This establishes a region of *hysteresis* analogous to that created by a subcritical pitchfork bifurcation. The hysteretic region can be identified in the bifurcation diagram of a subcritical Hopf bifurcation in Figure 3.4b. To illustrate hysteresis, consider a system that begins at a negative value of the control parameter less than the critical value defined by the SNLC. As the control parameter increases, the system continues to dwell on the stable fixed point until the control parameter becomes positive and the fixed point changes stability. Contrarily, if the system starts at a positive value of the control parameter, it resides on the stable limit cycle. As the control parameter decreases, limit-cycle oscillations continue for values of the control parameter less than zero until the operating point arrives at the SNLC. Taken together, the directionality in parameter space yields distinct patterns of behavior. In other words, the system is hysteretic rather than reversible.

In the case of a subcritical Hopf bifurcation or a subcritical pitchfork bifurcation, perturbations can change the pattern of behavior. Consider a system with a subcritical Hopf bifurcation that resides on a stable fixed point within the hysteretic region of parameter space. With a large perturbation, the system surpasses the third-order

unstable limit cycle. Because unstable limit cycles represent energy maxima, this propels the system onto an energy minimum that is the fifth-order stable limit cycle. Similarly, perturbations from the stable limit cycle can be large enough to force the system back onto a stable equilibrium. This behavior is a *separatrix crossing*, in which the *separatrix* is the energy maximum that the system must traverse (165, 166). Separatrices can be found in subcritical pitchfork bifurcations, subcritical Hopf bifurcations, and infinite-period bifurcations. They become important when considering the effects of stochastic noise in dynamical systems.

Codimension-2 bifurcations require two control parameters to specify their behavior. A ***cusp bifurcation*** is a local codimension-2 bifurcation that occurs at the meeting point of two saddle-node bifurcations (157). The normal form of a cusp bifurcation follows

$$\dot{X} = r_2 + r_1 X - X^3, \tag{3.8}$$

in which r_1 and r_2 are control parameters. The cusp bifurcation occurs at $r_1 = r_2 = 0$, and saddle-node bifurcations follow $r_2 = \pm \frac{2}{3\sqrt{3}} r_1^{3/2}$ for $r_1 > 0$ (Figure 3.5a). The cusp bifurcation generates two stable fixed points and one unstable fixed point for regions bounded by the saddle-node bifurcations in parameter space. Thus, cusp bifurcations create *bistable* regions. Perturbations within this region that displace a system beyond an unstable fixed point propel its motion toward another stable fixed point. The separatrix crossing in a cusp bifurcation is thus analogous to the one witnessed in a subcritical Hopf bifurcation. Without perturbations, a bistable system remains stationary at

equilibrium. When perturbations exceed a threshold defined by a separatrix, the system can switch between two stable equilibria.

A ***Bautin bifurcation*** is a local codimension-2 bifurcation that separates a subcritical Hopf bifurcation from a supercritical Hopf bifurcation (157). This bifurcation has a normal form in two dimensions that follows

$$\dot{X}_1 = r_2 X_1 - X_2 + r_1 X_1 (X_1^2 + X_2^2) + X_1 (X_1^2 + X_2^2)^2, \tag{3.9}$$

$$\dot{X}_2 = X_1 + r_2 X_2 + r_1 X_2 (X_1^2 + X_2^2) + X_2 (X_1^2 + X_2^2)^2, \tag{3.10}$$

in which r_1 and r_2 are control parameters. The Bautin bifurcation arises at $r_1 = r_2 = 0$ (Figure 3.5b). A line of subcritical Hopf bifurcations occurs at $r_1 > 0$ and $r_2 = 0$, and a line of supercritical Hopf bifurcations occurs at $r_1 < 0$ and $r_2 = 0$. The line of SNLC bifurcations follows $r_2 = -\frac{1}{4} r_1^2$ for $r_1 > 0$.

A ***Bogdanov-Takens bifurcation*** is a local codimension-2 bifurcation that occurs at the meeting point of a Hopf bifurcation, saddle-node bifurcations, and a saddle homoclinic bifurcation (157). The Bogdanov-Takens bifurcation possesses the normal form

$$\dot{X}_1 = X_2, \tag{3.11}$$

$$\dot{X}_2 = r_2 + r_1 X_1 + X_1^2 + X_1 X_2, \tag{3.12}$$

in which r_1 and r_2 are control parameters. The Bogdanov-Takens bifurcation occurs at the origin, $\{r_1, r_2\} = \{0,0\}$ (Figure 3.5c). Two saddle-node bifurcations follow $r_2 = \frac{1}{4} r_1^2$ for $r_1 > 0$ and $r_1 < 0$. A line of Hopf bifurcations exists for $r_1 < 0$ and $r_2 = 0$. Finally, a saddle

homoclinic bifurcation line follows $r_2 \approx -\frac{6}{25} r_1^2$ for $r_1 < 0$. A Bogdanov-Takens bifurcation causes two equilibria to collide at a saddle-node bifurcation, generates a limit cycle at a Hopf bifurcation, and destroys the limit cycle to a homoclinic orbit through a saddle homoclinic bifurcation.

Figure 3.5. Bifurcation diagrams and phase portraits of local codimension-2 bifurcations. (a) The bifurcation diagram of a cusp bifurcation (left) includes two saddle-node bifurcations that follow $r_2 = \pm\frac{2}{3\sqrt{3}} r_1^{3/2}$ for $r_1 > 0$ (purple lines). For parameters outside the cusp region (*1, blue*), there exists one stable fixed point. Within the cusp region (*2, red*), the stable fixed point becomes unstable and two stable fixed points are birthed, yielding a bistable system. (b) A Bautin bifurcation separates a subcritical Hopf bifurcation (dashed cyan line) from a supercritical Hopf bifurcation (solid dashed line). The bifurcation diagram (left) also depicts a saddle-node of limit cycles for $r_1 > 0$ (orange). On the stable side of the supercritical Hopf bifurcation ($r_1 < 0$ and $r_2 < 0$), there exists only one stable fixed point (*1, blue*). Within the hysteretic region of the subcritical Hopf bifurcation ($r_1 > 0$ and $r_2 < 0$), a stable limit cycle encloses both an unstable limit cycle and a stable fixed point (*2, red*). On the unstable side of the subcritical and supercritical Hopf bifurcations ($r_2 > 0$), the fixed point becomes unstable and the system resides on a stable limit cycle (*3, green*). (c) The Bogdanov-Takens bifurcation occurs at the meeting point of a Hopf bifurcation (cyan), saddle-node bifurcations (purple), and a saddle homoclinic bifurcation (orange). Within the region bounded by saddle-node bifurcations (*1, blue*), there are no stable points. Crossing a saddle-node bifurcation generates a stable fixed point (*2, red*), and crossing a Hopf bifurcation generates a stable limit cycle (*3, green*). Regions outside these bifurcations in parameter space undergo a saddle homoclinic bifurcation, generating an unstable fixed point and a saddle point (*4, purple*).

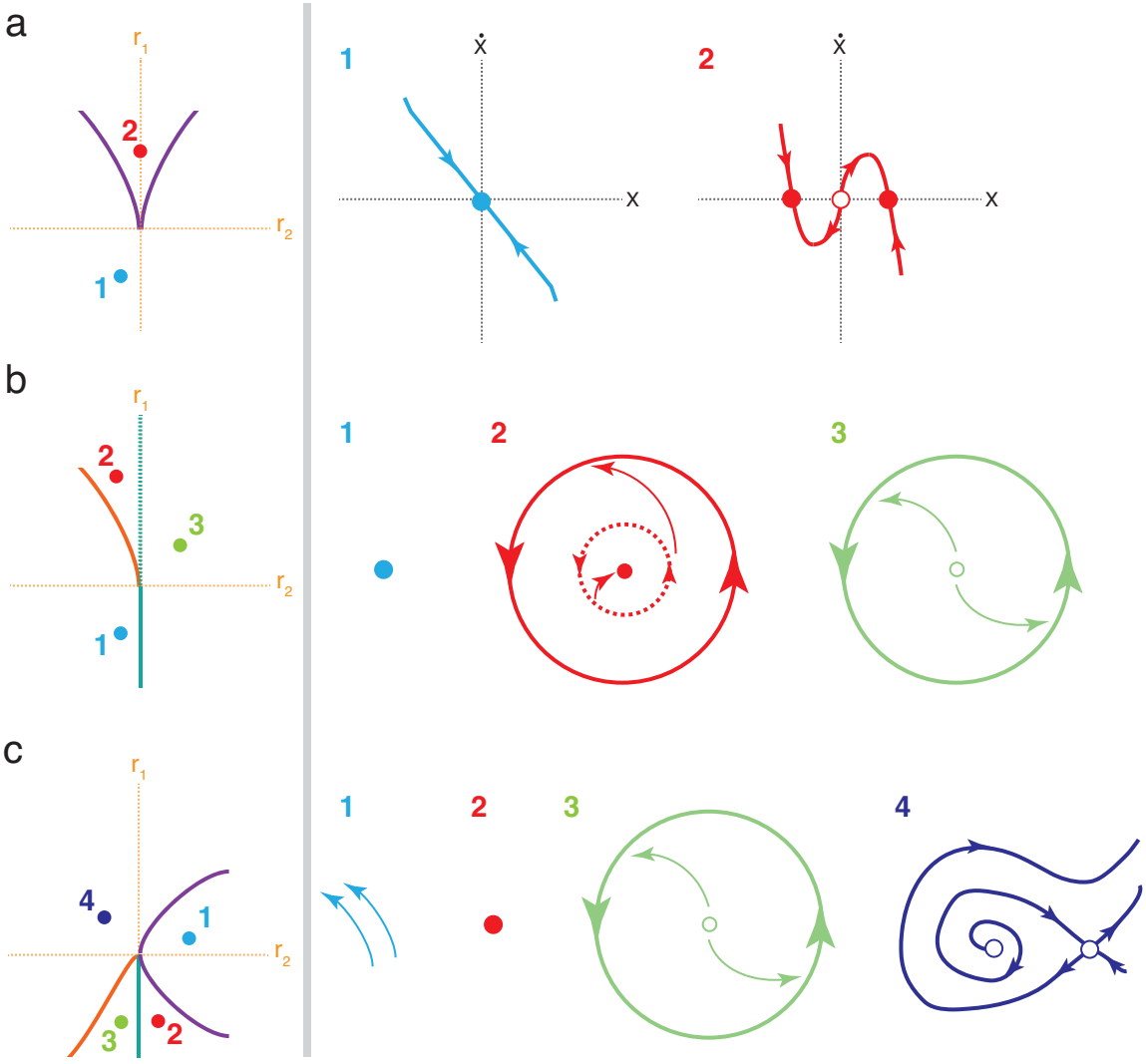
a
r1
r2
2
1
ẋ
x
1
ẋ
x
2
b
r1
r2
2
3
1
1
2
3
c
r1
r2
4
1
3
2
1
2
3
4

SECTION 3.4: *Global Bifurcations*

Unlike local bifurcations, global bifurcations cannot be restricted to a small sector of parameter space. Global bifurcations materialize when certain invariant sets collide with equilibria (157, 159). Like local bifurcations, global bifurcations may also be of different codimensions. These bifurcations include but are not limited to the saddle-node of limit cycles bifurcation and saddle-node on invariant cycle bifurcation. Dynamical modeling of hair-bundle mechanics predicts that both of these bifurcations can in principle describe a bundle's behavior (167).

A ***saddle-node of limit cycles (SNLC) bifurcation***, also called a *fold of limit cycles*, is a global codimension-1 bifurcation that arises when an unstable and a stable limit cycle collide and annihilate one another (Figure 3.6a) (159). The SNLC bifurcation inhabits the normal form of a subcritical Hopf bifurcation. In polar coordinates, this normal form follows

$$\dot{r} = \mu r + r^3 - r^5, \tag{3.13}$$

$$\dot{\theta} = \omega + br^2, \tag{3.14}$$

in which r is the radius of a trajectory, θ is its phase, ω is the frequency of oscillation, and μ is a control parameter (159). Note that equations 3.13 and 3.14 describe the same behavior as equation 3.7. A SNLC bifurcation occurs at μ_c = -0.25 in equations 3.13 and 3.14. For values of the control parameter between zero and μ_c, the system may reside on either a stable fixed point or a fifth-order stable limit cycle.

Figure 3.6. Phase portraits of global codimension-1 bifurcations. (a) An SNLC bifurcation occurs when a stable and an unstable limit cycle collide and annihilate one another and can be found in the normal form of a subcritical Hopf bifurcation (*see* Figure 3.4b *and* equations 3.7, 3.13, and 3.14). For $0 < \mu < \mu_c$, a higher-order stable limit cycle encloses an unstable limit cycle and a stable fixed point. A decrease in the control parameter μ causes the unstable limit cycle to expand and approach the stable limit cycle. The SNLC occurs at $\mu = \mu_c$ when the two limit cycles collide. For $\mu < \mu_c$, only the stable fixed point remains. (b) A SNIC bifurcation occurs when a saddle-node bifurcation approaches an invariant limit cycle. For $\mu < \mu_c$, one stable and one unstable fixed point each reside on a limit cycle. An increase in μ causes the fixed points to approach one another and collide at $\mu = \mu_c$, generating a saddle point. For $\mu > \mu_c$, the system follows the invariant cycle. However, a portion of the motion is constrained by a *ghost* of the saddle node (yellow box), causing an increase in the period of oscillation. The ghost appears at $\pi/2$ in equations 3.15 and 3.16. As μ continues to increase, the bottleneck created by the ghost opens and the period of oscillation decreases.

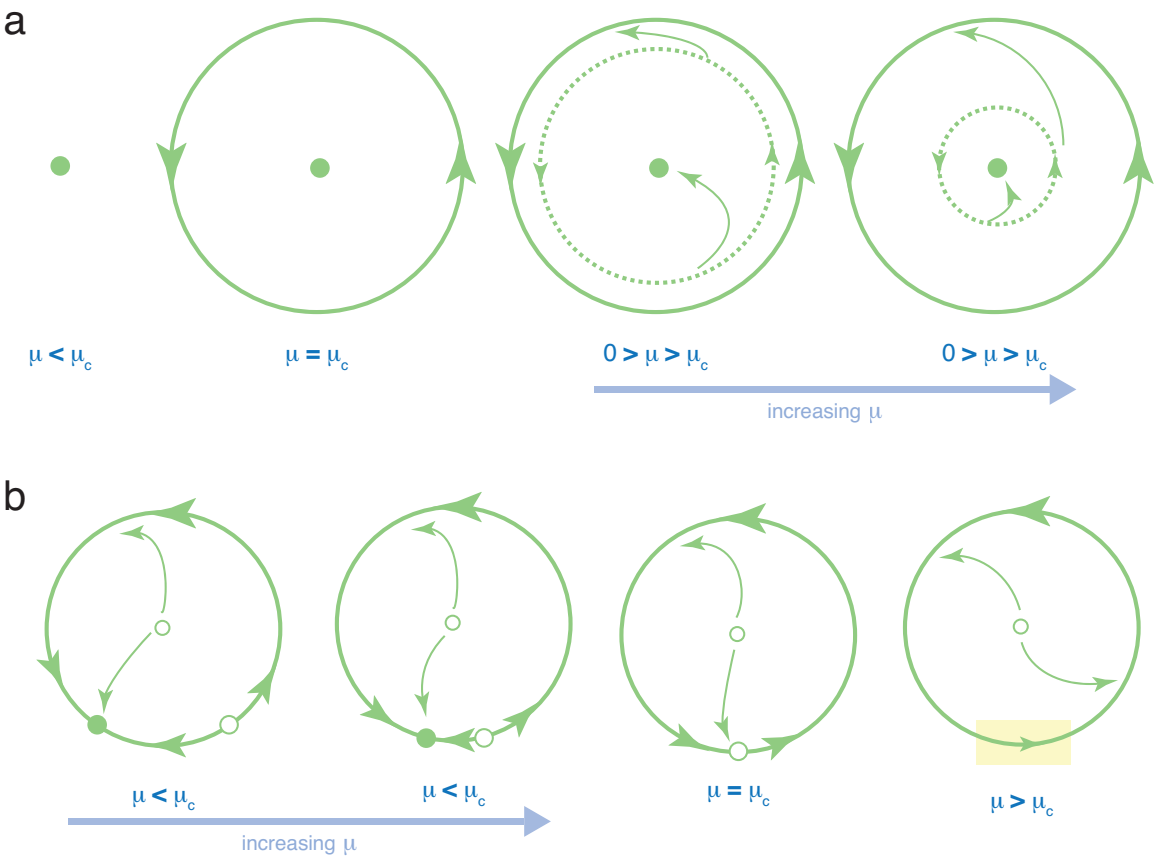
a
μ < μc
μ = μc
0 > μ > μc
0 > μ > μc
increasing μ
b
μ < μc
μ < μc
μ = μc
μ > μc
increasing μ

A ***saddle-node on invariant cycle (SNIC) bifurcation***, also called an *infinite-period* or *saddle-node infinite period (SNIPER) bifurcation*, is a global codimension-1 bifurcation that arises when a saddle-node bifurcation meets an invariant limit cycle (Figure 3.6b) (159). This invariant limit cycle contrasts with size-varying limit cycles described by Hopf bifurcations. The normal form of a SNIC bifurcation in polar coordinates is

$$\dot{r} = r(1 - r^2), \tag{3.15}$$

$$\dot{\theta} = \mu - \sin\theta, \tag{3.16}$$

in which r is the radius of a trajectory, θ is its angle, and μ is a control parameter (159). Another representation of the SNIC bifurcation is the *Ermentrout-Kopell canonical model*, or *theta model*, that describes only the phase of an oscillator. The theta model takes the form

$$\dot{\theta} = 1 - \cos\theta + \mu(1 + \cos\theta), \tag{3.17}$$

in which θ is the phase of a trajectory and μ is a control parameter (168). Ermentrout and Kopell proposed the theta model as a one-dimensional representation of spiking neurons that approximates the behavior of quadratic integrate-and-fire neurons (165, 168). The normal form in equations 3.15 and 3.16 and the model in equation 3.17 both capture the general behavior of a SNIC bifurcation. The SNIC bifurcation occurs at $\mu_c = 1$ in equation 3.16 (159) and $\mu_c = 0$ in equation 3.16 (166, 168). For $\mu < \mu_c$, two fixed points, one stable and another unstable, dwell on a limit cycle. As a result, the system settles on only the stable fixed point. As the value of the control parameter increases to $\mu = \mu_c$, the two fixed points approach and collide with one another, generating a saddle point.

Finally, for $\mu > \mu_c$, no fixed points reside on the limit cycle, permitting the system to oscillate along the trajectory defined by the cycle (157, 159).

A curious behavior near a SNIC bifurcation is that oscillations are not always of the same frequency for $\mu > \mu_c$. As the value of the control parameter decreases toward μ_c, the period of oscillation increases. Such a behavior arises from the *ghost* of a saddle node near the limit cycle that creates a bottleneck region over part of its trajectory (Figure 3.6b). This causes the system to slow as it passes through the bottleneck region, and the bottleneck narrows as the saddle-node approaches the limit cycle. As a result, the period of oscillation lengthens as the bifurcation is approached, with the period following $T = \frac{1}{\sqrt{\mu - \mu_c}}$ (159). As the difference between μ and μ_c decreases, the period T increases. For $\mu = \mu_c$, the period diverges to infinity. A SNIC bifurcation is aptly dubbed an *infinite-period bifurcation* because of this behavior.

For $\mu < \mu_c$, perturbations to a system residing on a stable fixed point that propel it beyond an unstable fixed point permit the system to follow the remaining part of the limit cycle. The unstable fixed point is yet another example of a *separatrix*. This behavior is convenient in models of spiking neurons. Perturbations below a threshold defined by the separatrix do not elicit a spike, whereas perturbations above a threshold will elicit one (165, 166). Thus, systems wielding separatrices, such as the SNIC bifurcation and the subcritical Hopf bifurcation, exhibit threshold phenomena. Threshold phenomena occupy a special role in excitable systems and will be addressed in experiments that study the mechanical excitability of hair bundles.

SECTION 3.5: *State Diagrams*

Surveying the attributes of a dynamical system requires a theoretical map of that system's behavior. A complete map of such behavior is called a *state space*, a limited sample of which may be represented as a *state diagram*. A state diagram portrays the behavior of a system at coordinates defined by one or more control parameters. A tractable example of a state diagram is the phase diagram of water (169). Here the control parameters are temperature and pressure and the states are water's solid, liquid, and vapor phases. At a pressure of 100 kPa and a temperature below 0 °C, water exists in its solid phase. An increase in the temperature to a value between 0 °C and 100 °C causes a phase transition to liquid water. Finally, for temperatures above 100 °C, water endures as a vapor. Adjusting the pressure can also effect equivalent phase changes. The melting and freezing, evaporation and condensation, and sublimation and deposition of water each represent a type of bifurcation in the water's behavior. Small changes in the temperature and pressure cause dramatic qualitative changes in phase. The temperature-pressure phase diagram of water thus represents one type of state diagram. Each region of the diagram corresponds to a different phase, with each region bounded by one or more types of bifurcation.

The state diagram of a dynamical system may include many control parameters. As will be seen, a state diagram of a hair bundle can include the control parameters of constant force, stiffness, drag, and mass (167) or it may include control parameters of adaptation force and the strength of calcium feedback (170).

SECTION 3.6: *Classic Models in Dynamical Systems*

Prior to the Second World War, Dutch physicist Balthasar van der Pol characterized the vibratory behavior of nonlinear electrical circuits (171, 172). Shortly thereafter he reduced the equation to

$$\ddot{x} + \mu(x^2 - 1)\dot{x} + x = 0\,, \tag{3.18}$$

in which μ is a control parameter (159, 173). Equation 3.18 mimics a simple harmonic oscillator. However, there exists a *nonlinear damping term*, $\mu(x^2 - 1)\dot{x}$. When the magnitude of x exceeds one, the system is positively damped. When the magnitude of x is below one, the system posesses *negative damping* (159). This constraint on the magnitude of x generates limit-cycle oscillations for $\mu > 0$. Put another way, the van der Pol oscillator undergoes a supercritical Hopf bifurcation at $\mu = 0$.

The van der Pol oscillator generates *relaxation oscillations* that mimic those created by nonlinear electrical circuits (Figure 3.7a) (159). Relaxation oscillators produce nonsinusoidal oscillations that include both slow and fast phases. For example, in a series resistor-capacitor circuit, charging the capacitor induces a slow phase, and rapid discharge induces a fast phase (Figure 3.7b) (174). Such a behavior has been witnessed not only in nonlinear electrical circuits, but it has also been proposed for the rhythmicity of heart beats (175), genetic oscillators (176), and the vibratory motion of hair bundles (Figure 3.7c) (135). Nonlinear oscillations thus apply to a wide variety of systems and van der Pol's initial description of relaxation oscillations offers the capacity to describe many of these behaviors.

Figure 3.7. Relaxation oscillators. (a) The van der Pol oscillator generates relaxation oscillations for $\mu > 0$. When $\mu = -5$, the system rapidly decays to equilibrium. When $\mu = 5$, the system exhibits periodic relaxation oscillations, in which each period is characterized by a slow and fast phase of oscillation. (b) A resistor-capacitor circuit that includes a light-bulb in parallel with the capacitor also generates relaxation oscillations. The capacitor's charging causes an exponential increase in its voltage. Once the voltage reaches a threshold defined by the properties of the bulb, V_T, the capacitor rapidly discharges and the cycle begins again. (c) Hair bundles from the bullfrog's sacculus exhibit relaxation oscillations under appropriate ionic conditions. This behavior arises from a combination of the bundle's nonlinear stiffness and an adaptation mechanism. Note that whereas a hair bundle's oscillations resemble the pattern generated by a van der Pol oscillator, the direction of the slow phase is inverted.

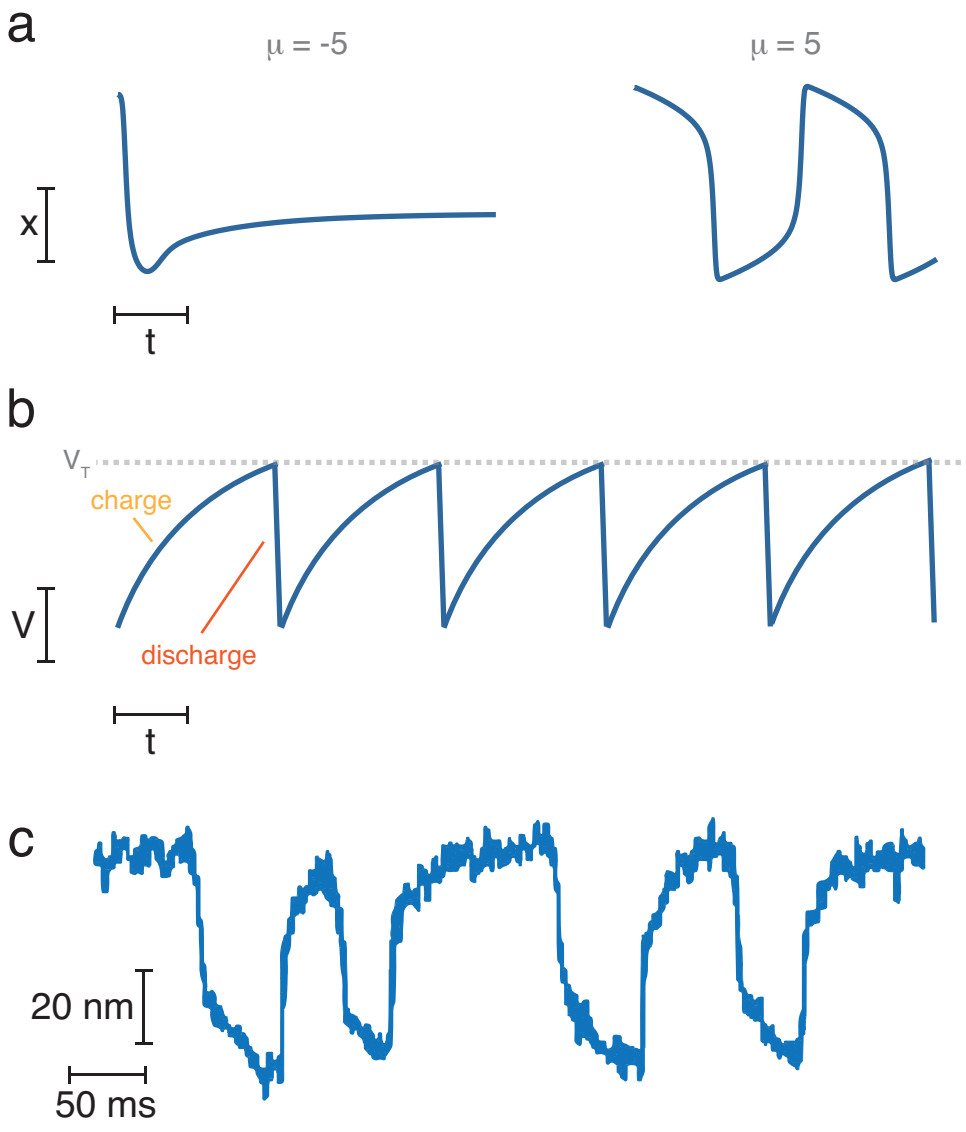
a
μ = -5
μ = 5
x
t
b
V_T
charge
discharge
V
t
c
20 nm
50 ms

Not long after the work of van der Pol, Alan Hodgkin and Andrew Huxley developed a mathematical description of action-potential propagation along neurons (177). Richard FitzHugh and Jin-Ichi Nagumo later simplified the Hodgkin-Huxley model as a modification of the van der Pol equation (178-180). The FitzHugh-Nagumo model reduces the four-dimensional Hodgkin-Huxley model to a descriptive two-dimensional one. The governing equations of the FitzHugh-Nagumo are

$$\dot{V} = V - \frac{V^3}{3} - W + I, \tag{3.19}$$

$$\dot{W} = 0.08(V + 0.7 - 0.8W), \tag{3.20}$$

in which V is a fast voltage-like variable instantiating the membrane potential, W is a slow recovery variable, and I is a stimulus current (179, 180). Like the van der Pol equation, equation 3.19 incorporates a cubic nonlinear term in V. The external current, I, is a control parameter. For $I < 0$, the system resides at a stable fixed point. The system crosses a Hopf bifurcation at $I = 0$, and for $I > 0$, the trajectory follows a limit cycle with relaxation oscillations.

The van der Pol and FitzHugh-Nagumo models highlight the generality of bifurcation normal forms. Each model includes unique details applicable to a particular system, whether that system is a nonlinear electrical circuit or an excitable membrane. Both models, however, accommodate a supercritical Hopf bifurcation. As a result, the characteristic behavior near a Hopf bifurcation applies to both models. Thus, the normal form of a bifurcation possesses the wherewithal to describe behaviors independent of the details of specific models.

CHAPTER 4

Nonlinear Dynamics of Hair Bundles

Sensory hair bundles feature characteristics that can be described by nonlinear dynamical systems. Specifically, behaviors arising from active hair-bundle motility resemble phenomena emerging from multiple bifurcation structures. These various behavioral divisions reside within different localities of a hair bundle's state diagram, which predicts distinct functional roles for particular sets of control parameters. In the auditory system, bundles poised near a supercritical Hopf bifurcation manifest sharp frequency tuning, large amplification, and a broad range of compression. By crossing a Hopf bifurcation, a hair bundle flaunts an epiphenomenon of spontaneous oscillation. In the vestibular system, bundles might be poised nearer to a subcritical Hopf, SNIC, or cusp bifurcation. Changes to one or more of a hair bundle's control parameters in close proximity to a SNIC bifurcation or both a subcritical Hopf and cusp bifurcation can increase or decrease the bundle's frequency of oscillation. Finally, the behavior of a hair bundle residing in a different sensory organ and species may be elicited by poising its operating point within a particular locus of its state space. Thus, a nonlinear description of hair-bundle behavior yields a functional map of sensory modalities and discloses an essential similarity of hair bundles.

This chapter explores specific models of active hair-bundle motility that incorporate different bifurcation types and particular state diagrams. These various

models are then integrated into a generalized hair-bundle model that captures the universality of bundle behavior.

SECTION 4.1: *Phenomena Near a Supercritical Hopf Bifurcation*

Auditory hair bundles are not simply passive detectors; they actively augment incoming signals. This is achieved through amplification of small stimuli, sharp frequency tuning, and compressive nonlinearity (146). As will be shown, bundles operating in close proximity to a supercritical Hopf bifurcation exhibit active-process phenomena.

An active process in audition was first noted by Thomas Gold. In his two-part treatise of 1948, Gold predicted that the resonant quality of the cochlea could not be accomplished by a passive system, simply due to challenges in overcoming viscous damping. He extended this with his regeneration hypothesis, whereby oscillators of negative resistance could permit high-quality resonance in hearing organs. Under appropriate conditions, critical oscillators could also exhibit spontaneous activity. These predictions mirrored observations in radio engineering, in which an oscillator whose amplificatory gain is too great will begin to self-oscillate (22). Years later, his hypotheses resurfaced under the guise of bifurcation theory (181).

Consider the normal form a supercritical Hopf bifurcation (equation 3.6). As previously noted, crossing a Hopf bifurcation yields limit-cycle oscillations, permitting a system to self-oscillate. This behavior is analogous to an active hair bundle's spontaneous oscillations that may generate spontaneous otoacoustic emissions from the cochlea (32, 34, 135, 159). On the stable side of the bifurcation, however, the oscillator

remains quiescent. When driven with periodic stimuli in this regime, compelling features emerge (Figure 4.1). Far from the bifurcation for $\mu < 0$, the oscillator responds poorly to weak stimuli at all driving frequencies. As μ approaches zero, the response amplitude at the characteristic frequency grows considerably. When driven at a frequency above or below the characteristic frequency, the response amplitude decays. In other words, a critical oscillator resonates at a particular frequency. Unlike its response to weak stimuli, the oscillator responds with diminished frequency selectivity for most operating points when driven by a large-amplitude stimulus (Figure 4.1) (67, 146, 162).

Let us consider these behaviors in more detail. An oscillator's steady-state response to a stimulus $f = \overline{f}e^{i\omega_d t}$ follows $z = \overline{y}e^{i\omega_d t}$, in which ω_d is the driving frequency. The magnitude of the stimulus and that of the oscillator approximately follow $\overline{f} = m\overline{y} + n\left|\overline{y}\right|^2 \overline{y}$. The linear coefficient m includes both a real and imaginary component $m \propto -\mu + i(\omega_d - \omega)$, and the cubic coefficient n is related to the coefficient from the normal form of the Hopf bifurcation $n \propto b$ (equation 3.6). The magnitude of the response achieves a peak at the characteristic frequency ω (Figure 4.2a). The peak's height is inversely proportional and width is proportional to the magnitude of μ. As the oscillator's operating point approaches the bifurcation and the magnitude of μ decreases, the resonant peak increases in height and quality. When $\mu = 0$, the response at the resonant frequency diverges to infinity. Thus, a hair bundle whose operating point is

poised near a supercritical Hopf bifurcation features amplification of weak stimuli with sharp frequency selectivity (67, 146, 162).

A driven Hopf oscillator boasts compressive nonlinearity. For weak stimuli and far from the bifurcation, the amplitude of the oscillator's response grows linearly with that of that stimulus (Figure 4.2b). As the stimulus increases in amplitude for an operating point close enough to the bifurcation, the response grows at a rate slower than that of the stimulus. This behavior compresses the range of response amplitudes to a range of amplitudes smaller than that of the stimuli (182). As μ approaches zero, this compression extends to weaker stimuli. When μ equals zero, compressively nonlinear responses extend to infinitesimal stimulus amplitudes, with the response amplitude following $|\bar{y}| \propto |\bar{f}|^{1/3}$ as governed by the cubic term in the bifurcation's normal form (146). The oscillator's sensitivity then follows $\chi = \frac{|\bar{y}|}{|\bar{f}|} \propto |\bar{f}|^{-2/3}$ (181). As the stimulus amplitude increases, the sensitivity subsequently decreases, and the extent of this feature again increases as the bifurcation is approached (Figure 4.2c). Taken together, the range over which compression occurs increases as the bifurcation is approached, and the oscillator's response is always nonlinear when $\mu = 0$. A hair bundle poised near a supercritical Hopf bifurcation thus wields a broad dynamic range because of this behavior (30, 34).

The normal form of a Hopf bifurcation can be used to optimize a hair cell's active process. In hair-bundle mechanoelectrical transduction, Ca^{2+} promotes channel reclosure and yields negative feedback on intrastereociliary Ca^{2+} concentration. A particular model of channel dynamics incorporates six channel states, including three open and three

closed states, with two Ca^{2+}-binding sites on the channel (183). Linear stability analysis of this six-state model exposes a supercritical Hopf bifurcation when eigenvalues cross the imaginary axis. Adjusting the model's parameters to poise it near a Hopf bifurcation maximizes the quality of resonance and amplificatory gain for weak stimuli. Interestingly, this model permits characteristic frequencies spanning the bandwidth of human hearing, ranging from as low as 0.02 to as high as 20 kHz by changing the number of stereocilia ($30 \leq N_S \leq 350$) and the channel's free energy barrier ($17 \leq \Delta G_C \leq 23.5$) (183). Thus, a simple model focusing exclusively on channel dynamics discloses a Hopf bifurcation, and the general phenomena near this bifurcation permit optimal auditory tuning.

Another model of hair-cell behavior near a supercritical Hopf bifurcation attends to the electrical resonance of a hair cell. A seven-dimensional model of electrical resonance includes the mechanically-gated cation conductance at the hair bundle in contact with endolymph and K^+ and Ca^{2+} conductances in contact with perilymph (184, 185). Linearization permits tuning of the hair cell's electrical properties to poise the system near a Hopf bifurcation. Near the bifurcation, electrical stimulation of the cell yields maximum gain and quality of resonance (185). It is thus apparent that not only can a hair bundle be poised near a Hopf bifurcation, but so too can the hair cell from which it projects. This feature highlights the general applicability of phenomena near a Hopf bifurcation to a multitude of specific models.

The nonlinear properties of hair bundles that can give rise to a Hopf bifurcation have been extensively modeled, and experimental evidence supports the presence of

these signatures in active hair cells. Stimulation of spontaneously oscillating hair bundles from the sacculus of the American bullfrog reveals active amplification and power-law scaling consistent with the cubic power law near a supercritical Hopf bifurcation (129). Additionally, stimulation of a hair bundle with a sum of two sinusoidal waveforms unveils cubic distortion products analogous to the cubic DPOAEs emerging from the cochlea. These distortion products presumably arise from the cubic nonlinearity of a Hopf bifurcation (186). Finally, bundle stimulation across multiple amplitudes and frequencies discloses a triangular region of 1:1 phase locking centered at the natural frequency known as an Arnold tongue (187). As the stimulus amplitude increases, the range of frequencies over which phase locking can be achieved grows. Once again, this behavior arises near a supercritical Hopf bifurcation (185). Though experimental evidence of a Hopf bifurcation is striking, no prior study has quantified the location of and distance to the bifurcation in a controlled manner. In other words, the effect of changing a control parameter to reveal a bifurcation and its associated phenomena was not investigated prior to the present work.

Signatures of a supercritical Hopf bifurcation are not limited to hair cells. Physiology of the mammalian cochlea divulges phenomena consistent with function near a Hopf bifurcation. When the ear is stimulated by two frequencies that differ by about 10%, additional combination tones are perceived and DPOAEs may be emitted from the ear (31, 32). Unlike a device at its saturating limit, these distortion products occur for non-saturating stimuli and thus imply an *essential nonlinearity* in the cochlea (41, 188). Cubic distortion products are the most prominent of the DPOAEs (41), and

they have also been witnessed as vibrations on the mammalian basilar membrane (189). Such cubic components arise from a nonlinear system with a supercritical Hopf bifurcation (190).

Vibration of the basilar membrane reveals power-law scaling consistent with a Hopf bifurcation. For stimuli of appropriate magnitude, the basilar membrane's response R_{BM} grows with respect to the sound pressure level P_S by $R_{BM} \propto P_S^{1/3}$ and exhibits a linear relationship for weak stimuli (164, 191). This pattern arises from the behavior of critical oscillators that selectively augment auditory stimuli (190).

Finally, critical oscillators not only permit the aforementioned behaviors within the cochlea, but they also produce the tsunami-like traveling wave along the cochlear partition. The traveling wave cannot be explained by passive properties alone, and the wave has instead been shown to be active and nonlinear with a requirement of *negative damping* (192). Oscillators near criticality supply negative damping to the cochlear partition (190, 193). If each oscillator is located at a particular location along the cochlear partition and is tuned to a location-dependent frequency, a traveling wave achieves its peak at a characteristic place defined by the stimulus frequency. After the wave achieves a peak, it rapidly decays to zero amplitude. This nonlinear, active amplification occurs when each oscillator is poised near a supercritical Hopf bifurcation (193). Thus, the behaviors near a Hopf bifurcation not only explain hair-bundle phenomena, but they permit the remarkable traits of audition.

Figure 4.1. Behavior of a supercritical Hopf oscillator. Deterministic simulations of a supercritical Hopf bifurcation reveal sharp frequency tuning and amplification of weak stimuli. A critical oscillator defined by the normal form of a supercritical Hopf bifurcation was delivered sinusoidal stimuli at amplitudes of 0.001 and 5 and frequencies of 0.5, 1, and 100 Hz (red). For each stimulus, the oscillator's response is shown at control parameters of μ = -5, -1, -0.1, and -0.01 with μ_C = 0 (blue). At a small stimulus amplitude of 0.001, the oscillator's response achieves maximum amplification at its characteristic frequency of 1 Hz when poised closest to the bifurcation (purple). Stimulation above or below the characteristic frequency at this operating point yields a diminished response amplitude. Departing from the bifurcation into the quiescent regime also yields a smaller response. When the stimulus amplitude is increased to 5, the frequency selectivity near the bifurcation is lost. However, the maximum response amplitude once again occurs closest to the bifurcation. For all simulations, the planar equations $\dot{x} = \mu x - y - x(x^2 + y^2)$ and $\dot{y} = x - \mu y - y(x^2 + y^2)$ were solved using the Euler-Murayama method in MATLAB for 100 seconds and a step size of 1 ms. These equations describe the same system as the complex normal form defined by equation 3.6. All results have been downsampled by a factor of 10 and rescaled at each stimulus amplitude for ease of visualization.

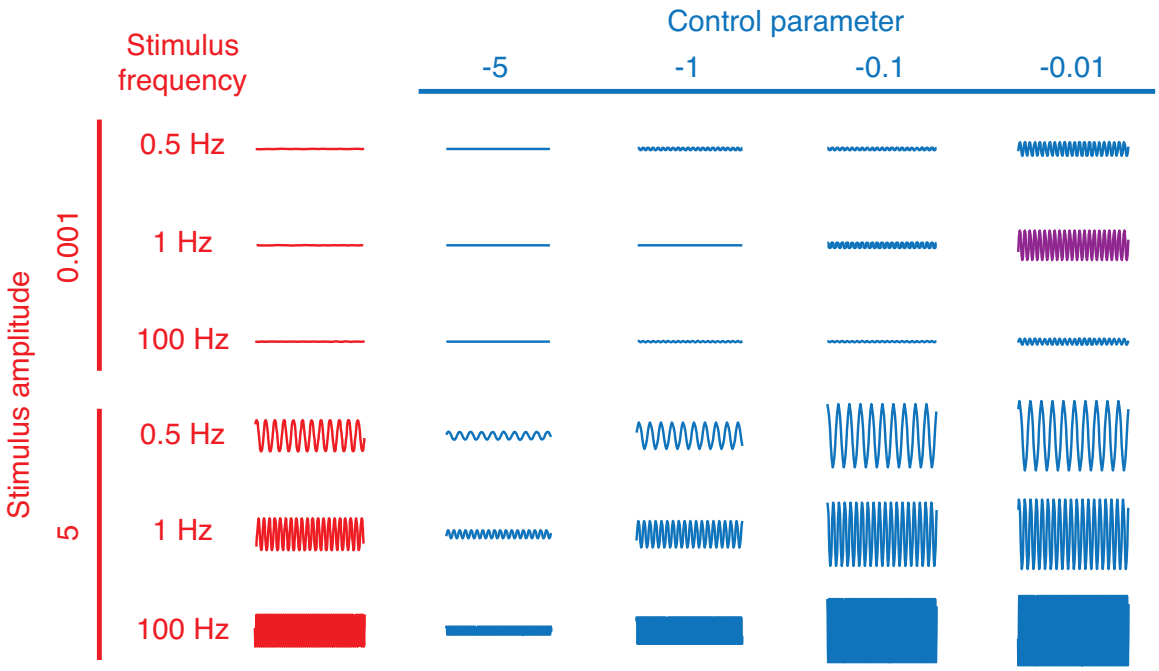
Control parameter
Stimulus frequency
-5
-1
-0.1
-0.01
Stimulus amplitude
0.001
5
0.5 Hz
1 Hz
100 Hz
0.5 Hz
1 Hz
100 Hz

Figure 4.2. Amplification near a supercritical Hopf bifurcation. (a) A critical oscillator poised at operating points of μ = -20, -10, -5, -1, and -0.01 was delivered sinusoidal stimuli of increasing frequency at a stimulus amplitude of 0.5. The oscillator's response achieves maximum amplification and frequency selectivity at μ = -0.01. The magnitude and quality of the resonant peak decreases as the operating point departs from the bifurcation. At μ = -20, the oscillator's response achieves only a small response across frequencies. (b) Stimuli of increasing amplitude at a frequency of 1 Hz were delivered to a supercritical Hopf oscillator poised at the same operating points in (a). Far from the bifurcation at μ = -20, the oscillator's response increases linearly with the stimulus amplitude and follows a slope of one (brown dashed line). As the oscillator's operating point approaches the bifurcation, the relationship between its response amplitude and the stimulus amplitude becomes nonlinear. This behavior compresses the range of responses for a given range of stimulus amplitudes. At μ = -0.01, the slope is approximately 1/3 for nearly all stimulus amplitudes (gray dashed line). (c) The oscillator's sensitivity—defined as the response amplitude divided by the stimulus amplitude—depicts compressive nonlinearity for the same simulations in (b). At low stimulus amplitudes and far from the bifurcation, the oscillator's response is linear and follows a slope of zero (brown dashed line). At high stimulus amplitudes and close to the bifurcation, the sensitivity decreases with stimulus amplitude and follows a slope of -2/3 (gray dashed line). The responses in all panels were calculated according to the relation $(\mu R - cR^3)^2 + (\omega_0 - \omega - dR^3)^2 = f^2$, in which μ is a control parameter, R is the system's response amplitude, f is the amplitude of the stimulus, ω is the frequency of driving, ω_0 is the Hopf frequency, and $c = d = 1$ are respectively the real and imaginary cubic coefficients in the normal form a supercritical Hopf bifurcation (194).

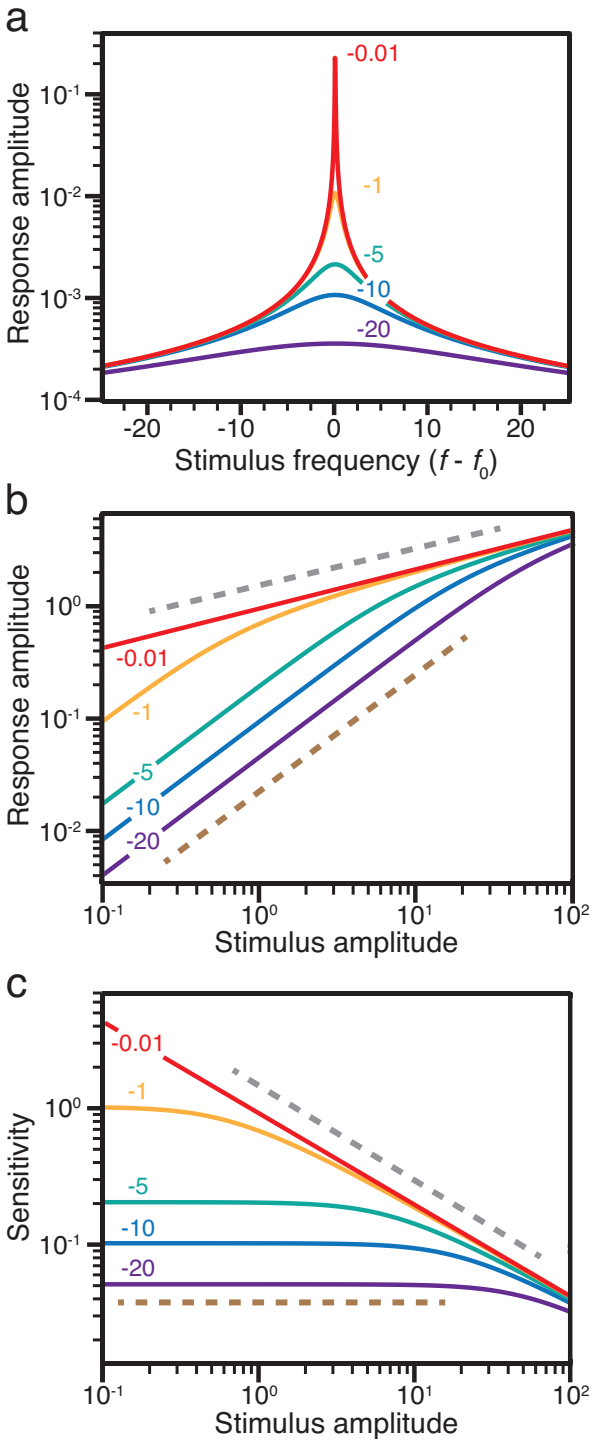
a
Response amplitude
10^{-1}
10^{-2}
10^{-3}
10^{-4}
-0.01
-1
-5
-10
-20
-20
-10
0
10
20
Stimulus frequency (f - f_0)
b
Response amplitude
10^{0}
10^{-1}
10^{-2}
-0.01
-1
-5
-10
-20
10^{-1}
10^{0}
10^{1}
10^{2}
Stimulus amplitude
c
Sensitivity
10^{0}
10^{-1}
-0.01
-1
-5
-10
-20
10^{-1}
10^{0}
10^{1}
10^{2}
Stimulus amplitude

SECTION 4.2: *Individual Models of Hair-Bundle Motility*

Dynamical models of hair-bundle motility incorporate different elements and make assumptions about others. The mechanoelectrical transduction apparatus includes a channel with multiple states that is in series with a gating spring and an adaptation motor complex, all of which may depend on Ca^{2+}. To model this process, one can consider independently the transduction channel's dynamics, Ca^{2+} dynamics, and adaptation motor dynamics (167). Each of these models comprises different sets of equations, yet all of them disclose a Hopf bifurcation. This section introduces an example of each class of model and concludes with a fourth model of hair-bundle motility that predicts a putative hair-bundle state diagram. The models will be incorporated into a generalized dynamical system with its own state diagram in the following section.

A model of the transduction channel's dynamics incorporates adaptive changes of the channel, assumes that Ca^{2+} equilibrates rapidly, and excludes motor dynamics. The hair bundle's equation of motion is given by

$$m_{HB}\ddot{X} + \xi_{HB}\dot{X} = F_S - K_{SP}(X - X_{SP}) - N_T\gamma\kappa_{GS}\left[\gamma(X - X_{GS}) - p_O d\right], \tag{4.1}$$

in which m_{HB} and ξ_{HB} are respectively the hair bundle's mass and stiffness, F_S is a stimulus force, K_{SP} is the combined stiffness of the stereociliary pivots, X_{SP} is the bundle's position at which the pivot forces are zero, N_T is the number of transduction channels, γ is the geometric gain. Each gating spring has a stiffness κ_{GS} that becomes taut when the bundle's position is X_{GS}. An individual channels possesses an open probability p_O and

opens with a gating swing distance d (183). Each transduction channel has two Ca^{2+}-binding domains, permitting three open and three closed states. The probability that a channel is open depends upon the force applied to it, and the channel adapts dynamically. By adjusting different parameters in the system, such as the number of transduction channels, the model bundle can be poised near a supercritical Hopf bifurcation with a unique characteristic frequency. Here it achieves maximum gain and sharpest frequency selectivity (183).

Unlike the previous model, an alternative representation of hair-bundle motility assumes that the transduction channel equilibrates quickly and instead models Ca^{2+} dynamics. As before, adaptation motor dynamics are assumed to be fast. Here the transduction channel has one open and two closed states (167, 195). Although Ca^{2+} does not close the channel, it stabilizes the closed state. The bundle's equation of motion is governed by

$$\xi_{HB}\dot{X} = -K_{SP}(X - X_m) - K_{GS}(X - d_O P_O - d_{C1}P_{C1} - d_{C2}P_{C2}) + F_S\,, \tag{4.2}$$

in which X_m is the length of the tip link under tension, K_{GS} is the combined stiffness of the gating springs, d_O is the gating swing of the channel's open state, d_{C1} and d_{C2} are the gating swings of the two closed states, P_O is the probability that the channel is in the open state, and P_{C1} and P_{C2} are the probabilities of the channel's two closed states (195). The probability of each channel state depends on the intracellular Ca^{2+} concentration C. Intracellular Ca^{2+} levels adapt dynamically and follow

$$\dot{C} = -\lambda(C - C_B - C_M P_O)\,, \tag{4.3}$$

in which λ is the relaxation rate of Ca^{2+} concentration changes, C_B is the steady-state Ca^{2+} concentration when channels are blocked and arises from diffusion of Ca^{2+} from other intracellular locations, and C_M is the maximal Ca^{2+} influx through open transduction channels. The inverse of the relaxation rate is on the order of milliseconds in the model, in contrast with the fast Ca^{2+} equilibration in the previous model of channel dynamics (195). Linear stability analysis of this model once again reveals a supercritical Hopf bifurcation. For a hair bundle to spontaneously oscillate, it must satisfy the condition

$$K_{SP} + N_T \gamma^2 (K_{TL} + f') < 0 , \tag{4.4}$$

in which K_{TL} is the tip-link stiffness and f' is the first derivative of the gating force that arises from the channel switching states (195). Since the passive stiffnesses K_{SP} and K_{TL} are always positive, f' must be negative and greater in magnitude than the combined passive stiffness to satisfy equation 4.4. In other words, the gating compliance must more than compensate for the passive bundle stiffness in order to permit the crossing of a Hopf bifurcation.

Interestingly, the model of Ca^{2+} dynamics can permit self-tuning to a supercritical Hopf bifurcation through control of intracellular Ca^{2+} concentration (195). When a bundle is quiescent, some mechanism adjusts the bundle's position to coerce its operating point into an unstable regime. When the bundle spontaneously oscillates, the same mechanism adjusts the bundle's operating point into a quiescent regime. This could be achieved through the addition of Ca^{2+}-dependent motor dynamics but has yet to be verified experimentally (45).

A third dynamical model of hair-bundle motility assumes fast equilibration of both the transduction channel and intracellular Ca^{2+} concentration. Instead, the model examines the dynamics of the adaptation motor (167). Hair-bundle motion is governed by two equations

$$\xi_{HB}\dot{X} = -K_{GS}(X - X_a - DP_O) - K_{SP}X + F_S + \eta\,, \tag{4.5}$$

$$\xi_a\dot{X}_a = K_{GS}(X - X_a - DP_O) - K_{ES}(X_a - X_{ES}) - F_{\max}(1 - SP_O) + \eta_a\,. \tag{4.6}$$

Here X_a is the position of the adaptation motor, D is the bundle's motion from channel opening and is related to the gating swing by $d = \gamma D$, ξ_a is the motor friction, F_{max} is the adaptation motor stall force when all channels are closed, S is the strength of Ca^{2+} feedback on motor force, and η and η_a are noise terms (196). The model also includes an extent spring of stiffness K_{ES} that anchors the mechanoelectrical transduction machinery to stereociliary actin. When the extent spring has zero tension, the adaptation motor resides at position X_{ES}. The total force produced by the motor complex $F_{max}(1\text{-}SP_O)$ decreases as channels open due to an increase in intracellular Ca^{2+} that acts on the adaptation motors. Once again, this model yields a supercritical Hopf bifurcation. By adjusting F_{max} and S, the bundle's operating point may be poised at an optimum of sensitivity (170, 196).

Taken together, three disparate models of hair-bundle mechanics accommodate a Hopf bifurcation. This highlights the general applicability of bifurcation analysis to bundle behavior. Since an oscillator achieves its highest gain, sharpest frequency selectivity, and largest dynamic range near a Hopf bifurcation, one can find a behavioral

optimum by tuning parameters in each model to find this critical locus. Put another way, the Hopf bifurcation is not a model *per se*, yet it divulges an optimal parameter set for a given model.

A hair bundle's state diagram is a map of the bundle's behavior for various sets of control parameters. One such diagram describes hair-bundle dynamics using both motor dynamics and Ca^{2+} dynamics. The bundle's motion is governed by

$$\xi_{HB}\dot{X} = -K_{GS}(X - X_a - DP_O) - K_{SP}X + F_S + \eta\,, \tag{4.7}$$

$$\xi_a\dot{X}_a = K_{GS}(X - X_a - DP_O) - \gamma N_a f_m p(C) + \eta_a\,, \tag{4.8}$$

$$\lambda\dot{C} = C_0 - C + C_M P_O + \delta c\,, \tag{4.9}$$

in which N_a is the total number of adaptation motors in the hair bundle, f_m is the force produced by a single motor, $p(C)$ is the Ca^{2+}-dependent probability that the motor is bound to actin, and δc accounts for fluctuations in Ca^{2+} (170). This model is directly related to the one described by equations 4.5 and 4.6. Ignoring nonlinear terms in $p(C)$, the maximum force a single motor can produce $f_{max} = Naf_m p_0$ and the strength of Ca^{2+} feedback on the motor's force $S = -C_M p_1/p_0$ control the bundle's proximity to a bifurcation, in which $p(C)$ is approximated to a linear order by $p(C) \approx p_0 + p_1 C$. This results in $\gamma N_a f_m p(C) \approx \gamma f_{\max}(1 - SC/C_M)$. Assuming instantaneous relaxation of Ca^{2+} ($\lambda = 0$), a two-parameter state diagram emerges. Large motor forces permit channel opening, and an f_{max} that is too small results in an open probability of zero and thus quiescent bundle behavior. Since Ca^{2+} decreases the force each motor can produce, an increase in the strength of the Ca^{2+} feedback S decreases the open probability and

produces monostability. Only for intermediate values of S and f_{max} will a hair bundle spontaneously oscillate. The state diagram illustrates this behavior for these control parameters and exposes lines of supercritical and subcritical Hopf bifurcations that enclose an oscillatory regime. Lines of fold bifurcations bound a bistable region in which channels may exist in closed or open states. By poising a sensory hair bundle's operating point at an appropriate location in its state space, the bundle can achieve maximum sensitivity (170).

The aforementioned state diagram poses a problem for the biologist. If a hair bundle's sensory function depends on the strength of Ca^{2+} feedback and the maximum force a myosin motor can produce, how can this be tested? Experimental control of these parameters proves to be a daunting and possibly insurmountable task. Indeed, there exists no experimental study that explores this state diagram. Furthermore, the question of how these parameters might be tuned *in vivo* remains unanswered. It is thus apparent that an experimentally tractable, biologically feasible, and generalized state diagram of hair-bundle behavior must be developed.

SECTION 4.3: *Generalized Model of Hair-Bundle Motility*

Although hair bundles comprise similar molecular constituents, the mechanical properties of bundles and their accessory structures vary along the tonotopic axis of the cochlear partition, between sensory organs, and amongst disparate species. Motivated by these differences, a dynamical model of hair-bundle motility was developed to describe general principles of bundle behavior. This generalized model incorporates and simplifies the dynamics of transduction channels, adaptation motors, and intracellular Ca^{2+} (167). The result is a dynamical system controlled only by mechanical loads, producing an experimentally tractable and biologically significant system.

Mechanical loads influence hair-bundle mechanics according to the following equations:

$$m_T\ddot{X} = -\xi_T\dot{X} - K_T X + a(X - f_a) - (X - f_a)^3 + F_T, \tag{4.10}$$

$$\tau_a\dot{f}_a = bX - f_a, \tag{4.11}$$

in which f_a is the force of adaptation, τ_a is the relaxation time of adaptation, and a and b are stiffnesses (167). The total mass of the system is $m_T = m_{HB} + m_E$, in which m_{HB} is the bundle's mass and m_E is the mass of an external load. The mass of a hair bundle is often assumed to be negligible. The total viscous drag of the system is $\xi_T = \xi_{HB} + \xi_E$, in which ξ_{HB} and ξ_E are respectively the damping coefficients of a hair bundle and an applied load. A bundle's stiffness when coupled to an external load is $K_T = K_{HB} + K_E$. Finally, the total force applied to the bundle is $F_T = F_{C,HB} + F_{C,E} + F_S$, in which $F_{C,HB}$ is an intrinsic constant offset force of a hair bundle, $F_{C,E}$ is a constant force applied to a hair bundle by

and external load, and F_S is an additional pulsatile or periodic forcing term. When mapping the state diagram of a hair bundle, F_S is set to zero. Equation 4.10 incorporates the nonlinear stiffness of a hair bundle in the term $a(X - f_a) - (X - f_a)^3$, and equation 4.11 characterizes an adaptive shift in the force-displacement relation that depends on the position of the bundle (167). Thus, the only requirements necessary for this model are nonlinear channel gating and an adaptation process. From these clear and conserved characteristics there rises a plethora of provocative phenomena.

A state diagram characterizes a hair bundle's behavior for combinations of mechanical control parameters (167). By adjusting only the constant force and load stiffness applied to a bundle, unique features emerge (Figure 4.3a). Lines of supercritical and subcritical Hopf bifurcations enclose a locus of spontaneous oscillation. Outside this region, the bundle wields only one stable state and is thus monostable or quiescent. Finally, a cusp bifurcation generates lines of fold bifurcations that encase a bistable region. Here a bundle can switch between states in which transduction channels are either fully open or fully closed. Changes to the constant force and load stiffness transform a bundle's unforced behavior. For example, increasing the load stiffness applied to a bundle coerces its operating point from an oscillatory regime, across a supercritical Hopf bifurcation, and into a monostable, non-oscillatory regime. Alternatively, increasing the constant force inflicted upon a bundle coaxes its operating point across either a subcritical or supercritical Hopf bifurcation, depending upon the associated load stiffness.

A hair bundle's operating point controls its motion. Within the oscillatory regime and at lower values of load stiffness, a hair bundle exhibits high-amplitude, low-frequency relaxation oscillations (Figure 4.3b). The bundle's motion decreases in amplitude, increases in frequency, and becomes approximately sinusoidal as the load stiffness increases toward a line of supercritical Hopf bifurcations (167). Both the bundle's intrinsic dynamics and the applied mechanical load define the frequency of oscillation at all operating points. Additional mechanical loads can adjust the hair bundle's two-dimensional state diagram. Mass loading increases the scope of the spontaneously oscillatory regime, whereas viscous damping shrinks the locus of spontaneous oscillations (Figure 4.3c). Taken together, the mechanical properties of a hair bundle and an additional load define its unforced behavior.

Though not explicitly mentioned in the original description of the generalized model, the size of a hair bundle should affect its state diagram. Remember that a bundle's gating force must exceed its total passive stiffness in order to achieve spontaneous oscillation (equation 4.4) (195). In the generalized model, this occurs when $K_T < a$, yielding a region of negative stiffness in the bundle's force-displacement relation of width $2\sqrt{(a - K_T)/3}$ (167). The stiffness a can be considered as proportional to the sum of all gating-spring stiffnesses. An increase in this stiffness causes an increase in the total gating force, $Z_T = N_T Z = N_T \gamma \kappa_{GS} d$, in which N_T is the total number of transduction apparatuses, Z is the gating force from an individual transduction channel, d is the gating swing, and κ_{GS} is the stiffness of an individual tip link (109, 196). In other words, boosting the number of transduction apparatuses increases the total stiffness of the

gating springs (rescaled as a) and thus the total gating force (Z_T). The lines of Hopf bifurcations in the absence of mass and viscous damping are governed by

$$F_C^2 = \frac{a - K_T - \frac{1}{\tau_a}}{27}\left[\frac{(2a + \frac{1}{\tau_a})(1-b) - (2+b)K_T}{1-b}\right]^2, \tag{4.12}$$

in which $F_C = F_{C,HB} + F_{C,E}$ is the total constant force of the bundle (167). Increasing a causes a growth in the size of the oscillatory region bounded by lines of Hopf bifurcations (Figure 4.4a). Correspondingly, both the magnitude and width of the negative-stiffness region grow within the bundle's force-displacement relation, given by $F = K_T X - a(X - f_a) - (x - f_a)^3$ (Figure 4.4b) (167). This agrees with the previous prediction that an increase in the stiffness a causes an upsurge in the total gating force. Though the original description of the model did not explicitly characerize this phenomenon, the effects of hair-bundle size must be considered throughout this study.

In sensory systems, hair bundles must detect and transduce different external forces. In the acousticolateralis system, auditory hair bundles detect periodic stimuli of a particular frequency, but vestibular hair bundles respond to force pulses and static offsets.

An active hair bundle's response to periodic forcing depends on its mechanical load (167). As seen before, the bundle achieves maximum amplification and quality of resonance when the constant force and load stiffness poise its operating point near a supercritical Hopf bifurcation. Additionally, the sensitivity of a hair bundle's response to stimuli of increasing amplitude at its resonant frequency obtains the largest range of

nonlinearity near the bifurcation. Poising the bundle's operating point far from a supercritical Hopf bifurcation in either the monostable or oscillatory regime diminishes the system's amplification, tuning, and range of compressive nonlinearity (167). Thus, an auditory hair bundle must possess mechanical properties that situate it near this critical locus.

Delivering force pulses to a hair bundle yields behaviors consistent with experiments across organs and organisms. Within a neighborhood of the monostable regime surrounding the locus of spontaneous activity, a bundle is underdamped. Here it rings in response to a force pulse (167). This phenomenon accords with experimental findings in the turtle (197). Outside this region, the bundle's response first overshoots its steady-state position before rapidly returning to a steady state (167). The dynamics of fast adaptation produce this twitch, an attribute observed in hair bundles of multiple species (107, 110). Finally, a hair bundle's steady-state position may exceed that of the stimulus (167). Such an overshoot was previously noted in the rat cochlea (114). Taken together, a hair bundle's otherwise species-specific response to force pulses depends instead on its mechanical load.

According to this dynamical model, the constant force and load stiffness of a bundle determine its sensory modality. The model provides an enticing set of predictions with experimentally tractable control parameters. This work evaluates this model in detail in order to confirm its predictions. Additionally, phenomena not predicted by the model, such as a change in the system's Arnold tongue and mechanical excitability of bundles, surfaced throughout these labors. To accomplish this, a feedback-

based clamp system was developed and implemented to control the mechanical loads applied to hair bundles.

Figure 4.3. The effects of mechanical loading on hair bundles. (a) A state diagram documents a hair bundle's expected behavior for various values of load stiffness and constant force. These parameters determine whether a bundle will spontaneously oscillate, remain quiescent, or manifest bistable switching. A spontaneously oscillatory regime (orange) is surrounded by a line of subcritical and supercritical Hopf bifurcations (thin and thick solid lines, respectively) demarcated by two Bautin points (filled circles). Fold bifurcations enclose a bistable regime (green). A hair bundle exhibits only one stable point within the monostable regime (white). (b, *left*) The amplitude of spontaneous oscillations increases as the load stiffness decreases (arrow). The amplitude's dependence on the constant force is more complex. Smaller amplitudes are denoted by darker shades of red. (b, *right*) The frequency of spontaneous oscillations rises as the load stiffness grows. Lower frequencies are denoted by darker shades of blue. (c, *left*) Mass loading a hair bundle theoretically increases the size of the spontaneously oscillatory regime (dark orange). (c, *right*) Viscous damping reduces the size of the spontaneously oscillatory regime (dark orange).

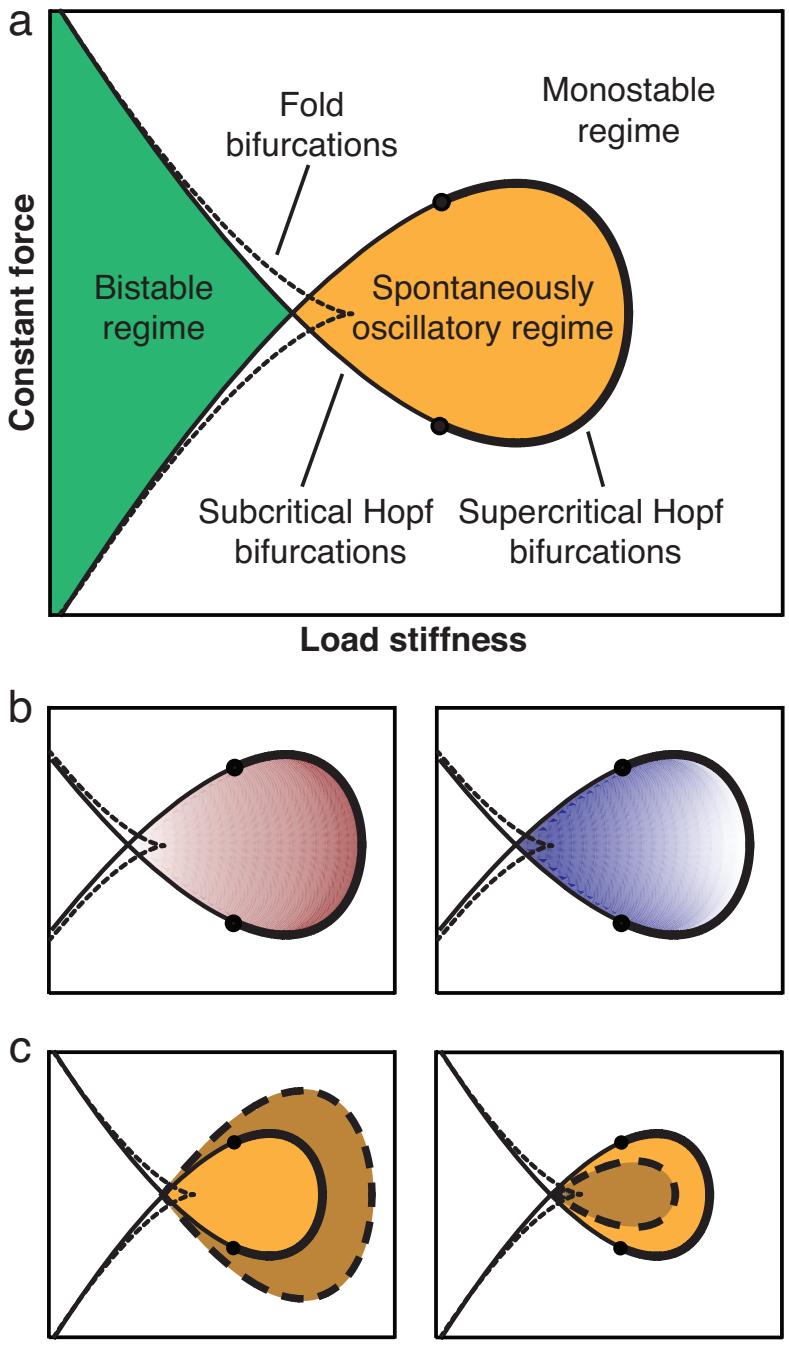
a
Fold
bifurcations
Monostable
regime
Bistable
regime
Spontaneously
oscillatory regime
Constant force
Subcritical Hopf
bifurcations
Supercritical Hopf
bifurcations
Load stiffness
b
c

Figure 4.4. Effects of gating stiffness on hair-bundle dynamics. (a) The state diagram of a hair bundle illustrates changes in the lines of supercritical Hopf bifurcations with total gating stiffness. As a increases from 3 (red) to 3.5 (green) and 4 (blue), the extent of the oscillatory region grows. This can be accomplished by increasing the total number of stereocilia, which would have the effect of increasing the total gating force. (b) The force-displacement relation for the same parameters in (a) discloses a change in the magnitude of negative stiffness and the width of the negative-stiffness region. An increase in a causes an increase in both the magnitude and width of this unstable regime. Thus, a larger constant force and stiffness is required to suppress spontaneous hair-bundle oscillations. For all simulations, b = 0.5, τ_a = 10, and f_a = 1. For panel (b), the bundle's stiffness was K_T = 2.

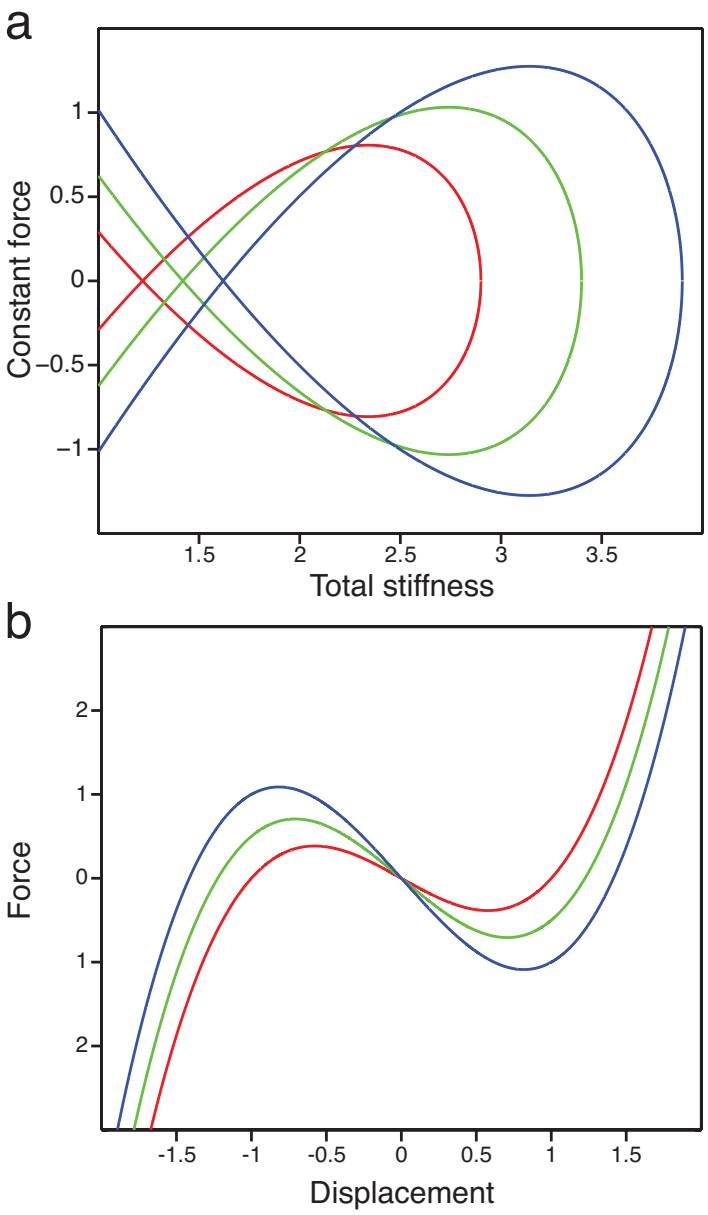
a
Constant force
1
0.5
0
−0.5
−1
1.5
2
2.5
3
3.5
Total stiffness
b
Force
2
1
0
1
2
-1.5
-1
-0.5
0
0.5
1
1.5
Displacement

CHAPTER 5

The Mechanical-Load Clamp

A mechanical-load clamp permits exploration of the state space of an individual hair bundle and investigation of the effects of mechanical loading on hair-bundle behavior. To deliver loads onto individual hair bundles, the tip of a flexible glass fiber is coupled to the top of a hair bundle and a piezoelectric actuator displaces the fiber's base. To control the load, a real-time processor compares the bundle's actual position, measured by a photomicrometer system, with that specified by a command signal, and then provides feedback to the actuator to minimize the difference between the two (Figure 5.1). By adjusting the strength of the system's feedback and the commanded position, one may independently manipulate the load stiffness and the constant force, permitting exploration of a hair bundle's state diagram. This chapter introduces two versions of the mechanical-load clamp. The first clamp system utilizes a proportional-integral-derivative (PID) feedback system to systematically adjust both the constant force and load stiffness applied to a hair bundle. The second system calculates the bundle's position, velocity, and acceleration on a point-by-point basis to control the external force, virtual stiffness, virtual drag coefficient, and virtual mass of a bundle.

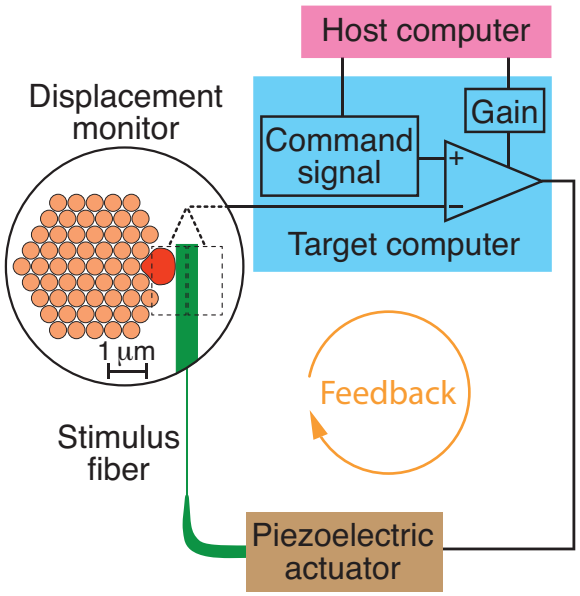

Figure 5.1. The mechanical-load clamp. As shown in the magnified circular inset, the tip of a flexible glass stimulus fiber exerts a force on the kinociliary bulb (red) at the top of a hair bundle while the position of the fiber's tip is projected onto a dual photodiode (dashed rectangles). Information from this displacement monitor is conveyed to a target computer, which compares the bundle's position with the displacement commanded by the host computer and provides feedback with gain to a piezoelectric actuator that displaces the fiber's base. The command signal and gain together define the stiffness and constant force confronting the hair bundle. Positive forces act toward the hair bundle's tallest edge, to the right, and negative forces in the opposite direction.

SECTION 5.1: *Two-Parameter Load Clamp*

In most clamp systems, such as the venerable voltage clamp, a negative feedback loop holds one experimental variable fixed while the conjugate variable is measured. Under displacement-clamp conditions, for example, a hair bundle is maintained at a commanded position while the ensuing force is evaluated (109, 198). A force clamp inverts this relationship: feedback imposes a constant force while the displacement is determined.

In the present experiments we implemented a generalization of this procedure, load-clamping, in which the feedback system simultaneously imposes on a hair bundle two conditions that mimic the bundle's environment *in vivo*. The system serves as a stiffness clamp that imposes a specified elastic load and at the same time acts as a force clamp that applies a commanded constant, sinusoidal, or pulsatile force. Load-clamping is possible because contemporary computers can solve the necessary differential equations on a timescale shorter than the mechanical relaxation time of the stimulus fiber and attached hair bundle (128, 199). In a further generalization of the approach, one can examine the hypothesized effects on hair bundles of inertia and drag, two parameters that may play a greater role in vestibular organs (167). This extended system will be described in *Section 5.2*.

At the point of contact between a stimulus fiber and hair bundle, the elastic force produced by the flexion of the fiber is balanced by the sum of the elastic and drag forces associated with the fiber and bundle:

$$K_{SF}(\Delta - X) = \xi_{XX}\dot{X} + \xi_{\Delta X}\dot{\Delta} - \xi_{HB}\dot{X} + K_{HB}X - F_A . \quad (5.1)$$

Here K_{SF} is the stiffness of the stimulus fiber and K_{HB} is that of the hair bundle, Δ is the position of the fiber's base and X is that of the hair bundle, ξ_{XX} is the drag coefficient of the stimulus fiber owing to motion at the fiber's tip and $\xi_{\Delta X}$ is that owing to motion at the fiber's base, and ξ_{HB} is the drag coefficient of the hair bundle. F_A represents any active or nonlinear force produced by the hair bundle. Note that all inertial effects of the bundle and fiber are assumed to be small.

The photodiode's output voltage V_D is linearly related to the hair bundle's position by a coefficient α: $V_D = \alpha X$. If the clamp accomplishes a commanded displacement X_C, the photodiode's output voltage is $V_C = \alpha X_C$. The error signal at the clamp's amplifier is therefore

$$V_E = V_C - V_D = \alpha(X_C - X) . \quad (5.2)$$

This signal is amplified by the proportional gain G to generate an output signal V_O that is delivered to the piezoelectric stimulator,

$$V_O = GV_E = \alpha G(X_C - X). \quad (5.3)$$

The stimulator's displacement output is linearly related to its input signal by a coefficient β, $\Delta = \beta V_O$, so the resultant displacement of the stimulus fiber's base is

$$\Delta = \alpha\beta G(X_C - X) . \quad (5.4)$$

Combining equations 5.1 and 5.4 yields

$$(\xi_{XX} - \alpha\beta G\xi_{\Delta X} + \xi_{HB})\dot{X} + [(1 + \alpha\beta G)K_{SF} + K_{HB}]X - F_A = \alpha\beta G(-\xi_{\Delta X}\dot{X}_C + K_{SF}X_C) . \quad (5.5)$$

When $|\alpha\beta G\xi_{\Delta X}| << \xi_{XX} + \xi_{HB}$ and $|K_{SF}X_C| >> |\xi_{\Delta X}\dot{X}_C|$, equation 5.5 becomes

$$(\xi_{XX} + \xi_{HB})\dot{X} + (K_E + K_{HB})X - F_A = \alpha\beta G K_{SF} X_C\,, \tag{5.6}$$

in which $K_E = (1 + \alpha\beta G)K_{SF}$ is the effective load stiffness due to the clamp. The condition $\left|\alpha\beta G\xi_{\Delta X}\right| << \xi_{XX} + \xi_{HB}$ is met for sufficiently small values of $\xi_{\Delta X}$ and G, in which $\alpha\beta \sim 1$ and $\xi_{HB} \geq 100$ nN·s·m^{-1}. The experiments presented here satisfy this condition, with G typically less than one and never exceeding two. For the fibers used here, ξ_{XX} = 50-70 nN·s·m^{-1} and $\xi_{\Delta X}$ = 30-40 nN·s·m^{-1}. When K_{SF} = 100-350 μN·m^{-1}, the condition $\left|K_{SF}X_C\right| >> \left|\xi_{\Delta X}\dot{X}_C\right|$ is satisfied for timescales greater than $\xi_{\Delta X}/K_{SF}$ < 0.1-0.3 ms. Additional forces owing to the drag from the base of the fiber are not significant for times exceeding this bound.

The displacement command may be used to apply various types of stimuli to the bundle. We may choose $X_C = X_{CC} + X_S\sin(\omega_s t) + X_P(t)$, such that $F_{C,E} = \alpha\beta G K_{SF} X_{CC}$ is a constant external force, $F_S\sin(\omega_s t) = \alpha\beta G K_{SF} X_S \sin(\omega_s t)$ is a sinusoidal force of angular frequency ω_S, and $F_P(t) = \alpha\beta G K_{SF} X_P(t)$ is a force pulse. Equation 5.6 then yields

$$(\xi_{XX} + \xi_{HB})\dot{X} + (K_{EFF} + K_{HB})X - F_A = F_{C,E} + F_S\sin(\omega_s t) + F_P(t)\,. \tag{5.7}$$

The clamp thus permits control of the stiffness and various forms of stimulus force independently through adjustment of the proportional gain G and command displacement X_C.

To demonstrate robust independent control of the stiffness and constant force with a mechanical-load clamp, a glass stimulus fiber was used to deliver stimuli to a vertically mounted glass fiber that served as a simulacrum of a hair bundle. This arrangement provided a system with a known, linear stiffness for calibration and

controls. For calibration purposes, steps were delivered for a series of forces and stiffnesses. For each constant force, the steady-state position of the fibers' tip is given by

$$X = \frac{\alpha\beta G X_C K_{SF}}{K_{SF}(1+\alpha\beta G) + K_{HB}} = \frac{F_{C,E}}{K_{EFF} + K_{HB}}. \tag{5.8}$$

The validity of this relation is confirmed in Figure 5.2a. As the load stiffness increased for a given constant force, a relationship consistent with that of a Hookean material appeared. These data verify that the mechanical-load clamp independently controls both the constant force and load stiffness applied to an individual hair bundle.

When periodic stimuli at frequencies of 5-100 Hz are delivered with multiple load stiffnesses, the fiber's motion matched the commanded value with an error of 2% and was independent of the fiber's stiffness (Figure 5.2b,c). The fiber's motion lagged the command in a frequency-dependent manner (Figure 5.2d). As the stimulus frequency increased from 5 to 100 Hz, the phase lag increased from near zero to more than fifteen degrees. These controls suggest that the load clamp can successfully deliver periodic stimuli independent of load stiffness. Additionally, there exists a limitation of the system at high frequencies, in which the fiber's motion begins to lag the commanded signal. This relationship is linear for the frequencies sampled and should be taken into account in the analysis of responses to high-frequency stimuli.

Figure 5.2. Verification of the two-parameter load clamp. (a) To verify that the clamp permits simultaneous control of the load stiffness and constant force, a stimulus fiber of stiffness K_{SF} = 350 μN·m^{-1} and damping coefficient ξ_{SF} = 164 nN·s·m^{-1} was used to deliver force steps to a vertically mounted glass fiber of stiffness K_{HB} = 560 μN·m^{-1} that acted as a simulacrum of a hair bundle. For a given constant force and load stiffness, the steady-state position X of the model bundle should behave as a Hookean material. The displacements of the test fiber (black circles) in response to forces delivered by a stimulus fiber are shown as a function of the added stiffness. For five levels of constant force, the application of a range of load stiffnesses yielded results demonstrating control of these parameters. Purple lines indicate fits to $X = \frac{F_{C,E}}{K_E + K_{HB}}$. (b) To test the clamp's capability to hold a hair bundle at an operating point ($F_{C,E}$ = 0 pN; K_E = 150 μN·m^{-1} and 175 μN·m^{-1}) while stimulating a hair bundle sinusoidally, time-varying stimuli were delivered to another test fiber of stiffness K_{SF} = 109 μN·m^{-1} and damping coefficient ξ_{SF} = 133 nN·s·m^{-1}. Stimulation at different frequencies yielded a response (black) that closely resembled that of a commanded signal (red). (c) The ratio of the amplitude of the fiber's motion to the amplitude of the command signal deviates from the ideal by less than 2% at all frequencies at a gain of 0.3 (cyan) and 0.46 (purple). (d) The fiber's displacement lags the stimulus force to a small degree at all frequencies, increasing to 16° at 100 Hz. This dependence of phase on frequency is the same for a gain of 0.3 (cyan) and 0.46 (purple). The time traces have been downsampled by a factor of 100 for presentation purposes.

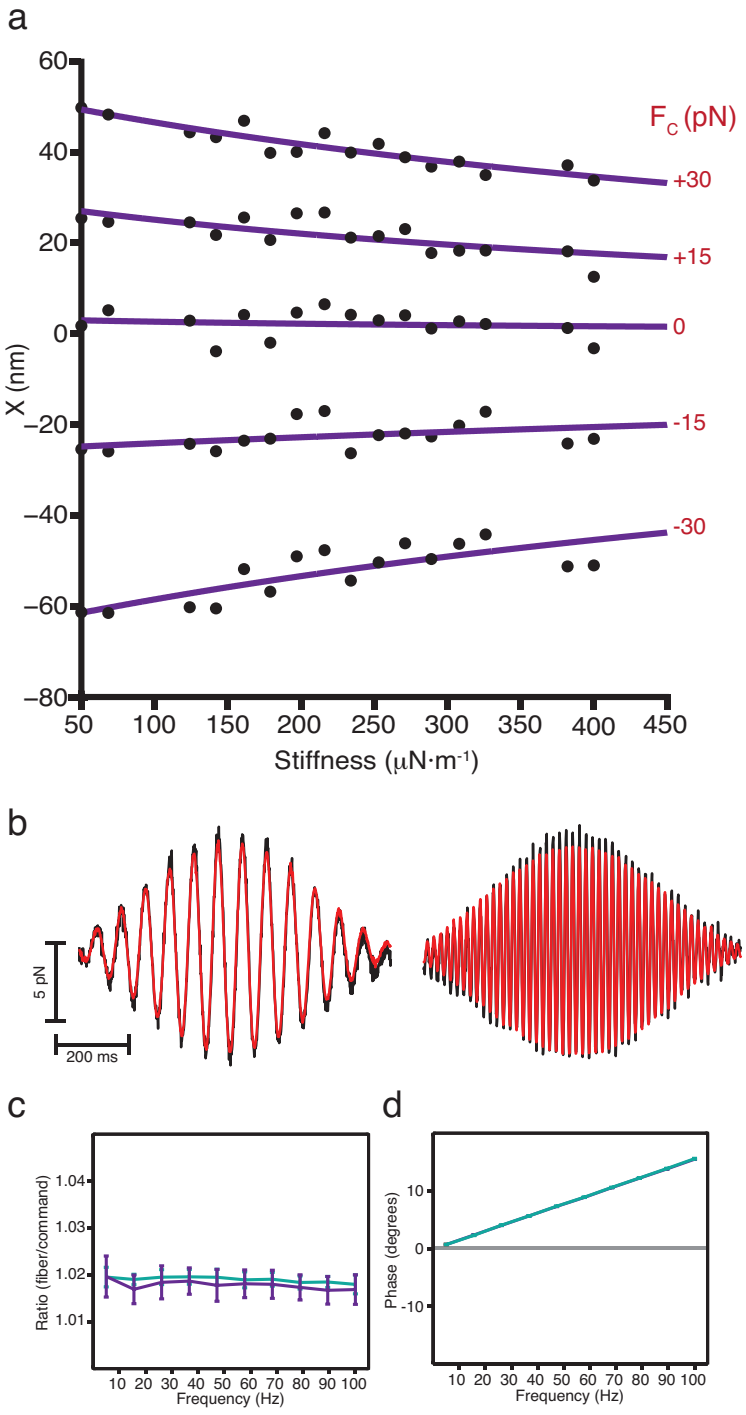
a
60
40
20
0
−20
−40
−60
−80
X (nm)
50
100
150
200
250
300
350
400
450
Stiffness (μN·m-1)
FC (pN)
+30
+15
0
-15
-30
b
5 pN
200 ms
c
Ratio (fiber/command)
1.04
1.03
1.02
1.01
10 20 30 40 50 60 70 80 90 100
Frequency (Hz)
d
Phase (degrees)
10
0
-10
10 20 30 40 50 60 70 80 90 100
Frequency (Hz)

In addition to imposing loads on a passive, linear system, the mechanical-load clamp must successfully do the same for an active, nonlinear system. Simulations of an active hair bundle coupled to a virtual load clamp assessed the clamp's abilities to adjust the constant force and load stiffness of an individual hair bundle. Before coupling a virtual stimulus fiber and a virtual load clamp to a simulated hair bundle, the bundle's dynamics in the absence of a fiber and clamp were first characterized. The theoretical state diagram of hair-bundle dynamics with known parameters depicts an oscillatory region bounded by Hopf bifurcations (Figure 5.3a). Upon adjustment of the bundle's intrinsic stiffness and offset, Itō integration of equations 4.10 and 4.11 in the absence of a stimulus fiber disclosed a state diagram with an oscillatory region that agreed with the theoretical state diagram (Figure 5.3b,c). Increasing the bundle's stiffness caused spontaneous oscillations to decrease in amplitude and increase in frequency as the hair bundle's operating point approached a supercritical Hopf bifurcation (Figure 5.3b-d). Additionally, an increase or decrease in the bundle's offset force in the absence of a stimulus fiber induced asymmetric oscillations. The pattern of this asymmetry depended on the sign and magnitude of the offset force, in which positive offsets cause the bundle to reside more often at a positive position and negative offsets cause the bundle to reside more often at a negative position (Figure 5.3d). Upon coupling a virtual stimulus fiber to the model bundle, the bundle's oscillations expectedly increased in frequency and decreased in amplitude (Figure 5.3d). When the virtual load clamp is turned on and the load stiffness set to zero, the system should mimic behavior of a hair bundle in the absence of a stimulus fiber. Indeed, activating the virtual load clamp provoked the

bundle's spontaneous oscillations to resemble those without any fiber attached (Figure 5.3d).

Further exploration of a state diagram revealed that mechanical-load clamping produced dynamics in agreement with those of the fiber-free model (Figure 5.4). Using the same set of parameters and assuming that the bundle's offset and intrinsic stiffness are zero for simplicity, a theoretical state diagram again reveals an oscillatory regime enclosed within lines of Hopf bifurcations for combinations of the constant force and load stiffness imposed on a hair bundle (Figure 5.4a). Simulations of a model hair bundle coupled to a virtual load clamp disclosed a state diagram comprising an oscillatory region in agreement with that of the theoretical state diagram (Figure 5.4b,c). As before, an increase in load stiffness caused the bundle to oscillate with lower amplitude and higher frequency as its operating point approached a supercritical Hopf bifurcation (Figure 5.4d). A small load stiffness induced high-amplitude, low-frequency relaxation oscillations, and a large load stiffness promoted low-amplitude, high-frequency sinusoidal oscillations. After the bundle's operating point crossed a supercritical Hopf bifurcation, the hair bundle's deterministic behavior was rendered quiescent (Figure 5.4d). In agreement with the fiber-free model, an increase in the constant force applied to a model hair bundle by a virtual load clamp prompted asymmetric spontaneous oscillations. Again, this asymmetry depended on the sign and magnitude of the constant force. Taken together, the mechanical-load clamp can robustly impose a constant force and load stiffness onto a hair bundle, and a bundle's

behavior under the influence of these loads accords with its behavior through changes to its intrinsic mechanical properties.

Figure 5.3. Effects of a bundle's mechanical properties on its dynamics. (a) A theoretical state diagram depicts hair-bundle behavior for combinations of the bundle's constant force and stiffness. Lines of Hopf bifurcations enclose an oscillatory region (orange). (b) Simulation of a hair bundle's motion for changes in its intrinsic constant force and stiffness yields an ovoid region of spontaneous activity. As the bundle's intrinsic stiffness increases, the amplitude of oscillations decreases (red) until the bundle is rendered quiescent (gray). (c) For the same simulation, the model bundle's frequency of oscillation increases with stiffness (blue). (d) Traces of a hair bundle's motion with and without noise (red and black, respectively) are shown for different combinations of the bundle's constant force and stiffness corresponding to the operating points shown in (a). When a stimulus fiber of stiffness 0.5 is coupled to the bundle, spontaneous oscillations decrease in amplitude and increase in frequency (red to orange). Turning on a virtual load clamp and setting the fiber's stiffness to zero causes the bundle's motion to behave as if there were no fiber attached (cyan and red). Removing the stimulus fiber and increasing the stiffness to 3.4 induces a further increase in the frequency and decrease in the amplitude of oscillation and the bundle's motion becomes sinusoidal (light blue). Changing the constant force of the bundle renders the motion asymmetric, and the shape of this asymmetry depends on the sign and magnitude of the force (dark blue and pink). Simulations were performed using the Euler-Murayama method in MATLAB across 10^4 points for 41 values each of constant force and stiffness. Stochastic simulations included a noise level of 0.2. Load-clamp simulations used $\alpha = 10$, $\beta = 0.1$, and $\xi_{XX} = \xi_{\Delta X} = 10^{-3}$, $a = 0.35$, $b = 0.5$, and $\tau_a = 10$ (equations 4.10 and 4.11). Quiescent operating points were defined as those in which the bundle's oscillatory amplitude fell below 0.01.

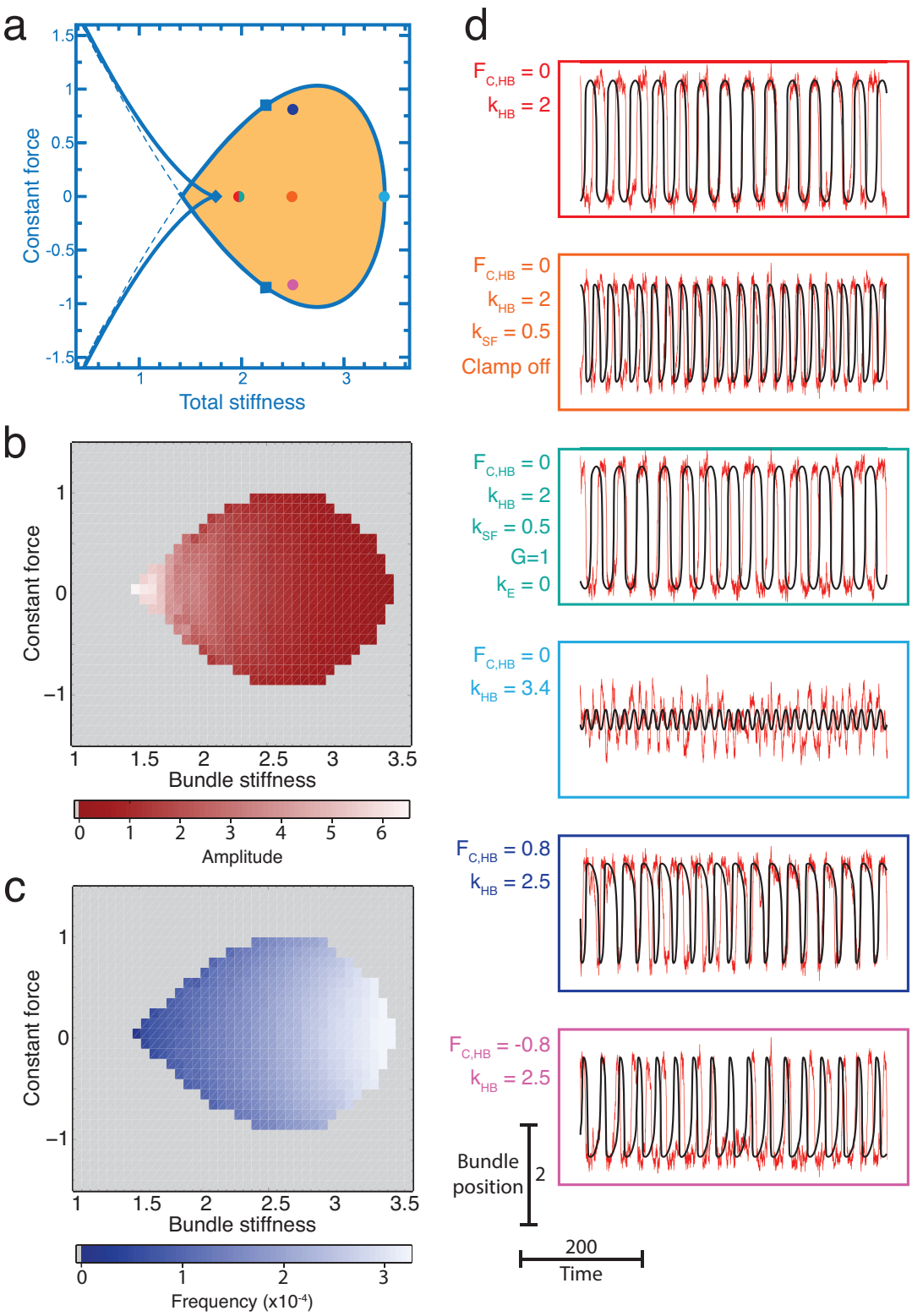
a
Constant force
Total stiffness
b
Constant force
Bundle stiffness
Amplitude
c
Constant force
Bundle stiffness
Frequency (x10-4)
d
FC,HB = 0
kHB = 2
FC,HB = 0
kHB = 2
kSF = 0.5
Clamp off
FC,HB = 0
kHB = 2
kSF = 0.5
G=1
kE = 0
FC,HB = 0
kHB = 3.4
FC,HB = 0.8
kHB = 2.5
FC,HB = -0.8
kHB = 2.5
Bundle position
2
200
Time

SECTION 5.2: *Four-Parameter Load Clamp*

Other mechanical loads are also expected to adjust the hair bundle's two-parameter state diagram. Mass loading should increase the size of the spontaneously oscillatory regime, whereas viscous damping should shrink the locus of spontaneous oscillations (Figure 4.3c). One may thus envision an experimental system that—analogously to accessory structures *in vivo*—imposes mechanical loads to adjust the behavior of an active hair bundle and allows the characterization of the bundle's mechanical behavior throughout its state diagram. Here we review a clamp system that imposes a variety of mechanical loads on a hair bundle. Like the two-parameter load clamp introduced in *Section 5.1* that employs negative feedback to impose on a hair bundle a constant force and load stiffness, the four-parameter mechanical-load clamp uses feedback to introduce to a hair bundle a virtual mass, a virtual drag coefficient, a virtual stiffness, or an external force.

The equation of motion for a hair bundle coupled to a flexible glass fiber is

$$m_{HB}\ddot{X} + \xi_{HB}\dot{X} + K_{HB}X - F_A = -\xi_{XX}\dot{X} - \xi_{\Delta X}\dot{\Delta} + K_{SF}(\Delta - X), \tag{5.9}$$

in which X is the position of the hair bundle and m_{HB}, ξ_{HB}, and K_{HB} are respectively its mass, drag coefficient, and stiffness. Δ is the position of the base of the stimulus fiber, K_{SF} is its stiffness, ξ_{XX} is the drag coefficient owing to motion at its tip, and $\xi_{\Delta X}$ is that owing to motion at its base. F_A represents any active force produced by the hair bundle. As before, the bundle's displacement is measured by a photodiode that generates the voltage $V_D = \alpha X$. The subsequent error signal owing to the difference in the bundle's position and a commanded position X_C is then $V_E = V_C - V_D = \alpha(X_C - X)$. This signal is

delivered to a differential amplifier and amplified by a proportional gain G to produce an output signal $V_O = GV_E$ that is fed to a piezoelectric actuator to yield a displacement of the stimulus fiber's base,

$$\Delta = \beta V_O = \beta G V_E = \alpha\beta G(X_C - X), \tag{5.10}$$

The dynamics of a hair bundle loaded by a virtual mass m_V, drag coefficient ξ_V, and stiffness K_V and subjected to an external force F_E is described by

$$m_{HB}\ddot{X} + \xi_{HB}\dot{X} + K_{HB}X - F_A = -m_V\ddot{X} - \xi_V\dot{X} - K_V X + F_E. \tag{5.11}$$

One can use the clamp to apply a mechanical load by combining equations 5.9 and 5.11 to yield

$$-\xi_{XX}\dot{X} - \xi_{\Delta X}\dot{\Delta} + K_{SF}(\Delta - X) = -m_V\ddot{X} - \xi_V\dot{X} - K_V X + F_E. \tag{5.12}$$

Equation 5.10 can be used to specify Δ such that the commanded position follows as

$$\xi_{\Delta X}\dot{X}_C - K_{SF}X_C = \frac{m_V\ddot{X} + (\xi_V - \xi_{XX} + \alpha\beta G\xi_{\Delta X})\dot{X} + \left[K_V - (1+\alpha\beta G)K_{SF}\right]X - F_E}{\alpha\beta G}. \tag{5.13}$$

Discretization using time intervals of length δt approximates the bundle's instantaneous velocity and acceleration,

$$\dot{X}_n = \frac{X_n - X_{n-1}}{\delta t} \text{ and } \ddot{X}_n = \frac{X_n - 2X_{n-1} + X_{n-2}}{(\delta t)^2}. \tag{5.14}$$

The appropriate command signal at the n^{th} time interval therefore becomes

$$V_{C,n} = \frac{\xi_{\Delta X}V_{C,n-1}}{\xi_{\Delta X} - K_{SF}\delta t} + \left\{\frac{m_V\ddot{X}_n + (\xi_V - \xi_{XX} + \alpha\beta G\xi_{\Delta X})\dot{X}_n + \left[K_V - (1+\alpha\beta G)K_{SF}\right]X_n - F_{E,n}}{\beta G(\xi_{\Delta X} - K_{SF}\delta t)}\right\}\delta t. \tag{5.15}$$

For specified values of m_V, ξ_V, K_V, and F_E, the mechanical-load clamp calculates a command voltage suitable for control of the virtual impedance and external force. Alternatively, independent control of two of the load parameters may be achieved if m_V, ξ_V, K_V, and F_E, are set to zero and the $\xi_{\Delta X}$ terms are small. Equation 5.13 then becomes

$$\alpha\beta G K_{SF} X_C = \xi_{xx}\dot{X} + (1 + \alpha\beta G) K_{SF} X , \tag{5.17}$$

in which the load stiffness $K_E = (1 + \alpha\beta G)K_{SF}$ is controlled by adjusting G and the constant external force $F_{C,E} = \alpha\beta G K_{SF} X_C$ is determined by adjusting both X_C and G. By providing independent control of two of the four control parameters introduced in equation 5.11, equation 5.17 offers an alternative method to equation 5.8 for exploration of the hair bundle's state diagram defined by the load stiffness and constant force. In other words, a four-parameter mechanical-load clamp reduces to a two-parameter load clamp defined by equation 5.8 when all the virtual parameters are set to zero.

To verify that the four-parameter mechanical-load clamp can impose a virtual mass, virtual drag coefficient, virtual stiffness, and external force on a bundle, a flexible glass stimulus fiber was again used to deliver stimuli to a vertically mounted glass fiber that acted as a model hair bundle. Delivery of force pulses of different magnitudes across an array of virtual stiffnesses yielded a relationship in agreement with the behavior of a Hookean material (Figure 5.5a). Additionally, an increase in virtual stiffness altered the shape of the fiber's step response (Figure 5.5b). At low stiffness, the step response rose to its steady-state position with a large time constant. As the virtual stiffness increased, the rise time accordingly decreased. For high values of virtual stiffness, the fiber began to overshoot and ring at the onset and offset of the force pulse.

Both the magnitude of this overshoot and the settling time of the ring increased with virtual stiffness. Taken together, these data indicate that the load clamp can successfully control both the virtual stiffness and external force imposed on a passive bundle.

The four-parameter load clamp controls a fiber's virtual drag coefficient. By holding the fiber's virtual stiffness constant and changing its virtual drag, force pulses disclosed behavior that accord with that expected of a change in viscous damping (Figure 5.5c). In response to a force pulse, the fiber's step response rose with a time constant that increased with the virtual drag coefficient. Exponential fits to these curves yielded a value for the fiber's total drag coefficient in agreement with its calibrated value. Thus, the system not only controls a fiber's stiffness and the constant force it applies, but the clamp can systematically adjust the fiber's drag coefficient.

To characterize a hair bundle's behavior under the influence of inertial loads, the load clamp must control a stimulus fiber's mass. To assess the clamp's capacity to robustly command virtual mass, a glass stimulus fiber was coupled to another, vertically mounted glass fiber. In this arrangement, the tip of the mounted fiber was coated with a spherical bead of silver-colloid glue in order to increase the fiber's mass in the absence of clamping. Motion of the bead coupled to a stimulus fiber was recorded over time and its power spectrum computed for three values of virtual mass (Figure 5.5d). As the virtual mass increased, the system's peak frequency decreased according to the relation $\omega \propto \sqrt{K_T / m_T}$, in which K_T and m_T are respectively the system's total stiffness and mass. As the virtual mass increased, so too did the magnitude and quality of the peak in the

power spectrum of motion. These data confirm the hypothesis that the load clamp successfully increases the fiber's virtual mass.

Simulations of a model hair bundle coupled to a virtual-load clamp revealed that a mechanical-load clamp could adjust mass and drag-coefficient parameters in a nonlinear dynamical system. Because the effects of virtual mass and virtual drag on a hair bundle's spontaneous oscillations are subtle, the model bundle was driven sinusoidally for discrete frequencies ranging from 0.01 to 1 at an amplitude of 0.01 (Figure 5.6). Calculating the Fourier amplitude of the bundle's response at the driving frequency and dividing by the stimulus amplitude revealed that the driven model bundle shared behaviors consistent with changes in its drag and mass. As expected, an increase in the virtual drag coefficient from $\xi_V = 0$ to $\xi_V = 6$ caused a more than sixfold reduction in the magnitude of gain at its resonant peak (Figure 5.6a). The bundle's resonant frequency correspondingly decreased by about threefold with an increase in the virtual drag coefficient. Increasing the model bundle's virtual mass from $m_V = 0$ to $m_V = 5$ caused the magnitude of its resonant peak to increase by more than twofold and its resonant frequency to decrease by about 20% (Figure 5.6b). Both of these results are consistent with a change in the bundle's drag coefficient and inertial load (167).

Taken together, the four-parameter mechanical-load clamp can in principle control a hair bundle's mass, drag coefficient, stiffness, and external force. The system's capacity to operate in the presence of noise, mechanical drift, and unexpected hair-bundle behavior shall be evaluated experimentally.

Figure 5.4. Effects of constant force and load stiffness by a mechanical-load clamp. (a) A hair bundle's theoretical state diagram depicts an oscillatory region bounded by lines of Hopf bifurcations as in Figure 5.3a. (b) By holding a bundle's force and stiffness at zero and adjusting the constant force and load stiffness exerted by a virtual mechanical-load clamp, an oscillatory region (red) bounded by a domain of quiescence (gray) emerges that resembles the state diagram in Figure 5.3b. As before, an increase in load stiffness causes a decrease in the amplitude of spontaneous oscillation. (c) The frequency of oscillation increases with load stiffness (blue). (d) Traces of a model bundle's motion with and without noise (red and black, respectively) under the influence of a virtual-load clamp disclose changes in its behavior with adjustments to each of two mechanical loads corresponding to operating points highlighted in (a). Increasing the load stiffness imposed on a bundle decreases the amplitude and increases the frequency of oscillation until the bundle crosses a Hopf bifurcation and is rendered quiescent (red to light blue). Holding the load stiffness constant and changing the offset force induces an asymmetry in the bundle's motion that depends on the magnitude and sign of the constant force (dark blue and pink). These results accord with those in Figure 5.3. Simulations were performed using the Euler-Murayama method of Itō integration in MATLAB across 10,000 points for 41 values each of constant external force and load stiffness. Stochastic simulations included a noise level of 0.2. Load-clamp simulations used $\alpha = 10$, $\beta = 0.1$, $G = 1$, and $\xi_{XX} = \xi_{\Delta X} = 10^{-3}$ and 10^{4} time points. Quiescent operating points were defined as those in which the bundle's oscillatory amplitude fell below 0.01. For all panels, $F_{C,HB} = 0$, $K_{HB} = 0$, $a = 0.35$, $b = 0.5$, and $\tau_a = 10$ (equations 4.10 and 4.11).

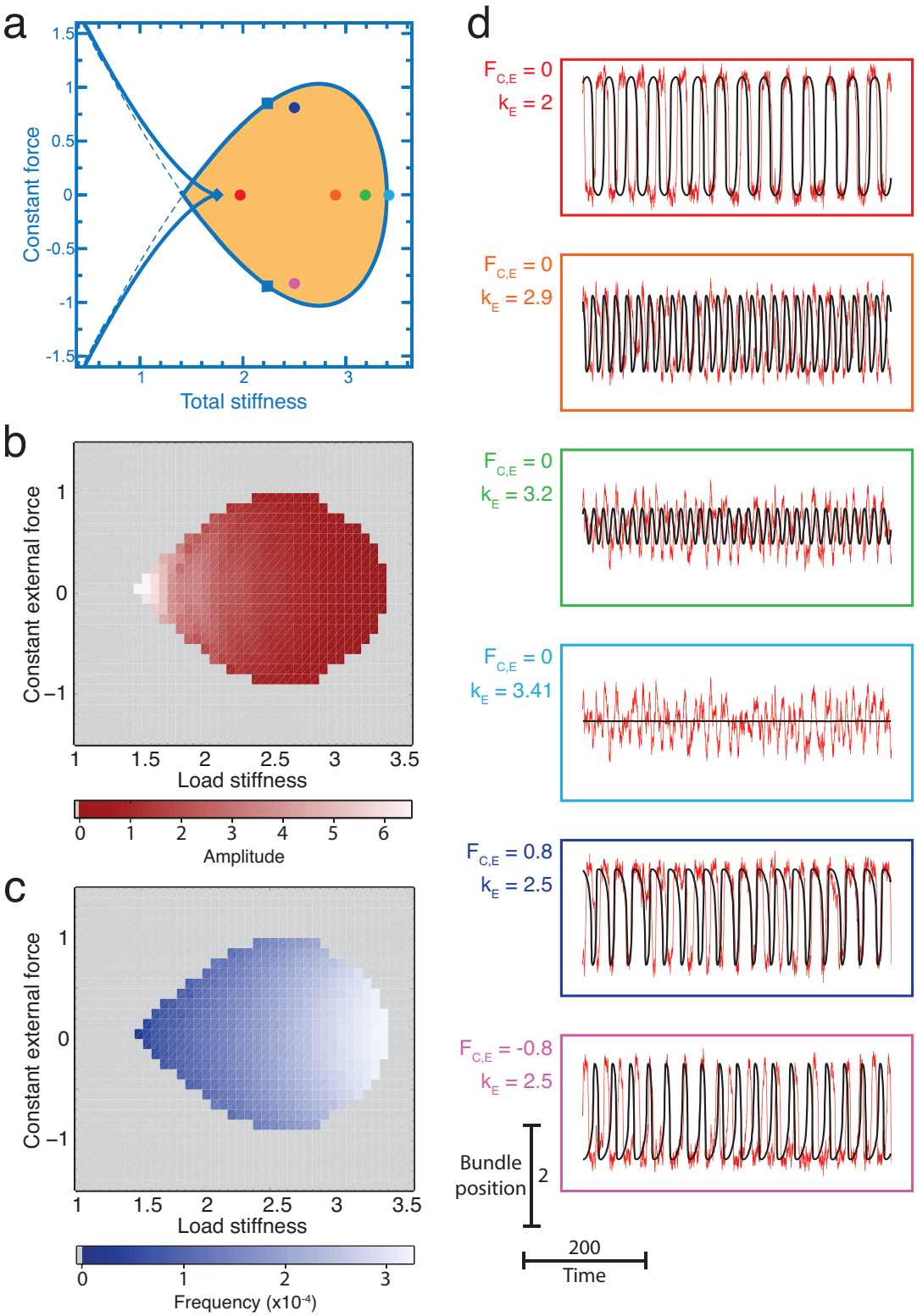
a
Constant force
Total stiffness
b
Constant external force
Load stiffness
Amplitude
c
Constant external force
Load stiffness
Frequency (x10-4)
d
FC,E = 0
kE = 2
FC,E = 0
kE = 2.9
FC,E = 0
kE = 3.2
FC,E = 0
kE = 3.41
FC,E = 0.8
kE = 2.5
FC,E = -0.8
kE = 2.5
Bundle position
2
200
Time

Figure 5.5. Verification of the four-parameter load clamp. (a) To verify that a load clamp can adjust a bundle's virtual stiffness and constant force, the tip of a glass stimulus fiber was coupled to a vertically-mounted fiber in order to deliver a series of constant forces ($F_{C,E}$ = 0, ±10, ±30, ±50 pN) at different values of virtual stiffness (-100 ≤ K_V ≤ 500 μN·m^{-1}). Fits to the same expression in Figure 5.2 yielded $R^2 > 0.99$ in all cases. (b) Example traces for the experiment in (a) at $F_{C,E}$ = 30 pN revealed a change in the rise time of the fiber's step response. As the load stiffness increased, the rise time decreased. For load stiffnesses exceeding 250 μN·m^{-1}, the response began to ring with a decay time that grew with stiffness. This accords with the prediction that the fiber's stiffness increases. (c) For a stimulus fiber with an actual drag coefficient of ξ_{SF} = 600 nN·s·m^{-1}, the fiber's virtual drag coefficient was adjusted and force pulses were delivered to a vertically mounted glass fiber. Changing the virtual drag coefficient from -100 to +100 nN·s·m^{-1} increased the time constant at the onset of the fiber's step response, in agreement with the prediction that the fiber's drag increases. All responses were fit to an exponential of the form $y = C*exp(K*t/\xi)+F/K$, in which C is a fitting parameter, F is the magnitude of the stimulus force, K is the fiber's stiffness, t is time, and ξ is the fiber's total drag coefficient. (d) A stimulus fiber of stiffness K_{SF} = 2 mN·m^{-1} was coupled to a vertically mounted glass fiber with a bead of silver-colloid glue at its tip with a radius of 11 μm and a mass of 36 ng. The motion of the coupled system was recorded over time and its power-spectral density computed for three values of virtual mass. As the virtual mass increased from -2 to +2 ng, the peak in its power spectrum of motion decreased in frequency from 1,231 Hz to 1,162 Hz (with f = 1,191 Hz for m_v = 0 ng). This accords with the expectation that the fiber's mass increases.

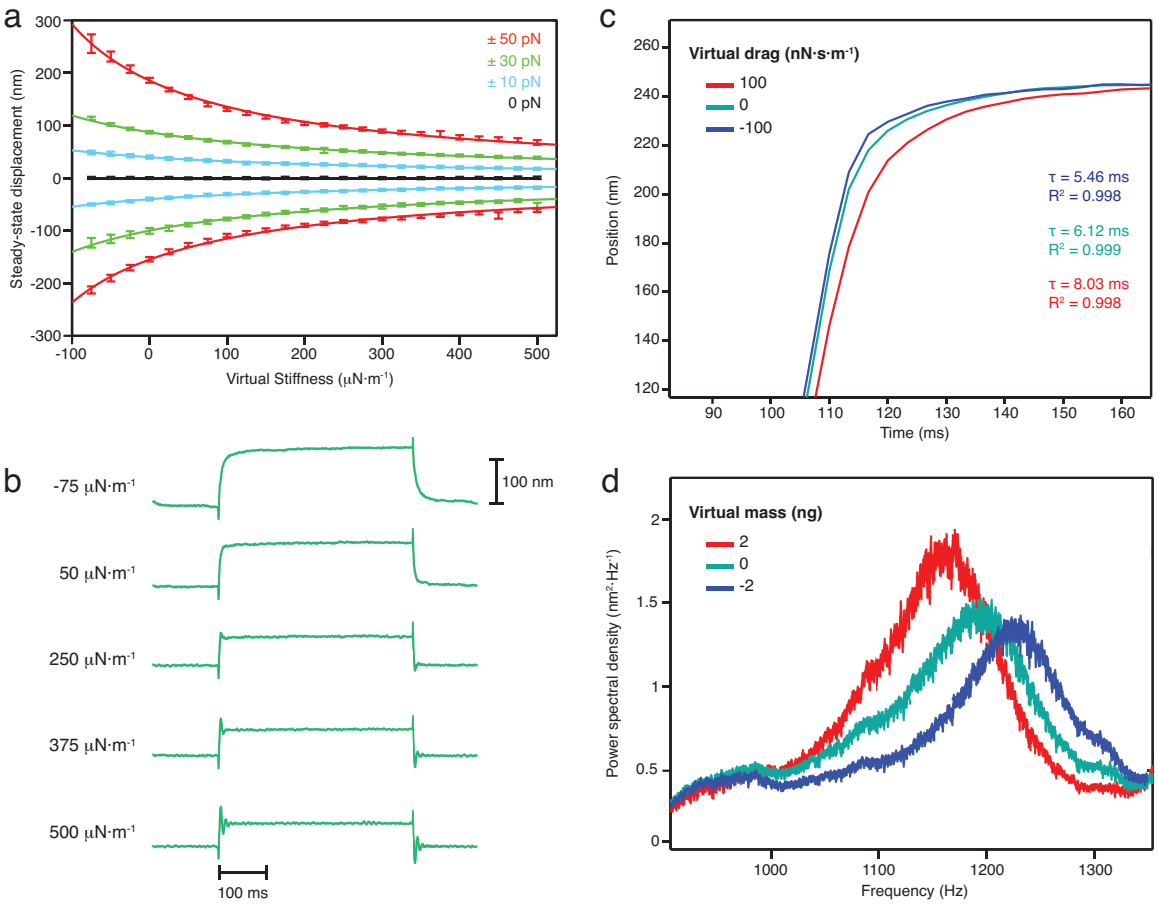
a
Steady-state displacement (nm)
Virtual Stiffness (μN·m⁻¹)
± 50 pN
± 30 pN
± 10 pN
0 pN
b
-75 μN·m⁻¹
50 μN·m⁻¹
250 μN·m⁻¹
375 μN·m⁻¹
500 μN·m⁻¹
100 nm
100 ms
c
Virtual drag (nN·s·m⁻¹)
100
0
-100
τ = 5.46 ms
R² = 0.998
τ = 6.12 ms
R² = 0.999
τ = 8.03 ms
R² = 0.998
Position (nm)
Time (ms)
d
Virtual mass (ng)
2
0
-2
Power spectral density (nm²·Hz⁻¹)
Frequency (Hz)

Figure 5.6. Effects of virtual drag and virtual mass on hair-bundle sensitivity. (a) A model hair bundle was subjected to an increasing virtual drag coefficient (ξ_V = 0, 1.5, 3, 4.5, 6 (*blue to orange*)) and a virtual mass of zero by a simulated mechanical-load clamp. As the virtual drag coefficient increased, the bundle's gain and resonant frequency in response to periodic stimuli decreased. (b) An artificial load clamp subjected a model bundle to an increasing virtual mass (m_V = 0, 1, 3, 5 (*blue to orange*)) and a virtual drag coefficient of zero. As the virtual mass increased, the bundle's gain increased and resonant frequency decreased in response to periodic stimuli. Gain was defined as the Fourier amplitude of the model bundle's response at the frequency of driving divided by the stimulus amplitude. Simulations were performed using the Euler-Murayama method of Itō integration in MATLAB across 10^5 points with sinusoidal stimuli wielding frequencies ranging from 0.01 to 1 (N = 500) and amplitude equal to 0.01. Model parameters included α = 10, β = 0.1, G = 1, and $\xi_{XX} = \xi_{\Delta X}$ = 0.001. For all panels, $F_{C,HB}$ = 0, K_{HB} = 0, m_{HB} = 0.1, ξ_{HB} = 0.2, K_V = 3.6, a = 0.35, b = 0.5, and τ_a = 10 (equations 4.10 and 4.11).

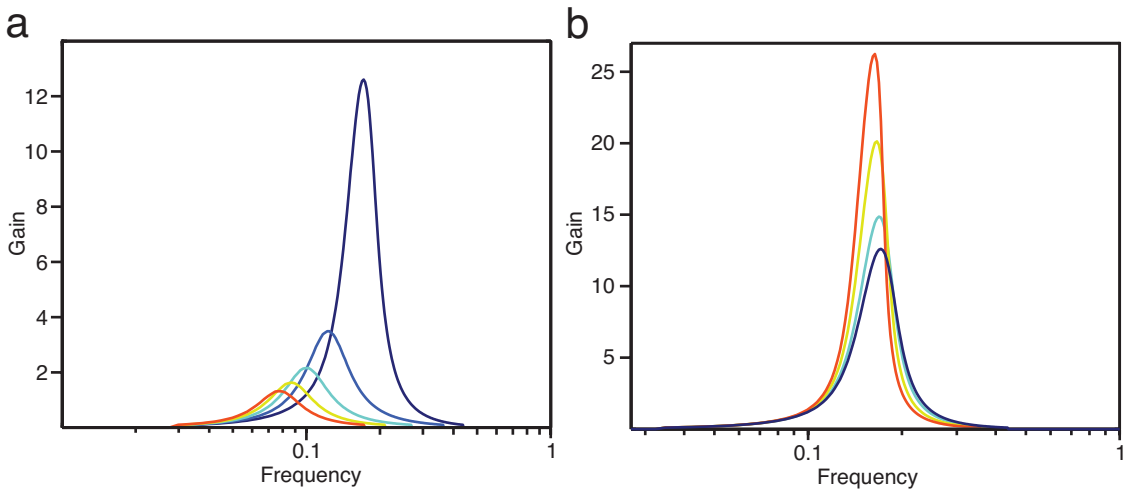
a
12
10
8
6
4
2
Gain
0.1
1
Frequency
b
25
20
15
10
5
Gain
0.1
1
Frequency

CHAPTER 6

Mapping the Hair Bundle's State Diagram

The mechanical load imposed on a sensory hair bundle might dictate the bundle's behavior. Motivated by a dynamical model of hair-bundle motility, we employed a two-parameter load clamp to systematically subject individual hair bundles to two mechanical loads: constant force and load stiffness. The system revealed an experimental state diagram for each hair bundle in agreement with theory. Furthermore, a striking phenomenon not explicitly predicted in the model emerged: a hair bundle's state diagram depends on the bundle's diameter. Taken together, the study systematically explores the state spaces of numerous hair bundles, a rare feat in biology and dynamical systems.

SECTION 6.1: *Materials and Methods*

Experimental preparation. All procedures were approved by the Institutional Animal Care and Use Committee of The Rockefeller University. Experiments were performed at 21 °C on hair cells from the saccular maculae of adult bullfrogs, *Rana catesbeiana*. Each dissected sacculus was placed in oxygenated artificial perilymph containing 114 mM Na^+, 2 mM K^+, 2 mM Ca^{2+}, 118 mM Cl^-, 5 mM HEPES, and 3 mM **D**-glucose. After isolation from the labyrinth and removal of otoconia, the saccular macula was sealed over a 1 mm hole in a 12 mm disk of aluminum foil with *n*-butyl cyanoacrylate

(Vetbond, 3M, St. Paul, MN) to form a partition in a two-compartment chamber. The apical surface was exposed to 67 $mg \cdot l^{-1}$ of protease (type XXIV, Sigma, St. Louis, MO) for 35 min at 21 °C to loosen the otolithic membrane, which was then removed with an eyelash. During recordings the lower chamber contained oxygenated artificial perilymph and the upper chamber held oxygenated artificial endolymph containing 2 mM Na^+, 118 mM K^+, 250 μM Ca^{2+}, 118 mM Cl^-, 5 mM HEPES, and 3 mM **D**-glucose. Both solutions had a pH of 7.3 and an osmotic strength of 230 $mOsmol \cdot kg^{-1}$.

Microscopic apparatus. Hair bundles were visualized by differential-interference-contrast optics through a 60X water-immersion objective lens of numerical aperture 0.9 on an upright microscope (BX51WI, Olympus, Tokyo, Japan). To detect spontaneously active hair bundles, the image was directed through a 0.35X or 4.0X telescope to a charge-coupled-device camera and a video processor (Argus-20, Hamamatsu Photonics K. K., Hamamatsu City, Japan). Digital subtraction of each frame from the average of the previous one to five frames eased the detection of hair-bundle oscillations. An infrared-reflecting mirror (21002b, Chroma Technology, Bellows Falls, VT) and a broadband interference filter (585 ± 30 nm; #220494, Chroma Technology) protected the tissue from photodamage. For experimental measurements, the polarizer and filter were removed from the light path and the sample was illuminated at 630 nm with a 900 mW light-emitting diode (UHP-Mic-LED-630, Prizmatix, Givat-Shmuel, Israel).

Mechanical stimulation. Mechanical stimuli were delivered by flexible glass fibers fabricated from borosilicate capillaries 1.2 mm in external diameter (TW120-3, World Precision Instruments, Sarasota, FL). After a capillary had been narrowed by an electrode puller (P-2000, Sutter Instruments, Novato, CA), a 120 V solenoid pulling at a right angle created a solid fiber no more than 100 μm in length and 0.5-0.8 μm in diameter. To enhance its optical contrast, each fiber was sputter-coated with gold-palladium (Hummer 6.2, Anatech, Hayward, CA). To improve its attachment to the kinociliary bulb, each fiber was treated for 15 min with 200 $\mu g \cdot l^{-1}$ concanavalin A (type IV, Sigma, St. Louis, MO).

To determine a fiber's stiffness and drag coefficient, its thermal fluctuations were analyzed while submerged in water. The power spectrum S_X as a function of frequency f from a 30 s record was fit to the Lorentzian relation (57)

$$S_X(f) = \frac{a}{f_0^2 + f^2}; \tag{6.1}$$

$$\xi_{SF} = \frac{k_B T}{\pi^2 a}; \tag{6.2}$$

$$K_{SF} = 2\pi \xi_{SF} f_0. \tag{6.3}$$

Here a is a fitting parameter, f_0 is the half-power frequency, k_B is Boltzmann's constant, T is the temperature, ξ_{SF} is the fiber's drag coefficient, and K_{SF} is the fiber's stiffness. Fibers had stiffnesses of 50-600 $\mu N \cdot m^{-1}$ and drag coefficients of 25-80 $nN \cdot s \cdot m^{-1}$.

The base of each stimulus fiber was secured to a high-frequency piezoelectric actuator (PA 4/12, Piezosystem Jena GmbH, Jena, Germany) driven by an 800 mA

amplifier (ENV 800, Piezosystem Jena). The actuator was mounted on a micromanipulator (ROE-200, Sutter Instruments) for positioning of the fiber's tip.

The tip of a horizontally mounted stimulus fiber was tightly coupled to the kinociliary bulb of an individual hair bundle. Each hair bundle was classified by its diameter at the insertion into the cuticular plate. A small bundle was estimated to have a diameter of less than 2 μm and about 20 stereocilia; a medium bundle was 2-4 μm in diameter and encompassed approximately 40 stereocilia, whereas a large bundle of more than 4 μm contained around 60 stereocilia.

Photometric recording. The motion of a hair bundle was tracked by imaging the stimulus fiber's tip on a dual photodiode at a magnification of 1,350X. The output of the photodiode was then relayed through a low-pass filter with a cutoff frequency of 2 kHz (BM8, Kemo Limited, Dartford, United Kingdom). The sensitivity of the photodiode system was calibrated by independently translating the fiber's image in 20 μm steps with a mirror coupled to a second piezoelectric actuator driven by a 300 mA amplifier (PA 120/14 SG and ENV 300 SG, Piezosystem Jena). This actuator was calibrated by a heterodyne interferometer (OFV 501, Polytec GmbH, Waldbronn, Germany).

Signal production and acquisition. Stimuli were generated and data recorded by a host computer running programs written in LabVIEW (version 10.0, National Instruments, Austin, TX) with a sampling interval of 100 μs. For mechanical load-clamp experiments, signals were relayed to a target computer running the LabVIEW Real-Time operating

system (version 10.0, National Instruments). To set a defined stiffness and constant force, the host computer adjusted the proportional gain and command displacement according to equation 5.8 and transmitted those values to the target computer. The target computer then rapidly executed a short program that implemented equation 5.3 and provided an appropriate signal to the piezoelectric stimulator.

State-diagram mapping and analysis. To construct an experimental state diagram, a hair bundle was subjected to a set of load stiffnesses and constant forces and its motion recorded at each operating point for 2-8 s. The control parameters were specified for each operating point by a constant command displacement X_C and proportional gain G. The duration was limited by the stability of the load clamp, which took about 3 min to recalibrate after each 1 min of recording, and by the time of 30 min during which the bundle's dynamics was unchanged by cellular deterioration. The procedure for classifying and analyzing the operating points that constituted the bundle's experimental state diagram is described below. The parameter values used for each diagram are listed in Table 6.1; the analysis was performed using MATLAB (R2014a, 8.3.0.532).

If a hair bundle was oscillating at a particular operating point, then the distribution of its displacements displayed more than one peak. To analyze this distribution, slow drift was first removed from the time trace of bundle displacement by subtracting the time trace smoothed by moving averages over a time window of a fixed length. Up to three statistical tests were then implemented determine whether the

displacement distribution was multimodal. Hartigans' dip statistic is larger for multimodal distributions than for unimodal ones (200). Using as the null distribution a normal distribution with the same mean and variance as the displacement distribution to make the test more sensitive, a *multimodality score* was defined to be equal to the dip statistic. Displacement distributions that differed statistically from normal, possessing a multimodality score exceeding a threshold, corresponded to oscillatory operating points. This procedure did not identify all the operating points at which a bundle oscillated, however, for noise could obscure the dips between peaks in a distribution, resulting in a distribution that was asymmetric or broad.

To determine if a distribution is excessively asymmetric two additional distributions were created. The right distribution was constructed by reflecting about the mean each displacement greater than the mean displacement; the left distribution was found in an analogous manner. This process yielded two symmetric distributions that corresponded to the mirroring of the left and right halves of the original distribution. The original distribution was considered asymmetric if the left distribution and right distribution were statistically distinct. An *asymmetry score* was defined as the Kolmogorov-Smirnov test statistic resulting from a comparison of the left and right distributions. A distribution was judged to be asymmetric if the score exceeded a threshold and was statistically significant.

Broad distributions were identified as those with negative excess kurtosis. A *thinness score* was defined as the excess kurtosis divided by its standard error. This score has a normal distribution for large samples (201). A distribution was considered broad if

the thinness score lay below a threshold and was statistically smaller than that of a normal distribution.

By searching iteratively for a set of thresholds corresponding to the three scores described above, a set of operating points was found that was continuous and devoid of holes: a simply connected region for which a hair bundle oscillated. Outside this region, the bundle was classified as quiescent. This classification scheme has the advantage that it is not based on the amplitude of a bundle's noisy displacement, which is difficult to determine for many operating points. To emphasize the fact that the amplitude of a bundle's noisy displacements was not used to classify operating points, quiescent operating points are illustrated with a color not found in the spectrum used to illustrate the amplitude of spontaneous oscillations.

The amplitude and frequency of spontaneous oscillations at each operating point corresponded to the main peak of the time trace's Fourier transform. To reduce spectral leakage owing to the short duration of each time trace, the trace was multiplied by a Hamming window after subtracting the mean displacement. The trace was then zero padded to improve the accuracy of determining the peak. Because the resulting Fourier transform contained spurious low-frequency and high-frequency peaks owing to the measurement system, the search algorithm found peaks between a minimum of 0-2 Hz and a maximum of 100 Hz, well within the range of best frequencies expected for the bullfrog's sacculus (202, 203). The algorithm excluded the power-supply frequency of 60 Hz. To account for the change in the height of this peak owing to windowing, the

value was rescaled by a factor determined by applying the procedure described above to a sinusoidal time trace with duration equal to that of the original trace.

To avoid including drift in the estimation of the root-mean-square (RMS) amplitude, the mean was subtracted from each time trace to find the local RMS magnitude for a moving window 1.5 times as large as the window used to remove the drift in the analysis of the displacement distribution. The drift was then removed from each of these time windows by subtracting a linear fit. The RMS magnitude of the entire time trace was defined to be the mean of the local RMS magnitudes.

Gentamicin controls. Activity of hair bundles was sometimes analyzed when oscillations were arrested. Transduction channels were blocked with 500 μM gentamicin sulfate applied in the upper chamber, a treatment whose reversibility allowed bundles to be reassessed after washout.

Hair-bundle modeling. Simulations of a model of hair-bundle dynamics were performed with Mathematica 9.0.0.0 and C. To mimic the stochastic effects observed experimentally, noise terms were added to equations 4.10 and 4.11 in the absence of mass and drag to yield the equations

$$\dot{X} = a(X - f_a) - (X - f_a)^3 - K_T X + F_{C,T} + F + \eta_x, \tag{6.4}$$

$$\tau_a \dot{f}_a = bX - f_a + \eta_f,, \tag{6.5}$$

in which X is the bundle's displacement, f_a is the force owing to adaptation, a is a negative stiffness owing to gating of the transduction channel, τ_a is the timescale of

adaptation, b is a compliance coupling bundle displacement to adaptation, K_T is the sum of the bundle's load stiffness and pivot-spring stiffness, $F_{C,T}$ is the sum of the constant force intrinsic to the hair bundle and that owing to the load, and F is any time-dependent force applied to the bundle. All simulation results used $a = 3.5$, $b = 0.5$, and $\tau = 10$ (167). The additional white noise terms η_x and η_f were δ-correlated random variables drawn from Gaussian distributions; the standard deviations of these distributions are denoted σ_x and σ_f. Equations 6.4 and 6.5 were integrated numerically by the Euler-Maruyama method. Because the model was designed to capture qualitative effects associated with active hair-bundle motility, the values of the variables and parameters have no quantitative meaning. To facilitate comparisons with the experimental results, however, all displacements, frequencies, sensitivities, stiffnesses, and forces were rescaled in figures.

The model qualitatively predicts the shape of the state diagram and the variation in oscillation amplitude and frequency within the region of spontaneous activity (167). As was done in Chapter 5, artificial state diagrams were created by simulating a stochastic version of the model for a set of load stiffnesses and constant forces to produce time traces similar to those recorded experimentally. To determine the parameter values for which the virtual bundles oscillated, the same procedures used to analyze the experimental results were applied.

Statistics. A single number was used to describe the correlation between any two quantities for a given state diagram by finding Spearman's rank-correlation coefficient

for all of the values of the two quantities in the oscillatory region of the diagram. Owing to the grid structure of the sampled state diagram, there were many duplicate values for the stiffness and constant force that in conjunction with correlations between multiple quantities in a state diagram limited the magnitude of any particular correlation coefficient. These ties were taken into account by a permutation test to determine the statistical significance of the correlation given the sampling structure and the data. The *p*-value for each coefficient was thus a better indication of the true significance of the correlation than the value of the coefficient itself.

SECTION 6.2: *Experimental and Artificial State Diagrams*

The hair bundle's state diagram characterizes its behavior for different combinations of two control parameters: load stiffness and constant force. These control parameters describe the mechanical load imposed on a hair bundle within a sensory organ. A theoretical model of hair bundle dynamics predicts the qualitative structure of the state diagram (Figure 4.3). To test this prediction experimentally, a mechanical-load clamp varied the load imposed on an individual hair bundle and monitored its displacement. The load was delivered to an individual hair bundle by attaching the tip of a flexible glass fiber to the bundle's top and by employing a piezoelectric actuator to displace the fiber's base. To control the load, a real-time processor compared the bundle's actual position, measured by a photomicrometer system, with that specified by a command signal, and then provided feedback to the actuator to minimize the difference between the two (Figure 5.1). By adjusting the strength of the system's feedback and the commanded position, one can independently manipulate both the load stiffness and the constant force, permitting systematic regulation of the bundle's operating point to reveal its experimental state diagram (*see* Chapter 5).

Before a complete map of the bundle's state diagram can be computed, the independent effects of load stiffness and constant force must be measured (Figure 6.1). Increasing the load stiffness from 133 $\mu N \cdot m^{-1}$ to 800 $\mu N \cdot m^{-1}$ decreased the amplitude of a bundle's oscillations from 20 nm to less than 10 nm and raised the frequency of oscillation from 5 Hz to more than 15 Hz (Figure 6.1a). Upon increase of the load stiffness to 933 $\mu N \cdot m^{-1}$ the amplitude declined further and the frequency grew until

oscillations were nearly suppressed. This behavior is consistent with the bundle's nearing a supercritical Hopf bifurcation from within the spontaneously oscillatory regime (146, 159).

Increasing the constant force imposed upon a second bundle initially changed the shape of spontaneous oscillations but had little effect on their amplitude (Figure 6.1b). At 0 pN the hair bundle exhibited relaxation oscillations at 6-7 Hz. As the constant force increased, the bundle's position became biased in the positive direction with rapid negative excursions. Further increases in the constant force extended the intervals between these excursions until the bundle's motion was nearly suppressed at 40 pN. This behavior accords with that expected for a system approaching a fold of limit cycles or an infinite-period bifurcation (159, 204).

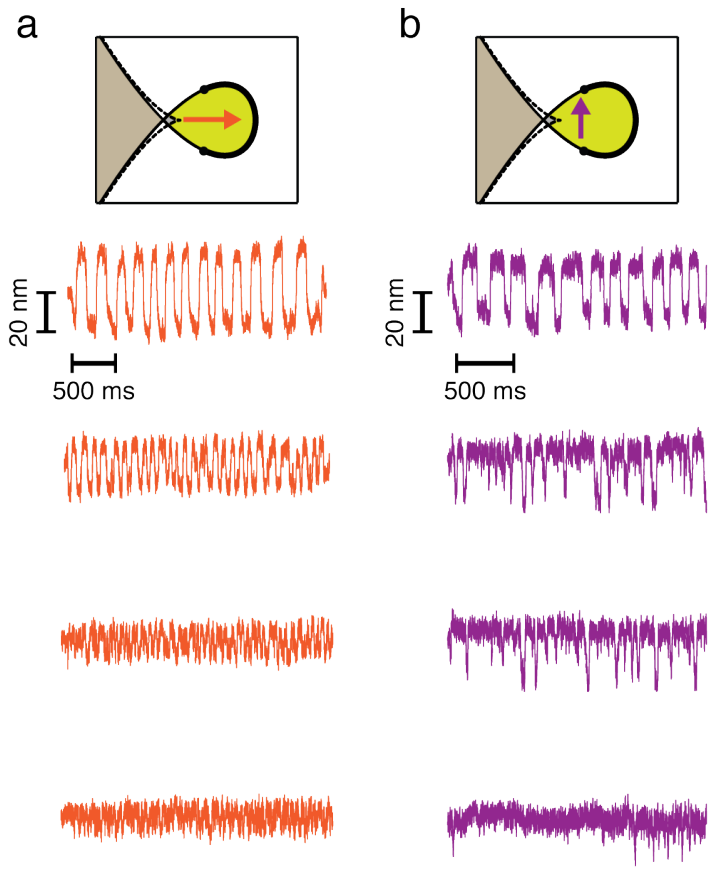

Figure 6.1. Effects of load stiffness and constant force on bundle behavior. (a) The schematic diagram at the top depicts an idealized state diagram with an arrow corresponding to the range of load stiffnesses imposed upon a hair bundle. Subjecting a spontaneously oscillating hair bundle to load stiffnesses of 133, 467, 800, and 933 $\mu N \cdot m^{-1}$ (top to bottom) caused systematic changes in the bundle's motion. (b) A second idealized state diagram shows an arrow corresponding to the range of constant forces exerted on another bundle. The bundle's motion is displayed for constant forces of 0, 13, 27, and 40 pN (top to bottom). In both cases, K_{SF} = 425 $\mu N \cdot m^{-1}$.

Following individual manipulations of mechanical loads, we computed two-dimensional state diagrams for operating points defined by both the constant force and the load stiffness imposed on individual hair bundles. In accord with previous manipulations of applied force (135), hair bundles oscillated spontaneously for operating points in certain regions of the experimental state diagram but were quiescent for others.

The activity and mechanical properties of hair bundles depended on their diameter, which resulted in oscillatory regions of varying extent. For the lowest values of load stiffness, small bundles exhibited multimodal oscillations (Figure 6.2) (205). The state diagram of a small bundle revealed an oscillatory regime almost completely bounded by a domain of quiescence. In addition, the qualitative appearance of the small bundle's diagram closely resembled the shape of a theoretical state diagram (167). State diagrams of medium-diameter hair bundles disclosed an oscillatory region larger in size than those of small bundles (Figure 6.3). The limited range of operating points for which the clamp was stable permitted exploration of only the region of spontaneous oscillation for the largest hair bundles (Figure 6.4). Though not predicted explicitly by the dynamical model (167), this size dependence remained consistent across all hair-bundle state diagrams and revealed an unexpected pattern in bundle dynamics.

In agreement with theory (167), an increase in the stiffness was correlated with a rise in the frequency of oscillation for many bundles and with a decrease in the amplitude of oscillation in all cases (Figures 6.2-6.4 and Table 6.1). These data imply that the state diagram for most bundles comprises a fish-shaped region oriented along an

axis of load stiffness. Some bundles, however, exhibited frequency and amplitude dependence along the axis of constant force (Table 6.1). In this scenario, the fish is rotated in the clockwise direction. This indicates the presence of an unknown parameter that may control the relative dependence of a hair bundle's dynamics on load stiffness and constant force.

As expected for an *in vitro* preparation, the activity of a hair bundle deteriorates gradually during protracted recording. If a hair cell were to exhibit significant changes in its state diagram over the course of an experiment, the conclusions would be compromised. To determine whether the results remained consistent over time, a bundle's experimental state diagram was computed twice over a period of ten minutes (Figure 6.5). Contrary to the general practice, artificial endolymph was not exchanged every 4-6 min. The data revealed little change in the bundle's state space over the course of the experiment, with correlation coefficients between the two diagrams of 0.92 ($p < 10^{-15}$) in amplitude and 0.86 ($p < 10^{-10}$) in frequency. The amplitude and frequency of the bundle's oscillation remained stable and the time traces did not yield obvious changes over the course of 10 min even without the regular change of artificial endolymph, verifying that the bundle's state diagram remains stable over the course of an experiment. The region of spontaneous oscillation was abolished upon addition of gentamicin, a drug that blocks mechanoelectrical-transduction channels (Figure 6.6). This result implies that the architecture of the experimental state diagram reflects active hair-bundle motility, which depends upon functional channels.

Figure 6.2. State diagram of a small-diameter hair bundle. (a) The oscillations of a small hair bundle changed in character as the effective stiffness of the stimulus fiber increased; a few operating points elicited complex oscillations whose multimodal nature is captured by the experimental records. (b) An experimental state diagram shows the behavior of the same hair bundle for various combinations of load stiffness and constant force, encompassing most of the oval locus of spontaneous oscillation. The gray region corresponds to quiescent operating points. Within the ruddy locus of spontaneous oscillation, color intensity represents the root-mean-square (RMS) magnitude of oscillation. The colored circles in the associated panels mark the operating points in (a). (c) In another representation of the experimental state diagram the color intensity encodes the amplitude of oscillation. (d) A third depiction of the experimental state diagram for the same bundle portrays the frequency of oscillation for various combinations of load stiffness and constant force. The actual stiffness and drag coefficient of the stimulus fiber were respectively $K_{SF} = 425\ \mu N \cdot m^{-1}$ and $\xi_{SF} = 53\ nN \cdot s \cdot m^{-1}$. Analysis parameters and statistics for each experimental state diagram can be found in Table 6.1.

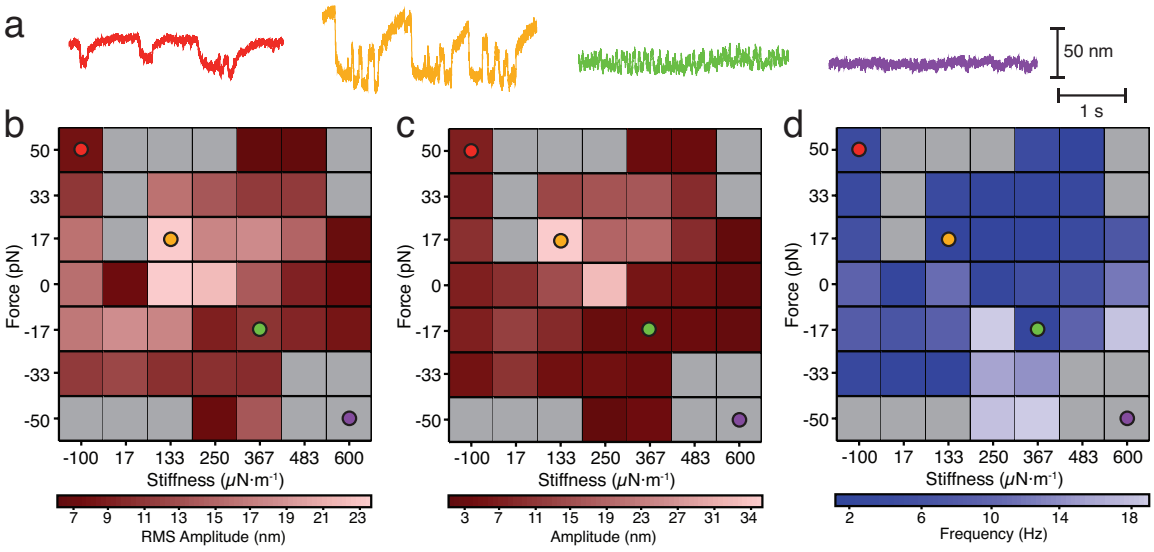
a
50 nm
1 s
b
c
d
Force (pN)
50
33
17
0
-17
-33
-50
-100 17 133 250 367 483 600
Stiffness (μN·m⁻¹)
7 9 11 13 15 17 19 21 23
RMS Amplitude (nm)
3 7 11 15 19 23 27 31 34
Amplitude (nm)
2 6 10 14 18
Frequency (Hz)

Figure 6.3. State diagrams of medium-diameter hair bundles. (a) Experimental records show the motions of a medium-sized hair bundle. Both the RMS magnitude (b) and the amplitude (c) of oscillation were smallest along the high-stiffness border of the oscillatory region. The colored circles in these panels represent the transect along which the records in (a) were obtained. (d) The oscillation frequency for the same hair bundle was greatest along the high-stiffness boundary of the oscillatory region. (e-i) Two additional state diagrams from medium-diameter hair bundles portray a domain of quiescence (gray) at high values of load stiffness. Near the border of spontaneous oscillation, the bundle's frequency achieved a peak of (d) 68 Hz, (g) 20 Hz, and (i) 10 Hz. The stimulus fiber's stiffness and drag coefficient were respectively K_{SF} = 425 μN·m^{-1} and ξ_{SF} = 53 nN·s·m^{-1}. Analysis parameters and statistics for each experimental state diagram can be found in Table 6.1.

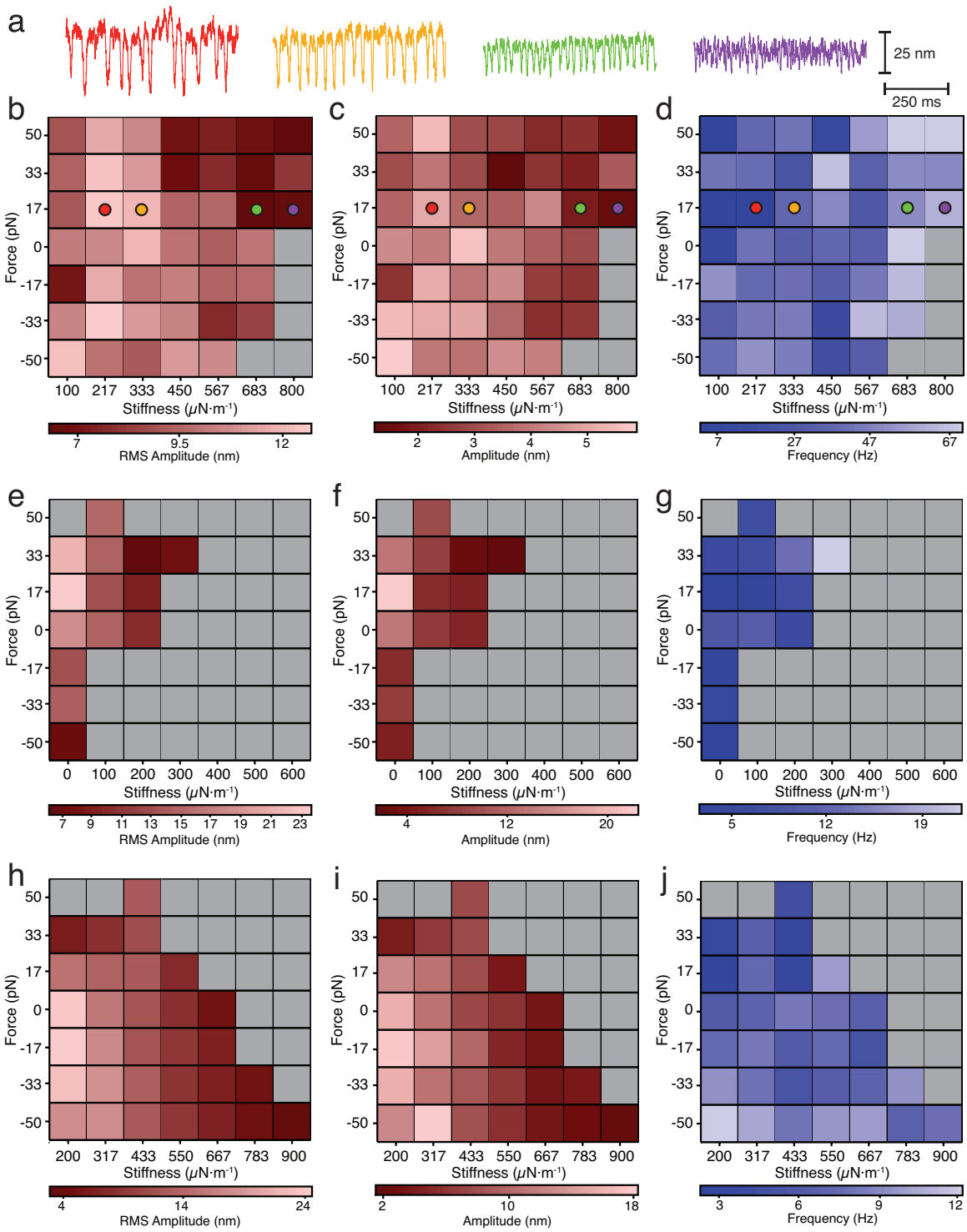
a
25 nm
250 ms
b
c
d
e
f
g
h
i
j
Force (pN)
50
33
17
0
-17
-33
-50
Stiffness (μN·m⁻¹)
100 217 333 450 567 683 800
200 317 433 550 667 783 900
0 100 200 300 400 500 600
RMS Amplitude (nm)
Amplitude (nm)
Frequency (Hz)
7 9.5 12
2 3 4 5
7 27 47 67
7 9 11 13 15 17 19 21 23
4 12 20
5 12 19
4 14 24
2 10 18
3 6 9 12

Figure 6.4. State diagrams of large-diameter hair bundles. (a) A large hair bundle oscillated spontaneously for all combinations of constant force and load stiffness. As the load stiffness increased, both the RMS magnitude (b) and amplitude (c) of spontaneous oscillation decreased. Colored circles correspond to the operating points whose experimental records are shown in (a). (d) Increasing the load stiffness evoked a corresponding increase in the frequency of oscillation. (e-g) The state diagram of a second large-diameter bundle revealed a similar pattern in amplitude and frequency. In all large bundles, an increase in the load stiffness and constant force was unable to suppress spontaneous oscillations. The stimulus fiber had a stiffness of $K_{SF} = 425\ \mu N \cdot m^{-1}$ and a drag coefficient of $\xi_{SF} = 53\ nN \cdot s \cdot m^{-1}$. Analysis parameters and statistics for each experimental state diagram can be found in Table 6.1.

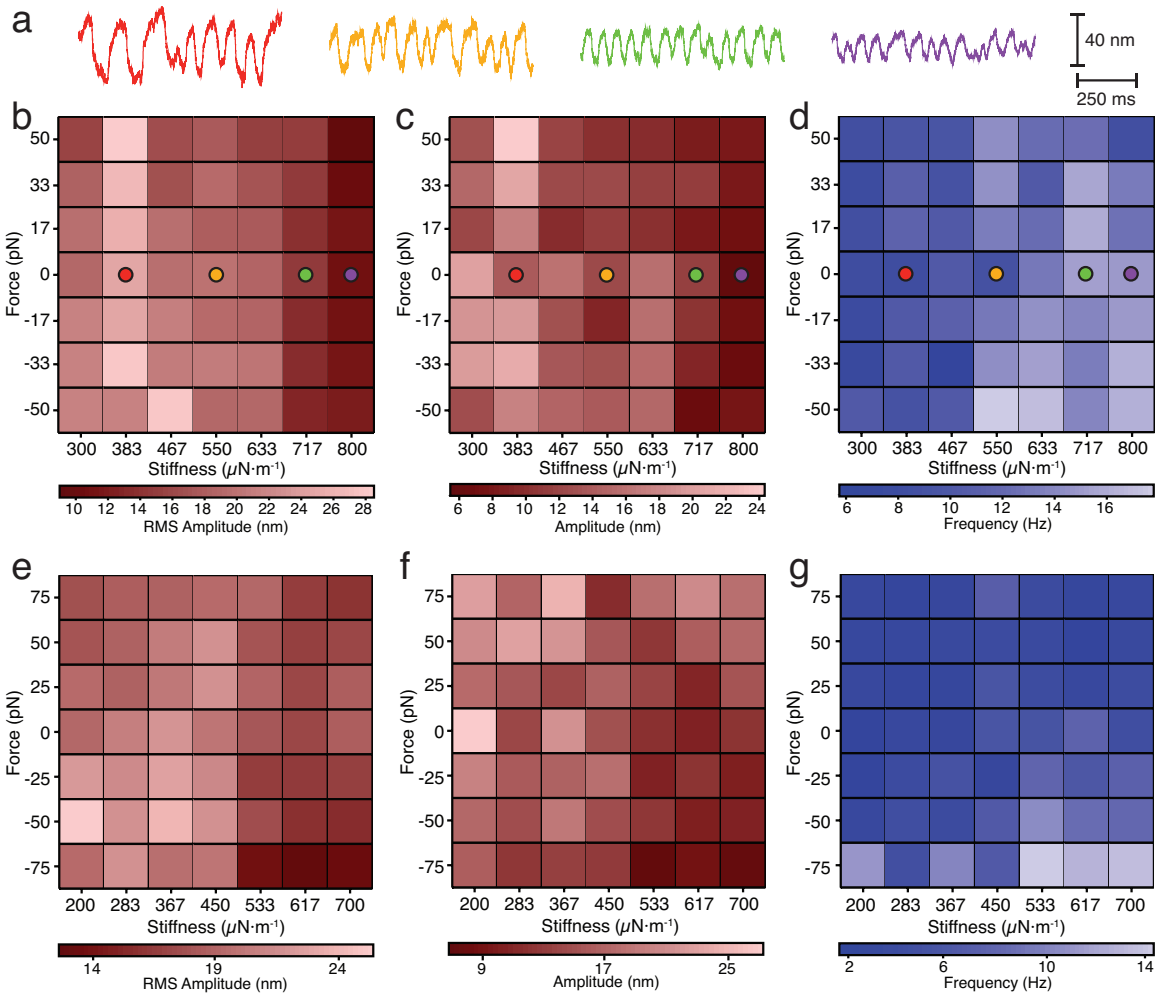
a
40 nm
250 ms
b
c
d
Force (pN)
50
33
17
0
-17
-33
-50
300 383 467 550 633 717 800
Stiffness (μN·m⁻¹)
10 12 14 16 18 20 22 24 26 28
RMS Amplitude (nm)
6 8 10 12 14 16 18 20 22 24
Amplitude (nm)
6 8 10 12 14 16
Frequency (Hz)
e
f
g
75
50
25
0
-25
-50
-75
200 283 367 450 533 617 700
14 19 24
9 17 25
2 6 10 14

Figure 6.5. Temporal changes in a bundle's state diagram. To verify that a hair bundle's state diagram exhibits little time dependence, a bundle's experimental state diagram was computed at (a) 0 min and (b) 10 min, and artificial endolymph was not exchanged over this duration. The shades of red and blue correspond respectively to the amplitude and frequency of spontaneous oscillation. Spearman's correlation coefficients for the amplitude and frequency maps are shown in red and blue, respectively. Time traces for selected operating points are displayed above each state diagram. Analysis parameters and statistics for these experiments may be found in Table 6.1.

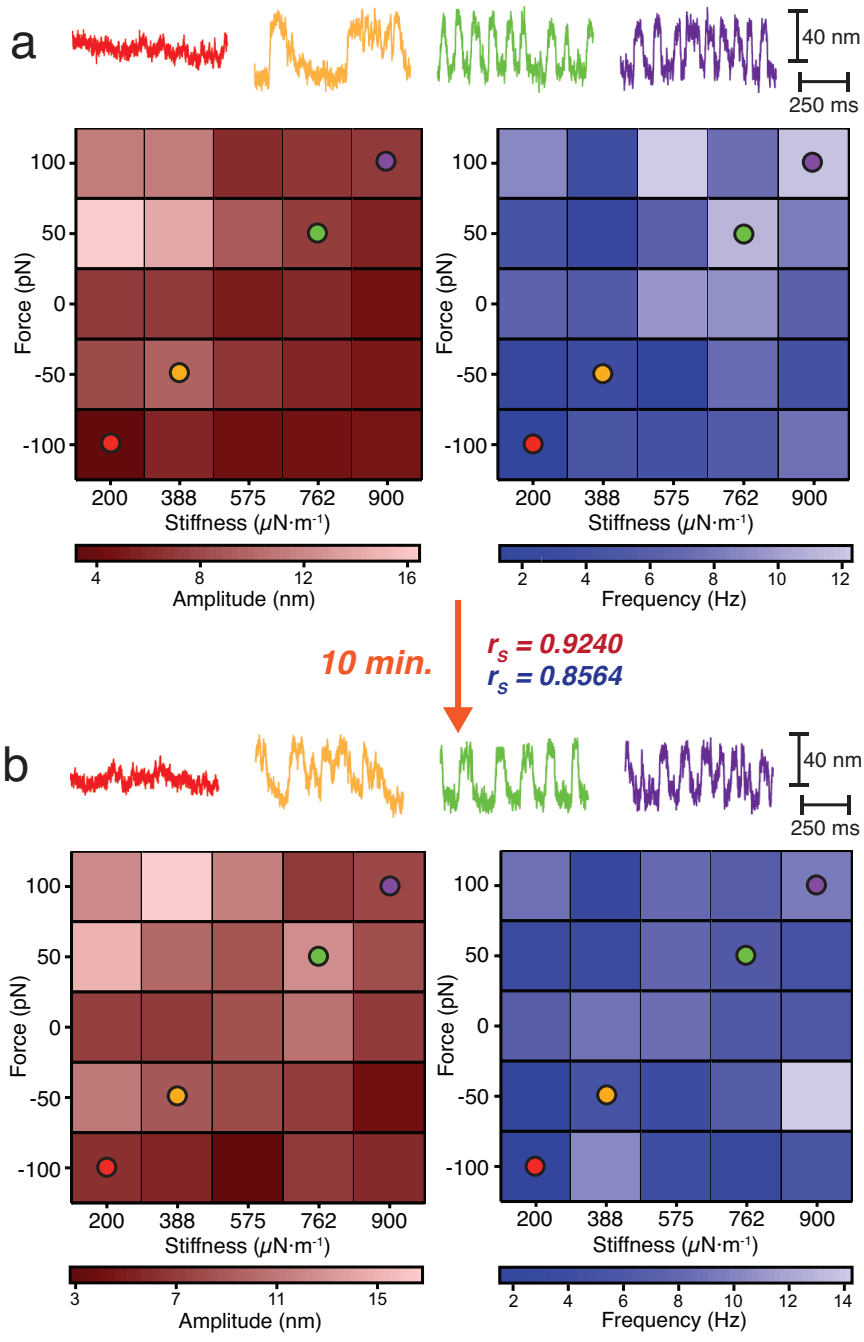
a
40 nm
250 ms
100
50
0
-50
-100
Force (pN)
200
388
575
762
900
Stiffness (μN·m-1)
4
8
12
16
Amplitude (nm)
2
4
6
8
10
12
Frequency (Hz)
10 min.
rs = 0.9240
rs = 0.8564
b
40 nm
250 ms
3
7
11
15
2
4
6
8
10
12
14

Figure 6.6. Effect of gentamicin on hair-bundle state diagrams. To better grasp the contribution of active hair-bundle motility on the bundle's state space, the experimental state diagrams were computed for two bundles bathed in 500 μM gentamicin, an agent that blocks mechanotransduction channels and arrests spontaneous oscillations. (a) A control experimental state diagram was first measured for a large hair bundle. Oscillations had a maximal RMS magnitude of 16 nm and a mean of 8.7 nm. (b) During exposure to gentamicin the bundle became quiescent at all operating points. The amplitude map shows consistently small amplitudes, with a maximum RMS magnitude of 2.0 nm and a mean of 1.4 nm. The correlation between the experimental state diagrams before and after treatment was not significant, with coefficients of 0.21 ($p = 0.14$) in amplitude and 0.01 ($p = 0.95$) in frequency. (c) Another experimental state diagram was measured for a medium hair bundle, in which the bundle oscillated for half of the operating points. The greatest RMS magnitude was of 15.6 nm and the mean RMS magnitude was 4.5 nm. (d) Upon exposure to gentamicin the bundle became quiescent at all operating points, with a maximal RMS magnitude of 1.6 nm and a mean of 1.4 nm. As before, there was no significant correlation between the experimental state diagrams, with coefficients of 0.28 ($p = 0.13$) in amplitude and 0.15 ($p = 0.32$) in frequency. In all cases, the experimental state diagrams before and after gentamicin treatment showed no significant positive correlations. These controls verify that a hair bundle without active motility possesses no oscillatory operating points and that its experimental state diagram changes dramatically when active motility is abolished. The analysis and parameters for these experiments may be found in Table 6.1.

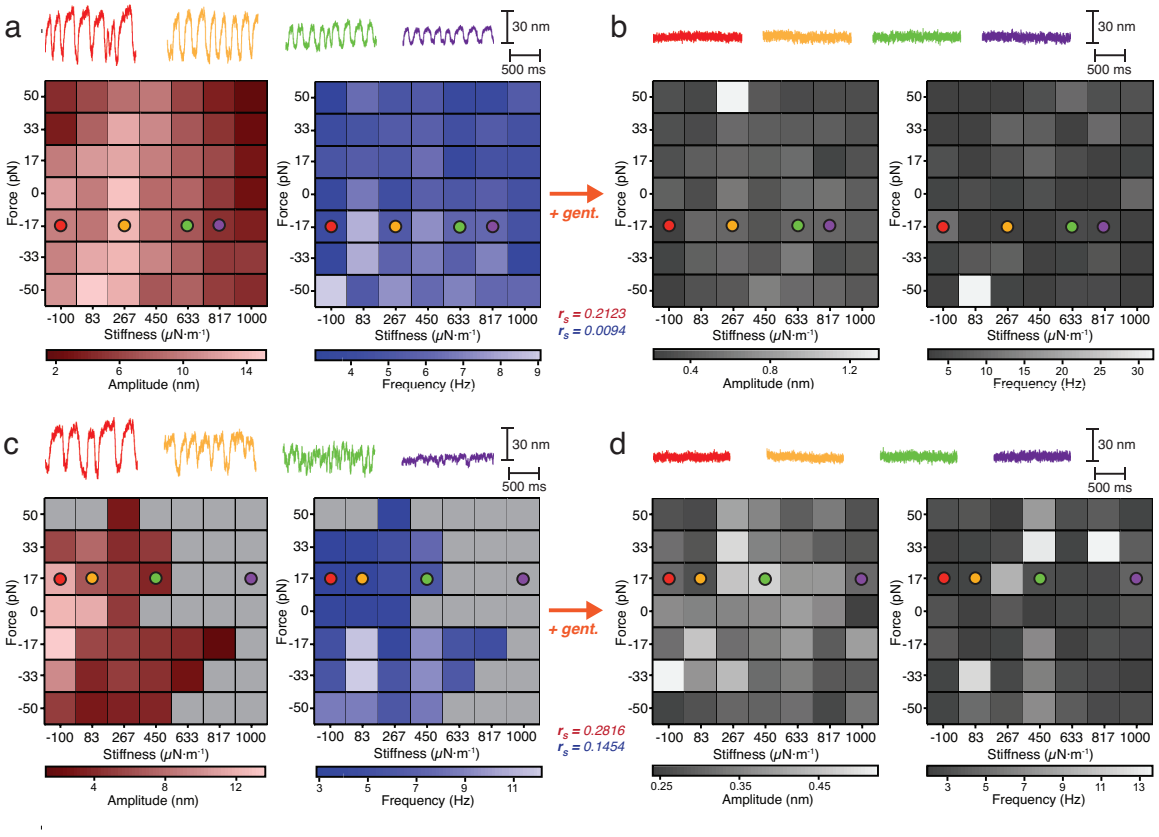
a
30 nm
500 ms
Force (pN)
50
33
17
0
-17
-33
-50
-100 83 267 450 633 817 1000
Stiffness (μN·m⁻¹)
Amplitude (nm)
2 6 10 14
Frequency (Hz)
4 5 6 7 8 9
+ gent.
r_s = 0.2123
r_s = 0.0094
b
0.4 0.8 1.2
5 10 15 20 25 30
c
4 8 12
3 5 7 9 11
r_s = 0.2816
r_s = 0.1454
d
0.25 0.35 0.45
3 5 7 9 11 13

A hair bundle's behavior depends not only on deterministic dynamics but also on thermal fluctuations. To assess the effects of noise on a hair bundle's state diagram, stochastic simulations of the dynamical model were implemented (equations 6.4 and 6.5). Artificial state diagrams were then generated from simulation results using the same procedures as was used for experimental state diagrams. Such a method not only served to evaluate the effects of noise on a hair bundle's dynamics, but it also tested the capacity of these analyses to accurately calculate an experimental state diagram. For a low level of noise, the procedure correctly identified all operating points bounded by a loop of Hopf bifurcations (Figure 6.7a,b). As the bundle's stiffness increased, its oscillatory amplitude decreased and frequency increased. When the noise was increased by a factor of 10^3, the algorithm identified oscillatory operating points within the monostable regime (Figure 6.7c,d). The pattern in amplitude and frequency persisted, but the diagram of frequency succumbed to noise. These results indicate that noise effects a reduction in the accuracy of experimental state diagrams. Strikingly, in the presence of large noise the model hair bundle oscillated at monostable operating points in the low-stiffness regime far from any bifurcation (Figure 6.7c,d). An excitable region surrounding the oscillatory regime could account for this unpredicted behavior. Systematic characterization of hair-bundle excitability affirms this hypothesis (*see* Chapter 10).

Figure 6.7. Artificial state diagrams. (a) An artificial state diagram was generated in a model of hair-bundle mechanics with a low noise level: the standard deviations of the noise terms were σ_x = 0.001 and σ_f = 0.001. The green lines correspond to a loop of Hopf bifurcations and a line of fold bifurcations. The gray operating points were classified as quiescent. Within the red region of spontaneous oscillation, color intensity corresponds to the amplitude of spontaneous oscillation. The smallest amplitudes were found near the high-stiffness border of the oscillatory region. (b) A second artificial state diagram under the same conditions depicts the oscillation frequency in blue. Near the edge of the region of spontaneous oscillation, frequencies reached their maximum. (c) Another artificial state diagram was generated with a high noise level: the standard deviations of the noise terms were σ_x = 1 and σ_f = 1. As before, the amplitude of spontaneous oscillation is displayed in red and quiescent operating points are presented in gray. In this case, the region of spontaneous oscillation increased in size. (d) For the same noise level, an artificial state diagram presents the frequency of spontaneous oscillation in blue. As for the previous cell, the amplitude and frequency of spontaneous oscillation were inversely correlated, with the minimum amplitude and maximum frequency both occurring near the high-stiffness edge of the oscillatory region. The constant force, stiffness, displacement, and frequency have been rescaled by a factor of 100. Because the model incorporates rescaled parameters, no units for the amplitude, constant force, and load stiffness are displayed. The analysis parameters and correlation statistics may be found in Table 6.1.

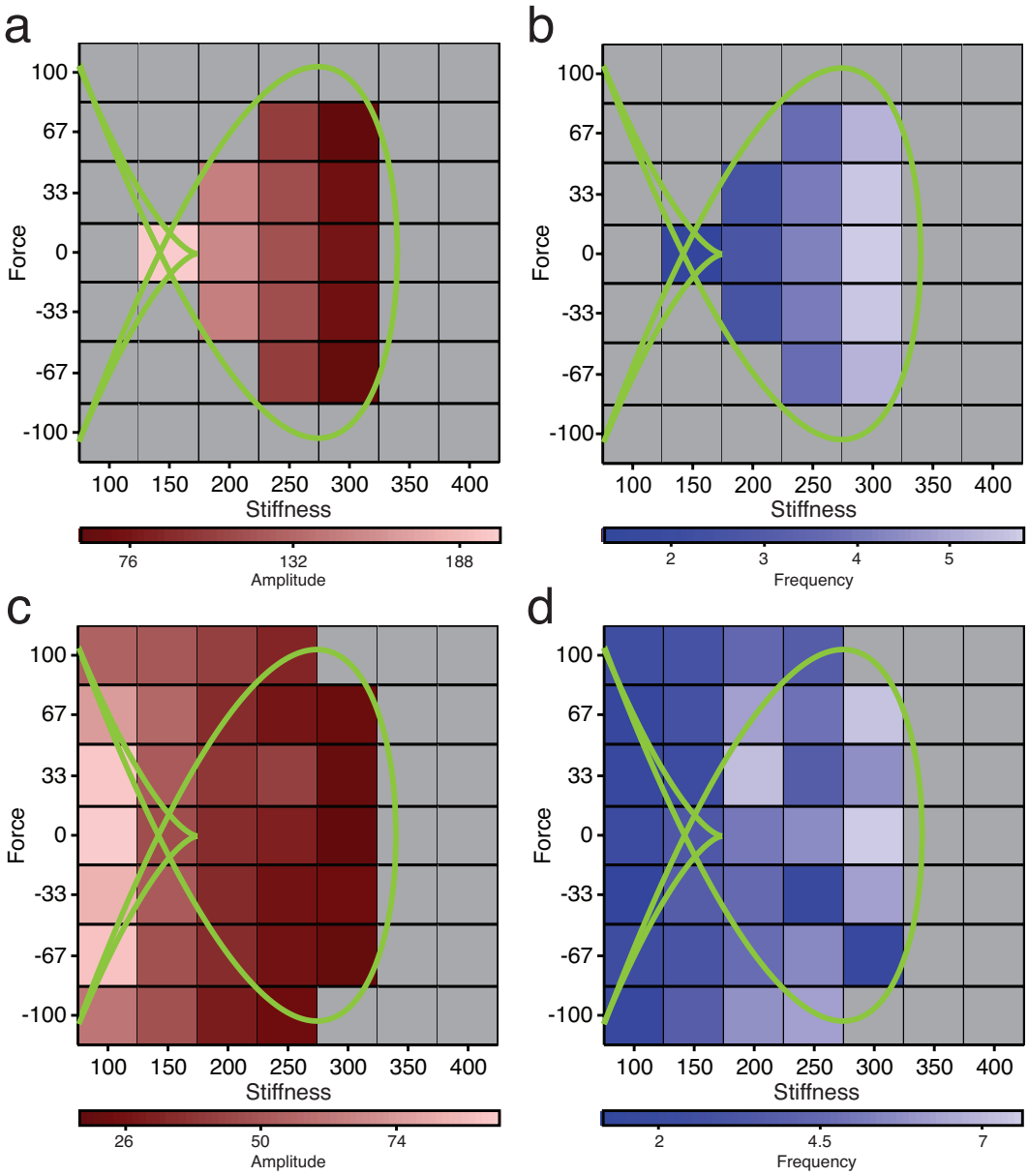
a
b
c
d
Force
Stiffness
Amplitude
Frequency
100
67
33
0
-33
-67
-100
100 150 200 250 300 350 400
76 132 188
2 3 4 5
26 50 74
2 4.5 7

Table 6.1. Summary of state-diagram analysis and statistics. Statistics are displayed for each of the state diagrams in Figures 6.2-6.7. The columns corresponding to Figures 6.5 and 6.6 depict the statistics for one hair bundle over the course of 10 min (Figure 6.5) and two bundles prior to gentamicin treatment (Figure 6.6). For each hair bundle, its size classification and analysis parameters are presented. Cells with dashed lines correspond to tests that were not required for that particular bundle. For each statistic, a threshold was placed both upon the statistic value presented and its corresponding p-value (*, $p < 0.01$; **, $p < 0.001$). Spearman's rank correlation between the bundle's RMS magnitude, amplitude, and frequency of spontaneous oscillations was calculated for each bundle with respect to both the load stiffness and constant force and between the amplitude and frequency of oscillation. Numbers in bold correspond to significant correlations ($p < 0.05$). In all cases a bundle's oscillatory amplitude decreased with increasing load stiffness. For half of the bundles the frequency of oscillation grew with increasing load stiffness. In half of the instances the amplitude and frequency of spontaneous oscillation were inversely correlated.

Figure	6.2a-d	6.3a-c	6.3d-f	6.3e-h	6.4a-c	6.4b-d	6.5a	6.5b	6.6a	6.6c	6.7a-b	6.7c-d
Bundle Size	*Small*	*Medium*	*Medium*	*Medium*	*Large*	*Large*	*Large*	*Large*	*Large*	*Medium*	*N/A*	*N/A*
Analysis Parameters												
Detrending Time	2/3 s	1/3 s	1/6 s	1/3 s	1/3 s	1/3 s	2/3 s	2/3 s	2/3 s	2/3 s	0	0
Multimodality > *	1.0×10^{-3}	1.0×10^{-3}	2.0×10^{-3}	1.0×10^{-3}	1.0×10^{-2}	5.0×10^{-3}	2.0×10^{-3}	2.0×10^{-3}	1.5×10^{-2}	6.0×10^{-3}	1.0×10^{-2}	1.0×10^{-2}
Asymmetry > **	8.0×10^{-2}	5.0×10^{-2}	5.0×10^{-2}	6.0×10^{-2}	-	-	2.0×10^{-2}	2.0×10^{-2}	6.0×10^{-2}	1.3×10^{-1}	-	1.0×10^{-1}
Thinness < **	-1.8×10^{1}	-	-2.0×10^{1}	-	-	-	-1.8×10^{1}	-1.8×10^{1}	-1.8×10^{1}	-2.8×10^{1}	-	-6.0×10^{1}
Minimum Fourier Frequency	1 Hz	2 Hz	2 Hz	2 Hz	0 Hz	2 Hz	1 Hz	1 Hz	2 Hz	2 Hz	0	0
Correlations												
RMS Magnitude vs. Stiffness:	**-4.0×10^{-1}**	**-5.4×10^{-1}**	**-5.7×10^{-1}**	**-8.1×10^{-1}**	**-6.6×10^{-1}**	**-8.0×10^{-1}**	-2.1×10^{-1}	-3.3×10^{-1}	**-7.8×10^{-1}**	**-6.9×10^{-1}**	**-9.5×10^{-1}**	**-9.7×10^{-1}**
p-value	**1.7×10^{-2}**	**1.4×10^{-4}**	**3.2×10^{-2}**	**2.7×10^{-8}**	**2.9×10^{-7}**	**7.7×10^{-12}**	3.1×10^{-1}	1.1×10^{-1}	**4.5×10^{-11}**	**6.7×10^{-5}**	**1.9×10^{-7}**	**4.6×10^{-20}**
Amplitude vs. Stiffness:	**-4.2×10^{-1}**	**-6.2×10^{-1}**	**-6.6×10^{-1}**	**-8.6×10^{-1}**	**-5.5×10^{-1}**	**-7.7×10^{-1}**	**-4.9×10^{-1}**	**-3.6×10^{-1}**	**-6.6×10^{-1}**	**-7.3×10^{-1}**	**-9.5×10^{-1}**	**-9.6×10^{-1}**
p-value	**1.1×10^{-2}**	**6.5×10^{-6}**	**1.1×10^{-2}**	**4.5×10^{-10}**	**3.9×10^{-5}**	**7.8×10^{-11}**	**1.2×10^{-2}**	**7.3×10^{-2}**	**2.1×10^{-7}**	**1.7×10^{-5}**	**1.9×10^{-7}**	**4.8×10^{-18}**
Frequency vs. Stiffness:	1.5×10^{-1}	**5.1×10^{-1}**	**6.0×10^{-1}**	1.0×10^{-1}	**4.1×10^{-1}**	**7.1×10^{-1}**	**4.8×10^{-1}**	2.7×10^{-1}	-3.1×10^{-2}	3.0×10^{-1}	**9.5×10^{-1}**	**6.8×10^{-1}**
p-value	4.0×10^{-1}	**4.6×10^{-4}**	**2.2×10^{-2}**	6.1×10^{-1}	**3.3×10^{-3}**	**9.3×10^{-9}**	**1.5×10^{-2}**	1.8×10^{-1}	7.9×10^{-1}	1.2×10^{-1}	**1.1×10^{-7}**	**1.5×10^{-5}**
RMS Magnitude vs. Force:	1.3×10^{-2}	**-3.7×10^{-1}**	1.7×10^{-1}	4.2×10^{-2}	-8.7×10^{-2}	-2.4×10^{-1}	**8.1×10^{-1}**	**8.3×10^{-1}**	-2.2×10^{-1}	8.2×10^{-2}	-1.2×10^{-2}	2.9×10^{-2}
p-value	9.4×10^{-1}	**1.5×10^{-2}**	5.6×10^{-1}	8.2×10^{-1}	5.5×10^{-1}	9.5×10^{-2}	**8.4×10^{-7}**	**2.6×10^{-7}**	1.3×10^{-1}	6.8×10^{-1}	9.6×10^{-1}	8.7×10^{-1}
Amplitude vs. Force:	**3.7×10^{-1}**	**-4.4×10^{-1}**	8.1×10^{-2}	1.0×10^{-1}	**5.1×10^{-1}**	-1.5×10^{-2}	**6.2×10^{-1}**	**6.6×10^{-1}**	**-2.8×10^{-1}**	2.7×10^{-1}	-1.6×10^{-2}	1.2×10^{-1}
p-value	**2.9×10^{-2}**	**3.1×10^{-3}**	7.8×10^{-1}	5.8×10^{-1}	**1.8×10^{-4}**	3.0×10^{-1}	**8.7×10^{-4}**	**3.1×10^{-4}**	**4.8×10^{-2}**	1.7×10^{-1}	9.6×10^{-1}	5.2×10^{-1}
Frequency vs. Force:	**-4.7×10^{-1}**	1.5×10^{-1}	5.0×10^{-1}	**-6.0×10^{-1}**	**-6.3×10^{-1}**	-2.4×10^{-1}	**4.8×10^{-1}**	2.5×10^{-1}	**-4.8×10^{-1}**	**-6.8×10^{-1}**	1.6×10^{-2}	6.8×10^{-3}
p-value	**4.4×10^{-3}**	9.2×10^{-1}	7.2×10^{-2}	**3.2×10^{-4}**	**1.6×10^{-6}**	1.0×10^{-1}	**1.6×10^{-2}**	2.3×10^{-1}	**5.0×10^{-4}**	**9.8×10^{-5}**	9.6×10^{-1}	9.7×10^{-1}
Amplitude vs. Frequency:	**-5.7×10^{-1}**	**-6.1×10^{-1}**	-2.1×10^{-1}	3.4×10^{-2}	**-7.5×10^{-1}**	**-4.5×10^{-1}**	-5.8×10^{-2}	-2.1×10^{-1}	2.6×10^{-1}	**-4.2×10^{-1}**	**-8.2×10^{-1}**	**-7.0×10^{-1}**
p-value	**3.6×10^{-4}**	**2.0×10^{-5}**	4.6×10^{-1}	8.6×10^{-1}	**6.6×10^{-10}**	**1.2×10^{-3}**	7.8×10^{-1}	3.3×10^{-1}	7.4×10^{-2}	**3.0×10^{-2}**	**3.4×10^{-4}**	**1.2×10^{-5}**

SECTION 6.3: *Discussion of Results*

Biological systems must respond robustly to environmental perturbations. Whether these systems comprise signaling pathways possessing complex chemical processes or the dynamic interactions of species as they compete, evolve, and disperse in a struggle for existence, their behavior can be described by dynamical systems (206-210). Owing to the complexity of cells, organisms, and ecosystems, however, biomathematicians struggle to produce mathematical models that make testable predictions about such systems. Moreover, experimental tools are seldom available to test theoretical predictions about biological dynamics. By systematically mapping the state diagrams of multiple hair bundles, the present work represents an exception to these generalizations. A simple model of hair-bundle dynamics predicts a state diagram that captures the effects of mechanical loading on bundles (167). The present experimental results accord with these predictions. The experimental state diagrams revealed by mechanical-load clamping display a bounded locus of spontaneous activity. Within that locus, increasing the load stiffness imposed on a hair bundle causes an increase in frequency and decrease in amplitude of spontaneous oscillation.

In a few cases, the amplitude and frequency of oscillation depended not only on the load stiffness but also on the constant force. These bundles exhibited state diagrams with broken symmetry, whose explanation requires an additional control parameter previously omitted for simplicity (167). Such a control parameter might be intrinsic to the hair bundle and obstinate to manipulation or it might be experimentally tractable. If the former case is true, the parameter could be related to the relaxation time or strength

of a Ca^{2+}-dependent self-tuning mechanism (45). If the latter scenario pertains, the parameter might represent an additional mechanical load or it might be another control parameter that could be adjusted through pharmacological intervention. An example of such a parameter is the strength of Ca^{2+} feedback on the force produced by adaptation motors (170). To adjust this directly, an agent such as quercetin or phenylarsine oxide could reduce Ca^{2+}-dependent binding of a myosin's IQ motif to phosphatidylinositol-4,5-bisphosphate (PIP_2) and thus cause a decrease in the strength of Ca^{2+} feedback with a corresponding increase in the force produced by adaptation motors (211). Taken together, however, the dependence of a bundle's oscillatory amplitude and frequency on the constant force and load stiffness agree with the theoretical model, and details regarding the relative dependence of these parameters must be investigated in future work.

Increasing the stiffness and constant force confronting a hair bundle drives it from the region of spontaneous oscillation into a domain of quiescence. The boundary between the two regimes represents a bifurcation, that is, a dramatic change in behavior in response to continuous variation of one or more control parameters. Observations indicate that the boundary associated with large values of the load stiffness constitutes a line of supercritical Hopf bifurcations (129, 167, 186, 212, 213). Here the amplitude of spontaneous movement grows continuously from zero as the operating point progresses into the region of spontaneous oscillation. A hair bundle whose operating point is poised near a supercritical Hopf bifurcation should achieve maximum amplification, frequency tuning, and compressive nonlinearity. These features are explored further in

Chapter 7. For low values of the load stiffness, however, the amplitude of spontaneous oscillation does not change as the bifurcation is approached, a behavior more consistent with a fold of limit cycles or an infinite-period bifurcation (157, 159, 204).

The characteristic frequencies measured near a supercritical Hopf bifurcation accord with those of saccular afferent axons *in vivo* (202, 203), suggesting that hair bundles normally reside at operating points near the high-stiffness arc of bifurcations. Consistent with this idea, the elastic load imposed experimentally at the bifurcation resembled the stiffness of the otolithic membrane that ordinarily confronts a saccular hair bundle (144). This result reinforces the thesis that mechanical loads dictate the behavior of hair bundles *in vivo*. Additionally, a reduction of these elastic loads *in vivo* should affect the oscillatory behavior of hair bundles, for example by increasing the prevalence and amplitude of otoacoustic emissions.

CHAPTER 7

Exposing the Varied Functional Roles of Hair Bundles

In the previous chapter, numerous hair-bundle state diagrams revealed a common pattern in a bundle's unforced behavior that agreed with a simple dynamical model and betrayed additional, unpredicted phenomena. However, sensory systems require that hair bundles detect and transduce mechanical forces *in vivo*. These signals depend on the organ in which a bundle is situated and may be periodic at some characteristic frequency, or they may be static forces. Changes in a hair bundle's geometry and its microenvironment confer different mechanical loads within a given sensory organ. These mechanical properties may then dictate the sensory bundle's behavioral response. Here we explore the effects of load stiffness and constant force on hair-bundle function. A two-parameter load clamp again imposes loads and delivers various stimuli to individual ciliary bundles. The experiments reveal varied sensory modalities of active hair bundles that depend on mechanical control parameters. A state diagram therefore not only captures a bundle's unforced behavior but also provides a detailed map of sensory function.

SECTION 7.1: *Materials and Methods*

This study employed same experimental preparation and dynamical model from *Chapter 6* with the addition of mechanical stimulation and corresponding analyses.

Sensitivity. To evaluate a hair bundle's response to periodic stimuli, we calculated a bundle's phase-locked response $\left\langle \tilde{X}(\omega_s) \right\rangle$, in which $\tilde{X}(\omega_s)$ is the bundle's Fourier amplitude at the frequency of driving, ω_s. Sensitivity was then defined as the modulus of the bundle's response function

$$\tilde{\chi}(\omega_s) = \frac{\left\langle \tilde{X}(\omega_s) \right\rangle}{\tilde{F}(\omega_s)}, \tag{7.1}$$

in which $\tilde{F}(\omega_s)$ is the Fourier amplitude of the stimulus force at the driving frequency.

Phase difference with respect to stimulation. For those instances in which a sinusoidal stimulus was provided, the phase difference between the sinusoidal component of motion commanded at the fiber's base $\Delta_C(t)$ and that of the hair bundle $X(t)$ was determined by the relation

$$\phi = \phi_\Delta - \phi_X = \tan^{-1} \frac{\Im(\tilde{\Delta}_C(\omega_S))}{\Re(\tilde{\Delta}_C(\omega_S))} - \tan^{-1} \frac{\Im(\tilde{X}(\omega_S))}{\Re(\tilde{X}(\omega_S))}, \tag{7.2}$$

in which $\tilde{X}$ (ω_s) and $\tilde{\Delta}_C$ (ω_s) are the Fourier transforms of the motions at the frequency of driving, ω_s, and $\Re$ indicates the real and $\Im$ the imaginary part of a variable. A negative phase difference corresponds to a phase lead of the hair bundle with respect to

the fiber and a positive difference corresponds to a phase lag. This convention was used to accord with previously published phase differences between a stimulus and the hair bundle's response (117, 124, 129).

Quality factor. The response of a hair bundle often displayed resonance at some characteristic frequency f_C. To estimate the bundle's sharpness of tuning, an operational definition of the quality factor was employed

$$Q = \frac{f_C}{\Delta f}. \tag{7.3}$$

Here Δf corresponds to the bandwidth at amplitude $A_C/\sqrt{2}$, in which A_C is the amplitude of the bundle's response at the characteristic frequency. Larger values of Q correspond to sharper resonance. In most cases this operational definition underestimated the quality of resonance.

Vector strength. To assess the degree of entrainment between the stimulus fiber and the hair bundle, the vector strength between the two signals was measured. To do so, the Hilbert transform of each signal was first calculated,

$$X_H(t) = F^{-1}\left[-i \cdot \mathrm{sgn}(\omega) \cdot \tilde{X}(\omega)\right], \tag{7.4}$$

in which F^{-1} is the inverse Fourier transform, *sgn* is the signum function, and $\tilde{X}$ is the Fourier transform of the bundle's motion. The analytic signal $X_A(t) = X(t) + iX_H(t)$ was then used to calculate the instantaneous phase

$$\varphi(t) = \varphi_{\Delta_C}(t) - \varphi_X(t) = \tan^{-1}\frac{\Delta_{C,H}(t)}{\Delta_C(t)} - \tan^{-1}\frac{X_H(t)}{X(t)}, \tag{7.5}$$

in which $\Delta_{C,H}(t)$ is the Hilbert transform of the sinusoidal component of motion commanded at the fiber's base, $\Delta_C(t)$. The mean vector length, or vector strength from a signal of length N, is then given by

$$VS = \left| \frac{1}{N} \sum_{j=1}^{N} e^{i\varphi(t_j)} \right|, \tag{7.6}$$

in which $0 \le VS \le 1$. The vector strength equals one if two signals are identical and completely entrained and approaches zero as two signals become dissimilar in instantaneous phase. This parameter thus corresponds to the degree of entrainment between two signals. The angle of the mean vector is given by its argument.

Statistics. Paired Student's *t*-tests were used to determine the significance of amplitude responses, quality factors, and vector strengths; significance was defined as $p < 0.05$. Binned phase differences were evaluated with Rayleigh's test for non-uniformity of circular data.

SECTION 7.2: *Mechanical Resonance*

The principal role of hair cells in the auditory system is the detection of periodic forces derived from sound. Although modeling suggests that a quiescent hair bundle should respond with maximal frequency tuning and nonlinearity at the boundary of the region of spontaneous oscillation (45, 129, 164, 181, 186, 199), no experimental study has systematically examined bundles near this critical locus. What follows is an exploration of how hair bundles situated at various operating points in the experimental state diagram respond to sinusoidal stimulation over a range of amplitudes and frequencies.

The boundary between the regions of spontaneous activity and quiescence lay between operating points for which the bundle's behavior could be clearly classified as either oscillatory or quiescent based on the distribution of its displacement. When poised near this border, a hair bundle exhibited resonant frequency tuning: its phase-locked response to sinusoidal stimulation—the magnitude of its average oscillation amplitude at the stimulus frequency—displayed a clear peak (Figures 7.1-7.2). As the bundle's operating point was displaced into the quiescent region, the response at this resonant frequency progressively diminished. The sharpness of tuning, quantified by the quality factor of the resonance, was greatest on the oscillatory side of the boundary and in one instance approached that of auditory organs (2, 10, 23, 33, 67) (Figures 7.1a and 7.2a,c).

When a hair cell's apical surface was exposed to gentamicin to abolish active hair-bundle motility, a hair bundle's tuning diminished at all operating points; the response at the original resonant frequency collapsed to the noise floor (Figures 7.1a and

7.2a). This result confirmed that the peak response and sharpness of tuning stem from active hair-bundle motility that augments the bundle's mechanical response. Indeed, the response of an untreated hair bundle exceeded that of a treated bundle for most stiffness values and stimulus frequencies. Unlike the response of an untreated bundle, that of a treated bundle was insensitive to the load stiffness and resembled behavior of a low-pass filter.

The phase of an active hair bundle's response led that of the stimulus for frequencies below the bundle's resonant frequency and lagged for frequencies exceeding that value (Figures 7.1b and 7.2b,d). This pattern accorded with previous micromechanical manipulations of active hair bundles operating under a single mechanical load (129). Here an increase in the bundle's load stiffness poised it far from the boundary of spontaneous oscillation eliminated any phase lead. The phase lead diminished far from and on the quiescent side of the border of spontaneous oscillation and disappeared upon application of gentamicin, indicating that the lead was generated by active hair-bundle motility (Figures 7.1b and 7.2b).

To compare the experimental behavior of hair bundles with the predictions of a dynamical model of hair-bundle activity, stochastic simulations were conducted of the responses expected in the presence of thermal noise. The model's response agreed qualitatively with the experimental observations (Figure 7.1). An auditory hair bundle thus achieves maximum amplification and frequency selectivity near the border of spontaneous oscillation defined by a supercritical Hopf bifurcation.

Figure 7.1. Load-dependent mechanical resonance of active hair bundles. (a) The behavior of a medium-sized hair bundle in the absence of stimulation was first classified for different operating points. The bundle's response to sinusoidal stimulation was then analyzed as a function of stimulus frequency for a stimulus amplitude of 1.5 pN and a constant force of zero. The response peaked at 10 Hz for a load stiffness of 300 $\mu N \cdot m^{-1}$, with the amplitude and quality of the resonant peak decreasing as the stiffness increased. When the bundle was exposed to 500 μM gentamicin, the frequency response lost its peak for a load stiffness of 300 $\mu N \cdot m^{-1}$ (dashed line). (b) The phase of hair-bundle motion with respect to the corresponding stimuli is shown for the operating points defined in (a). A negative angle corresponds to the bundle's motion leading the stimulus. The dashed lines signify phase differences of ±90°. At a load stiffness of 300 $\mu N \cdot m^{-1}$, the bundle's motion switched from a phase lead to a phase lag near the bundle's resonant frequency. This pattern disappeared for higher stiffnesses (orange and blue) and upon application of gentamicin (gray dashed line). (c) In a model of hair-bundle responsiveness with an intermediate level of noise ($\sigma_x = 0.1$ and $\sigma_f = 0.1$), a bundle yielded responses similar to those in (a). The resonant peak was greatest for a stiffness of 339 near the boundary of the oscillatory region, which occurred for zero constant force and a load stiffness of 340 in the absence of noise. (d) In the same model, the phase of the bundle's motion with respect to that of the stimulus displayed a pattern similar to that for the oscillatory point in (b). The magnitudes of the maximum phase lead and phase lag peaked at a stiffness of 339. For all experiments, the stiffness and damping coefficient of the stimulus fiber were respectively 425 $\mu N \cdot m^{-1}$ and 53 $nN \cdot s \cdot m^{-1}$. The stiffness, frequency, and force have been rescaled by a factor of 100 for simulations in (c-d) to facilitate comparison with the experimental data. Because the model was rescaled, no units are displayed for simulated results. Error bars are calculated from three stochastic simulations.

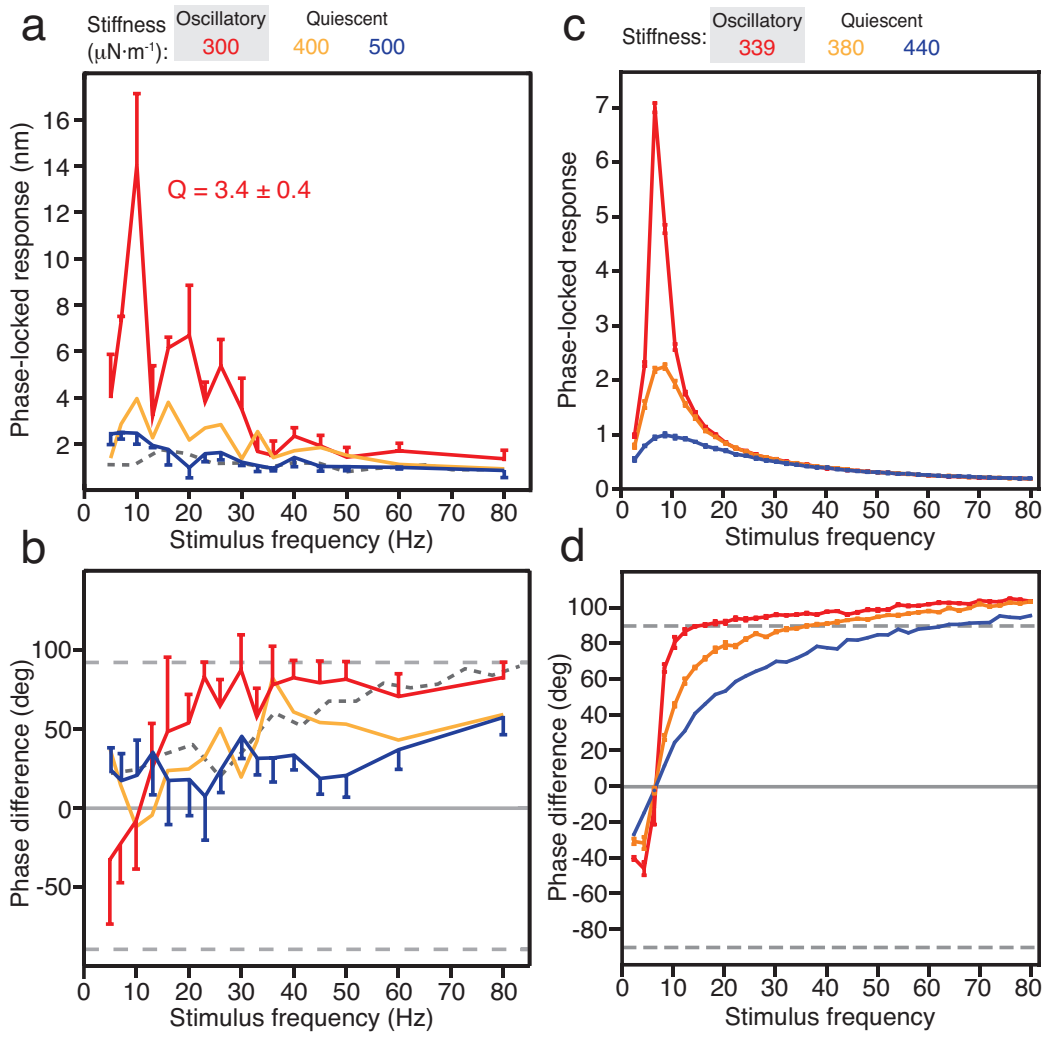
a
Stiffness (μN·m-1):
Oscillatory
Quiescent
300
400
500
Q = 3.4 ± 0.4
Phase-locked response (nm)
Stimulus frequency (Hz)
b
Phase difference (deg)
Stimulus frequency (Hz)
c
Stiffness:
Oscillatory
Quiescent
339
380
440
Phase-locked response
Stimulus frequency
d
Phase difference (deg)
Stimulus frequency

Figure 7.2. Additional examples of hair-bundle resonance. (a,c) The behavior of two hair bundles was first classified for different operating points in the absence of stimulation. The hair bundle's amplitude of vibration in response to sinusoidal stimulation was then analyzed as a function of the stimulus frequency. The responses peaked at 40 Hz (a) and 20 Hz (c). The largest and sharpest responses occurred for operating points near the boundary of the oscillatory region. (a) When the bundle was exposed to 500 μM gentamicin, the frequency response lost its peak for a load stiffness of 300 $\mu N \cdot m^{-1}$ (gray dashed line). (b,d) The phase difference between the bundle's motion and that of the stimulus was calculated. A reversal from a phase lead to a phase lag occurred near the bundle's resonant frequency. The magnitude of this phase change was associated with a reversal diminished upon increasing the load stiffness of the hair bundle, which moved its operating point farther from the edge of the oscillatory regions.

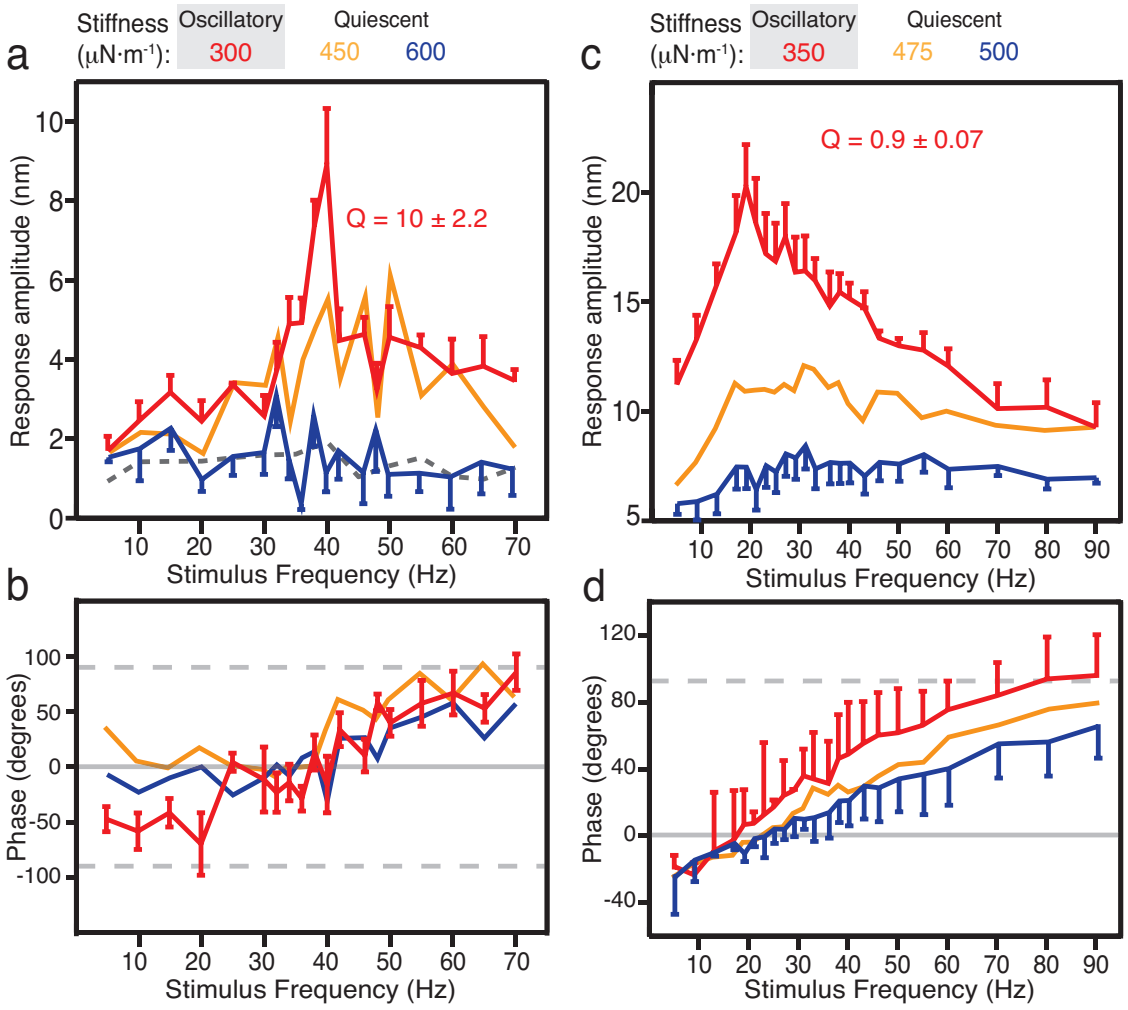
a
Stiffness (μN·m-1):
Oscillatory
300
Quiescent
450
600
Q = 10 ± 2.2
Response amplitude (nm)
Stimulus Frequency (Hz)
b
Phase (degrees)
Stimulus Frequency (Hz)
c
Stiffness (μN·m-1):
Oscillatory
350
Quiescent
475
500
Q = 0.9 ± 0.07
Response amplitude (nm)
Stimulus Frequency (Hz)
d
Phase (degrees)
Stimulus Frequency (Hz)

SECTION 7.3: *Entrainment*

A competent sensory system must adequately detect and transmit information about some environmental perturbation. In the auditory system, a hair bundle achieves this by entraining to periodic forces and subsequently transducing these signals. Motivated by this principle, we investigated the dependence of hair-bundle entrainment on a bundle's mechanical load.

Far from the border of the oscillatory region, a hair bundle's maximal response to weak stimulation was smaller and the response as a function of frequency was less sharply tuned than near the border (Figure 7.3a). Hypothesizing that this observation reflected reduced entrainment to the stimulus, we assessed the ability of the responses to follow corresponding stimuli by computing the vector strength at the resonant frequency for a range of load stiffnesses. The vector strength peaked at the edge and on the quiescent side of the boundary of spontaneous oscillations (Figure 7.3b). This affirms the previously unexpected hypothesis that a hair bundle achieves maximum phase locking at its resonant frequency near the boundary of spontaneous oscillation.

To better characterize entrainment, we delivered stimuli of both increasing force and increasing frequency to oscillatory hair bundles subjected to three load stiffnesses. A hair bundle achieved its maximum vector strength for operating points nearest the boundary of oscillation and for a stimulus frequency near that of spontaneous oscillation (Figures 7.4, 7.5, and 7.6a). The dependence of vector strength on the operating point diminished for stimulation away from the bundle's characteristic frequency (Figure 7.4 and 7.6b).

In agreement with published observations (187, 212), entrainment was frequency-dependent for a range of stimulus forces. A map of vector strength computed across a range of stimulus forces and frequencies disclosed a phase-locked region—an Arnold tongue—that depended on load stiffness. Although experiments were limited by the bundle's low resonant frequency, the entrainment region appeared to become more sharply tuned as the load stiffness increased (Figure 7.6d-f), an effect that was previously obscured by the use of different hair bundles for each load stiffness (212). A hair bundle's degree of phase locking under the influence of different mechanical loads indicates that these loads control the bundle's capacity to encode auditory stimuli.

Figure 7.3. Dependence of bundle resonance on the degree of entrainment. (a) The behavior of a medium hair bundle was first classified for different operating points surrounding a Hopf bifurcation in the absence of stimulation. The bundle's frequency response to stimuli of 0.5 pN in amplitude peaked at 10 Hz for all operating points. When the bundle was exposed to 500 μM gentamicin, its frequency response lacked a peak for load stiffnesses of 300 $\mu N \cdot m^{-1}$ and 800 $\mu N \cdot m^{-1}$ (dark and light gray dashed lines, respectively). (b) Quantified by the vector strength for each operating point in (a), the degree of entrainment peaked at a stiffness of 380 $\mu N \cdot m^{-1}$. Error bars represent standard errors of the mean for three observations; those not shown resembled in magnitude those that are included. The stiffness and damping coefficient of the stimulus fiber were respectively 425 $\mu N \cdot m^{-1}$ and 53 $nN \cdot s \cdot m^{-1}$.

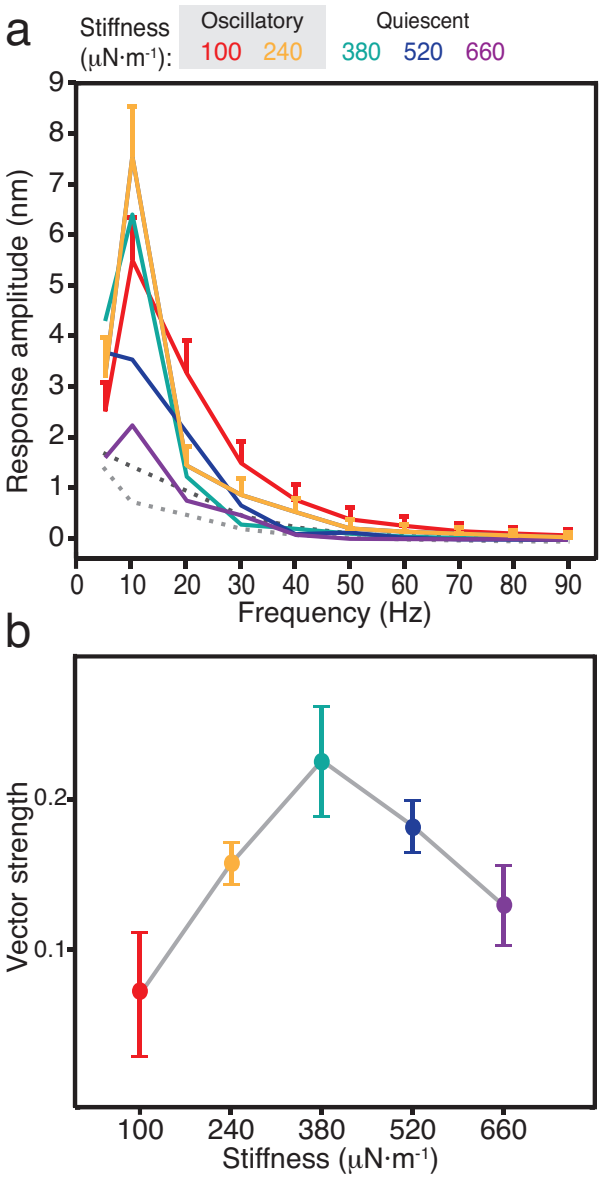
a
Stiffness
(μN·m-1):
Oscillatory
100
240
Quiescent
380
520
660
Response amplitude (nm)
0
1
2
3
4
5
6
7
8
9
0
10
20
30
40
50
60
70
80
90
Frequency (Hz)
b
Vector strength
0.1
0.2
100
240
380
520
660
Stiffness (μN·m-1)

Figure 7.4. Bundle entrainment as a function of stimulus frequency and force. A hair bundle oscillated at load stiffnesses of (a,d) 100 $\mu N \cdot m^{-1}$, (b,e) 167 $\mu N \cdot m^{-1}$, and (c,f) 250 $\mu N \cdot m^{-1}$. Here the hair bundle exhibited relaxation oscillations of large amplitude and low frequency. (a-c) Stimuli of successively increasing forces were delivered at frequencies of 5, 9, 13, 17, 21, 24, 27, 30, 40, 60, and 80 Hz (dark to light). The degree of entrainment between the hair bundle's motion and that of the stimulus fiber is represented by the vector strength. (d-f) Successively increasing stimulus forces were then delivered at frequencies of 5 Hz, 9 Hz, 13 Hz, 17 Hz, 21 Hz, 24 Hz, 27 Hz, 30 Hz, 40 Hz, 60 Hz, and 80 Hz. The degree of entrainment is again represented by the vector strength. In all cases, a bundle achieved maximum phase locking at a stimulus frequency of 5 Hz. The sharpness of the relation between vector strength and stimulus frequency peaked at a load stiffness of 250 $\mu N \cdot m^{-1}$.

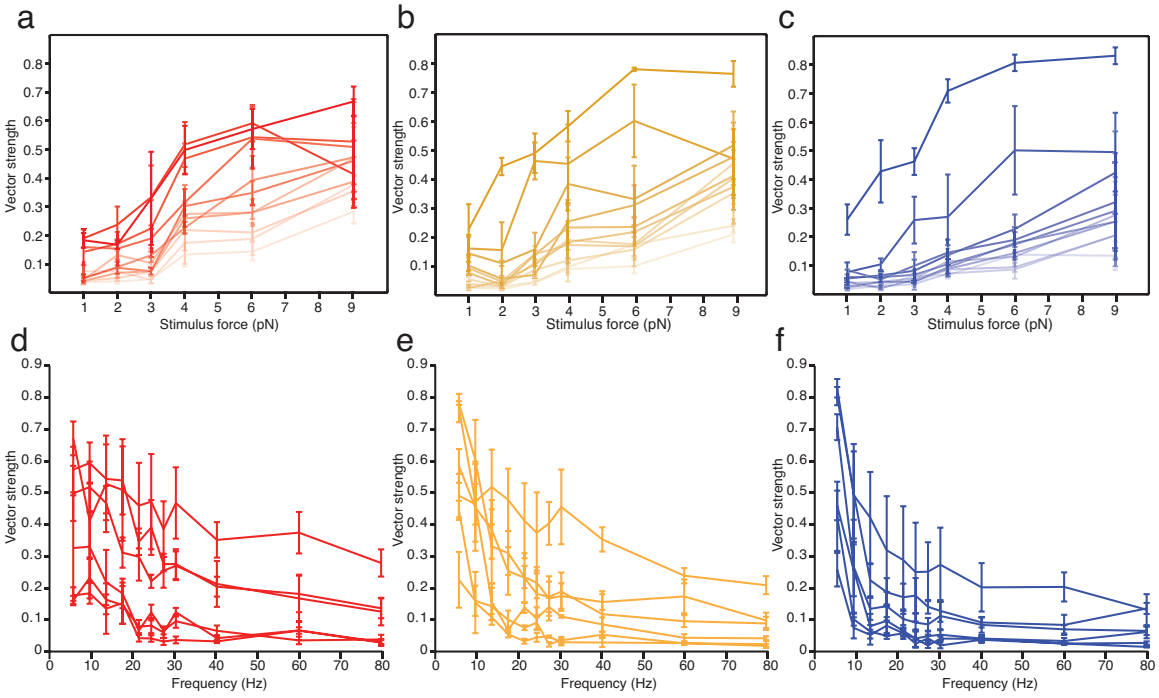
a
b
c
d
e
f
Vector strength
Stimulus force (pN)
Frequency (Hz)

Figure 7.5. Comparison of hair-bundle entrainment across operating points. The same hair bundle from Figure 7.4 oscillated at load stiffnesses of 100 $\mu N \cdot m^{-1}$ (red), 167 $\mu N \cdot m^{-1}$ (yellow), and 250 $\mu N \cdot m^{-1}$ (blue). Sinusoidal forces were then delivered at amplitudes of (a) 1 pN, (b) 2 pN, (c) 3 pN, (d) 4 pN, (e) 6 pN, and (f) 9 pN. The degree of entrainment between the stimulus fiber's motion and that of the hair bundle is represented by the vector strength. For all stimulus forces, a hair bundle achieved maximum phase locking at a stimulus frequency of 5 Hz, near its frequency of spontaneous oscillation.

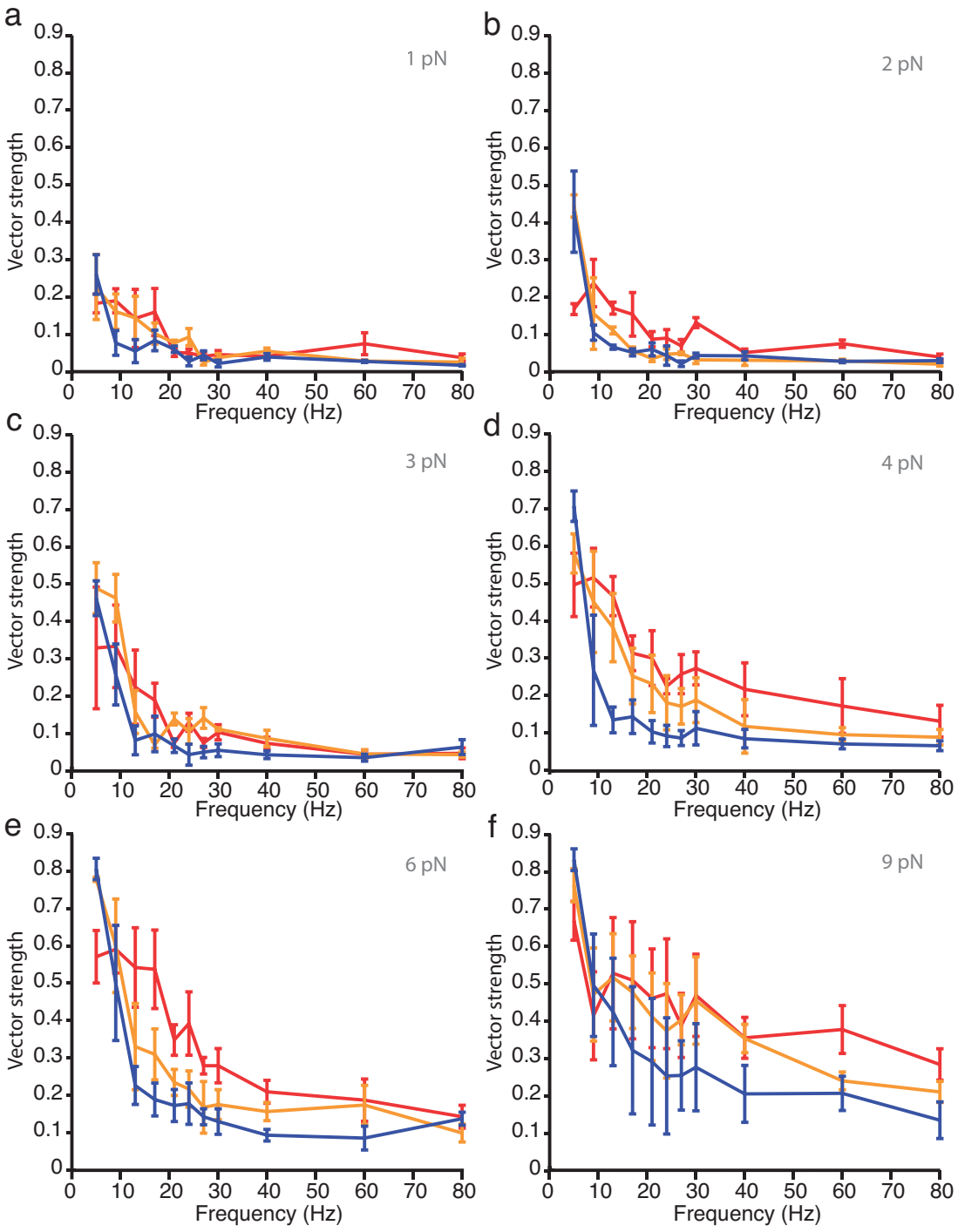
a
1 pN
b
2 pN
c
3 pN
d
4 pN
e
6 pN
f
9 pN
Vector strength
Frequency (Hz)
0
0.1
0.2
0.3
0.4
0.5
0.6
0.7
0.8
0.9
0
10
20
30
40
50
60
70
80

Figure 7.6. Load-dependent changes in a hair bundle's degree of entrainment. (a) A hair bundle oscillated at all three load stiffnesses of 100 $\mu N \cdot m^{-1}$ (red), 167 $\mu N \cdot m^{-1}$ (yellow) and 250 $\mu N \cdot m^{-1}$ (blue) (*inset*). The vector strengths for all operating points increased with stimulus force during stimulation at 5 Hz (solid lines). When stimulated at 80 Hz, away from the frequency of spontaneous oscillation, the bundle was entrained poorly by the stimulus (dashed lines). (b) For a load stiffness of 250 $\mu N \cdot m^{-1}$ the bundle displayed a gradual decrease in the slope of the relation of vector strength to stimulus force as the frequency increased (5 Hz, 9 Hz, 21 Hz, and 80 Hz; dark to light). (c) For a stimulus force of 6 pN, the same bundle achieved maximum entrainment at 5 Hz for a load stiffness of 250 $\mu N \cdot m^{-1}$. (d-f) Heat maps depict the vector strength as a function of stimulus force and stimulus frequency for load stiffnesses of 100 $\mu N \cdot m^{-1}$ (d), 167 $\mu N \cdot m^{-1}$ (e), and 250 $\mu N \cdot m^{-1}$ (f). The error bars represent standard errors of the mean for three observations. The stiffness and damping coefficient of the stimulus fiber were respectively 425 $\mu N \cdot m^{-1}$ and 53 $nN \cdot s \cdot m^{-1}$.

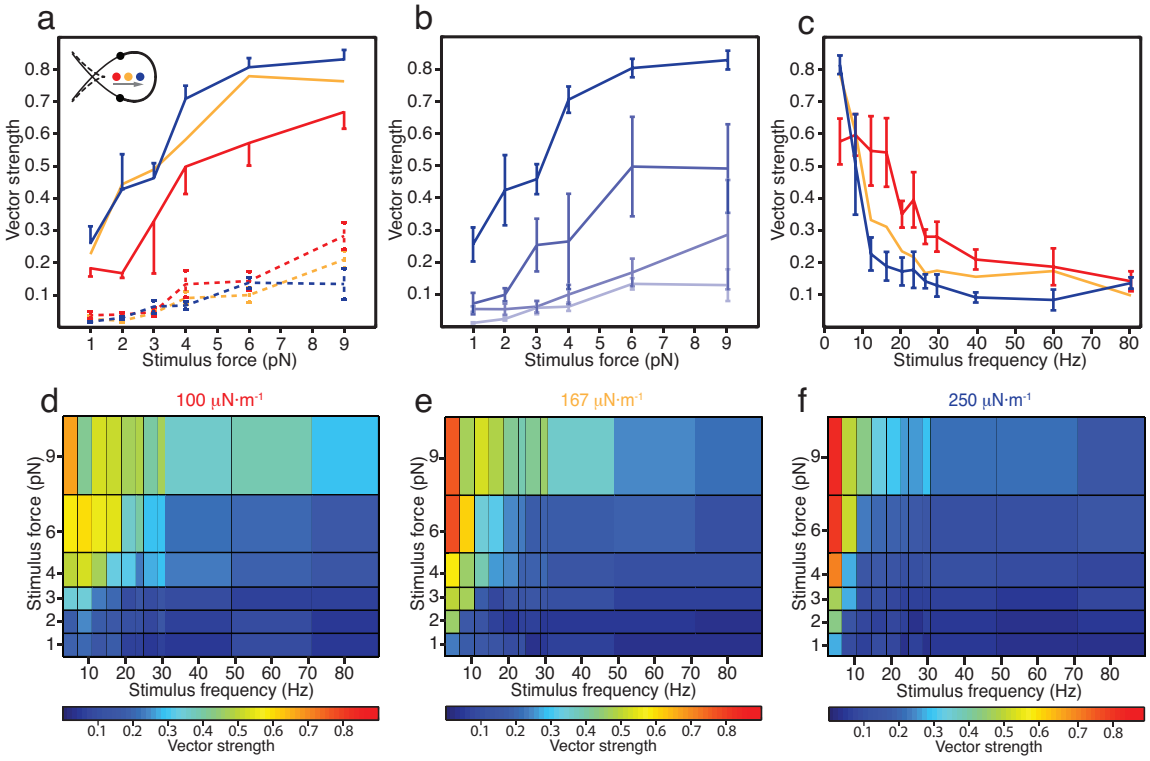
a
b
c
Vector strength
Stimulus force (pN)
Stimulus frequency (Hz)
d
e
f
100 μN·m⁻¹
167 μN·m⁻¹
250 μN·m⁻¹
Stimulus force (pN)
Stimulus frequency (Hz)
Vector strength

SECTION 7.4: *Sensitivity*

Auditory hair bundles are remarkable in their dynamic range. For example, bundles residing in the human cochlea can respond to incoming pressure signals ranging over 120 dB in amplitude (21, 34). This is possible because of nonlinearity in the bundle's response. Mechanical loads may control a bundle's dynamic range *in vivo* by adjusting the degree and range of nonlinearity. To assess the dependence of compressive nonlinearity on mechanical control parameters, we again delivered periodic stimuli to individual hair bundles and investigated the relationship between the magnitude of the stimulus and the sensitivity of the bundle's response.

A hair bundle's sensitivity—its phase-locked response divided by the magnitude of the stimulus force—decreases for forces of increasing amplitude (Figure 7.7a,e), consistent with previous investigations of hair-bundle sensitivity at a single operating point (129). This change in the sensitivity is greatest for spontaneously oscillating bundles and the sensitivity appears to become independent of the operating point for large forcing. The sensitivity is largest for operating points at which the hair bundle oscillates, although the bundle is most strongly entrained when it operates on the quiescent side of and near the border of spontaneous oscillation for forces of intermediate magnitude (Figure 7.7b,f). Unlike previous experimental and theoretical work that described a linear response for large-amplitude forcing (170), no such effect was found in the present work owing to an experimental limit on the maximal stimulus force possible.

To investigate hair-bundle behavior in the context of dynamical-systems theory, the responses of model hair bundles were simulated in the presence of noise. The model's response in both sensitivity and vector strength agreed with the experimental observations (Figure 7.7c,d). The model bundle achieves its broadest range of nonlinearity for operating points bordering a supercritical Hopf bifurcation, and its vector strength reaches a maximum for smaller stimulus amplitudes at these stiffnesses.

Taken together, a hair bundle's response to periodic stimuli depends on its mechanical load. By adjusting the load stiffness confronting a hair bundle so that it is poised near a supercritical Hopf bifurcation, it can achieve maximum amplification, frequency tuning, entrainment, and compressive nonlinearity.

Figure 7.7. Load-dependent mechanical sensitivity of hair bundles. (a) The behavior of a small hair bundle in the absence of stimulation was first classified for different operating points. The sensitivity is portrayed as a function of stimulus force at 5 Hz, near the bundle's frequency of spontaneous oscillation. (b) The vector strength of the bundle's motion with respect to that of the stimulus is displayed for the same operating points as in (a). (c) A simulated bundle's sensitivity is portrayed as a function of stimulus force for stimulus frequencies 10% greater than the frequency of spontaneous oscillation. The pattern resembled that shown in (a). The dashed line corresponds to a slope of -2/3. (d) The vector strength of the simulated bundle's motion is plotted against stimulus force. The bundle was best entrained at a stiffness of 341 for a range of intermediate to large forces. (e) Stimuli of increasing magnitudes were delivered at frequencies near those of spontaneous oscillations to another hair bundle poised near the edge of its oscillatory region. The bundle's load stiffness was decreased to coax its operating point farther into the oscillatory region. (f) For each operating point, entrainment to stimuli was quantified by vector strength. A value less than 0.2 (shaded area) corresponds to a region with poor phase locking as quantified by the Rayleigh test. The error bars for experiments represent standard errors of the means for four observations. For all experiments, the stiffness and damping coefficient of the stimulus fiber were respectively 425 $\mu N \cdot m^{-1}$ and 53 $nN \cdot s \cdot m^{-1}$. For the panels resulting from simulations, the stiffness, frequency, and force have been rescaled by a factor of 100 to facilitate comparison with the experimental data. Because the model was rescaled, no units are displayed for simulated results. The error bars are calculated from three stochastic simulations.

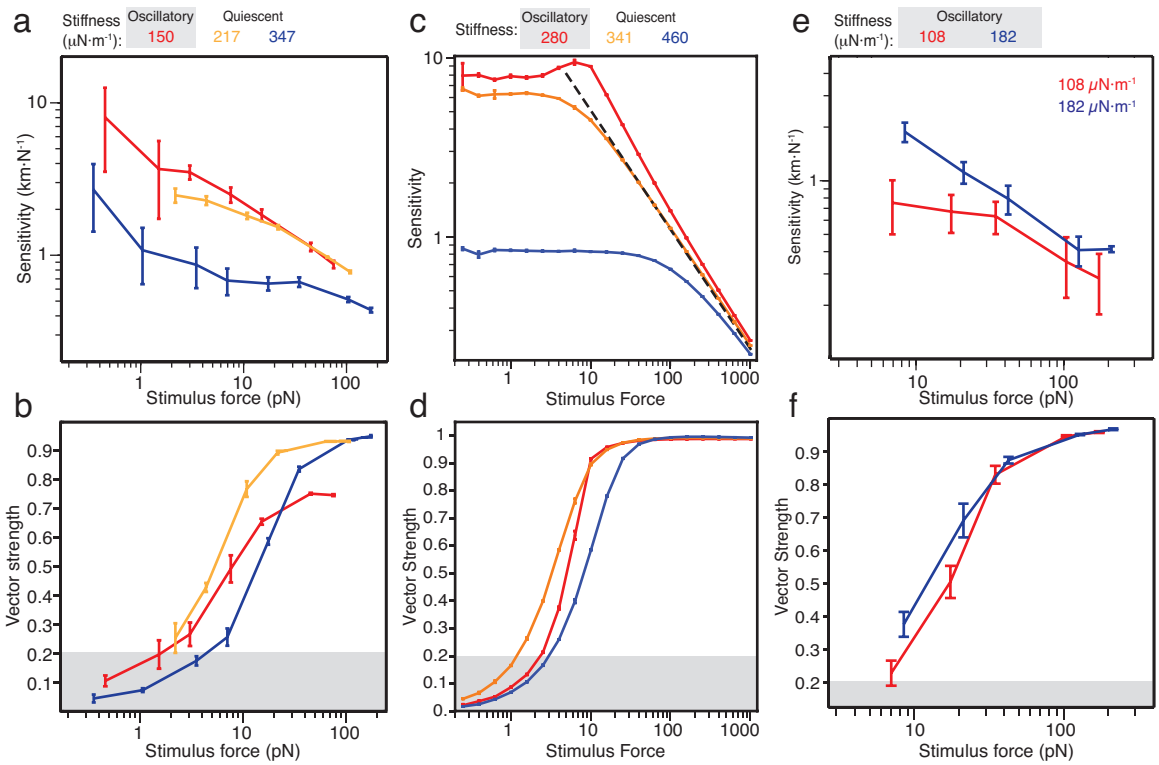
a
Stiffness (μN·m⁻¹):
Oscillatory
Quiescent
150
217
347
Sensitivity (km·N⁻¹)
Stimulus force (pN)
b
Vector strength
Stimulus force (pN)
c
Stiffness:
Oscillatory
Quiescent
280
341
460
Sensitivity
Stimulus Force
d
Vector Strength
Stimulus Force
e
Stiffness (μN·m⁻¹):
Oscillatory
108
182
108 μN·m⁻¹
182 μN·m⁻¹
Sensitivity (km·N⁻¹)
Stimulus force (pN)
f
Vector Strength
Stimulus force (pN)

SECTION 7.5: *Response to Force Pulses*

Hair bundles are often investigated *in vitro* with pulses of displacement or force (68, 114, 120, 196, 202) that additionally correspond to the stimulation of some vestibular organs *in vivo* (214). Because a bundle's response to such stimuli is expected to depend upon its load, we recorded responses to force pulses from hair bundles subjected to mechanical loads representing operating points within and outside their regions of spontaneous oscillation.

As the constant force applied to a bundle became more negative, hair-bundle oscillations decreased in frequency but not in amplitude until they ceased altogether (Figure 7.8a), in agreement with the results of previous studies that employed a low load stiffness (187). Positive force pulses delivered to a hair bundle subjected to successively more negative constant forces first induced oscillations and subsequently evoked twitches (128, 196), rapid movements that transiently exerted negative forces on the stimulus fiber (Figure 7.8a). A second bundle held with a constant negative force responded to a positive pulse by moving less than the stimulus fiber's base (Figure 7.8b). When the bundle was subjected to a still more negative constant force, however, the bundle's displacement in response to a pulse exceeded that of the stimulus fiber's base. During this movement, the force delivered to the hair bundle was negative in sign, implying that the hair bundle exerted a positive force on the fiber (Figure 7.8c). This phenomenon, which had previously been observed only once before for an outer hair cell's bundle in the rat's cochlea (114), demonstrates that amphibian vestibular hair

bundles can be induced to respond qualitatively like mammalian auditory bundles despite their different morphologies. The behavior arises from the nonlinear stiffness of a bundle owing to channel gating, a feature conserved in bundles across receptor organs.

Figure 7.8. Load-dependent responses to force pulses. (a) Movement of a stimulus fiber's base (black) subjected a large hair bundle under a load stiffness of 40 $\mu N \cdot m^{-1}$ to a force pulse. For constant forces of -15 pN and -20 pN, the bundle's response (red) to the pulse (blue) displayed an increase in the rate of spontaneous oscillation. For a constant force of -25 pN, the bundle responded to a positive force pulse with a twitch and a negative force transient of 1.2 pN that decayed with a time constant of 5 ms (inset). (b) When a large hair bundle was subjected to a load stiffness of 100 $\mu N \cdot m^{-1}$ and a constant force of -66 pN, a positive force pulse elicited a response (red) smaller than the displacement of the fiber's base (black). The force applied by the fiber during the pulse (blue) was therefore positive. (c) When the constant force was increased to -100 pN, a positive force pulse (black) elicited a response (red) exceeding the displacement of the fiber's base; the force applied by the fiber (blue) was accordingly negative. The stiffness and damping coefficient of the stimulus fiber were respectively 105 $\mu N \cdot m^{-1}$ and 71 $nN \cdot s \cdot m^{-1}$ (a) or 425 $\mu N \cdot m^{-1}$ and γ_{SF} 53 $nN \cdot s \cdot m^{-1}$ (b,c). The time traces have been downsampled by a factor of 100 for presentation purposes.

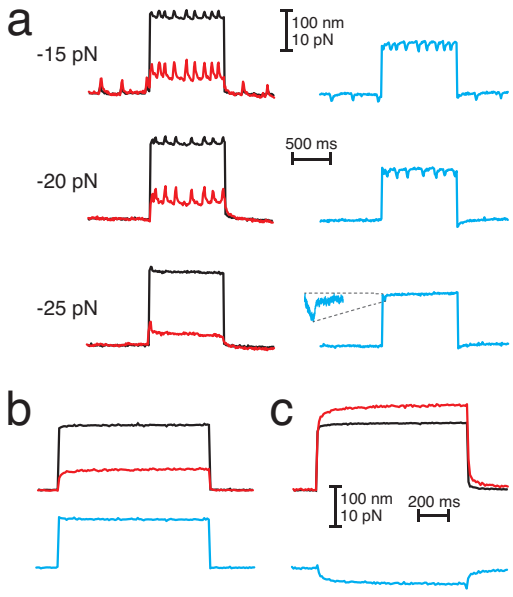
a
-15 pN
100 nm
10 pN
500 ms
-20 pN
-25 pN
b
c
100 nm
10 pN
200 ms

SECTION 7.6: *Discussion of Results*

A hair bundle's state diagram describes the function of a hair bundle for different sets of control parameters. Here the parameters of load stiffness and constant force imposed on an individual bundle control its sensory modality. While poised in the high-stiffness regime, a frog's hair bundle—like an auditory bundle—responds best to periodic stimuli. In the low-stiffness regime, a bundle—like a vestibular bundle—responds efficiently to force pulses. In other words, the hair bundle's state diagram is a map of sensory function, and this function depends on various mechanical loads.

The observations presented here are consistent with the hypothesis that the high-stiffness boundary of spontaneous oscillation constitutes a line of supercritical Hopf bifurcations. Both the tuning and degree of entrainment of a bundle are maximal near the bifurcation, and the frequency of spontaneous oscillations on one side matches the resonant frequency on the quiescent side. This feature is potentially useful for signaling in the auditory system (34).

Although the measured sharpness of tuning was less than that of afferent neurons in high-frequency regions of the mammalian cochlea (27), it largely accounts for frequency tuning in the amphibian auditory system (183). Moreover, the sharpness of tuning and the degree of nonlinearity found here represent lower estimates owing to the limited frequency resolution of the recordings. In agreement with theory, hair bundles situated at operating points distant from the oscillatory region lost their resonant character and behaved as low-pass filters.

Within a receptor organ, a hair bundle must counter viscous damping in order to minimize the loss of stimulus energy. These results indicate that the bundle accomplishes this task when poised near its boundary of spontaneous activity. Although all bundles may potentially exhibit this behavior, mechanical loading by accessory structures controls their ability to amplify external signals. It remains to be determined how a hair bundle *in vivo* finds operating conditions that foster optimal responsiveness (45, 195).

The results presented here demonstrate an essential similarity of hair bundles, whose responsiveness in various receptor organs is controlled by mechanical loading. Although previous studies used different stimulus fibers to investigate the effects of stiffness and constant force on different hair bundles (187, 212, 213), this approach revealed multiple mechanosensory modes in individual bundles. Depending upon its operating point, an individual bundle may twitch and oscillate like those in amphibian and reptilian receptor organs (196) or overshoot the stimulus like those in the mammalian cochlea (114). Although hair bundles in the mammalian cochlea detect frequencies extending two or three orders of magnitude greater than those detected by the bullfrog's sacculus, these results indicate that bundles from both organs rely on the same essential mechanisms. Adjustments to these mechanisms—the rate of adaptation and the degree of nonlinearity—regulate the speed and range of responsiveness. It is probable that the physical properties of hair bundles and their accessory structures have evolved to adjust the functions of different receptor organs within a range of organisms.

In contrast to a manufactured device that is designed to produce or respond to signals in a stereotypical fashion, a single hair bundle can function in various capacities. Here an individual hair bundle can behave like any of four different devices. A bundle may generate spontaneous oscillations like an oscillator that produces repetitive square or sine waves. It can resonate with high frequency resolution like a resonant circuit that responds to one frequency with greater amplitude than to any other. By attenuating high-frequency stimuli, a bundle may serve as a low-pass filter that attenuates signals above a cutoff frequency. Finally, by twitching at the onset of a pulse displacement, a bundle can mimic a step detector that identifies discontinuities in incoming signals. These observations for a particular sensory organelle reveal a general principle that may be utilized by both biological and artificial systems: a nonlinear system can be controlled to serve many different functions by adjusting only a few key parameters.

CHAPTER 8

Extended State-Diagram Mapping

In the previous chapters, we explored how a change to the constant force and load stiffness imposed on a hair bundle might adjust its mechanosensory behavior. In addition to these parameters, a hair bundle subjected to an inertial load and viscous damping exhibits further changes to its dynamics. Introducing a mass load to a bundle should expand the spontaneously oscillating regime of its state diagram, whereas increasing its viscous damping should shrink this region. Here we employ a four-parameter mechanical-load clamp to investigate the effects of the mass and drag coefficient on a hair bundle's behavior. These data accord with theory and reveal striking effects with variations in these control parameters.

SECTION 8.1: *Virtual Stiffness*

A four-parameter load clamp possesses the capacity to adjust a hair bundle's virtual mass, virtual drag coefficient, virtual stiffness, and an external force. Previous studies in this work employed a two-parameter clamp capable of adjusting only the load stiffness and constant force imposed on a bundle. Before any study comprising these virtual impedances can be pursued, the four-parameter clamp must successfully recapitulate the previous results by subjecting a virtual stiffness onto a hair bundle.

A large-diameter hair bundle spontaneously oscillated with high-amplitude, low-frequency relaxation oscillations in the absence of a stimulus fiber. Upon coupling a fiber, the bundle's frequency of oscillation increased. A mechanical-load clamp subsequently adjusted the fiber's virtual stiffness (Figure 8.1a). As the fiber's stiffness increased, the hair bundle's frequency of spontaneous oscillation rose and its amplitude decreased until its motion became sinusoidal at a stiffness of 900 $\mu N \cdot m^{-1}$. A reduction in virtual stiffness produced the opposite effect. At a virtual stiffness of -500 $\mu N \cdot m^{-1}$, the bundle resided most often at a positive displacement with a negative excursion every 700-800 ms (Figure 8.1a). Excursions at 1.2-1.4 Hz have not previously been described by other groups, in whose observed frequencies of oscillation typically achieved a minimum near 5 Hz (115).

Another small-diameter hair bundle oscillated spontaneously and was again subjected to changes in virtual stiffness (Figure 8.1b). As the virtual stiffness increased, the hair bundle's motion decreased in amplitude and increased in frequency until its oscillations were arrested around a stiffness of 500 $\mu N \cdot m^{-1}$. The bundle also exhibited

multimodal oscillations at virtual stiffnesses below 100 $\mu N \cdot m^{-1}$. Power spectra of the bundle's motion at each of these operating points capture this behavior (Figure 8.1c). At a virtual stiffness of -100 $\mu N \cdot m^{-1}$, the spectrum displayed peaks at 3.5 and 6.5 Hz. This result accords with previous observations of multimodal oscillations. As before, an increase in virtual stiffness caused a decrease in the total power of the bundle's motion.

Taken together, the four-parameter load clamp successfully controls the virtual stiffness applied to an active hair bundle in agreement with previous results that employed a two-parameter load clamp.

Figure 8.1. Hair-bundle motion with changes in virtual stiffness. (a) A spontaneously oscillating large-diameter hair bundle was subjected to virtual stiffnesses of -500 through 900 $\mu N \cdot m^{-1}$. As the stiffness increased, the bundle's oscillations increased in frequency and decreased in amplitude. At a virtual stiffness of -500 $\mu N \cdot m^{-1}$, the hair bundle resided mostly in the positive position with a downward excursion occurring approximately every 700 ms. (b) Imposing on a small-diameter hair bundle virtual stiffnesses ranging from -100 through 700 $\mu N \cdot m^{-1}$ revealed a similar pattern in amplitude and frequency. Virtual stiffnesses exceeding 500 $\mu N \cdot m^{-1}$ suppressed the hair bundle's oscillations. (c) A power spectral density for the same bundle in (b) discloses a decrease in the total power and an increase in the peak frequency with an increase in virtual stiffness. At -100 $\mu N \cdot m^{-1}$, the power spectrum exhibited two peaks, revealing the presence of multimodal oscillations. All power spectra were computed in MATLAB with Thomson's multitaper estimate of power spectral density with five discrete Slepian tapers. The total acquisition time was 30 s at a scan rate of 5 kHz. The stimulus fiber had a stiffness of 150 $\mu N \cdot m^{-1}$ and a drag of 100 $nN \cdot s \cdot m^{-1}$. In all panels, $m_V = \xi_V = F_C = 0$ and $G = 0.01$.

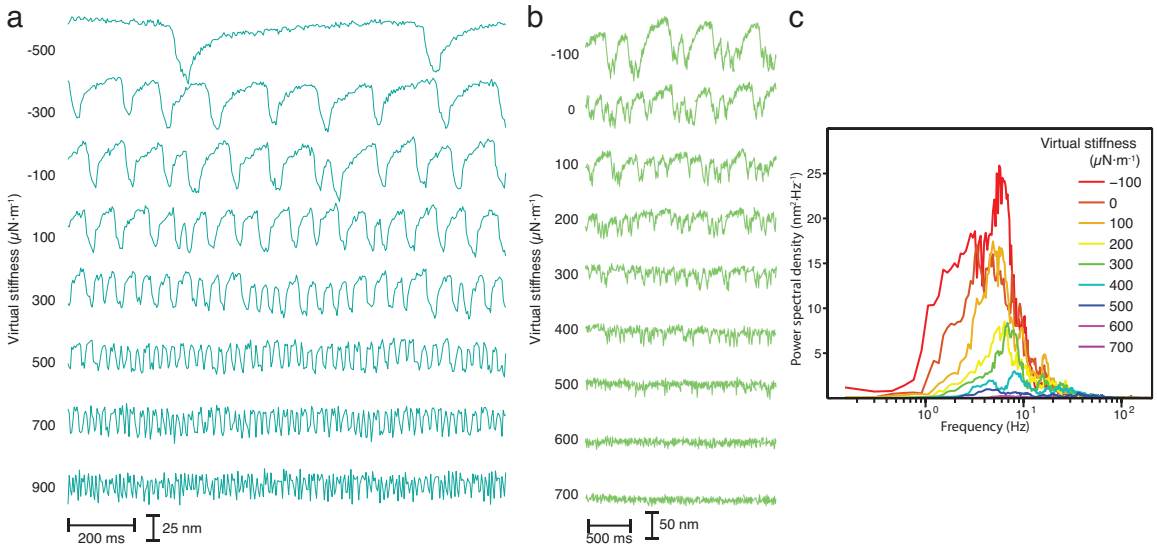
a
-500
-300
-100
100
300
500
700
900
Virtual stiffness (μN·m⁻¹)
200 ms
25 nm
b
-100
0
100
200
300
400
500
600
700
Virtual stiffness (μN·m⁻¹)
500 ms
50 nm
c
Virtual stiffness (μN·m⁻¹)
−100
0
100
200
300
400
500
600
700
Power spectral density (nm²·Hz⁻¹)
25
20
15
10
5
10⁰
10¹
10²
Frequency (Hz)

SECTION 8.2: *Virtual Drag*

Viscous damping dissipates stored energy. When forced, a passive, linear oscillator responds with reduced resonant quality as damping is increased. Active, nonlinear oscillators can in principle overcome the effects of frictional losses, and indeed hair bundles surmount viscous damping *in vivo* (163, 164, 183, 215, 216). If damping is too great, however, an auditory hair bundle cannot achieve its remarkable amplification and tuning characteristics. Indeed, an increase in a model hair bundle's drag coefficient reduces the magnitude of the bundle's response to periodic stimuli until the response approximates a low-pass filter (151, 159). Dynamical modeling predicts that the oscillatory region of a hair bundle's state diagram decreases in size with an increase in damping (167). The twitch in a hair bundle's step response also disappears when this friction becomes too great. Taken together, the extent of viscous damping controls a hair bundle's capacity to manifest active-process phenomena.

To assess the effects of damping on active hair-bundle motility, we used a mechanical-load clamp to subject multiple spontaneously oscillating bundles to different values of virtual drag. The motion of each hair bundle in the absence of external forcing revealed striking changes in bundle behavior with modifications to the bundle's total drag.

The load clamp imposed on a spontaneously oscillating hair bundle a series of virtual drags extending to 1,280 $nN \cdot s \cdot m^{-1}$ (Figure 8.2a). Power spectra of the bundle's motion at each operating point displayed a decrease in total power as virtual drag increased. Motion of another hair bundle subjected to both an increase and decrease in

drag disclosed similar results (Figure 8.2b). Increasing the bundle's total drag induced a decrease in the peak power of its motion. Decreasing the total drag by only 40 $nN \cdot s \cdot m^{-1}$ increased the peak in the bundle's power spectrum of motion by about 70%. These data indicate that a hair bundle's drag coefficient controls its spontaneous activity.

A dynamical model of hair-bundle mechanics predicts that viscous damping reduces in size the region of spontaneous oscillation (167). To assess how a hair bundle's state diagram changes under the influence of damping, combinations of virtual stiffness and virtual drag were imposed on individual bundles (Figure 8.3). An active hair bundle was delivered a range of virtual stiffnesses with and without virtual drag (Figure 8.3a). As the virtual stiffness increased, the peak power in the spectrum of bundle motion expectedly decreased in magnitude. When the bundle was loaded with a virtual drag coefficient of 600 $nN \cdot s \cdot m^{-1}$, the power decreased at all stiffnesses. Alternatively, a hair bundle subjected to a virtual drag coefficient of -1000 $nN \cdot s \cdot m^{-1}$ experienced an increase in the magnitude of its peak power for all values of virtual stiffness (Figure 8.3b). This result implies that the virtual drag coefficient regulates the extent of a hair bundle's locus of spontaneous activity. An increase in damping shrinks this region, and a decrease in damping expands it.

Figure 8.2. Hair-bundle motion with changes in virtual drag. (a) Increasing the virtual drag coefficient imposed on a spontaneously oscillating bundle from 0 to 1,280 $nN \cdot s \cdot m^{-1}$ decreased the peak in the bundle's power spectral density by approximately eightfold. (b) A second oscillating hair bundle was subjected to both positive and negative values of virtual drag coefficient. Increasing the bundle's drag coefficient from 0 to 80 $nN \cdot s \cdot m^{-1}$ decreased the peak in its power spectral density of its motion by approximately 30%, whereas decreasing its drag by 40 $nN \cdot s \cdot m^{-1}$ (red) increased the peak in power by about 70%. Both panels employed multitaper estimation of power-spectral density estimation with five discrete tapers. The total acquisition time was 30 s at a scan rate of 1 kHz. The stimulus fiber possessed a stiffness of 150 $\mu N \cdot m^{-1}$ and a drag coefficient of 100 $nN \cdot s \cdot m^{-1}$. In all panels, $m_V = K_V = F_C = 0$ and $G = 0.01$.

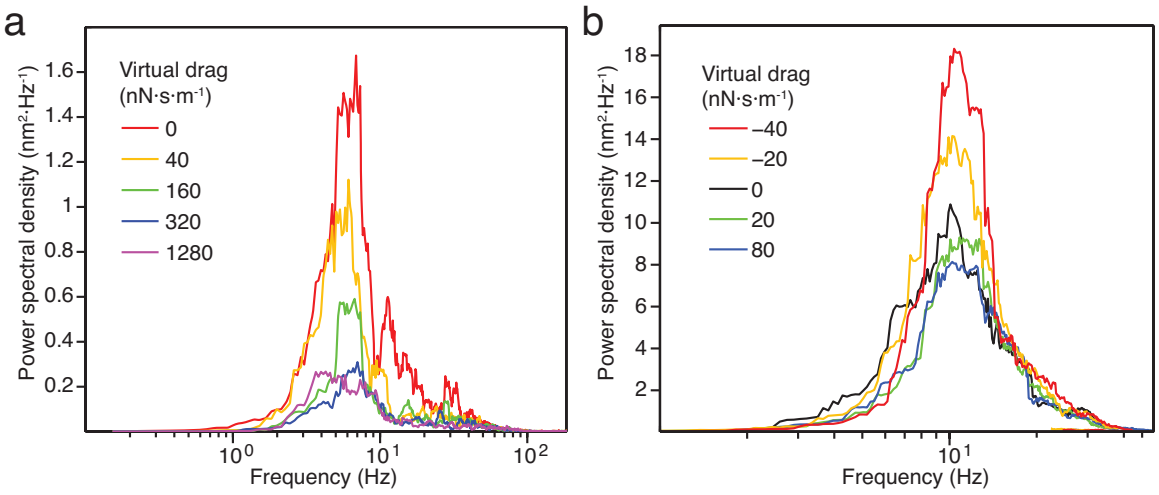
a
Power spectral density (nm²·Hz⁻¹)
1.6
1.4
1.2
1
0.8
0.6
0.4
0.2
Virtual drag
(nN·s·m⁻¹)
0
40
160
320
1280
10⁰
10¹
10²
Frequency (Hz)
b
Power spectral density (nm²·Hz⁻¹)
18
16
14
12
10
8
6
4
2
Virtual drag
(nN·s·m⁻¹)
–40
–20
0
20
80
10¹
Frequency (Hz)

Figure 8.3. Effects of virtual drag on hair-bundle motion with changes in virtual stiffness. (a) To assess the effects of virtual drag on the spontaneous motion of a hair bundle at different operating points, an oscillating bundle was subjected to three virtual stiffnesses and a virtual drag coefficient of 0 or 600 nN·s·m^{-1}. An increase in virtual stiffness expectedly decreased the total power of the bundle's motion (solid lines). Poising the hair bundle's operating point at the same three virtual stiffnesses and imposing a virtual drag coefficient of 600 nN·s·m^{-1} caused a further decrease in power at all operating points (dashed lines). (b) The load clamp subjected a second hair bundle to three virtual stiffnesses and a virtual drag coefficient of 0 or -1000 nN·s·m^{-1}. As before, increasing the stiffnesses caused a decrease in the total power spectral density of the motion of the bundle (solid lines). However, decreasing the bundle's drag coefficient by 1000 nN·s·m^{-1} caused the peak in its power spectral density to increase at a virtual stiffness of -300 μN·m^{-1}. No such effect was seen at higher stiffnesses. In both panels, the multitaper estimate of power spectral density was employed in MATLAB with five Slepian tapers over a total acquisition time of 30 s and a scan rate of 1 kHz. The fiber's stiffness and drag were respectively 150 μN·m^{-1} and 100 nN·s·m^{-1}. In all panels, m_V = F_C = 0 and G = 0.01.

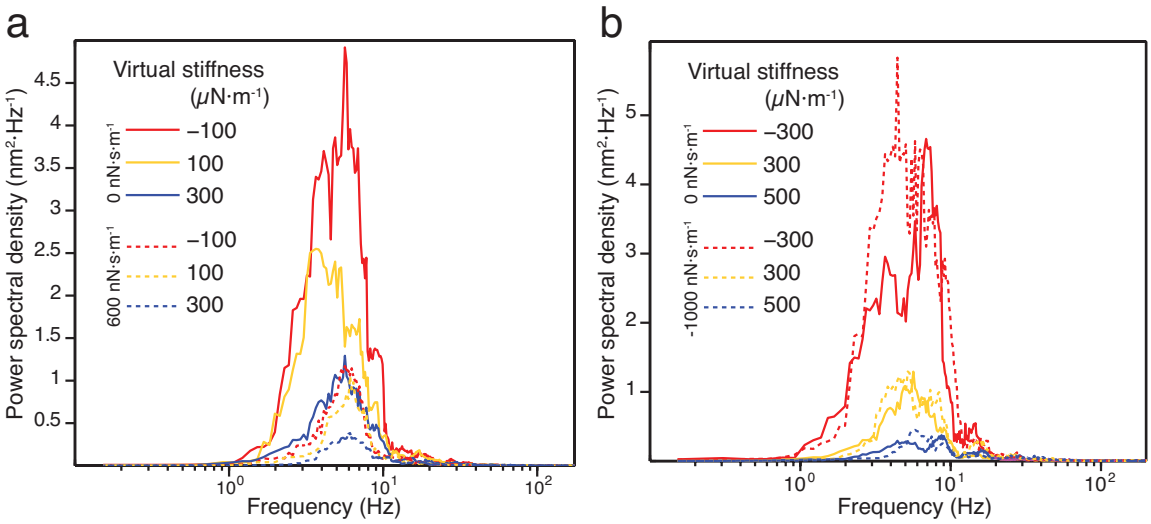
a
Virtual stiffness
(μN·m-1)
0 nN·s·m-1
–100
100
300
600 nN·s·m-1
–100
100
300
Power spectral density (nm2·Hz-1)
4.5
4
3.5
3
2.5
2
1.5
1
0.5
10^0
10^1
10^2
Frequency (Hz)
b
Virtual stiffness
(μN·m-1)
0 nN·s·m-1
–300
300
500
-1000 nN·s·m-1
–300
300
500
Power spectral density (nm2·Hz-1)
5
4
3
2
1
10^0
10^1
10^2
Frequency (Hz)

SECTION 8.3: *Virtual Mass*

In addition to the stiffness, drag, and constant force experienced by a hair bundle, many bundles are coupled *in vivo* to an inertial load. For example, outer hair cell bundles of the mammalian cochlea project into a tectorial membrane that varies in mass from 35 through 100 ng per 10 μm section (17). Alternatively, a mass of calcium carbonate crystals loads hair bundles residing in otolith organs. For example, the bullfrog's sacculus possesses an otolithic mass of about 5 mg (unpublished observations). These differences may confer unique tuning characteristics on bundles in different organs and across vertebrates.

Dynamical modeling predicts that a hair bundle's active-process phenomena are enhanced by mass loading (167). An increase in a bundle's total mass precipitates an inflation of the spontaneously oscillatory regime, an increase in both the magnitude and quality of resonance, and ringing in the bundle's step response for certain sets of control parameters. These effects might assist a hair bundle in tuning its organ-specific behavior of an otherwise dissipative situation.

To assess the effects of mass loading on a hair bundle's state diagram, we used the mechanical-load clamp to deliver a range of virtual masses to an individual hair bundle (Figure 8.4). In the absence of virtual mass, the hair bundle oscillated with poor resonant quality and a peak in its power spectrum of motion of only 0.5 $nm^2 \cdot Hz^{-1}$. An increase of the virtual mass to 24 ng more than doubled the quality of resonance and increased the peak magnitude in the power spectrum of the bundle's spontaneous

motion by fivefold. These effects support the hypothesis that a hair bundle coupled to a mass load possesses a state diagram with an expanded oscillatory regime.

The combined effects of virtual mass and virtual stiffness reveal changes in a hair bundle's state diagram (Figure 8.5). Increasing the virtual stiffness expectedly induced a decrease in the total power of the bundle's spontaneous oscillations. When a virtual mass of 1 μg was added to the bundle, the magnitude of the peak in its power spectrum of motion increased at all values of virtual stiffness (Figure 8.5a). On the other hand, decreasing another bundle's virtual mass by 3 μg elicited a corresponding decrease in the peak's height (Figure 8.5b). These data imply that a hair bundle's state diagram possesses an oscillatory regime that is sensitive to mass loading. Boosting the mass expands this region, and reducing the mass contracts it.

Figure 8.4. Hair-bundle motion with changes in virtual mass. A spontaneously oscillating hair bundle was subjected to increasing virtual mass and its motion recorded. Increasing the mass from 0 to 24 ng elicited an increase in the magnitude of the peak in the power spectrum of the bundle's motion by approximately fivefold. The spectrum's quality correspondingly more than doubled. To compute the power spectral density, Thomson's multitaper method was employed with five Slepian tapers for an acquisition time of 30 s and a scan rate of 500 Hz. The stimulus fiber had a stiffness of 150 $\mu N \cdot m^{-1}$ and a drag of 100 $nN \cdot s \cdot m^{-1}$. Load clamp parameters included $\xi_V = K_V = F_C = 0$ and $G = 0.01$.

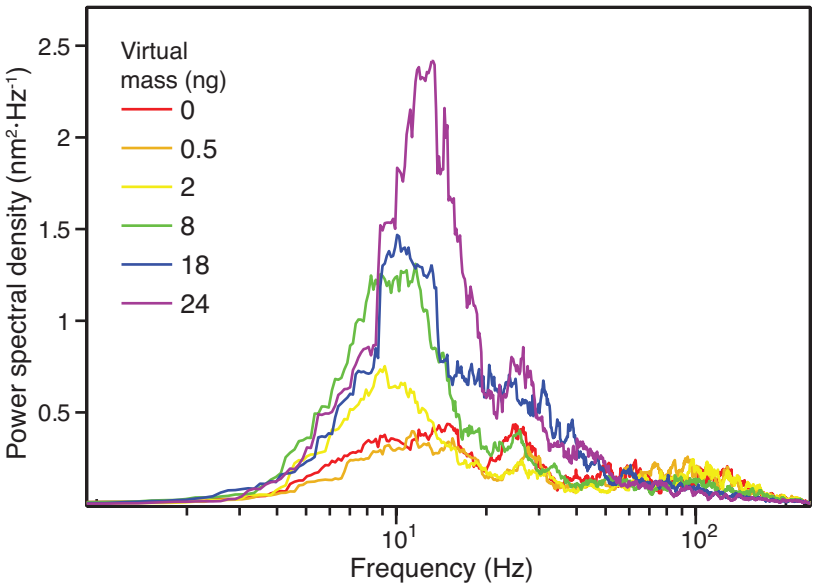
Virtual
mass (ng)
0
0.5
2
8
18
24
Power spectral density (nm²·Hz⁻¹)
2.5
2
1.5
1
0.5
10¹
10²
Frequency (Hz)

Figure 8.5. Effects of virtual mass on hair-bundle motion with changes in virtual stiffness. (a) A spontaneously oscillating hair bundle was subjected to two virtual stiffnesses and two virtual masses and its motion tracked over time. Increasing the bundle's stiffness elicited a decrease in the magnitude of the peak in the power spectral density of the motion of the bundle. When the bundle was loaded with a virtual mass of 1 μg, the peak increased in height at both virtual stiffnesses. (b) Imposing on a second active hair bundle two virtual stiffnesses with a virtual mass of either 0 or -3 μg revealed a decrease in the power of the bundle's motion associated with a decrease in virtual mass at each virtual stiffness. Thomson's multitaper method was employed to compute each power spectral density using five Slepian tapers over an acquisition time of 30 s and a scan rate of 500 Hz. The fiber's stiffness and drag coefficient were respectively 150 $\mu N \cdot m^{-1}$ and 100 $nN \cdot s \cdot m^{-1}$. Load clamp parameters included $\xi_V = F_C = 0$ and $G = 0.01$.

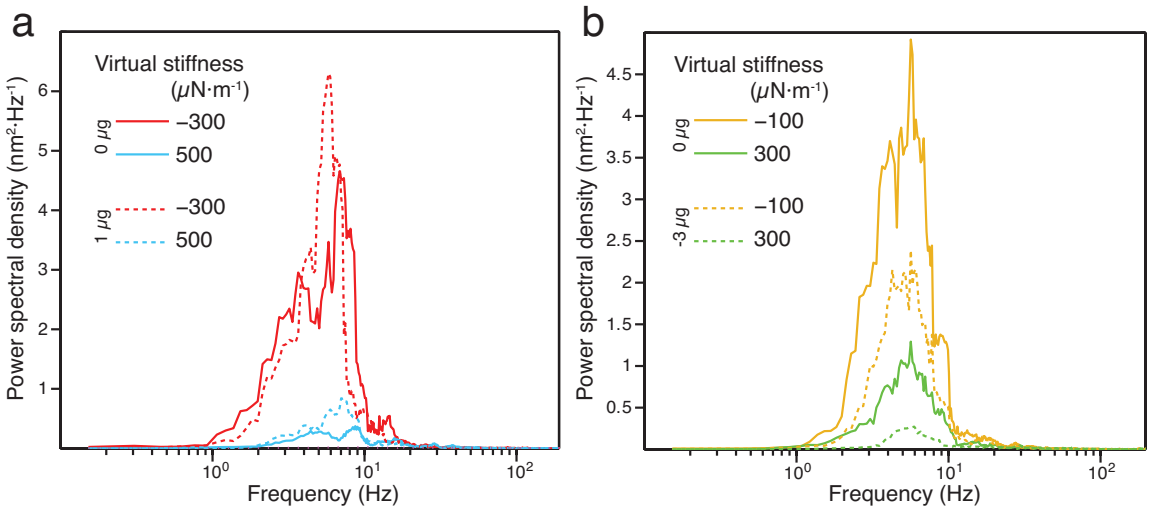
a
Virtual stiffness
(μN·m-1)
0 μg
−300
500
1 μg
−300
500
Power spectral density (nm2·Hz-1)
Frequency (Hz)
b
Virtual stiffness
(μN·m-1)
0 μg
−100
300
-3 μg
−100
300
Power spectral density (nm2·Hz-1)
Frequency (Hz)

SECTION 8.4: *Discussion of Results*

Hair bundles within a given sensory organ encounter myriad mechanical loads. Otolithic and tectorial membranes impose stiffnesses and offset forces on bundles. Membranes and otoconia impose inertial loads. Fluid, cupulae, and other structures impose viscous drag. The combination of a hair bundle's intrinsic properties and those of its microenvironment modulate the bundle's behavioral response. Combining the delivery of three virtual impedances and an external force reveals the relative effects of these parameters.

The four-parameter load clamp successfully recapitulates results from the two-parameter load clamp employed in previous chapters. Virtual stiffness is positively correlated with the frequency and negatively correlated with the amplitude of oscillation. Additionally, the extended clamp permits exploration of stiffness values previously limited by clamp stability. At the low-stiffness extremum, a hair bundle may oscillate with a frequency smaller than the minimum reported in the literature or may exhibit multimodal oscillations.

Both the mass and drag coefficient imposed on a hair bundle should regulate the size of the bundle's oscillatory regime in its state diagram. Preliminary evidence illustrates these striking effects. Changes in virtual mass and virtual drag coefficient are respectively positively and negatively correlated with the extent of the oscillatory regime. This behavior manifests itself in the magnitude and quality from the bundle's power spectrum of motion.

It remains to be seen how an inertial load and viscous drag coefficient control a bundle's response to both periodic stimuli and force pulses. The present evidence suggests that these behaviors should accord with theory, and future work will rigorously explore this parameter space.

CHAPTER 9

Self-Tuned Criticality

A hair bundle's sensory behavior depends on its operating point. Near a supercritical Hopf bifurcation, the bundle achieves optimal responsiveness to periodic stimuli. A subtle change in as little as one control parameter impairs the bundle's sensitivity, frequency selectivity, and dynamic range. For example, a small change in load stiffness annihilates the resonant peak in the response to periodic stimuli, transforming the hair bundle into a low-pass filter. Because of this, the sensitivity of a hair bundle might easily deteriorate with changes to any control parameter *in vivo*. Such a system requires robust maintenance of mechanical loads, endocochlear potentials, and relative ionic concentrations. In reality, however, these parameters are sensitive to biological noise. Given that an auditory hair bundle must remain poised near a Hopf bifurcation to ensure robust responsiveness, is there an additional mechanism to guarantee proximity to the bifurcation?

A hair bundle might employ a mechanism of self-tuned criticality, in which it self-regulates one or more control parameters to ensure a critical position of its operating point. When the bundle's operating point departs from the bifurcation, the bundle coerces its operating point back to criticality. How might this response come about? One proposed mechanism of self-tuned criticality employs regulation of the intracellular Ca^{2+} concentration, which controls the magnitude of force generation by molecular motors (45). The motors in question are myosin molecules bound to stereociliary actin and

dynein coupled to kinociliary microtubules. Transduction channels detect the forces generated by these motors and allow Ca^{2+} into the cell. In this model, Ca^{2+} in turn regulates motor activity and its concentration C serves as a control parameter. When C exceeds a critical concentration C_C the bundle remains quiescent, whereas the bundle oscillates when $C < C_C$. Assuming that the regulation of Ca^{2+} occurs on a timescale slower than that of spontaneous oscillations, the oscillatory amplitude is roughly proportional to C-C_C. Thus, a hair bundle might sense the location of its operating point by detecting the amplitude of spontaneous oscillation through a change in C. A feedback mechanism subsequently adjusts C so that it approaches C_C

$$\dot{C} = \frac{C}{\tau}\left(\frac{X^2}{\delta^2} - 1\right), \tag{9.1}$$

in which X is the bundle's position, δ is the amplitude of spontaneous oscillation near the bifurcation, and τ is the relaxation time of tuning. When the oscillatory amplitude exceeds δ, C increases. When the bundle's amplitude of motion is less than δ, C decreases (45). The behavior described by equation 9.1 thus ensures that the hair bundle's operating point is poised near a supercritical Hopf bifurcation.

The above model describes a pattern of self-tuning, but it does not capture a complete biological mechanism. For example, what defines δ? How might C change with bundle deflection? How might one dissect this model experimentally? Here we explore one possible Ca^{2+}-based mechanism that possesses two requirements. First, Ca^{2+} must control the amplitude and frequency of hair-bundle oscillations. Second, the concentration of Ca^{2+} must rely both on this motion and on some regulatory element.

These requirements generate a feedback loop between Ca^{2+} and spontaneous oscillations that controls a hair bundle's operating point to poise it within a critical locus.

In agreement with the first constraint, Ca^{2+} governs the amplitude and frequency of spontaneous hair-bundle oscillations (115, 196). An increase in the endolymphatic Ca^{2+} concentration induces a decrease in the amplitude and increase in the frequency of oscillation, whereas a decrease in Ca^{2+} concentration yields the opposite effect. This phenomenon may arise from the regulation of adaptation motors by Ca^{2+}, in which Ca^{2+} precipitates a decrease in the total force produced by adaptation motor complexes (170). Because the motor's stall force declines, the bundle's amplitude is constrained to smaller deflections and the tip-link tension reaches the stall force more rapidly. The result is a corresponding change in both the amplitude and the frequency of spontaneous oscillation akin to that imposed by an increase in the load stiffness on a hair bundle from within the unstable regime.

In agreement with the second requirement, a bundle's deflection regulates the intracellular Ca^{2+} concentration. The resting concentration reflects a balance between inward Ca^{2+} flux through transduction channels and outward Ca^{2+} flux through plasma membrane Ca^{2+}-ATPase (PMCA) pumps (217). When a bundle is deflected in the positive direction, the flux through transduction channels increases and the intracellular Ca^{2+} concentration rises. Deflection in the negative direction reduces the intracellular Ca^{2+} concentration. If this process were instantaneous, hair-bundle motion in the positive and negative directions would cause no change in the expected value of Ca^{2+} within a bundle. However, another mechanism that integrates Ca^{2+} might be in play.

The Ca^{2+} concentration might display a mechanism of self-regulation. Upon entering a cell, Ca^{2+} associates with calmodulin. This in turn activates the enzyme adenylate cyclase, which converts ATP to cAMP. cAMP then activates multiple kinases including protein kinases A and C (PKA and PKC). Numerous studies reveal that cAMP-dependent protein kinases control both the maximal velocity and Ca^{2+} affinity of PMCA channels (218-221). This signaling cascade integrates Ca^{2+} concentration over a timescale exceeding that of Ca^{2+} fluctuations, and a net increase in the integral of Ca^{2+} causes a corresponding increase in Ca^{2+} extrusion by PMCA. Intracellular Ca^{2+} therefore regulates itself: an increased concentration generates heightened Ca^{2+} efflux that subsequently diminishes the Ca^{2+} levels.

Biophysical dissection of cAMP-dependent effects on hair-bundle activity supports this hypothesis (135). Bathing a bullfrog's saccular hair bundles in forskolin, an activator of adenylate cyclase, reduces the frequency of spontaneous oscillation. 3-Isobutyl 1-methylxanthine, an inhibitor of cAMP phosphodiesterase, produces the same effect. Sp-adenosine 3',5'-cyclic monophosphorothioate and 8-bromo-cAMP, analogs of cAMP that activate the same protein kinases, also reduce the oscillatory frequency. Okadaic acid, a protein phosphatase inhibitor, yields similar results. Finally, Rp-adenosine 3',5'-cyclic monophosphorothioate, an inhibitor of cAMP-dependent protein kinases, increases the frequency of spontantaneous oscillation. Because cAMP-dependent protein kinases increase Ca^{2+} efflux through PMCA pumps, the activation of this pathway reduces the intracellular Ca^{2+} concentration, whereas inhibition of the pathway increases the concentration. A change in Ca^{2+} concentration then modulates the

force produced by adaptation motors to produce the expected transformations in oscillatory behavior.

The constant force, load stiffness, viscous damping, and inertial load to which a hair bundle is subjected poise its operating point near a critical locus. Subtle changes in the bundle's microenvironment that would otherwise degrade its sensory responsiveness can be surmounted by self-tuning, which is limited to a narrow region in parameter space by the maximal and minimal Ca^{2+} fluxes into and out of the cell. Mechanical control parameters and a self-tuning mechanism thus work in concert to assure optimal audition.

How might one model a mechanism of self-tuned criticality? Based on the aforementioned mechanism, the model experiences at least three constraints. First, a self-tuning mechanism must sense the amplitude of spontaneous oscillation. This can be achieved by requiring that the self-tuning parameter be sensitive to the open probability of transduction channels. Second, self-tuned criticality must employ an integrator. The model must therefore incorporate a long relaxation time for this tuning parameter. Finally, the parameter must control the hair bundle's oscillatory behavior. Changes in the self-tuning parameter might directly control the bundle's operating point through adjustment of one or more control parameters, or they might influence another property such as the force of adaptation. To generate such a model, the identity of the affected parameters and how these processes work in concert must first be determined through micromechanical and pharmacological manipulation of hair-bundle behavior.

Intracellular Ca^{2+} may serve as the self-tuning parameter. The aforementioned description of self-tuned criticality introduces two effects of Ca^{2+} within a hair bundle. First, Ca^{2+} entry reduces the amplitude and increases the frequency of spontaneous oscillation. Second, a rise in the intracellular Ca^{2+} concentration potentiates Ca^{2+} efflux through PMCA pumps. Although both mechanisms work in concert to control a hair bundle's behavior, each can be studied independently.

Which parameters might Ca^{2+} regulate to modify a bundle's oscillatory behavior? Ca^{2+} could directly manipulate the control parameters of stiffness, damping coefficient, or constant force. Alternatively, Ca^{2+} influx might adjust only the force of adaptation and have no effect on these control parameters. By investigating each of these effects independently, one may realize a model of self-tuned criticality.

Because an increase in Ca^{2+} concentration induces a decrease in the amplitude and an increase in the frequency of spontaneous oscillation, an obvious choice for a parameter sensitive to ionic changes is the bundle's stiffness. To assess whether Ca^{2+} controls hair-bundle stiffness, one can iontophorese Ca^{2+} to raise its local concentration near a hair bundle and subsequently measure the bundle's stiffness with a flexible glass fiber. Delivery of force pulses should reveal any changes in hair-bundle stiffness. If an effect on stiffness exists, a load clamp can subject a bundle to different values of virtual stiffness. Changes in the bundle's oscillatory behavior at each operating point can then be compared with the behavior resulting from Ca^{2+}-dependent changes in bundle stiffness. This experiment not only serves to assess whether Ca^{2+} tunes the bundle by adjusting the stiffness parameter but also quantifies the magnitude of this effect.

The Ca^{2+} concentration might instead control the hair bundle's drag coefficient. To investigate this experimentally, a similar paradigm can be employed. As before, iontophoresis controls the local Ca^{2+} conentration and a glass fiber delivers forces. Here the stimuli are triangular waveforms of constant velocity that permit calculation of hair-bundle friction (222). By noting the effects of the Ca^{2+} concentration on bundle friction and comparing bundle oscillations with changes in virtual drag, any influence of Ca^{2+} on this control parameter can be quantified.

Similar techniques can be applied to the constant force applied to a hair bundle. Upon Ca^{2+} iontophoresis, any change in the offset force of the bundle can be measured with a glass fiber. Hair-bundle behavior under the influence of an external force from a load clamp can then be compared with the behavior resulting from a change in Ca^{2+} concentration. Together, manipulation of the Ca^{2+} concentration and corresponding modifications to the stiffness, drag coefficient, and constant force of the bundle can reveal the effects of this self-tuning parameter on the hair bundle's operating point.

However, Ca^{2+} might not adjust the sensory bundle's mechanical load and Ca^{2+} might control only the force of adaptation. To assess this effect, one can manipulate the strength of Ca^{2+} feedback on the force generated by adaptation motors (170). Ca^{2+} is hypothesized to control this force through regulation of myosin-1c attachment to actin filaments (211). An elevated Ca^{2+} concentration induces dissociation of calmodulin from myosin's IQ domains. This permits the IQ1 lipid-binding site to associate with phosphatidylinositol 4,5-bisphosphate (PIP_2), freeing myosin from the cytoskeleton and reducing the total adaptive force. Indeed, inhibition of PIP_2 synthesis with phenylarsine

oxide (PAO) or quercetin reduces the rate of slow adaptation (211). This proposed mechanism would allow Ca^{2+} to control hair-bundle oscillations without the need to adjust the mechanical control parameters.

Preliminary evidence supports the hypothesis that Ca^{2+} regulates the force of adaptation (Figure 9.1). Bathing an oscillating hair bundle in 200 μM PAO caused the bundle's oscillations to decrease in frequency until the bundle was rendered quiescent over the course of six minutes (Figure 9.1a,b). This behavior is consistent with the time course of PAO-dependent inhibition of slow adaptation in the frog's saccular hair cells (211). In the presence of 200 μM PAO, the current response decayed by about 90% over 5.5 min with a corresponding increase in the time constant of slow adaptation. Because PAO inhibits PIP_2 synthesis, this behavior likely reflects an inhibition of Ca^{2+} feedback on the force of adaptation (211).

In addition to affecting the activity of myosin motors, Ca^{2+} could alter a hair bundle's stiffness. However, the bundle's stiffness exhibited no change in the presence of PAO (Figure 9.1c). These data imply that Ca^{2+} controls a hair bundle's spontaneous activity through regulation of the adaptive force alone.

In addition to a mechanism of behavioral control by Ca^{2+}, self-tuned criticality requires a homeostatic mechanism. As mentioned before, an obvious candidate is the Ca^{2+}-dependent potentiation of Ca^{2+} efflux, in which a cAMP-dependent kinase phosphorylates PMCA pumps to increase their activity. Previous work reveals that activation of this pathway reduces the frequency of spontaneous oscillation, and inhibition yields the opposite effect (124). However, cAMP-dependent kinases could also

change a hair bundle's stiffness. To evaluate this possibility, active hair bundles were bathed in the calcineurin inhibitor tacrolimus (FK506) (223). Because calcineurin dephosphorylates target proteins, inhibition of calcineurin by FK506 should promote the phosphorylated state of PMCA and thus increase Ca^{2+} efflux. Application of FK506 to an oscillating hair bundle caused a dose-dependent decrease in the frequency of oscillation (Figure 9.2a,b). These data accord with the hypothesis that cAMP-dependent phosphorylation potentiates Ca^{2+} efflux. Additionally, the bundle exhibited no change in its stiffness (Figure 9.2c). This implies that the effects of this homeostatic pathway do not affect additional mechanical control parameters.

Figure 9.1. Effects of PAO on hair-bundle dynamics. (a) A hair bundle oscillated spontaneously in the presence of artificial endolymph and its frequency of oscillation nearly doubled upon the addition of 0.5% DMSO. When 200 μM PAO was added in addition to 0.5% DMSO, the bundle's oscillations steadily decreased in frequency until the bundle was rendered quiescent over the course of six minutes. (b) Quantification of the bundle's frequency of oscillation reveals an increase in frequency with 0.5% DMSO (*D*) and a steady decrease in frequency in the presence of PAO from one (P_1) to six (P_6) minutes. (c) The displacement-force relation discloses no change in the bundle's linear stiffness when bathed in endolymph prior to the start of the experiment (black) or after eight minutes of PAO exposure (blue). The hair bundle's frequency of oscillation was calculated over the course of 30 s in panel (b). Each point in the force-displacement relation in panel (c) represents the mean of 20 time averages over the course of 20 ms both 30 ms prior to and 30 ms after the onset of a force pulse.

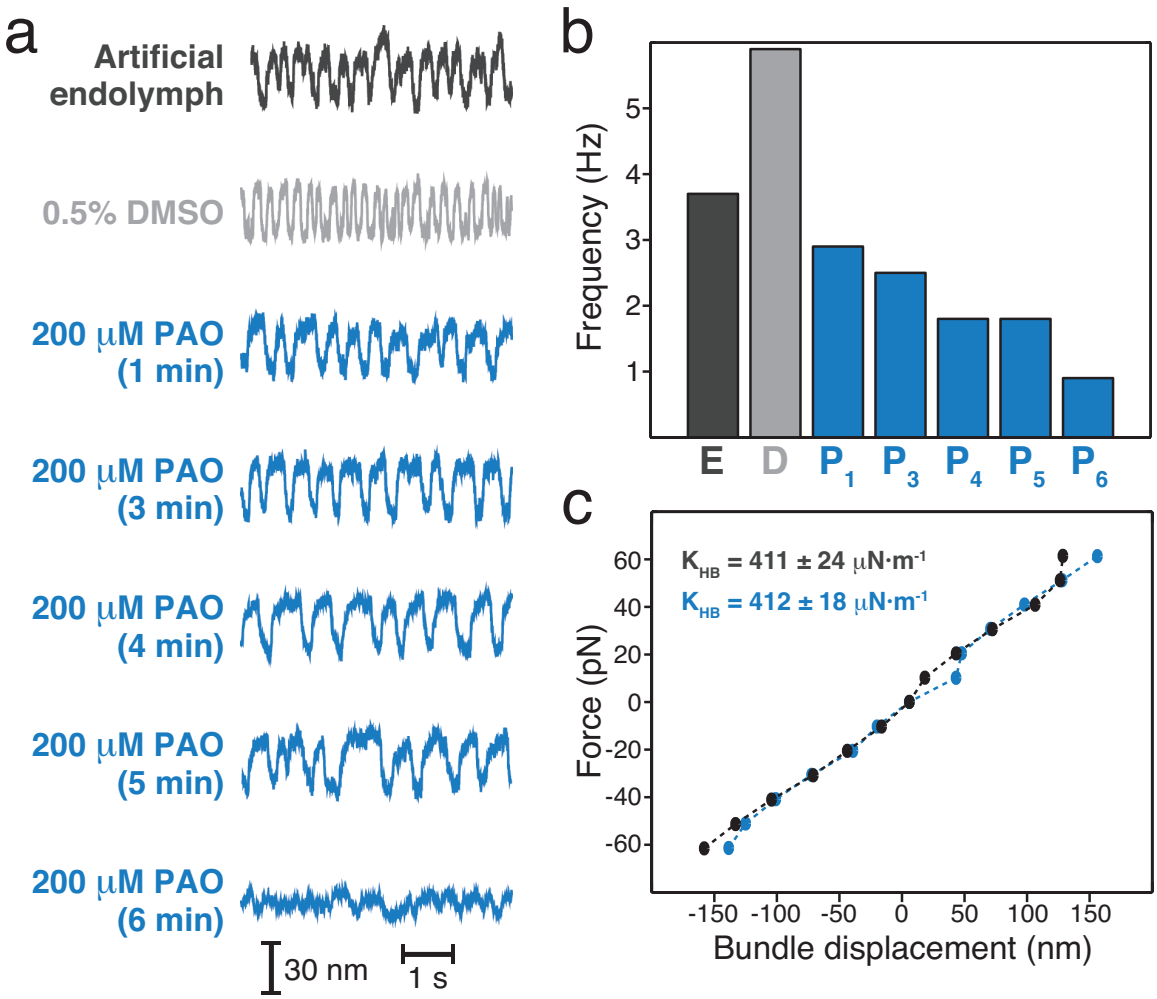
a
Artificial endolymph
0.5% DMSO
200 μM PAO (1 min)
200 μM PAO (3 min)
200 μM PAO (4 min)
200 μM PAO (5 min)
200 μM PAO (6 min)
30 nm
1 s
b
Frequency (Hz)
1
2
3
4
5
E
D
P1
P3
P4
P5
P6
c
KHB = 411 ± 24 μN·m-1
KHB = 412 ± 18 μN·m-1
Force (pN)
60
40
20
0
-20
-40
-60
-150
-100
-50
0
50
100
150
Bundle displacement (nm)

Figure 9.2. Effects of FK506 on hair-bundle dynamics. (a) A hair bundle oscillated spontaneously when bathed in artificial endolymph and its frequency of oscillation increased upon the addition of 0.5% DMSO. The addition of either 15 μM or 50 μM FK506 caused the bundle's oscillations to decrease in frequency. (b) Quantification of hair-bundle oscillations in artificial endolymph (*E*), 0.5% DMSO (*D*), and two examples with FK506 at a concentration of either 15 μM (F_{15}) or 50 μM (F_{50}) revealed a dose-dependent decrease in the bundle's frequency of oscillation. (c) A force-displacement relation for the bundle bathed in endolymph (black) and 50 μM FK506 (yellow) reveals no change in the treated bundle's linear stiffness. In panel (b), the hair bundle's frequency of oscillation was calculated over the course of 30 s. In panel (c), each point in the force-displacement relation represents the mean of 20 time averages over the course of 20 ms both 30 ms prior to and 30 ms after the onset of a force pulse. Paired Student's t-tests were performed in panel (b) over 10 averages (* $p < 0.05$, ** $p < 0.01$, *** $p < 0.001$; black: *vs. E*, orange: *vs.* F_{15}).

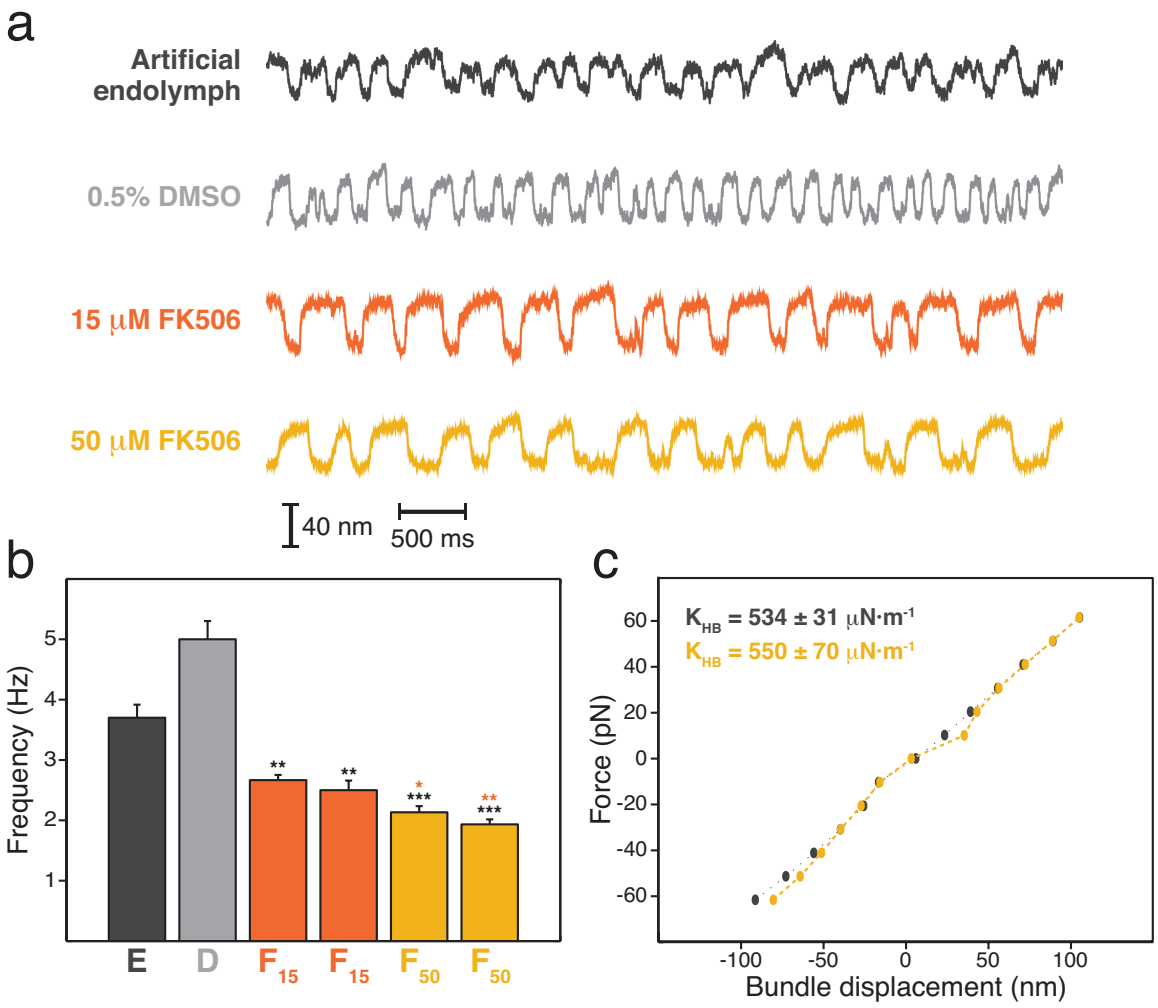
a
Artificial endolymph
0.5% DMSO
15 μM FK506
50 μM FK506
40 nm
500 ms
b
Frequency (Hz)
E
D
F15
F15
F50
F50
c
KHB = 534 ± 31 μN·m-1
KHB = 550 ± 70 μN·m-1
Force (pN)
Bundle displacement (nm)

Although additional data must confirm this hypothesis, a probable mechanism of self-tuning incorporates Ca^{2+}-dependent changes in both the force of adaptation and the rate of Ca^{2+} efflux. Although a generalized dynamical model of hair-bundle mechanics might describe self-tuned criticality in the absence of a specific biological mechanism, a detailed biological model should incorporate this phenomenon. A hair bundle's behavior can be described by

$$\xi_T \dot{x} = -k_T x + a(x - f_a) - (x - f_a)^3 + F\,, \tag{9.2}$$

$$\tau_a \dot{f}_a = bx - f_a(1 + S\frac{C}{C_M})\,, \tag{9.3}$$

$$\tau_C \dot{C} = \tau_{MT} v_{MT} P_O - \tau_P v_P \frac{C^n}{C^n + k_P^n}\,. \tag{9.4}$$

Equations 9.2 and 9.3 describe the same generalized model employed throughout this work with the addition of Ca^{2+}-dependent modulation of the adaptation force. The force of adaptation depends on the intracellular Ca^{2+} concentration C relative to a maximal concentration C_M with a strength of Ca^{2+} feedback S. The open probability of transduction channels follows

$$Po = \frac{x - x_0}{\sqrt{1 + (x - x_0)^2}}\,, \tag{9.5}$$

in which x_0 is the hair bundle's position when half the channels are open. Equation 9.4 captures the homeostasis of C and is a balance between the inward flux of Ca^{2+} through mechanotransduction channels and the outward flux through PMCA pumps. Here v_{MT} and v_P are the maximum fluxes through respectively mechanotransduction channels and PMCA pumps, and τ_{MT} and τ_P are the relaxation times of each route with $\tau_P > \tau_{MT}$. The

relaxation time of C should exceed the relaxation time of the adaptation force. The activity of the PMCA pump is described by a Hill equation, in which k_P is the equilibrium constant of PMCA for Ca^{2+} and n is the Hill coefficient (224). For the PMCA pump, v_P = 0.75 μM·s^{-1}, n = 2, and k_P = 0.6 μM (225, 226). With $\tau_C = \tau_{MT}$ = 0.1 ms, τ_P = 37.4 ms, and v_{MT} = 280 μM·s^{-1}, equation 9.4 possesses a stable point at C = 0.25 μM for P_O = 0.15 and C = 14.2 μM for P_O = 1 (170, 224, 227). These values are consistent with previously recorded intracellular Ca^{2+} concentrations upon positive deflection of the bullfrog's saccular hair bundles (227). Equation 9.4 thus describes a biologically relevant mechanism of Ca^{2+} homeostasis, and equation 9.3 captures the effect of Ca^{2+} on bundle behavior in a manner that accords with data.

Numerical simulations of the model capture the effects of Ca^{2+} homeostasis (Figure 9.3). The Ca^{2+} concentration achieves a steady-state value that depends on the position of the bundle, the relative fluxes through the mechanotransduction and PMCA channels, and the extracellular Ca^{2+} concentration. For a given set of mechanical control parameters and the resting level of Ca^{2+}, a hair bundle achieves a steady-state oscillatory amplitude and frequency. Artificially decreasing or increasing the Ca^{2+} concentration causes the bundle's oscillations to increase or decrease in amplitude, consistent with previous manipulations of saccular hair bundles (Figure 9.3a) (124, 196). The hair bundle's operating point thus depends on its mechanical load and Ca^{2+} homeostasis attenuates minor fluctuations around this point by controlling the bundle's oscillatory behavior. Delivering a force pulse to a model bundle elicits a twitch whose amplitude and time constant depend on the magnitude of the stimulus (Figure 9.3b). Interestingly,

the bundle's oscillations at the offset of the force initially possess a smaller amplitude than those prior to the stimulus. The amplitude subsequently grows until it achieves a steady-state value after a time that increases with the magnitude of the stimulus. The time needed to reach the steady state depends not only on the magnitude of the force pulse but also on its duration (Figure 9.3c). As the duration of the pulse grows, so too does the time required to reach a steady-state oscillatory amplitude. These phenomena, which were noted previously in micromechanical stimulation of vestibular hair bundles, can be explained by this model of Ca^{2+} feedback (228).

Taken together, a model of Ca^{2+} homeostasis describes a mechanism of self-regulating bundle behavior. Although the bundle's mechanical load controls its operating point, self-regulation of the Ca^{2+} concentration produces a robust system that adjusts its behavior in response to biological fluctuations. Future endeavors may confirm these hypotheses and suggest another rescaled model of self-tuned criticality independent of specific biological mechanisms.

Figure 9.3. Homeostatic regulation of hair-bundle behavior. (a) Dynamical simulations of a model that incorporates Ca^{2+} homeostasis exhibit self-tuning behavior. (a, *left*) At a stiffness of 3.5 and strength of Ca^{2+} feedback S = 1.7, a sudden decrease in the Ca^{2+} concentration (pink bar) causes the bundle's oscillations to increase in amplitude and decrease in frequency. When the stimulation is turned off, the Ca^{2+} concentration returns to its steady-state value and hair-bundle oscillations relax to their original pattern. (a, *right*) A sudden increase in the Ca^{2+} concentration (pink bar) at the same stiffness and S = 1.3 causes bundle oscillations to decrease in magnitude until they cease altogether. After the Ca^{2+} concentration relaxes to its steady-state value, the bundle's behavior relaxes to its original oscillatory amplitude. (b) Delivering force pulses of increasing magnitude (*top*) to a hair bundle whose stiffness and strength of Ca^{2+} feedback are respectively 3.3 and 3 elicit twitches at the onset of each pulse (*middle*). Both the magnitude and the time constant of the twitch depend on the magnitude of the force pulse. At the offset of the pulse, the bundle's oscillations achieve a steady-state amplitude over a duration that increases with the magnitude of the force and depends on the concentration of Ca^{2+} (*bottom*). (c) After a force pulse, hair-bundle oscillations achieve their maximal amplitude after some time t_{SS}. Pulses delivered to simulated bundles of stiffness 3.3 and S = 3 revealed that the time required to achieve a steady state depends on the duration of the step. This behavior accords with previous manipulations of the frog's saccular hair bundles. All simulations employed the Euler-Murayama method of integration for equations 9.2-9.5 in MATLAB. For all panels, a = 3.5, b = 0.5, τ_a = 10, ξ_T = 1, τ_C = 5×10^4, τ_{MT} = 1, τ_P = 374, k_P = 0.6, v_{MT} = 280, v_P = 0.75, and C_M = 1.

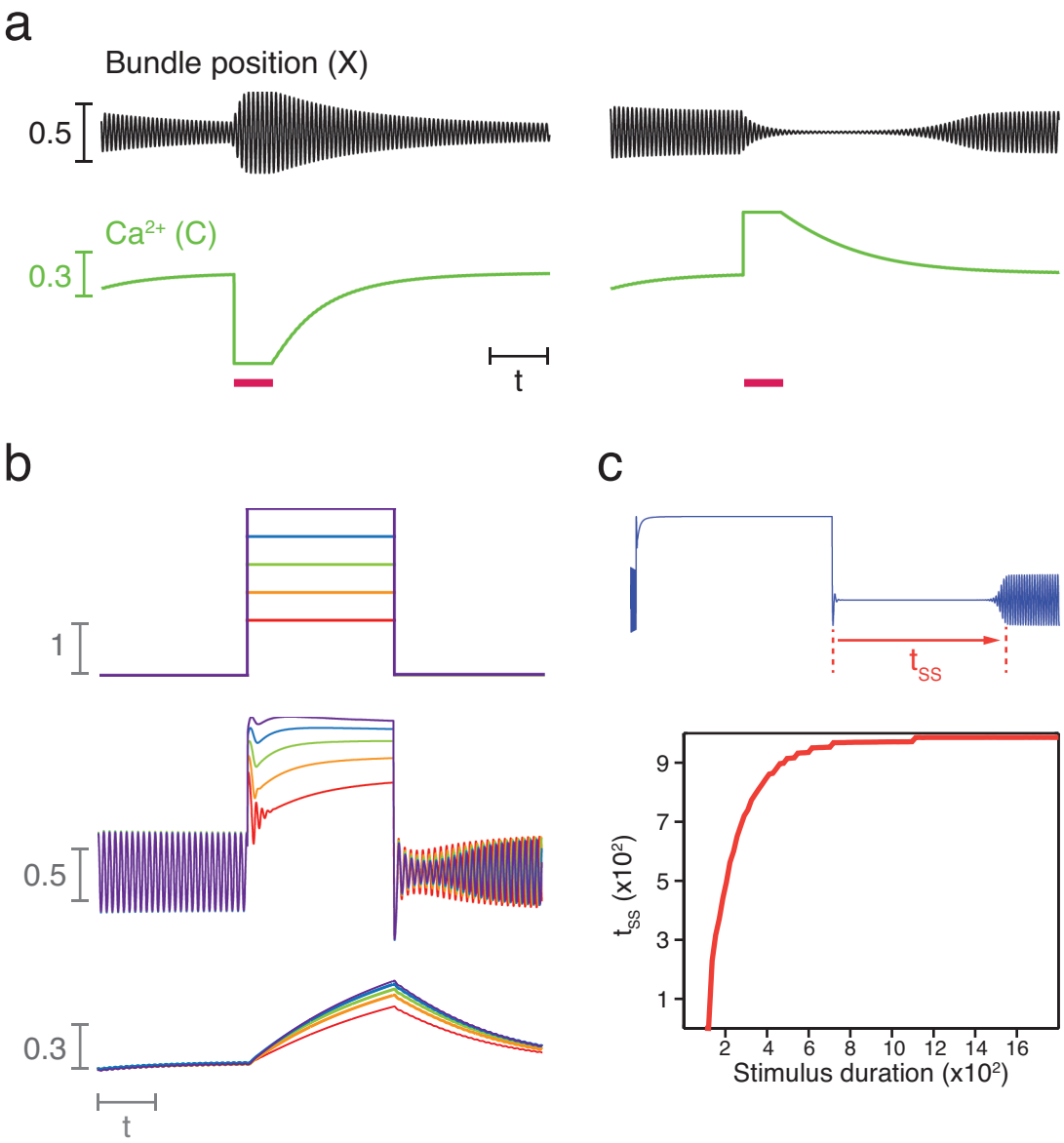
a
Bundle position (X)
0.5
Ca2+ (C)
0.3
t
b
1
0.5
0.3
t
c
tss
tss (x10²)
9
7
5
3
1
2 4 6 8 10 12 14 16
Stimulus duration (x10²)

CHAPTER 10

Hair-Bundle Excitability

Recent observations suggest that hair bundles exhibit multiple classes of mechanical excitability analogous to the electrical excitability of neurons. These dramatic differences in behavior depend on the load stiffness to which the bundle is subjected and might correspond to the dual sensory roles of bundles within the bullfrog's sacculus. To distinguish among these behaviors, we can classify a bundle's motion according to its operation near a specific bifurcation. Here we explore excitability in the context of dynamical-systems theory and highlight an attempt to distinguish a system's behavior in proximity to multiple bifurcations. In doing so, we attempt to develop a protocol to classify bifurcation structure that employs time-series data alone without prior model-specific assumptions. By applying this algorithm to the motion of a hair bundle, we may determine the type of excitability with which the bundle operates and thus infer mechanisms of auditory and vestibular function in the context of the bundle's dynamical behavior.

SECTION 10.1: *Electrical Excitability of Neurons*

In 1948, Alan Hodgkin classified excitability into multiple types in his studies of isolated crab axons (229). Here he stimulated the cells with currents of different strengths. With a small current, the neuron remained quiescent. After the current exceeded its rheobase, the neuron would fire. Further increases in the magnitude of the injected current elicited different patterns in neuronal firing rates among the cells he studied. He separated these behaviors into two types of neuronal excitability. *Type I excitability* occurs when neuronal firing rates can become arbitrarily low for small currents, and the firing rate grows as the magnitude of the injected current rises. A neuron exhibiting *type II excitability* generates action potentials within a certain band of frequencies, and the spike rate rises discontinuously from zero after a critical value of injected current is exceeded. The spike rates in type II excitable neurons are relatively insensitive to changes in the injected current. Thus, an important distinction between type I and type II neural excitability is the frequency of oscillation upon crossing a threshold. Type I neurons generate action potentials that emerge with near-zero frequency, and this frequency rises continuously with current. Type II neurons instead generate action potentials that emerge with non-zero frequency, corresponding to a discontinuous rise in spike rate.

Neuronal excitability can be modeled in the context of dynamical systems. Indeed, Richard FitzHugh first described these phenomena in this way, and Rinzel and Ermentrout later expanded this with the use of bifurcation theory (230, 231). Here the injected current serves as a control parameter. An increase in the control parameter causes a corresponding change in the membrane potential until a critical value of the

control parameter is exceeded and spontaneous oscillations in membrane potential ensue. Although myriad bifurcation structures may give rise to this behavior, the analysis becomes simpler if one includes only codimension-1 bifurcations. In this context, type I or type II excitability can be described respectively by behavior near a saddle-node on invariant cycle (SNIC) bifurcation or a Hopf bifurcation. Under certain conditions, operation near an asymmetric subcritical Hopf bifurcation may also result in type I behavior.

If a model of neuronal dynamics incorporates a SNIC bifurcation, it will generate action potentials if the injected current exceeds a critical value. A reduction in the injected current causes a saddle node to encroach upon the limit cycle, which increases the period of oscillation until the period diverges to infinity (*see* Chapter 3). Thus, a neuron crossing a SNIC bifurcation possesses the behavior associated with a type I excitable system. On the stable side of the bifurcation, one unstable and one stable fixed point each reside on the limit cycle. In the absence of noise, the neuron's membrane potential remains indefinitely on the stable fixed point. However, the addition of noise or a small perturbation large enough to force the system beyond the unstable fixed point permits the system to traverse the limit cycle once before residing again on the stable fixed point. Here the unstable fixed point represents a type of threshold called a *separatrix*, and crossing the separatrix elicits an all-or-none action potential. Within this region of the stable manifold, the system does not spontaneously oscillate but is instead *excitable* (165, 166, 230, 232).

If a model of neuronal behavior instead incorporates a Hopf bifurcation, the neuron again generates action potentials if the injected current exceeds a threshold. An example of a Hopf bifurcation can be found in the Hodgkin-Huxley model (166). When the injected current lies below a threshold, the neuron's membrane potential remains at rest. As the injected current crosses a critical value, however, spikes emerge at a non-zero frequency. Unlike a system poised near a SNIC bifurcation, a system crossing a Hopf bifurcation does not experience spikes with an arbitrarily low frequency, and the frequency of spontaneous spiking remains almost insensitive to the magnitude of injected current. Thus, behavior near a Hopf bifurcation fits the description of type II excitability.

The criticality of the Hopf bifurcation also determines its threshold behavior. On the stable side of a subcritical Hopf bifurcation for control parameters exceeding the critical value associated with a saddle-node of limit cycles, a stable fixed point resides within both an unstable and stable limit cycle. Here the system may reside indefinitely on either the stable fixed point or the stable limit cycle, depending upon the initial conditions. However, the addition of noise or an external perturbation can cause the system to cross the unstable limit cycle and fall onto either the stable limit cycle or the stable fixed point. This unstable limit cycle represents another separatrix, revealing threshold behavior in the subcritical Hopf bifurcation.

The supercritical Hopf bifurcation, on the other hand, possesses only one stable fixed point on the stable side of the bifurcation, and there resides only a stable limit cycle and an unstable fixed point on the unstable side of the bifurcation. In this scenario, no

separatrix exists, and the system does not display threshold phenomena. However, systems bearing a supercritical Hopf bifurcation may exhibit *quasi-threshold phenomena*. This can be appreciated in the FitzHugh-Nagumo model, in which the system possesses a linear and a cubic nullcline. Here small perturbations follow the cubic nullcline and result in a small response along a canard trajectory. Larger perturbations depart from the canard and result in a noticeably larger response. This behavior in the absence of a true threshold mimics threshold phenomena in other systems (179, 180, 230).

An important distinction between type I and type II excitable neurons in the context of bifurcation theory is the responsiveness to stimuli. Generally, type I excitable neurons function as *integrators*, whereas type II excitable neurons behave as *resonators* (165). Consider a weakly connected network of type I neurons modeled according to the Ermentrout-Kopell canonical model (232, 233). Here an incoming spike to an individual neuron causes the phase of the oscillator to advance. If the phase advances sufficiently, the system crosses a separatrix and the tneuron fires (234). This is the foundation of *integrate-and-fire* neurons and highlights type I excitable systems as integrators (165, 166). If a neuron is instead modeled as a system near a Hopf bifurcation, the system selects the frequency component of the stimulation corresponding to the Hopf frequency. Thus, type II excitable systems behave as resonators (235). Interestingly, the capability of a neuron to entrain to its stimulus depends on its classification. Type I excitable neurons synchronize poorly, whereas type II neurons are easily entrained (233, 234, 236). These varied responses to different stimuli highlight the functional differences between neurons of opposing excitability.

Note that a Hopf bifurcation with an asymmetric topology in phase space can exhibit type I excitable behavior (157, 159). Here a constant offset induces asymmetric oscillations that resemble spikes whose inter-spike intervals grow as the bifurcation is approached. In particular, a system's behavior near a subcritical Hopf bifurcation with added offset closely resembles that near a SNIC bifurcation. However, a system poised near a supercritical Hopf bifurcation with an offset exhibits oscillations whose amplitude changes appreciably with the control parameter. A true threshold also persists for only the subcritical Hopf bifurcation. When considering models of type I excitability, both the SNIC bifurcation and asymmetric Hopf bifurcations must therefore be included.

SECTION 10.2: *Mechanical Excitability of Hair Bundles*

Within different locales of a hair bundle's state diagram, the bundle flaunts distinct sets of behaviors. Along the high-stiffness arc of the oscillatory regime, the bundle responds with sharp frequency selectivity and a high degree of entrainment. As the bundle's operating point approaches this critical locus from within the spontaneously oscillatory regime, its oscillations decay in amplitude and rise in frequency until they are suppressed. This behavior occurs in close proximity to a supercritical Hopf bifurcation and is analogous to the behavior of a type II excitable neuron.

When a bundle's load stiffness is reduced, however, its spontaneous activity changes considerably and mimics the behavior of a type I excitable neuron (Figure 10.1). A hair bundle subjected to a load stiffness of 50 $\mu N \cdot m^{-1}$ exhibits asymmetric spontaneous oscillations that resemble the electrical spiking of neurons. The frequency of mechanical spikes depends on the magnitude of constant force, in which an increase in constant force induces a reduction in spike rate until oscillations are altogether suppressed (Figure 10.1a). Poising the same hair bundle at multiple constant forces and tracking motion over time discloses a continuous decrease to arbitrarily low spike rates near a constant force of 82 pN (Figure 10.1b).

These observations suggest that a hair bundle exhibits mechanical excitability analogous to type I and type II electrical excitability of neurons and that the mechanical loads imposed on individual bundles dictate in which class the bundle operates. In particular, an auditory hair bundle achieves its resonant properties through a type II excitable mechanism in a domain of high stiffness, and a vestibular hair bundle achieves

its integration and edge detection properties through a type I excitable mechanism in the low-stiffness domain. If this is the case, multiple types of mechanical excitability among saccular hair bundles should coexist with multiple types of electrical excitability among saccular afferent neurons.

Figure 10.1. Type I mechanical excitability of a hair bundle. (a) A hair bundle was subjected to a load stiffness of 50 $\mu N \cdot m^{-1}$ and delivered a ramp in force from +90 to +15 pN. As the force declined, the bundle first exhibits asymmetric oscillations resembling spikes of low frequency, after which the frequency of spikes rise with a decrease in force. (b) The bundle was next subjected to multiple values of constant force and its motion tracked over the course of 40 s. For each trace, the number of spikes was quantified with a peak-detection algorithm whose threshold was determined by two-means clustering. When the force exceeded 80 pN, the spike rate decays to zero. For constant forces below 80 pN, the spike rate rises with a decrease in force. These patterns resemble the electrical excitability of class I neurons.

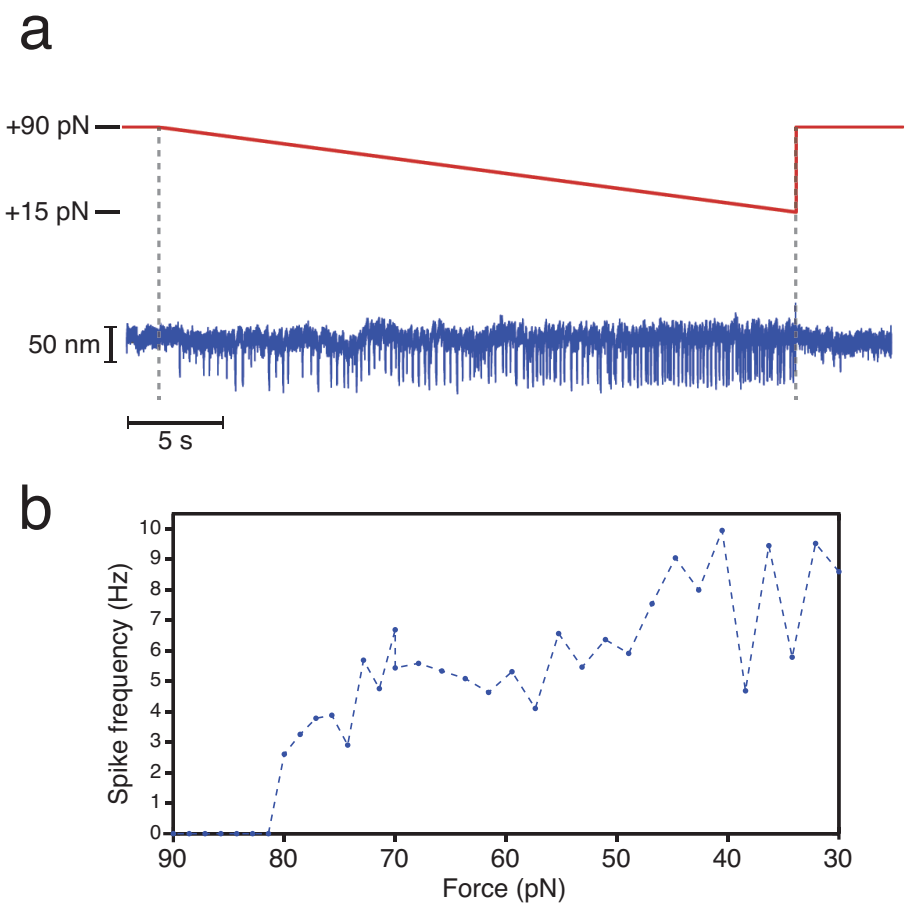
a
+90 pN
+15 pN
50 nm
5 s
b
Spike frequency (Hz)
0
1
2
3
4
5
6
7
8
9
10
90
80
70
60
50
40
30
Force (pN)

SECTION 10.3: *Afferent Neuron Subpopulations in Otolith Organs*

Evidence for the existence of two types of excitability for hair cells of the sacculus and utriculus is not limited to the preliminary indications of mechanical excitability of hair bundles. Recordings from vestibular afferent neurons reveal two neuronal subpopulations defined by the cells' spontaneous activities (237). *Regular afferents* generate action potentials with a highly regular inter-spike interval (ISI), as quantified by a low coefficient of dispersion—defined as the variance divided by the mean—of the ISI distribution. *Irregular afferents*, however, exhibit spikes with highly irregular ISIs and a high coefficient of dispersion. Both regular and irregular afferents have been described across genera, and each subpopulation differs in its region of innervation across a vestibular sensory epithelium.

Do these neuronal subpopulations also constitute type I and type II excitable systems? Though this terminology has not been described explicitly in the literature, existing data indicate that regular afferents behave like type I excitable neurons and irregular afferents can be described as type II excitable neurons. For example, a regular afferent from the rat vestibular ganglion generates action potentials with a frequency that depends on the magnitude of injected current (238). Indeed, the spike rate becomes arbitrarily small until all spontaneous activity is suppressed. These data support the hypothesis that regular afferents behave as type I excitable neurons. Irregular afferents, on the other hand, respond best to periodic stimuli, and their spike rates remain relatively insensitive to the magnitude of injected current (239). These results indicate that irregular afferents instead function as type II excitable neurons. Finally, recent work

described the behavior of regular afferents as superb integrators of synaptic input, whereas irregular afferents behave optimally as resonators (238, 239).

The foregoing data provide ample evidence that regular and irregular vestibular afferent neurons can be described as respectively type I and type II excitable neurons. Evidence that these dual roles exist in afferent neurons lends support to the hypothesis that hair bundles possess the capacity to exhibit mechanical excitability in an analogous manner.

SECTION 10.4: *Noisy Simulations of Bifurcation Normal Forms*

Because each class of excitability can be modeled as a system operating near a specific bifurcation, we sought to develop a protocol with which to distinguish bifurcation structures from noisy time-series data alone and in the absence of external perturbation. Such a protocol not only permits behavioral classification based on bifurcation type, but it also provides a tool otherwise absent from the literature. Here we employ simulations of the normal forms of supercritical Hopf bifurcation, subcritical Hopf bifurcation, SNIC bifurcation, and cusp bifurcation. We selected the Hopf bifurcations and the cusp bifurcation because they are prominent in the hair bundle's state diagram (167). The SNIC bifurcation was included due to its association with type I neuronal excitability (165, 166, 234).

Stochastic Simulations of Bifurcation Normal Forms

All simulations were performed in MATLAB R2014a (8.3.0.532) with the Euler-Murayama method of integration. Simulations of the normal forms of the supercritical Hopf bifurcation, subcritical Hopf bifurcation, and SNIC bifurcation were integrated over $5\text{x}10^7$ points and 10^4 time steps. The normal form of the cusp bifurcation was integrated over $5\text{x}10^8$ points and 10^5 time steps. Each simulation incorporated Brownian noise increments $dW = \varepsilon\sqrt{\Delta t}$, in which ε was pseudorandom variable chosen from $N(0,\sigma)$ generated by the Mersenne twister pseudorandom number generator with standard deviations σ of 0.05, 0.1, 0.2, or 0.4. Each simulation was repeated for 500

operating points ranging from -5 through +5 for the supercritical Hopf, subcritical Hopf, and SNIC bifurcations, and -0.5 through 0 for the cusp bifurcation. The resulting time series from each operating point and noise level was subsequently divided into five equal partitions for independent analysis prior to averaging.

Supercritical Hopf bifurcation normal form

Simulations of the supercritical Hopf bifurcation employed two coupled planar equations defined as

$$\dot{x} = \mu x - \omega y - x(x^2 + y^2) + \eta_x + C, \tag{10.1}$$

$$\dot{y} = \omega x + \mu y - y(x^2 + y^2) + \eta_y + C, \tag{10.2}$$

in which μ is a control parameter, $\omega = 2\pi$ is the Hopf frequency, and η_x and η_y are Brownian noise terms with $\eta_x = \eta_y$. In some cases, an offset C was added to equations 10.1 and 10.2. For simulations of the supercritical Hopf bifurcation with an offset $C = 10$, simulations were performed for 500 values of μ ranging from 5 through 15, in which a stable limit cycle appears at $\mu \approx 7.47$. In the absence of an offset, $C = 0$.

Subcritical Hopf bifurcation normal form

Simulations of the subcritical Hopf bifurcation employed two coupled planar equations defined as

$$\dot{x} = \mu x - \omega y + x(x^2 + y^2) - x(x^2 + y^2)^2 + \eta_x + C, \tag{10.3}$$

$$\dot{y} = \omega x + \mu y + y(x^2 + y^2) - y(x^2 + y^2)^2 + \eta_y + C, \tag{10.4}$$

in which μ is a control parameter, ω is the Hopf frequency, and η_x and η_y are Brownian noise terms. In a second set of simulations, an offset C = -10 was added to equations 10.3 and 10.4 with simulations extending across 500 values of μ ranging from 15 through 30, in which a stable limit cycle appears at $\mu \approx 20.82$. When no offset was incorporated, $C = 0$.

SNIC bifurcation canonical model

The SNIC bifurcation was simulated according to the Ermentrout-Kopell canonical model (*theta model*), in which only the phase of the oscillator is integrated (165, 166, 168, 234). In the absence of noise, the theta model follows the form

$$\dot{\theta} = 1 - \cos\theta + \mu(1 + \cos\theta), \tag{10.5}$$

in which θ is the phase of the oscillator and μ is a control parameter. To incorporate additive white noise to equation 10.5, the noise takes the following form in the quadratic form of the saddle-node bifurcation (240)

$$\dot{x} = x^2 + \mu + \sigma_x \dot{W}. \tag{10.6}$$

Here x is the position of the oscillator, σ_x is the standard deviation of the noise in x, and W is a Brownian noise term (240). Assuming that $x = \tan(\theta/2)$, the theta model with noise is defined as (233, 234, 240)

$$\dot{\theta} = \left[1 - \cos\theta + (1 + \cos\theta)\left(\mu - \frac{\sigma_x^2}{2}\sin\theta\right)\right]dt + \sigma_x(1 + \cos\theta)dW. \tag{10.7}$$

Cusp bifurcation normal form

Simulations of the cusp bifurcation employed the normal form defined by

$$\dot{x} = \beta_1 + \beta_2 x - x^3 + \eta_x , \tag{10.8}$$

in which β_1 and β_2 are control parameters and η_x is a Brownian noise term. In the following simulations, $\beta_2 = 0.64633$ so that lines of fold bifurcations occur at $\beta_1 = \pm 0.2$.

Peak detection and threshold selection

For each time series, local maxima and minima were defined as respectively the peaks and troughs in the signal with a modified peak-detection algorithm (241). Peaks and troughs were defined for a threshold δ by

$$x_{P_j} \equiv x_{T_i} + \delta \le x_{P_j} \cap x_{T_{i+1}} + \delta \le x_{P_j} , \tag{10.9}$$

$$x_{T_i} \equiv x_{P_j} - \delta \ge x_{T_i} \cap x_{P_{j+1}} - \delta \ge x_{T_i} , \tag{10.10}$$

in which P_j and T_i correspond respectively to the locations of each peak and trough (241). We defined N thresholds by the maximum noise floor $\varsigma_{\max}$ from time series across all operating points plus equal divisions of the maximum difference between the noise floor ς_x and RMS magnitude x_{RMS} of each time series across operating points, such that each threshold followed

$$\delta_k = \varsigma_{\max} + k \frac{\max\left(x_{RMS} - \varsigma_x\right)}{N+1} . \tag{10.11}$$

The noise floor and RMS magnitude were calculated from the Fourier transform of each time series. We defined a noise floor as the square root of the total power of all Fourier

components less than half of the Nyquist frequency whose height did not exceed the mean height within this range plus two standard deviations of the spectral heights. The total RMS magnitude was taken as the square root of the sum of all Fourier components. We defined the peak-to-peak magnitude as the difference in the heights between neighboring peaks and troughs.

Spike rate and coefficient of dispersion

After finding the location of each peak in a time series, these peaks were used to calculate a spike rate. The mean spike rate $\langle r \rangle$ was defined as the spike count $n(x_P)$ divided by the length of the signal in time T: $\langle r \rangle = \frac{n(x_P)}{T}$.

We next calculated the variability in the length of time between each peak, the inter-peak interval (*IPI*), given by $IPI_{P_k} = t_{P_{k+1}} - t_{P_k}$ for neighboring spike times at $t_{P_{k+1}}$ and t_{P_k}. The mean inter-peak interval $\langle IPI \rangle$ is related to the mean spike rate by $\langle IPI \rangle = \frac{1}{\langle r \rangle}$. To do so, we defined a coefficient of dispersion as

$$D = \frac{\langle \Delta IPI^2 \rangle}{\langle IPI \rangle}, \tag{10.12}$$

in which $\langle \Delta IPI^2 \rangle = \langle IPI^2 \rangle - \langle IPI \rangle^2$ is the variance of the inter-peak interval (242). In the case where $D = 1$, *IPI* is Poisson-distributed. For $D < 1$, *IPI* approximates a binomial distribution and is under-dispersed, and for $D > 1$ it is over-dispersed. In the limiting case where $D = 0$, the *IPI* distribution is a Dirac delta function. Thus, the coefficient of

dispersion provides a direct indication of the degree of coherence in the spontaneous or evoked activity in a time series. We define the border between a coherence and incoherence at $D = 1$, such that a *coherent zone* exists for $D < 1$ and an *incoherent zone* resides at all operating points for which $D > 1$.

Coherence in the power spectral density

We next wished to quantify the degree of coherence in the power spectrum of a noisy time series. Power spectra were computed with Welch's algorithm and ten non-overlapping rectangular windows. Peaks were defined by the local maxima of the power spectrum using a threshold calculated from two-means clustering of the spectrum (241). To determine whether a maximum was a peak, we found all peaks less than or equal to half the power of the peak of interest. A maximum was classified as a peak if there existed at least one point at a frequency greater than and another less than the frequency of the maximum of interest whose heights were significantly smaller than that of the peak (two-tailed Student's *t*-test with $p < 0.001$). After all peaks in the power spectrum had been found, the peak of maximum height was classified as the primary peak.

To compute the degree of coherence in the power spectrum, we calculated a quality factor of the primary peak, defined as

$$Q_{FFT} = \frac{\omega(S_{\max})}{\Delta\omega}, \tag{10.13}$$

in which $\omega(S_{\max})$ is the frequency of the primary peak, and $\Delta\omega$ is the half-power bandwidth. The half-power bandwidth is the difference in frequency of the two spectral

components nearest to the primary peak whose heights were at least less than half the power of the primary peak and differed significantly differed from the height of the primary peak according to the algorithm above.

Phase portraits and vector strength

To estimate the phase portraits of individual time series, we first computed the Hilbert transform of the signal. This yields an analytic signal that incorporates both real and imaginary components, given by $x_A = x + ix_H$, in which x is the original time series and x_H is its Hilbert transform. We computed phase portraits of the real and imaginary components by applying a bivariate Gaussian kernel density estimator with a square grid of 2,048 points. This yields a bivariate histogram of the amount of time the signal resides at each point in phase space. We converted this to a bivariate probability mass function by dividing by the sum of all counts. Each bin then corresponds to the probability that the signal resides at a particular location in the real-imaginary plane.

We next wished to measure whether the signal possessed a preferred phase. To quantify this, we calculated the vector strength of the analytic signal of the time series, given by

$$VS = \left| \frac{1}{N} \sum_{k=1}^{N} e^{i\phi_k} \right|, \tag{10.14}$$

$$\phi_k = \tan^{-1}\left(\frac{\Im(x_{A,k})}{\Re(x_{A,k})} \right), \tag{10.15}$$

in which $x_{A,k}$ is the analytic signal of the time series at index *k* and $\Im(x_{A,k})$ and $\Re(x_{A,k})$ are respectively its imaginary and real components.

We computed displacement histograms by taking the real component of the signal and binning the positions into bins of equal width defined by the Freedman-Diaconis rule. To determine whether the histogram was bimodal we employed Hartigan's dip statistic (200).

Simulation results

We wished to develop a protocol that incorporates a set of qualitative observations and statistical analyses both to classify a noisy system's bifurcation structure and to approximate the location of the bifurcation in the absence of noise. To assess the behavior of a system in the vicinity of each bifurcation, we simulated the normal forms according to the aforementioned procedures.

The time series and phase portraits reveal striking differences in the behaviors of these systems. In the absence of noise, all systems remain quiescent for values of the control parameter on the stable side of a bifurcation ($\mu < \mu_c$) (Figure 10.2). A system operating in the vicinity of a fold bifurcation remains at one stable fixed point for all values of the control parameter. Upon increasing the control parameter to poise each system on the unstable side of a supercritical Hopf, subcritical Hopf, or SNIC bifurcation, spontaneous oscillations emerge. In the case of a supercritical Hopf bifurcation oscillations appear with a non-zero frequency and the frequency of oscillation remains constant with further increases in the value of the control parameter.

The amplitude of oscillation, on the other hand, grows as the control parameter is boosted. This can be appreciated in the phase portrait, in which the diameter of the limit cycle grows with the value of the control parameter.

For a subcritical Hopf bifurcation, spontaneous oscillations again emerge with a non-zero frequency, but the amplitude of oscillation is large and exhibits relatively little change (Figure 10.2). This is consistent with a system residing on a fifth-order stable limit cycle and can be recognized in the large-diameter limit cycle illustrated in the system's phase portraits.

Figure 10.2. Simulations of bifurcation normal forms in the absence of noise. We first simulated the behavior of a system near a supercritical Hopf, subcritical Hopf, SNIC, and cusp bifurcation in the absence of noise. Example time series and phase portraits in the real-imaginary plane are depicted for each normal form. Control parameters are included both below (*red*) and above (*blue*) the critical value of the control parameter at which the bifurcation resides. In the absence of noise, the system remained quiescent for all operating points on the stable side of the supercritical Hopf, subcritical Hopf, and SNIC bifurcations. Spontaneous activity was absent in all simulations of the cusp bifurcation across all operating points. On the unstable side of the supercritical Hopf bifurcation ($\mu \geq \mu_c$), oscillations emerged at a non-zero frequency and the amplitude increased with the value of the control parameter. The phase portraits depict circular limit cycles whose diameter increased with the amplitude of oscillation. A system poised on the unstable side of a subcritical Hopf bifurcation generated high-amplitude spontaneous oscillations of non-zero frequency. Because there was little change in the amplitude of oscillation, the phase portraits exhibited relatively little change in diameter. Biphasic oscillations emerged on the unstable side of the SNIC bifurcation of arbitrarily low frequency, and the frequency grew with the value of the control parameter. No qualitative change in the amplitude of oscillations appeared. Phase portraits of the behavior near a SNIC bifurcation depict an asymmetry at an operating point near the bifurcation ($\mu = 0.01$), and this asymmetry disappears as the operating point is coerced farther from the bifurcation ($\mu = 0.1$).

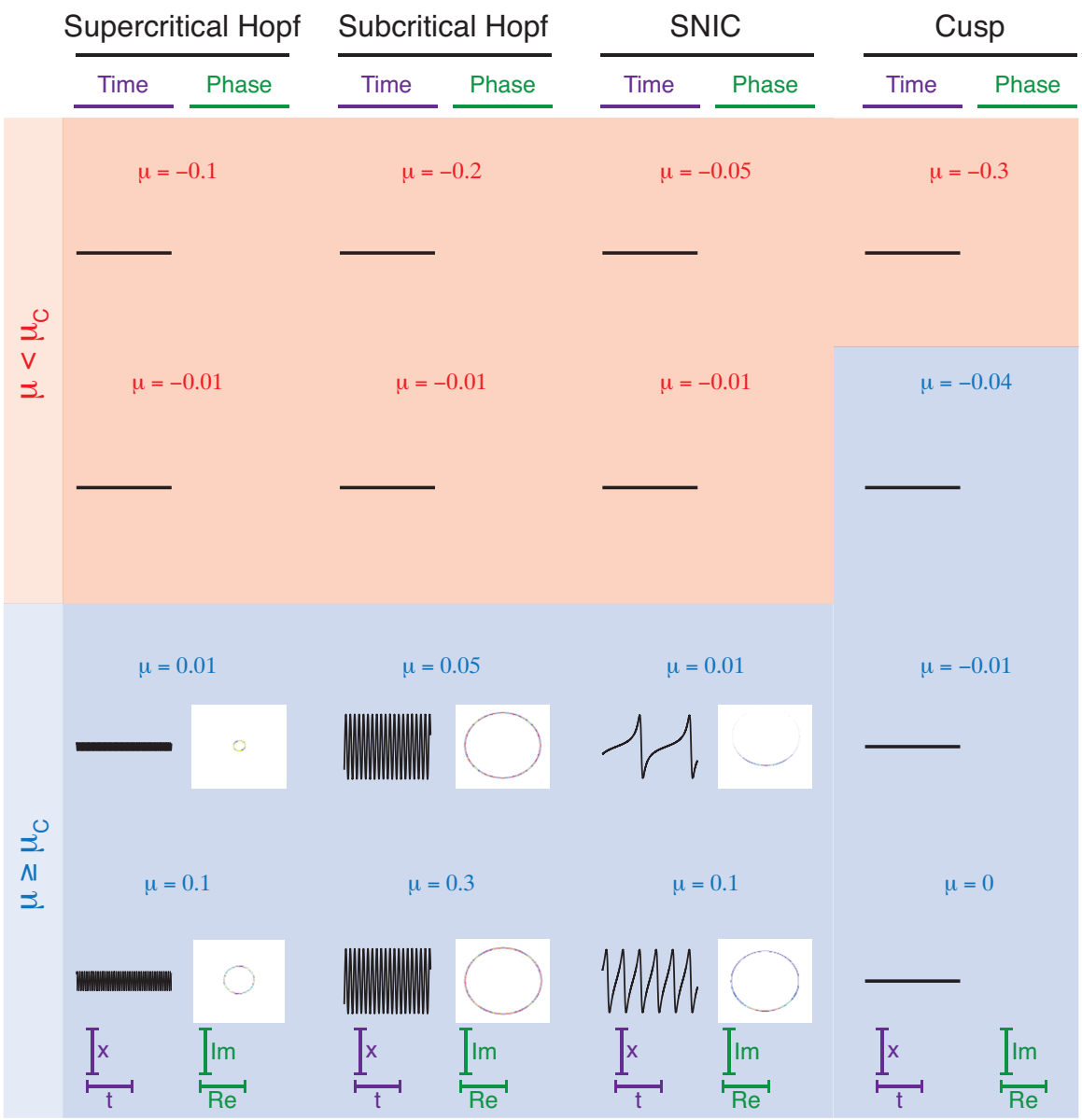
Supercritical Hopf
Subcritical Hopf
SNIC
Cusp
Time
Phase
μ < μc
μ ≥ μc
μ = −0.1
μ = −0.2
μ = −0.05
μ = −0.3
μ = −0.01
μ = −0.01
μ = −0.01
μ = −0.04
μ = 0.01
μ = 0.05
μ = 0.01
μ = −0.01
μ = 0.1
μ = 0.3
μ = 0.1
μ = 0
x
t
Im
Re

Finally, a system operating in the vicinity of a SNIC bifurcation exhibits spikes that emerge with near-zero frequency and whose frequency increases but amplitude remains constant as the control parameter rises in value (Figure 10.2). The phase portraits reveal an asymmetry at the ghost of a saddle-node bifurcation on the limit cycle. This distribution becomes symmetric along the limit cycle as the system departs from the bifurcation farther into the unstable regime.

When noise is added to each simulation, oscillations emerge with a distinct pattern on the stable side of each bifurcation (Figure 10.3). A system poised near a supercritical Hopf bifurcation exhibits *ringing* in its time series. Phase portraits reveal a unimodal bivariate distribution for all operating points on the stable side of the bifurcation ($\mu < \mu_c$). On the unstable side of the bifurcation, noise may obscure the structure of the limit cycle, rendering its appearance again unimodal. However, circular distributions, which appear bimodal in a displacement histogram, appear only for operating points on the unstable side of a supercritical Hopf bifurcation.

Additive noise elicits *bursting* on the stable side of the subcritical Hopf bifurcation for values of the control parameter on the stable side of the bifurcation ($\mu < \mu_c$) and greater than the critical value of the saddle-node of limit cycles ($\mu_c > \mu > \mu_{c,SNLC} = -0.25$) (Figure 10.3). Here bursting refers to a behavior by which the system resides either at a stable fixed point or on a stable limit cycle, the two of which are separated by separatrix defined by an unstable limit cycle. A burst occurs when the system crosses the separatrix from the stable fixed point onto the stable limit cycle. The burst terminates when the system crosses the separatrix back onto the stable fixed point.

This behavior can be appreciated in the phase portrait at μ = -0.2. Here the system may reside either on a stable limit cycle or at the stable fixed point at its center. Because the associated time series depicts only a short interval, only the termination of a burst is shown.

Operation near a SNIC bifurcation elicits *spikes* in each time series (Figure 10.3). Because the saddle-node bifurcation occurs here at $\theta = -\pi/2$, the spikes are biphasic. The addition of noise causes the spike rate to increase for operating points near the bifurcation and elicits spikes on the stable side of the bifurcation. Here additive noise permits the system to cross a separatrix defined by the unstable fixed point residing on the invariant limit cycle. As a result, the system may traverse the cycle once prior to returning to the stable fixed point and thus generate a spiking pattern distinct from the bursting behavior of the subcritical Hopf bifurcation. This behavior may be observed in the phase portraits of the SNIC bifurcation. As the value of the control parameter decreases, the system resides more often at point on the lower half of the limit cycle. On the unstable side of the bifurcation ($\mu > \mu_c$), this results from the ghost of a saddle node. On the stable side of the bifurcation ($\mu < \mu_c$), this region corresponds to a stable fixed point residing on the cycle. Because the Euclidean distance between the stable and unstable fixed points increases with a decrease in the value of the control parameter, the probability that the system can cross the separatrix declines. This corresponds to an increased probability of residence at the stable fixed point.

Finally, simulations of a cusp bifurcation reveal bistable switching for values of the control parameter greater than the critical value corresponding to a fold bifurcation

($\mu > \mu_c = -0.2$) (Figure 10.3). Within this regime, two stable fixed points are separated by a separatrix defined by an unstable fixed point. As the control parameter's value increases, this barrier decreases in magnitude. This behavior permits the system to switch more readily between the two stable points, as can be seen in the relative probabilities in each phase portrait. Here an increase in the control parameter causes the probability of the leftmost stable fixed point to decrease and that of the rightmost point to increase until the two probabilities coincide at $\mu = 0$.

Figure 10.3. Simulations of bifurcation normal forms in the presence of noise. We performed simulations of the normal forms of the supercritical Hopf, subcritical Hopf, SNIC, and cusp bifurcations in the presence of noise with a standard deviation of 0.1. The chart shows the time series and phase portraits resulting from the simulations at selected operating points both below (*red*) and above (*blue*) the critical values of the control parameters at which the bifurcations reside. For the supercritical Hopf bifurcation, oscillations exhibit *ringing* on both the unstable and stable sides of the bifurcation. In phase space, the system's distribution is unimodal for all $\mu \leq \mu_c$ and is only clearly multimodal (or circular) for $\mu > \mu_c$. In the case of the subcritical Hopf bifurcation, oscillations appear on both sides of the bifurcation and exhibit *bursting* behavior. Phase portraits indicate a stable fixed point in the center of a stable limit cycle under certain conditions on the stable side of the bifurcation ($\mu = -0.2$). A system poised near a SNIC bifurcation also exhibits oscillations that resemble *spikes* for $\mu < \mu_c$ in the presence of noise. The frequency of oscillation again grows with the value of the control parameter, but the frequency approaches zero only for $\mu < \mu_c$. Both the subcritical Hopf bifurcation and SNIC bifurcation possess a separatrix within this region, which can account for the apparently all-or-none behavior for a noisy system poised on the stable side of each bifurcation. Finally, simulations of a system modeled according to the normal form of a cusp bifurcation reveal bistable switching in both the time series and phase portraits. As μ approaches zero, the residence time at each stable fixed point becomes equal. Separating the stable fixed points is an unstable fixed point that serves as another separatrix and can be crossed in the presence of noise.

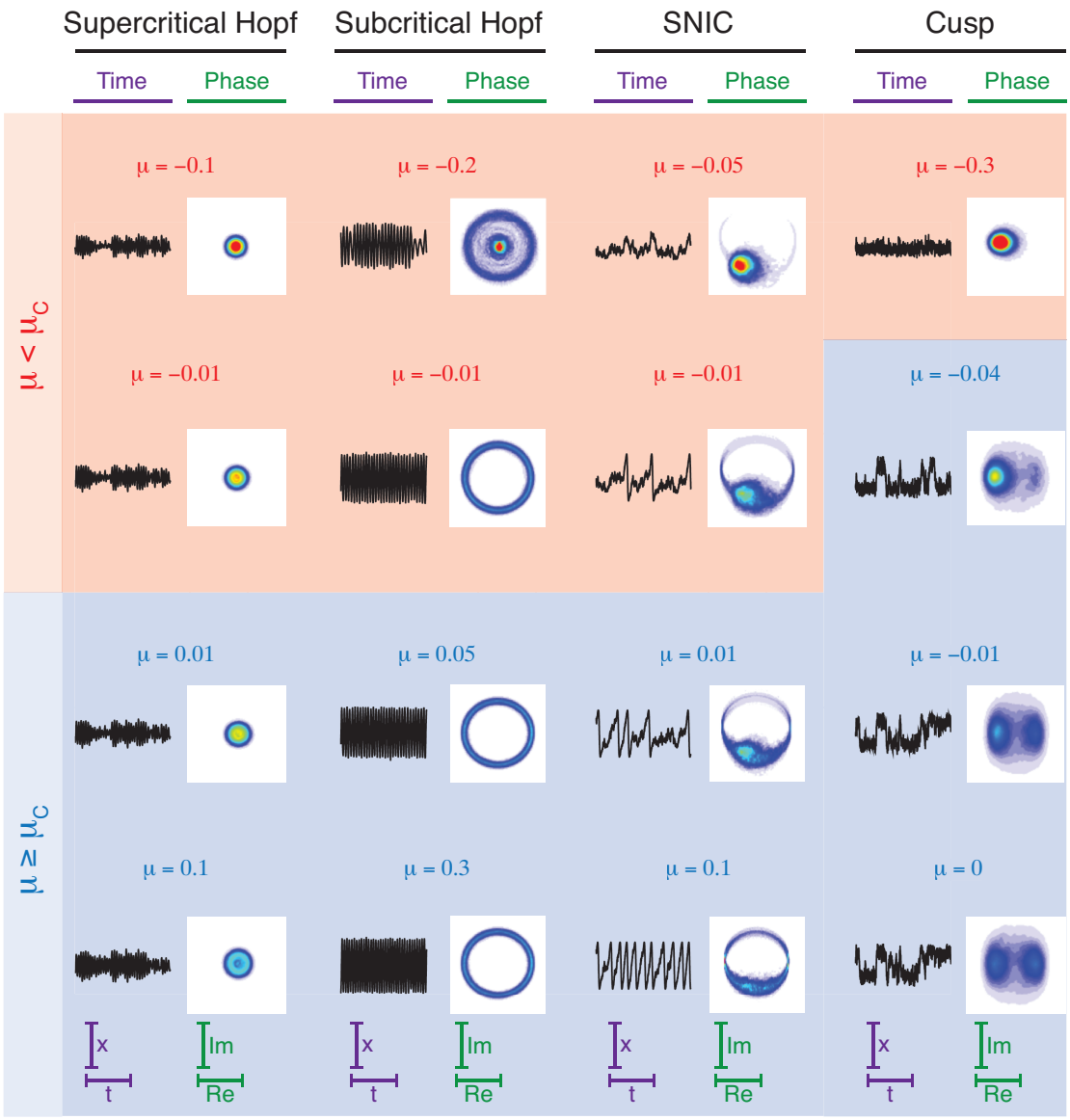
Supercritical Hopf
Subcritical Hopf
SNIC
Cusp
Time
Phase
μ < μc
μ ≥ μc
μ = −0.1
μ = −0.2
μ = −0.05
μ = −0.3
μ = −0.01
μ = −0.01
μ = −0.01
μ = −0.04
μ = 0.01
μ = 0.05
μ = 0.01
μ = −0.01
μ = 0.1
μ = 0.3
μ = 0.1
μ = 0
x
t
Im
Re

We next characterized the relationship between spike rate and control parameter for each bifurcation's normal form (Figure 10.4). To do so, we employed a peak-detection algorithm with the two thresholds defined by equations 10.9-10.11. In each case, we included multiple noise levels to assess the effects of noise on our classification scheme. For a system operating in the vicinity of a supercritical Hopf bifurcation, the spike rate rises discontinuously to a non-zero value when the control parameter's value exceeds zero (Figure 10.4a). Further increases to the control parameter do not change the spike rate. Additive noise reduces the slope in the rise of the spike rate, and the slope decreases further as the noise level increases. The peak-detection threshold identifies only oscillations that exceeded threshold in amplitude, which shifts the rise in spike rate to a value of the control parameter greater than zero. As expected, adjusting the threshold causes the curve to shift along the abscissa. However, the shape of the spike rate relationship and the slope of the rise in spike rate remain unaffected by a change in threshold. Furthermore, when the control parameter is large, all spike rates converge to the constant value associated with the noiseless case at all noise levels and all thresholds.

Simulations of a system near a subcritical Hopf bifurcation reveal a pattern distinct from that of the supercritical Hopf bifurcation (Figure 10.4b). In the absence of noise, the spike rate rises sharply when the control parameter's value exceeds zero. The addition of small noise ($\sigma = 0.1$) causes oscillations to appear on the stable side of the bifurcation ($\mu < 0$). These oscillations persist with a decrease in the value of the control parameter until the system crosses a saddle node of limit cycles. For a larger noise level ($\sigma = 0.2$), oscillations persist beyond the saddle node of limit cycles. Here the system no

longer exhibits bursting behavior but instead rings in a manner similar to that of the supercritical Hopf bifurcation. Changing the peak-detection threshold results in either no change in the spike rate relationship (*for* $\sigma = 0.1$) or a change in the slope of the rise in spike rate (*for* $\sigma = 0.2$). As with the supercritical Hopf bifurcation, all spike rates converge to the same values for large values of the control parameter.

In the vicinity of a SNIC bifurcation, spikes appear in the noiseless case for values of the control parameter that exceed zero (Figure 10.4c). Here the spike rate emerges at an arbitrarily small value and grows with an increase in μ. Additive noise causes the spike rate to increase near the bifurcation and induces spikes within the stable regime. Changing the magnitude of the peak-detection threshold results in a change in the slope of the spike rate relationship near the bifurcation. This response contrasts with the shifted curve in the case of a supercritical Hopf bifurcation. Once again, however, all spike rates converge to the same values when the value of the control parameter is large.

A system modeled according to the normal form of a cusp bifurcation displays no spikes in the absence of noise (Figure 10.4d). The addition of noise permits the system to switch between two stable states, which increases the spike rate in a noise-dependent manner. Adjusting the value of the peak-detection threshold changes both the shape of the spike rate relationship and the maximum spike rate across control parameters. Unlike all previous scenarios, the spike rates do not converge when the control parameter's value is large.

Figure 10.4. Spike-rate dependence on control parameter and threshold. (a) Simulations of the normal form of a supercritical Hopf bifurcation reveal changes in the frequency of oscillation with control parameter. Here the bifurcation resides at $\mu = 0$ (gray line). In the absence of noise, the spike rate is expected to discontinuously jump to a non-zero value and remain constant upon crossing the bifurcation (dashed line). When noise is added, the slope of the spike rate relationship decreases as a function of the noise level (e.g. red *vs.* blue). Changing the peak-detection threshold at a given noise level shifts the spike rate relationship without changing its slope (e.g. red *vs.* pink). (b) A subcritical Hopf bifurcation resides at $\mu = 0$ (gray line), and a saddle node of limit cycles resides at $\mu = -0.25$ (green line). In the absence of noise the spike rate rises discontinuously upon crossing the Hopf bifurcation, and slowly rises until it achieves a constant value $\mu > 0$. Adding noise causes oscillations to appear for $\mu < 0$. With a small noise level, the spike rate follows the same trajectory as the deterministic case and falls to zero at the saddle-node of limit cycles (red and pink). Higher noise levels skew this behavior and induce ringing at smaller values of μ (blue and cyan). Changing the threshold yields either no change in the spike rate relationship (red *vs.* pink) or a change in its slope near the bifurcation (blue *vs.* cyan). (c) A SNIC bifurcation occurs at $\mu = 0$ (gray line). Oscillations emerge at arbitrarily low frequency at $\mu = 0$ and grow in frequency as μ increases. Adding noise induces both increases the frequency of spikes near the bifurcation and induces spikes for $\mu < 0$. Changing the peak-detection threshold changes the slope of the spike rate relationship. (d) A fold bifurcation occurs at $\mu = -0.2$. No oscillations exist in the absence of noise, and the frequency of oscillation at all control parameters increases with the noise level. Changing the peak-detection threshold adjusts the slope of the spike rate relationship. Maximum spike rates did not converge across different thresholds, unlike those in (a-c). All error bars represent standard errors of the means of five replicates.

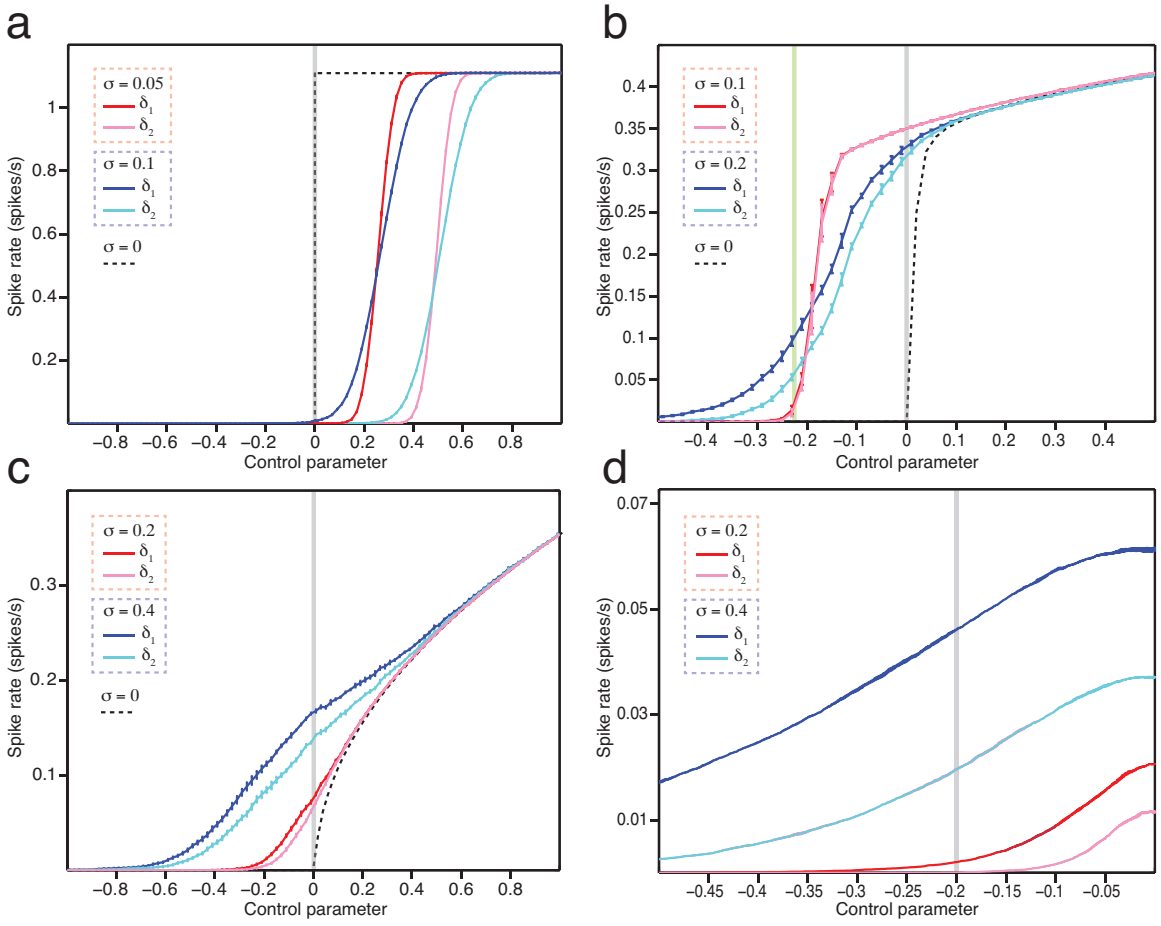
a
σ = 0.05
δ1
δ2
σ = 0.1
δ1
δ2
σ = 0
Spike rate (spikes/s)
Control parameter
b
σ = 0.1
δ1
δ2
σ = 0.2
δ1
δ2
σ = 0
Spike rate (spikes/s)
Control parameter
c
σ = 0.2
δ1
δ2
σ = 0.4
δ1
δ2
σ = 0
Spike rate (spikes/s)
Control parameter
d
σ = 0.2
δ1
δ2
σ = 0.4
δ1
δ2
Spike rate (spikes/s)
Control parameter

In addition to assessing the frequency of spiking for a system poised near a particular bifurcation, we wished to classify each system by its degree of coherence when operating near a critical locus. To do so, we calculated a coefficient of dispersion for each time series at each operating point and noted how the coherence of oscillations changed with the value of the peak-detection threshold (Figure 10.5). In all cases, the coefficients of dispersion never exceed 10^{-2} in the absence of noise.

For a system poised near a supercritical Hopf bifurcation, additive noise causes an increase in the coefficient of dispersion (Figure 10.5a). Here the coefficient of dispersion exceeds a threshold of one on the stable side of the bifurcation ($\mu > 0$). Adjusting the peak-detection threshold causes a shift of the curve along the abscissa. Thus, the estimate of a coherent zone and by extension the bifurcation's location depends strongly on the selected threshold.

Unlike a supercritical Hopf bifurcation, a system operating close to a subcritical Hopf bifurcation displays coefficients of dispersion that remain insensitive to threshold selection (Figure 10.5b). Here the coefficient of dispersion crosses one at a control parameter between the critical value of the saddle-node of limit cycles and the critical value of the subcritical Hopf bifurcation for all noise levels. However, an increase in the peak-detection threshold causes no change in the point at which the coefficient of dispersion crosses one. Thus, the coefficient of dispersion systematically classifies a coherent zone on the stable side of the bifurcation and is independent of the chosen threshold. This statistic distinguishes the subcritical Hopf bifurcation from the

supercritical Hopf bifurcation and places a bound on the bifurcation's location within its stable regime.

Behavior near a SNIC bifurcation mimics that of the subcritical Hopf bifurcation (Figure 10.5c). Like a system near a subcritical Hopf bifurcation, a system near a SNIC bifurcation displays a coefficient of dispersion that crosses one at a value of the control parameter independent of the selected threshold. Unlike the subcritical Hopf bifurcation, however, the coefficients of dispersion cross one on the unstable side of a SNIC bifurcation. This yields an estimate of the coherent zone whose border systematically resides within the unstable regime and provides another distinguishing characteristic for this bifurcation's structure.

Finally, a system modeled according to the normal form of a cusp bifurcation yields coefficients of dispersion always exceeding one (Figure 10.5d). Because the system's oscillations depend solely on additive noise, no coherent zone exists. Thus, one cannot employ the coefficient of dispersion to pinpoint the location of a fold bifurcation.

In addition to the aforementioned analyses, we analyzed each bifurcation type in the context of multiple metrics (Table 10.1). Multiple measures together yield defining characteristics that permit classification of a system by bifurcation type using time-series data alone. Future analyses will incorporate thresholds on certain metrics to allow a complete and quantitative classification scheme. Nonetheless, these results indicate unique features of a system poised near each bifurcation. We shall employ these metrics in our assessment of hair-bundle mechanics. Before doing so, however, let us return to a simple model of hair-bundle motility.

Figure 10.5. Coefficients of dispersion in the presence of noise. (a) Simulations of the normal form of a supercritical Hopf bifurcation ($\mu_c = 0$, gray line), reveal coefficients of dispersion that grow with a decrease in the value of the control parameter. In the absence of noise, all coefficients of dispersion fall below 10^{-2}. When noise is added, the coefficient of dispersion exceeds one (orange line) at $\mu > 0$, and the control parameter at which the coefficient crosses this threshold increases with the noise level. Increasing the peak-detection threshold increases the coefficient of dispersion at all operating points and thus shifts the operating point at which the coefficient equals one. (b) Coefficients of dispersion surpass one for $\mu < 0$ for a system poised near a subcritical Hopf bifurcation. As with the supercritical Hopf bifurcation, an increase in the noise level increases the operating point at which the coefficient of dispersion crosses this threshold (orange line). Changes to the peak-detection threshold yields no difference in the location at which the threshold is crossed. (c) Simulations of a SNIC bifurcation yield coefficients of dispersion that exceed one for $\mu > 0$ in the presence of noise. However, neither a change in the noise level nor the peak-detection threshold shift the control parameter at which this threshold is crossed (orange line). (d) The coefficients of dispersion exceed one at all control parameters for a system modeled according to the normal form of a cusp bifurcation. Adjusting the threshold reveals little change in the value of the coefficient. All error bars represent standard errors of the means of five replicates.

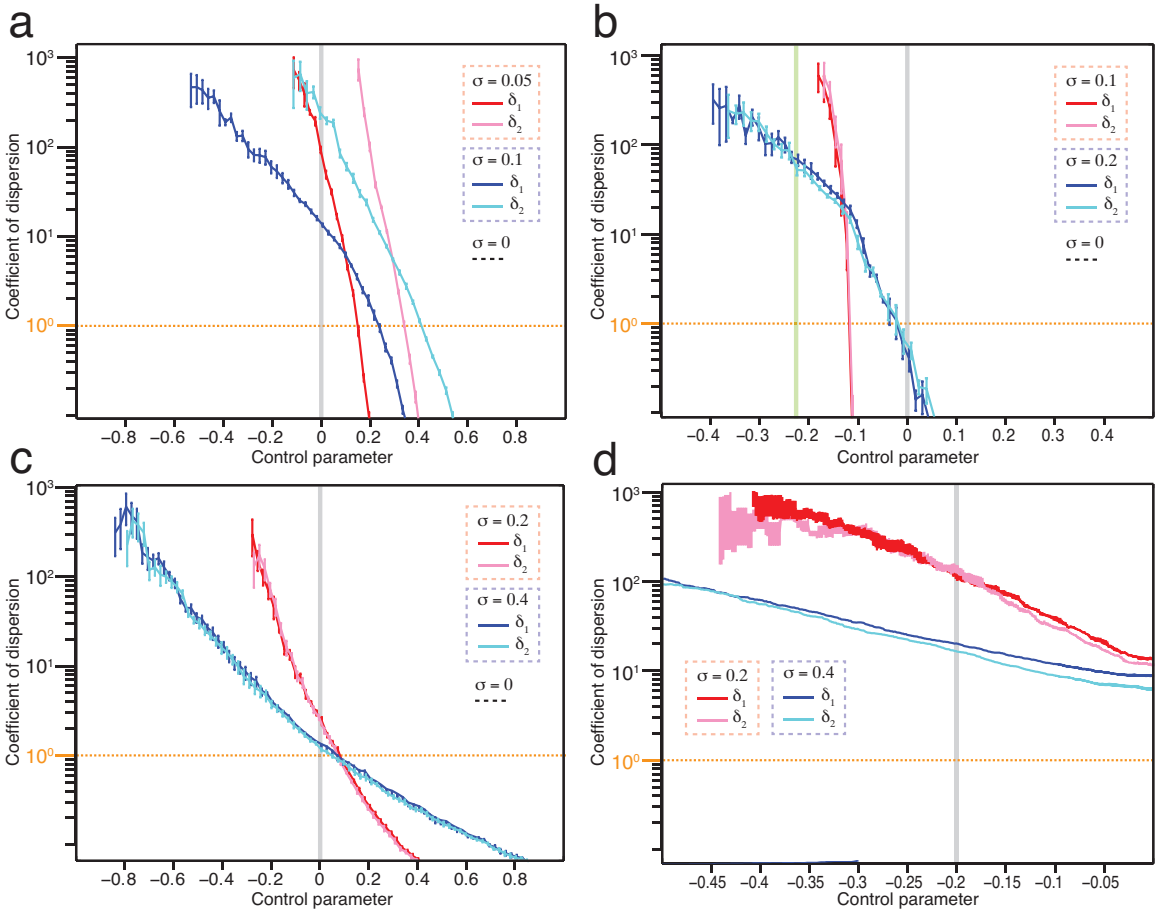
a
b
c
d
Coefficient of dispersion
Control parameter
σ = 0.05
σ = 0.1
σ = 0.2
σ = 0.4
σ = 0
δ1
δ2

Table 10.1. Distinguishing features of selected bifurcations. Displayed in the table above are the expected characteristics of each bifurcation described by both qualitative appearances and quantitative measures.

Bifurcation	Time Series	Phase Portrait	Coefficient of Dispersion	Displacement Histogram	Spike Rate	Amplitude (peak-to-peak)	Vector Strength	Quality (spectrum)
Supercritical Hopf	"Ringing"	• $\mu<0$: point • $\mu>0$: cycle • Cycle grows with μ • Symmetric	• Curves shift with threshold • Estimated μ_c on unstable side of bifurcation	• Multimodal only on unstable side of bifurcation	• Maximum spike rate • Change in threshold shifts curve but does not change its shape • Spike rates converge	• Amplitude grows with μ	• Low for all values of μ	• Coherent on unstable side of the bifurcation
Subcritical Hopf	"Bursting"	• $\mu<0$: point • $\mu>0$: large cycle • Symmetric • Stable point within cycle	• No shift with threshold • Estimated μ_c on stable side of bifurcation	• Multimodal only on unstable side of saddle-node of limit cycles	• No maximum spike rate • Change in threshold changes shape of the curve • Spike rates converge	• Amplitude grows little with μ	• Low for all values of μ	• Coherent on unstable side of the bifurcation • Coherent in excitable regime
Saddle- Node on Invariant Cycle	"Spiking"	• $\mu<<0$: point • Fixed point resides on cycle • Probability of residence at fixed point changes with μ • Asymmetric	• No shift with threshold • Estimated μ_c on unstable side of bifurcation	• Multimodal on unstable or stable side of bifurcation	• No maximum spike rate • Change in threshold changes shape of the curve • Spike rates converge	• Amplitude remains constant	• High near bifurcation • Low far from the bifurcation in unstable and stable regimes	• Coherent in unstable regime far from the bifurcation • Incoherent near the bifurcation
Cusp	"Switching"	• $\mu<\mu_c$: one point • $\mu>\mu_c$: two stable points • Probability of residence at fixed point changes with μ	• Coefficient always exceeds one	• Multimodal only in the bistable regime	• Maximum spike rate • Change in threshold changes shape of the curve • Spike rates do not converge	• Amplitude remains constant	• High near bifurcation • Low far from the bifurcation in unstable and stable regimes	• Incoherent for all μ

SECTION 10.5: *Noisy Simulations of Hair-Bundle Motility*

We next wished to test the classification scheme outlined in the previous section on a model of hair-bundle motility. Given only time-series data, is it possible to distinguish among bifurcation types for a detailed model in the presence of noise? To address this question, we performed simulations of an artificial hair bundle described by equations 6.4 and 6.5 and the same parameters used in *Chapter 6*. The noise terms in x and f were equal and possessed standard deviations of 0.05, 0.1, 0.2, 0.4, 0.5, and 1. All simulations were integrated using the Euler-Murayama method over 10^6 time steps and 5×10^8 points. We performed six simulations that scanned distinct regions of the bundle's state diagram. Five scans across 500 values of constant force were implemented at stiffnesses of 1.5, 1.75, 2, 2.5, and 3. One scan across 500 values of total stiffness was completed at a constant force of 0. Each time series was subdivided into five equal segments for averaging.

By employing analyses on only the spike rate and coefficients of dispersion, we may successfully classify hair-bundle behavior according to one or more bifurcation types (Figure 10.6). Holding an artificial hair bundle at a stiffness of 2 and increasing the force from 0 to 2 reveals behavior consistent with a subcritical Hopf or SNIC bifurcation (Figure 10.6a). In the absence of noise, the bundle's spike rate rises sharply to a near-constant value at a critical value of constant force. As expected, additive noise obscures the sharp rise in spike rate. Further increases in the noise level reduce the slope of the rise in spike rate. Changes to the peak-detection threshold do not change the estimated

spike rate. This behavior is consistent with either a subcritical Hopf or SNIC bifurcation with a low noise level.

We next characterized an artificial bundle held at a constant force of 0 and stiffnesses ranging from 1.5 to 3.5 (Figure 10.6b). In the case without noise, spontaneous hair-bundle oscillations emerge with a non-zero frequency. The frequency falls with a decrease in total stiffness. In the presence of noise, the rise in spike rate decreases in slope. Unlike the scan through force, however, the spike-rate relationship depends on the peak-detection threshold. Any change in the peak-detection threshold induces a shift of the curve. This pattern is consistent with behavior near a supercritical Hopf bifurcation. Unlike the pattern in spike rate from the normal form in the previous section, however, the spike rate changes with the control parameter in this scenario. A change in the frequency of oscillation with the control parameter is also possible in normal form of a supercritical Hopf bifurcation if the imaginary part of the cubic coefficient is of the correct sign. Thus, the bundle's behaviors remain consistent with those of a supercritical Hopf bifurcation.

To find both the location of each bifurcation and further distinguish among bifurcation types, we calculated coefficients of dispersion for the same hair-bundle simulations (Figure 10.6c,d). When the hair bundle is held at one stiffness and its constant force increased, the coefficient of dispersion crosses a threshold of one near but on the unstable side of the bifurcation at all noise levels (Figure 10.6c). However, changes to the peak-detection threshold cause no change in the location at which the coefficient matched one. For an artificial hair bundle poised at a constant force of zero

and various stiffness values, the coefficients of dispersion once again cross a threshold of one near but on the unstable side of the bifurcation (Figure 106.d). However, a change in the peak-detection threshold induces a shift in the point at which the coefficient matches one. These data support the hypothesis that the behavior of a bundle upon scanning through force at low stiffness occurs near either a subcritical Hopf or a SNIC bifurcation, whereas the behavior for a bundle poised at zero force and multiple stiffnesses may be described by a supercritical Hopf bifurcation.

Indeed, the hair bundle's theoretical state diagram indicates that a subcritical Hopf bifurcation and a supercritical Hopf bifurcation were crossed respectively in the force and stiffness scans presented here (167). However, analysis of only the spike rates and coefficients of dispersion do not possess distinguishing characteristics between a subcritical Hopf bifurcation and a SNIC bifurcation. As shown in Table 10.1, the clearest distinguishing features may be found in the time series and phase portraits of the bundle's motion. Results from simulations of hair-bundle motility reveal that the artificial bundle exhibits spiking and possesses in its phase portrait one or two regions of high probability that reside on a cycle and that resemble fixed points (not shown). The relative intensity between these points changes with force, such that their probabilities become equal at a constant force of zero. Although these data imply that the bundle operates near a SNIC bifurcation, no such bifurcation is present near any of the selected operating points (167). Instead, the artificial bundle may exhibit SNIC-like behavior due to its operation near both a subcritical Hopf bifurcation and a fold bifurcation. Alternatively, the addition of an offset in the normal form of a subcritical Hopf

bifurcation could account for this pattern of behavior (not shown). The artificial hair bundle nonetheless exhibits behavior in the presence of noise analogous to type I excitability of neurons when its constant force is increased at low stiffness. Upon an increase in the bundle's stiffness at zero force, however, the system exhibits behavior in the presence of additive noise consistent with that of type II neuronal excitability.

Figure 10.6. Two classes of behavior in an artificial hair bundle. (a) An artificial hair bundle was poised at a total stiffness of 2 and 500 constant forces ranging from 0 through 2 and its motion tracked over time. In the absence of noise, the bundle exhibits spontaneous oscillations whose frequency rises discontinuously at a critical value of the force parameter. In the presence of of noise, the slope of the spike rate relationship decreases as a function of the noise level, obscuring the discontinuity in frequency of the noiseless case. Changes in the peak-detection threshold did not appreciably change the spike-rate relationship. (b) An artificial bundle was poised at a constant force of 0 and at 500 stiffnesses ranging from 1.5 through 3.5 and its motion monitored over time. In the absence of noise, spontaneous oscillations with non-zero frequency emerge at a critical value of the total stiffness, and the frequency of oscillation declines with decreased stiffness. Adding noise causes the slope of the rise in spike rate to decrease. Changing the peak-detection threshold shifts the spike rate curves. (c) The coefficients of dispersion for the same bundle in (a) reveal a dependence of the force at which the coefficient crosses one on the noise level. Here an increased noise level shifts rightward the point at which the coefficient of dispersion matches one. However, changes in the magnitude of the peak-detection threshold do not change the point at which the coefficient exceeded this threshold. (d) The coefficients of dispersion for the artificial bundle in (b) indicate a dependence of the coefficient on both noise and the peak-detection threshold. As expected, an increase in the noise level induces a rightward shift in the point at which the coefficient of dispersion matches one. Furthermore, changing the peak-detection threshold causes a shift in the coefficient's curve. All error bars represent standard errors of the means of five iterations.

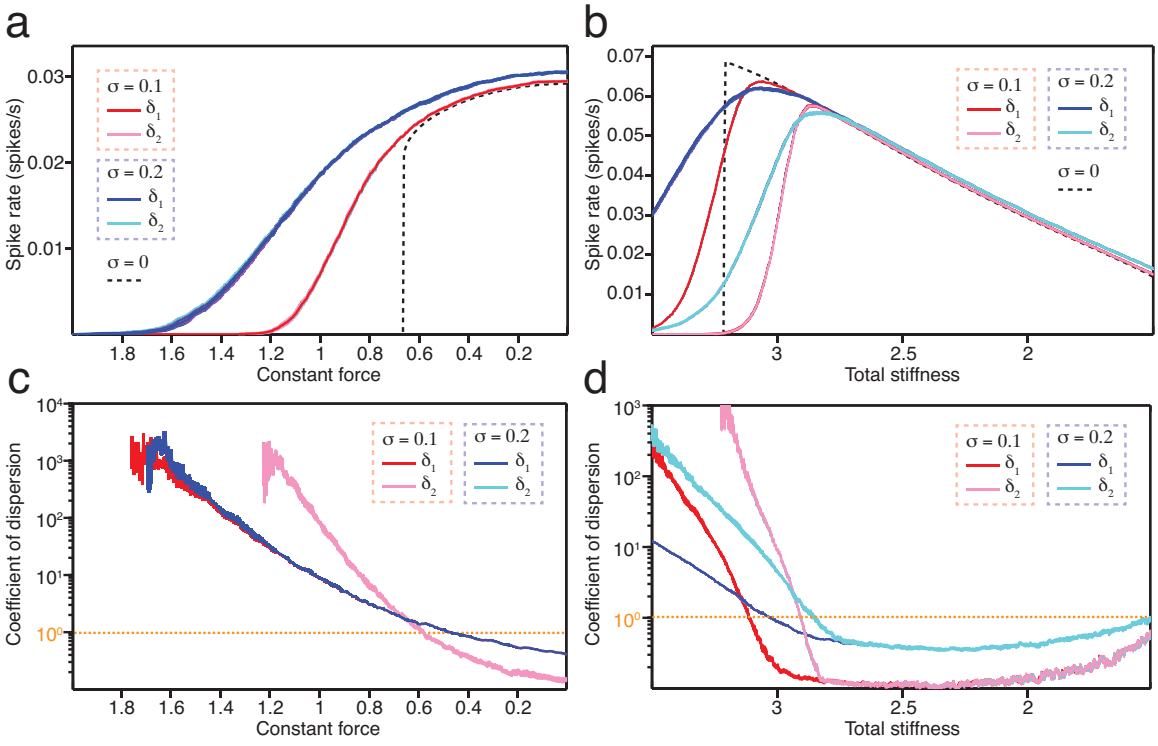
a
b
c
d
Spike rate (spikes/s)
Constant force
Total stiffness
Coefficient of dispersion
σ = 0.1
σ = 0.2
σ = 0
δ1
δ2

SECTION 10.6: *Experimental Evidence of Hair-Bundle Excitability*

Hair bundles possess state diagrams that comprise multiple bifurcations. When coupled to an accessory structure *in vivo*, a bundle may operate in the vicinity of one or more bifurcations, each of which generates a unique topology that promotes specific activity for that region of the bundle's state diagram. Here we experimentally evaluate the hypothesis that hair bundles of the bullfrog's sacculus exhibit at least two classes of excitable behavior.

We coupled the kinociliary bulb a large-diameter hair bundle to the tip of a flexible glass stimulus fiber and delivered increasing values of constant force with a mechanical-load clamp at a load stiffness of 50 $\mu N \cdot m^{-1}$ (Figure 10.7a-c). The bundle spontaneously oscillated for small values of constant force, but developed asymmetric oscillations that resembled downward spikes as the force was increased (Figure 10.7a). The period between successive downward excursions increased with an elevation of constant force until all spikes were suppressed at a constant force of 40 pN. A phase portrait of the bundle's motion at this operating point depicted a single fixed point. However, reducing the force to 29 pN unveiled a limit cycle upon which rested a fixed point. When the bundle was subjected to smaller values of constant force, its trajectory followed the limit cycle with greater probability. Surprisingly, another fixed point appeared within the limit cycle for constant forces less than or equal to 19 pN. Unlike the symmetric phase portrait of a subcritical Hopf bifurcation, this fixed point rested near the edge of the cycle. This implies that the hair bundle operated in the vicinity of a subcritical Hopf bifurcation with a constant offset.

As the constant force imposed on the hair bundle decreased, spikes emerged at a near-zero frequency and grew with further decreases in force (Figure 10.7b). Increasing the peak-detection threshold caused a rightward shift in the point at which the lowest-frequency spikes were detected. However, the spike rates estimated from all thresholds converged to the same for small values of constant force.

In order to approximate the location of a bifurcation, we calculated the coefficients of dispersion from the estimated spike rates at each peak-detection threshold (Figure 10.7c). The coefficients surpassed one for all thresholds when the constant force exceeded 22-24 pN. Because this measure systematically estimates the bifurcation's location on the unstable side of the deterministic bifurcation, we defined this as a lower bound on the critical value of constant force. The precise location of the bifurcation lies between the constant force at which the spike rate was zero and the force at which the coefficients of dispersion exceeded this threshold.

The above observations indicate that this hair bundle operated in the vicinity of a subcritical Hopf bifurcation with a constant offset. Both the bundle's spiking behavior and phase portraits were consistent with the trajectory of a system near this bifurcation. Furthermore, existence of a fixed point within a limit cycle provided strong support of this conclusion. The relationship of the hair bundle's spike rate and its coefficients of dispersion with changes in constant force agreed with stochastic simulations of a subcritical Hopf bifurcation. Finally, by noting the points at which the bundle's activity was suppressed and the coefficients of dispersion exceeded a threshold, we estimated that a subcritical Hopf bifurcation occurs at a constant force between 22 and 35 pN.

We subjected a second large-diameter hair bundle to a constant force of 0 pN and load stiffnesses ranging from 150 through 900 $\mu N \cdot m^{-1}$ (Figure 10.7d-f). The bundle oscillated spontaneously with high frequency and low amplitude at a load stiffness of 900 $\mu N \cdot m^{-1}$ (Figure 10.7d). Reducing the load stiffness induced a decrease in frequency and a corresponding increase in the amplitude of oscillation. Representing the bundle's motion in phase space revealed limit cycles whose diameters depended on load stiffness. As expected, a decrease in load stiffness caused an increase in the size of the limit cycle.

The bundle's oscillations emerged with a high spike rate at a load stiffness of 900 $\mu N \cdot m^{-1}$; the spike rate then fell with a decrease in stiffness (Figure 10.7e). Increasing the magnitude of the peak-detection threshold reduced the estimated spike rate at all operating points. The oscillations remained coherent for all load stiffnesses, indicating that the bundle's operating points all resided on the unstable side of a bifurcation (Figure 10.7f).

These results imply that this bundle operates in the vicinity of a supercritical Hopf bifurcation. Phase portraits of the bundle's motion revealed a limit cycle whose size grew with a decrease in load stiffness. This topology indicated a growth in the amplitude of oscillation with a change in control parameter. Furthermore, the bundle's spike rate achieved a maximum at the highest load stiffness, consistent with stochastic simulations of hair-bundle motility and the emergence of oscillations with non-zero frequency near a supercritical Hopf bifurcation. Because the coefficients of dispersion never exceeded one and the spike rate remained non-zero, the bifurcation rests at a load stiffness above 900 $\mu N \cdot m^{-1}$.

Taken together, these results indicate that a hair bundle exhibits at least two classes of behavior. For a low value of load stiffness, an increase in constant force coerces the bundle's operating point across a subcritical Hopf bifurcation with an asymmetric phase portrait. This results in behavior that closely resembles type I neuronal excitability. When a bundle is subjected to a constant force of 0 pN and its stiffness is increased, the bundle's operating point crosses a supercritical Hopf bifurcation. Within this region of state space, a hair bundle exhibits mechanical excitability akin to the type II neuronal excitability.

Figure 10.7. Two classes of hair-bundle behavior. (a-c) A hair bundle was subjected to a load stiffness of 50 $\mu N \cdot m^{-1}$ and constant forces ranging from -10 to 50 pN and its motion tracked over a course of 30 s. (a, *left*) At a constant force of 40 pN, the bundle's position in time revealed complete suppression of spontaneous activity. Decreasing the force caused downward excursions to emerge at low frequency and further decreases in constant force increased the frequency of each excursion. (a, *right*) Phase portraits of the bundle's motion indicate the presence of a single fixed point at a constant force of 40 pN. Reducing the force to 29 pN unveiled a limit cycle upon which rested a fixed point. Further decreases in constant force caused the bundle to reside with greater probability on the cycle. For forces below 19 pN, a fixed point appeared within the limit cycle. (b) The bundle's spike rate grew with a reduction in constant force. The position and slope of the rise in spike rate depended on the value of the peak-detection threshold. (c) Coefficients of dispersion indicate a loss of coherence for values of constant force exceeding 22-24 pN. (d-f) A second hair bundle was subjected to a constant force of 0 pN and load stiffnesses ranging from 150 through 900 $\mu N \cdot m^{-1}$ and its position monitored over the course of 30 s. (d, *left*) The bundle spontaneously oscillated with high frequency and low amplitude at a load stiffness of 660 $\mu N \cdot m^{-1}$. Reducing the load stiffness caused the bundle's oscillations to decreased in frequency and increase in amplitude. (d, *right*) Phase portraits of the bundle's motion reveal a limit cycle whose diameter increased with a decrease in load stiffness. (e) The hair bundle's spike rate achieved its maximum for the largest value of load stiffness, and the spike rate fell as the stiffness decreased. (f) Coefficients of dispersion indicate that the bundle's oscillations remained coherent for all values of load stiffness. This suggests that all operating points reside on the unstable side of a bifurcation. All data were acquired at a scan rate of 1 kHz. The stimulus fiber possessed a stiffness of 260 $\mu N \cdot m^{-1}$ and a drag coefficient of 130 $nN \cdot s \cdot m^{-1}$.

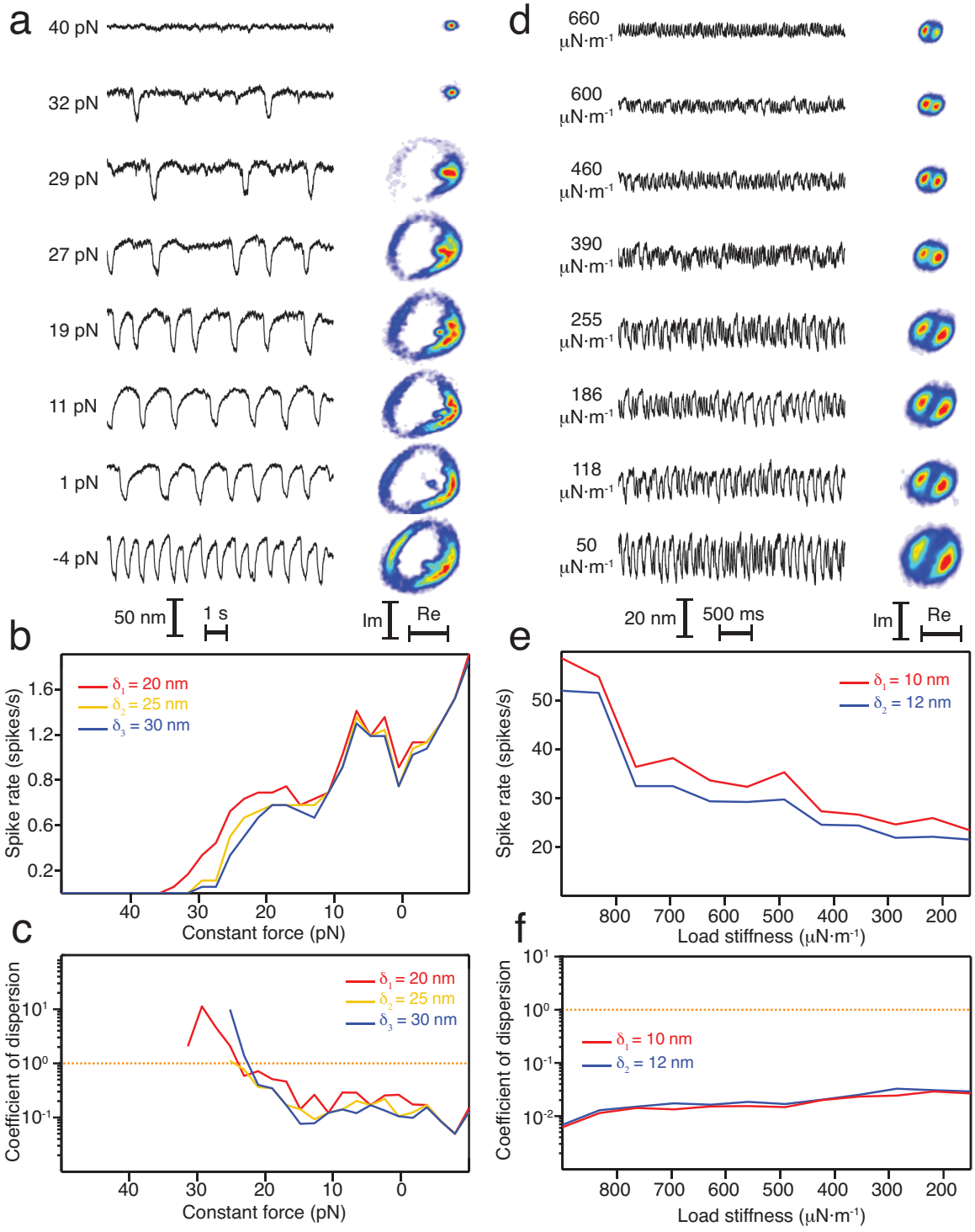
a
40 pN
32 pN
29 pN
27 pN
19 pN
11 pN
1 pN
-4 pN
50 nm
1 s
Im
Re
d
660 μN·m-1
600 μN·m-1
460 μN·m-1
390 μN·m-1
255 μN·m-1
186 μN·m-1
118 μN·m-1
50 μN·m-1
20 nm
500 ms
Im
Re
b
δ1 = 20 nm
δ2 = 25 nm
δ3 = 30 nm
Spike rate (spikes/s)
Constant force (pN)
e
δ1 = 10 nm
δ2 = 12 nm
Spike rate (spikes/s)
Load stiffness (μN·m-1)
c
δ1 = 20 nm
δ2 = 25 nm
δ3 = 30 nm
Coefficient of dispersion
Constant force (pN)
f
δ1 = 10 nm
δ2 = 12 nm
Coefficient of dispersion
Load stiffness (μN·m-1)

SECTION 10.7: *Discussion of Results*

Under appropriate conditions, neurons exhibit electrical excitability that may be divided into at least two classes of behavior (166, 229). Each type of excitability bestows a neuron or network of neurons with a distinct pattern of sensory responsiveness. A type I excitable neuron may modulate its firing rate with the magnitude of a stimulus and functions as an integrator. A type II excitable neuron, on the other hand, generates action potentials with a frequency that remains insensitive to the stimulus magnitude. Instead, type II neurons resonate in response to periodic stimuli (235).

Each class of excitability can be modeled as a system operating in the vicinity of one or more bifurcations. Poising the system's operating point near a SNIC bifurcation or an asymmetric subcritical Hopf bifurcation generates behavior consistent with type I excitability. If the system instead operates near a supercritical Hopf bifurcation or a symmetric subcritical Hopf bifurcation, its behavior resembles that of a type II excitable system.

Classification of a biological system by its operation near a particular bifurcation presents a remarkable challenge. In the presence of noise, behaviors in a deterministic system become obscured. Both the location of the bifurcation and its hallmark features are thus clouded in a stochastic dynamical system. To overcome this predicament, we developed a protocol that permits classification of a system by bifurcation type when provided with only noisy time-series data. This diagnostic method satisfies multiple conditions. First, the protocol requires nothing more than an array of signals generated from a system across operating points near a bifurcation. Second, classification remains

possible in the absence of stimulation. This simplifies the experimental paradigm and renders the method applicable to systems in which perturbation is not possible. Third, the method functions well at high noise levels. Unlike electrical circuits or similar systems with a relatively high signal-to-noise ratio, biological processes succumb to significant levels of additive noise. Our method permits classification in these extreme scenarios. Fourth, the diagnostic criteria rely on few, if any, choices by the experimenter. The classification scheme requires only that the number of peak-detection thresholds be chosen, but not the values of these thresholds. Additionally, thresholds may be placed on test statistics such as Hartigan's dip statistic. All other analyses remain automated. Finally, multiple criteria may be employed to evaluate at least four types of bifurcation.

By applying only a portion of this protocol to the behaviors of both artificial and real hair bundles, we successfully identify two bifurcation types near which the bundles operate. Along the high-stiffness arc of a hair bundle's oscillatory regime, the bundle operates near a supercritical Hopf bifurcation. This accords with results described in previous chapters. When a hair bundle's operating point exits the oscillatory regime through an increase in constant force at low stiffness, it crosses an asymmetric subcritical Hopf bifurcation. This finding is contrasted with previous predictions that hair bundles exhibiting this behavior operate near a SNIC bifurcation (243-245). Although a SNIC bifurcation may permit behavior that qualitatively resembles the hair-bundle spiking, our results indicate that the bundle instead operates in the vicinity of a subcritical Hopf bifurcation.

Here we revealed in hair bundles mechanical excitability analogous to the electrical excitability of neurons. Although types I and II excitability classically refer to the behavior of neurons or neuronal populations, a single hair bundle displays phenomena consistent with either class of excitability. An auditory bundle may thus respond optimally to periodic forces when poised near a supercritical Hopf bifurcation, whereas a vestibular hair bundle can detect force pulses when operating near a subcritical Hopf bifurcation. This subdivision of a hair bundle's state diagram highlights the dual mechanosensory roles of bundles in auditory and vestibular systems.

CHAPTER 11

Concluding Remarks

From the tympanal ear of the insect through the cochlea of the bat, hearing organs are endowed with an active process that augments auditory signal transduction. Within these organs, sensory cilia or hair bundles serve as mechanical antennae that transduce forces into biochemical signals. The cilia of insects and the bundles of vertebrates possess an active process, granting hearing organs remarkable sensory fidelity. However, hair bundles are not restricted to audition. In otolith organs of the vestibular system, bundles detect static forces and force pulses. In the cristae of semicircular canals and lateral-line organs, hair bundles respond to hydrodynamic stimuli. Although hair bundles behave differently across such receptor organs, the two ingredients required for active hair-bundle motility—nonlinear channel gating and adaptation—have been preserved in evolution.

What differs from organ to organ is a bundle's microenvironment. A hair bundle may be free-standing or it may be coupled to a tectorial membrane, an otolithic membrane, a cupula, or a sallet. Each structure can impart a load stiffness, a drag, an inertial load, and a constant force to the bundle. We find that changing a bundle's load controls its function, promoting a broad array of mechanosensory roles in signal detection.

Dynamical systems describe behaviors ranging from the motion of a pendulum through the economy of a nation to the cycles of glaciation. By applying dynamical-systems theory to hair-bundle mechanics, we can make a set of testable predictions that captures the active behaviors of these mechanosensitive organelles. Unique to this work is the design and implementation of a mechanical-load clamp that permits direct adjustment of up to four of a hair bundle's control parameters. By using this system, we systematically explored the state diagrams of multiple bundles. Upon poising a hair bundle's operating point within different regions of its state diagram, we found that the bundle can behave as one of many distinct types of receptor: an oscillator, a quiescent resonator, an edge detector, or an integrator. The bundle's state diagram may be subdivided into low- and high-stiffness regimes that correspond respectively to vestibular and auditory modes of function. Strikingly, a hair bundle from an amphibian vestibular organ can respond in a manner qualitatively similar to that of a mammalian auditory organ.

Bundles may also flaunt mechanical excitability akin to the electrical excitability of neurons. To test this notion, we designed a diagnostic protocol that permits classification of any noisy system by the bifurcation near which it operates. The application of this method requires only a set of time series from the system as its operating point is adjusted. Not only does the protocol possess general applicability, but its simple methods may be applied to biological processes that succumb to high levels of additive noise. By employing this approach, we successfully classified a hair bundle's

behavior into two distinct types, each analogous to a different type of neuronal excitability.

Organelles have evolved to serve distinct functions in various contexts. The hair bundle, by contrast, has maintained a remarkably stable structure throughout the evolution of vertebrates. Evolution has instead acted upon the mechanical load imposed on a bundle. Accessory structures that impart these loads might dictate the bundle's sensory role and serve to optimize mechanosensitivity in each receptor organ. Hair bundles thus possess both an essential structural similarity and a capacity to operate as many types of detector, and it is a bundle's mechanical niche that grants it a distinct mechanosensory function.

APPENDIX I

Supplemental Analyses and Derivations

Here we review additional mathematical concepts not described in the main text of this work. Such derivations serve to supplement mathematical descriptions of hair-bundle motility.

SECTION I.1: *Normal Form of the Hopf Bifurcation*

Consider first the following planar system

$$\dot{x}_1 = \mu x_1 - x_2 + A x_1 (x_1^2 + x_2^2), \tag{I.1}$$

$$\dot{x}_2 = x_1 + \mu x_2 + A x_2 (x_1^2 + x_2^2). \tag{I.2}$$

Let $z = x_1 + i x_2$ and $\overline{z} = x_1 - i x_2$. Equations I.1 and I.2 then become

$$\dot{z} = \dot{x}_1 + i\dot{x}_2 = \mu x_1 - x_2 + A x_1 (x_1^2 + x_2^2) + i\left[x_1 + \mu x_2 + A x_2 (x_1^2 + x_2^2) \right], \tag{I.3}$$

which simplifies to

$$\dot{z} = \mu z + i z + A(x_1^3 + i x_2^3 + x_1 x_2^2 + i x_1^2 x_2). \tag{I.4}$$

We also note that

$$z^2 = (x_1 + i x_2)(x_1 + i x_2) = x_1^2 + 2 i x_1 x_2 - x_2^2, \tag{I.5}$$

$$z^2 \overline{z} = (x_1^2 + 2 i x_1 x_2 - x_2^2)(x_1 - i x_2) = x_1^3 + i x_2^3 + x_1 x_2^2 + i x_1^2 x_2. \tag{I.6}$$

Combining equations I.4 and I.5 yield the normal form of the Hopf bifurcation up to the third-order term

$$\dot{z} = \mu z + iz + Az^2\bar{z} \,. \tag{I.7}$$

Linear stability analysis of equations I.1 and I.2 reveals the conditions for a Hopf bifurcation. The Jacobian matrix J of the planar system at the fixed point $(x_1^*, x_2^*) = (0,0)$ is

$$J = \begin{pmatrix} \mu & -1 \\ 1 & \mu \end{pmatrix}. \tag{I.8}$$

For a Hopf bifurcation to occur, the determinant of J must exceed zero, and the trace of J must cross zero. This occurs when

$$Tr(J) = 2\mu = 0 \,, \tag{I.9}$$

$$Det(J) = \mu^2 + 1 > 0 \,. \tag{I.10}$$

Because $Det(J) > 0$ for all μ, a Hopf bifurcation occurs at $\mu = 0$. The real parts of the eigenvalues of the system $\lambda_{1,2} = \mu \pm i$ reveal topological classifications. For $\mu < 0$, the fixed point is a hyperbolic attractor, and the point is a hyperbolic repeller for $\mu > 0$. When $\mu = 0$, the system has a non-hyperbolic fixed point. Thus, the system is monostable for $\mu \leq 0$ and self-oscillates for $\mu > 0$.

For a supercritical Hopf bifurcation, $A < 0$ and the origin is globally asymptotically stable. For a subcritical Hopf bifurcation, $A > 0$ and the origin is locally asymptotically stable but is surrounded by an unstable circular cycle. An alternative representation of the Hopf normal form in polar coordinates follows

$$\dot{\rho} = \rho(\mu + i\omega + A\rho^2) \,, \tag{I.11}$$

$$\dot{\varphi} = 1 \,, \tag{I.12}$$

in which ω is the characteristic frequency of the Hopf oscillator and μ is a control parameter. Here it becomes apparent that the stable limit cycle can be approximated by a circle with radius $\sqrt{\mu}$ for a supercritical Hopf bifurcation or an unstable limit cycle with radius $\sqrt{-\mu}$ for a subcritical Hopf bifurcation.

SECTION I.2: *Hopf Bifurcation in the van der Pol Oscillator*

Consider the van der Pol oscillator governed by

$$\ddot{x} + \mu(x^2 - 1)\dot{x} + x = a\,. \tag{I.13}$$

This equation can be rewritten as

$$\dot{x} = y\,, \tag{I.14}$$

$$\dot{y} = a - x - \mu(x^2 - 1)y\,. \tag{I.15}$$

There exists an x-nullcline at $y = 0$ and a y-nullcline at $y = (a\text{-}x)/(\mu(x^2\text{-}1))$: the two nullclines intersect at $x = a$. The Jacobian of equations I.14 and I.15 is

$$J = \begin{pmatrix} 0 & 1 \\ -1 - 2\mu yx & -\mu(x^2 - 1) \end{pmatrix}. \tag{I.16}$$

The trace and determinant of the Jacobian at the fixed point $(a,0)$ are

$$Det(J) = 1 + 2\mu yx = 1 + 2\mu 0a = 1\,, \tag{I.17}$$

$$Tr(J) = -\mu(x^2 - 1) = -\mu(a^2 - 1)\,. \tag{I.18}$$

Because $Det(J) > 0$, $Tr(J)$ must switch signs and equal zero at a Hopf bifurcation. This is satisfied when

$$0 = -\mu(a^2 - 1)\,. \tag{I.19}$$

Thus, a Hopf bifurcation occurs when $\mu = 0$ or $a = \pm 1$ in the system described by equation I.13.

SECTION I.3: *Analysis of a Simplified Hair-Bundle Model*

A hair bundle's motion may be described by the following simplified equations:

$$\dot{X} = -\frac{K_T}{\xi_T} X + \frac{A}{\xi_T} f_a, \tag{I.20}$$

$$\dot{f}_a = \frac{B}{\tau_a} X - \frac{f_a}{\tau_a}, \tag{I.21}$$

in which X is the bundle's position, f_a is the force produced by the adaptation motors, K_T is the bundle's total stiffness, ξ_T is the bundle's total drag coefficient, τ_a is the relaxation time of adaptation, A is a scaling parameter for the force of adaptation, and B is a parameter linking the force of adaptation to motion of the bundle. Note that these equations do not include the same complexities and cubic components as the dynamical models introduced in *Chapter 4*. Here we use a simplified system to illustrate the effects of stiffness, damping, and the rate of adaptation on the behavior near a supercritical Hopf bifurcation.

The equation can be written in matrix form, given by

$$\begin{pmatrix} \dot{X} \\ \dot{f}_a \end{pmatrix} = J = \begin{pmatrix} -\frac{K_T}{\xi_T} & \frac{A}{\xi_T} \\ \frac{B}{\tau_a} & -\frac{1}{\tau_a} \end{pmatrix}. \tag{I.22}$$

For the system to reside on the unstable side of a bifurcation, the trace and determinant of J must both exceed zero. This occurs when

$$Tr(J) = -(\frac{K_T}{\xi_T} + \frac{1}{\tau_a}) > 0, \tag{I.23}$$

$$Det(J) = \frac{K_T - AB}{\xi_T \tau_a} > 0 . \tag{I.24}$$

Assuming that the drag coefficient and relaxation time of adaptation are both positive, then equation I.23 can be satisfied only when $K_T < 0$. Thus, negative hair-bundle stiffness is a prerequisite for a bundle to reside on the unstable side of a bifurcation and to spontaneously oscillate when constrained by a nonlinear term. Additionally, we see from the condition of negative stiffness that $K_T > AB$ to satisfy equation I.24. In other words, the magnitude of the bundle's negative stiffness must exceed any passive compliances in the hair bundle.

At the bifurcation, $Tr(J) = 0$, yielding

$$K_T = -\frac{\xi_T}{\tau_a} . \tag{I.25}$$

The hair bundle will oscillate at an angular frequency defined by the square root of $Det(J)$, such that

$$\omega_H = \sqrt{Det(J)} = \sqrt{\frac{\frac{\xi_T}{\tau_a} - AB}{\xi_T \tau_a}} . \tag{I.26}$$

When AB is negligible, equation I.26 yields

$$\omega_H \approx \sqrt{\frac{\frac{\xi_T}{\tau_a}}{\xi_T \tau_a}} = \sqrt{\frac{1}{\tau_a^2}} = \frac{1}{\tau_a} . \tag{I.27}$$

At this limit, the hair bundle oscillates with a frequency defined by the relaxation time of adaptation. Adjusting this parameter through chemical means should subsequently change the frequency of spontaneous oscillation and the total stiffness of the bundle. For

example, increasing the relaxation time occurs with a decrease in the bundle's total stiffness and a corresponding decrease in the frequency of oscillation. Although the system differs from the more descriptive models in *Chapter 4*, this simplified model captures the crossing of a bifurcation and the effects of bundle stiffness on the frequency of spontaneous oscillation.

SECTION I.4: *The Cusp Bifurcation Diagram*

Consider the normal form of a cusp bifurcation:

$$\dot{X} = r_2 + r_1 X - X^3 . \tag{I.28}$$

Fold bifurcations occur on the (r_1,r_2)-plane defined by the following set of equations:

$$f(X) = r_2 + r_1 X - X^3 = 0 , \tag{I.29}$$

$$f'(X) = r_1 - 3X^2 = 0 . \tag{I.30}$$

One can solve for the control parameters r_1 and r_2 by eliminating X in equations I.29 and I.30

$$X = \pm\sqrt{\frac{r_1}{3}} , \tag{I.31}$$

$$r_2 \pm r_1\sqrt{\frac{r_1}{3}} \pm \left(\frac{r_1}{3}\right)^{3/2} = 0 . \tag{I.32}$$

Assuming that $r_1 > 0$, equation I.32 yields a solution for lines of saddle-node bifurcations:

$$r_2 = \pm\frac{2}{3\sqrt{3}} r_1^{3/2} . \tag{I.33}$$

In this system, a cusp bifurcation occurs at $r_1 = 0$. Fold bifurcations defined by equation I.33 enclose a region for $r_1 > 0$ with three stable points, and the surrounding region possesses only one stable point.

SECTION I.5: *Saddle-Node of Limit Cycles Bifurcation*

Consider the normal form of a Hopf bifurcation given by

$$\dot{r} = \mu r + Br^3 + Cr^5, \tag{I.34}$$

$$\dot{\theta} = 1, \tag{I.35}$$

in which B and C are complex numbers with real and imaginary parts respectively (B_R,C_R) and (B_I,C_I). For a supercritical Hopf bifurcation $B_R < 0$. In the subcritical Hopf bifurcation, $B_R > 0$ and $C_R < 0$. A Hopf bifurcation occurs at $\mu = 0$ in both cases. For the subcritical Hopf bifurcation, an unstable limit cycle and a higher-order stable limit cycle coexist until they meet and annihilate one another at a saddle-node of limit cycles (SNLC) bifurcation. To find the SNLC, set equation I.34 equal to zero and solve for the radius of the trajectory:

$$0 = \mu r + Br^3 + Cr^5, \tag{I.36}$$

$$r^2(B + Cr^2) = -\mu, \tag{I.37}$$

$$r_1 = \pm \frac{\sqrt{-\frac{B}{C} - \sqrt{\frac{B^2 - 4C\mu}{C}}}}{\sqrt{2}}, \tag{I.38}$$

$$r_2 = \pm \frac{\sqrt{-\frac{B}{C} + \sqrt{\frac{B^2 - 4C\mu}{C}}}}{\sqrt{2}}. \tag{I.39}$$

The SNLC occurs at the point where $r_1 = r_2$. Combining equations I.38 and I.39 and solving for the control parameter μ yields

$$\mu = \frac{B^2}{4C}. \tag{I.40}$$

When B = 1 and C = -1, the SNLC occurs at μ = -0.25. When B = -1 and C = 0, the system now describes a supercritical Hopf bifurcation with one stable limit cycle of radius $r = \sqrt{\mu / B}$.

SECTION I.6: *Saddle-Node on Invariant Cycle Bifurcation*

The one-dimensional normal form of a SNIC bifurcation follows

$$\dot{\theta} = 1 - \cos\theta + (1 + \cos\theta)\mu \,. \tag{I.41}$$

When equation I.41 equals zero, the system has two fixed points at

$$\theta^* = \pm\cos^{-1}\left(\frac{-1-\mu}{-1+\mu}\right). \tag{I.42}$$

These fixed points are purely imaginary when $\mu > 0$ and purely real when $\mu < 0$. In the case where $\mu = 0$, there is only one fixed point at $\theta^* = 0$. Thus, there exists at least one fixed point on the invariant cycle only when $\mu \leq 0$.

Solving for the derivative of equation I.41 at the fixed point yields

$$0 = \sin\left(\pm\cos^{-1}\left(\frac{-1-\mu}{-1+\mu}\right)\right)(1-\mu) \tag{I.43}$$

The constraint from equation I.43 yields a bifurcation at $\mu = 0$.

The period of oscillation near a SNIC bifurcation can be found by finding the time required for θ to complete a cycle from 0 to 2π

$$T = \int_0^{2\pi} dt = \int_0^{2\pi} \frac{dt}{d\theta} d\theta = \int_0^{2\pi} \frac{d\theta}{1-\cos\theta+(1+\cos\theta)\mu} = \frac{\pi}{\sqrt{\mu}} \,. \tag{I.44}$$

Thus, as μ approaches zero for $\mu > 0$, the period T increases. Equation I.44 is undefined for $\mu = 0$ and is purely imaginary for $\mu < 0$. As $\mu \to 0^+$, the period T approaches positive infinity. For this reason, the SNIC bifurcation is commonly called an *infinite-period bifurcation*.

APPENDIX II

Example MATLAB Code

This appendix includes example code used in MATLAB simulations and analysis. All code was created and run in MATLAB R2014a (8.3.0.532; maci64). Descriptions of the code are included as comments rather than separate descriptions in the text.

SECTION II.1: *Forced Hopf Oscillator*

```
function [Xdet, Xsto, Fext] =
hopfstochsine(mu,fosc,Fextmax,fr,xNoiseSTD,yNoiseSTD,tvec)
%
% This function simulates the normal form of the supercritical Hopf
% bifurcation, given by two planar equations:
%
% x_dot = mu*x - omega*y - x*(x^2 + y^2)
% y_dot = omega*x + mu*y - y*(x^2 + y^2)
%
% where mu is the control parameter. For mu>0, the system will oscillate at
% an amplitude that grows with sqrt(mu). Alternatively, one may express the
% above equations in polar coordinates, making the amplitude relationship
% with respect to mu more apparent:
%
% rho_dot = rho*(mu + i*omega - rho^2)
%
% Here we simulate both the deterministic and stochastic cases for the
% supercritical Hopf bifurcation
%
% [Xdet Xsto] = hopfstoch(mu,fosc,xNoiseSTD,yNoiseSTD,tvec)
%
% Xdet : deterministic result
% Xsto : stochastic result
%
%
% tvec : time vector
% mu : control parameter
% xNoiseSTD : standard deviation of stochastic noise in x
% yNoiseSTD : standard deviation of stochastic noise in y
% fosc : frequency of oscillation on the unstable side of the bifurcation
%
% By modifying the code, you can also add a step function or external
% forcing.
%
% jsalvi@rockefeller.edu
% Based on code by D.O M.

% Initial conditions
xzero = 1;
yzero = -1;
```

```
% Add external forcing if desired
sinusoidalstim = 1; pulsestim = 0;  % pulse or sinusoid?
%Fextmax = 1;         % amplitude of sinusoidal stim OR pulse
%fr = 5;              % frequency of stimulation
pulsestart = 1;     % start of pulse
pulseend = 2;       % end of pulse

% Decrease time step size by factor of Dtfac to ensure convergence
Dtfac = 10^2;
Dt = (tvec(2)-tvec(1))/Dtfac;

N = tvec(end)/Dt;

%Set the default random number stream
RandStream.setGlobalStream(RandStream('mt19937ar','seed',1))
xdW = sqrt(Dt)*randn(1,N); % White noise increments
ydW = sqrt(Dt)*randn(1,N); % White noise increments


xdet = zeros(1,N); xdet(1) = xzero;
xsto = zeros(1,N); xsto(1) = xzero;
ydet = zeros(1,N); ydet(1) = yzero;
ysto = zeros(1,N); ysto(1) = yzero;

% External forcing
if sinusoidalstim == 1
    Ftime = linspace(tvec(1),tvec(end),N);
    Fext = Fextmax*cos(2*pi*fr*Ftime);
elseif pulsestim == 1
    Ftime = linspace(tvec(1),tvec(end),N);
    Fext = ((Ftime<pulseend)-(Ftime<pulsestart))*Fextmax;
else
    Fext = zeros(1,N);
end

% Euler-Murayama Method with Ito Integration
for j = 2:N
%Deterministic integral
xdet(j) = xdet(j-1) + Dt*(mu*xdet(j-1) - 2*pi*fosc*ydet(j-1) - xdet(j-1)*(xdet(j-
1)^2 + ydet(j-1)^2) + real(Fext(j)));
ydet(j) = ydet(j-1) + Dt*(2*pi*fosc*xdet(j-1) + mu*ydet(j-1) - ydet(j-1)*(xdet(j-
1)^2 + ydet(j-1)^2) + imag(Fext(j)));

%Stochastic integral
xsto(j) = xsto(j-1) + Dt*(mu*xsto(j-1) - 2*pi*fosc*ysto(j-1) - xsto(j-1)*(xsto(j-
1)^2 + ysto(j-1)^2) + real(Fext(j))) + xNoiseSTD*xdW(j);
ysto(j) = ysto(j-1) + Dt*(2*pi*fosc*xsto(j-1) + mu*ysto(j-1) - ysto(j-1)*(xsto(j-
1)^2 + ysto(j-1)^2) + imag(Fext(j))) + yNoiseSTD*ydW(j);

end
Xdet = zeros(2,length(tvec)-1);
Xsto = zeros(2,length(tvec)-1);

%Return vectors at times specified by Time.
Xdet(1,:) = xdet(1:Dtfac:N);
Xdet(2,:) = ydet(1:Dtfac:N);
Xsto(1,:) = xsto(1:Dtfac:N);
Xsto(2,:) = ysto(1:Dtfac:N);
```

SECTION II.2: *Dynamical Model with Load Clamp*

```
function [Xdet, Xsto, Deltadet, Deltasto] =
hbtoymodelloadclamp(Fc,k,noiselevel,Fextmax,fr,ksf,Fe,kv,ev,mv,G,tvec)
%
% This function simulates the hair-buyndle model from PNAS 2012.
%
% [Xdet, Xsto, Delta, Fext2] =
hbtoymodelloadclamp(Fc,k,noiselevel,Fextmax,fr,ksf,Fe,kv,gv,mv,tvec)
%
% Xdet : deterministic result
% Xsto : stochastic result
% Deltasto/det : motion of the base of the fiber
% Fext2 : external force independent of fiber
%
%
% tvec : tvec vector
% Fc,k : control parameters
% noiselevels : standard deviation of stochastic noise in x and y
% fr : frequency of oscillation on the unstable side of the bifurcation
% Fextmax : amplitude in force of sinusoidal stimulation.
% ksf : fiber stiffness
% kv,ev,mv : virtual impedances from fiber
% Fe : external force from fiber
% G : proportional gain of clamp
%
% Note that stiffnesses are scaled by a factor of 100 in the manuscript.
%
% By modifying the code, you can also add a step function or other external
% forcing.
%
% jsalvi@rockefeller.edu
% Based on code by D.O M.

%Stochasic HB model integration

%EM Euler-Maruyama method
%Ito integral

a = 3.5;b = 0.5;tau = 10;xzero = 1;fzero = 0;
Deltadet(1:3) = 0;Xcdet(1:3) = 0;
Deltasto(1:3) = 0;Xcsto(1:3) = 0;
Vc(1:2) = 0;alpha = 10;beta = .1;
edx = 1e-3;exx = 1e-3;

%Decrease tvec step size by factor of Dtfac to ensure convergence
Dtfac = 1;
Dt = (tvec(2)-tvec(1))/Dtfac;

N = round(tvec(end)/Dt);

%Set the default random number stream
RandStream.setGlobalStream(RandStream('mt19937ar','seed',1))
xdW = sqrt(Dt)*randn(1,N); % White noise increments
fdW = sqrt(Dt)*randn(1,N); % White noise increments

xdet = zeros(1,N);
fdet = zeros(1,N);
xsto = zeros(1,N);
fsto = zeros(1,N);
xdet(1) = xzero;xsto(1) = xzero;
fdet(1) = fzero;fsto(1) = fzero;
```

```
%Not using FD theorem
xNoiseSTD = noiselevel; fNoiseSTD = noiselevel; % equal noise levels

Ftvec = linspace(tvec(1),tvec(end),N);
Fext = Fextmax*cos(2*pi*fr*Ftvec);


for j = 2:N

if j > 3

%Load Clamp – Deterministic

xdetd(j) = diff([xdet(j-1) xdet(j-2)]);
xdetdd(j) = diff([xdet(j-1) xdet(j-2) xdet(j-3)],2);
xstod(j) = diff([xsto(j-1) xsto(j-2)]);
xstodd(j) = diff([xsto(j-1) xsto(j-2) xsto(j-3)],2);
Xcdet(j) = (edx*Xcdet(j-1))/((edx-ksf*Dt)*alpha) + Dt*((mv*xdetdd(j)+(ev-
exx+alpha*beta*G*edx)*xdetd(j)+(kv-(1+alpha*beta*G)*ksf)*xdet(j-1)-
Fe)/(alpha*beta*G*(edx-ksf*Dt)));
Xcsto(j) = (edx*Xcsto(j-1))/((edx-ksf*Dt)*alpha) + Dt*((mv*xstodd(j)+(ev-
exx+alpha*beta*G*edx)*xstod(j)+(kv-(1+alpha*beta*G)*ksf)*xsto(j-1)-
Fe)/(alpha*beta*G*(edx-ksf*Dt)));
Deltadet(j) = G*beta*alpha*(Xcdet(j)-xdet(j-1));
Deltasto(j) = G*beta*alpha*(Xcsto(j)-xsto(j-1));
%Vcdet(j) = (edx*Vcdet(j-1))/(edx-ksf*Dt) + Dt*((mv*xdetdd(j)+(ev-
exx+G*edx)*xdetd(j)+(kv-(1+G)*ksf)*xdet(j)-Fe)/(G*(edx-ksf*Dt)));
%Vcsto(j) = (edx*Vcsto(j-1))/(edx-ksf*Dt) + Dt*((mv*xstodd(j)+(ev-
exx+G*edx)*xstod(j)+(kv-(1+G)*ksf)*xsto(j)-Fe)/(G*(edx-ksf*Dt)));
%Deltadet(j) = (Vcdet(j)) - xdet(j-1);
%Deltasto(j) = (Vcsto(j)) - xdet(j-1);

if G == 0
    Deltadet(j) = 0;
    Deltasto(j) = 0;
end
end


%Deterministic integral
fsfdet(j) = ksf*(Deltadet(j)-xdet(j-1));
xsfdet(j) = fsfdet(j)/k;
xdet(j) = xdet(j-1) + Dt*(-k*xdet(j-1) + a*(xdet(j-1)-fdet(j-1)) - (xdet(j-1)-
fdet(j-1))^3 + Fc + Fext(j) + fsfdet(j));
fdet(j) = fdet(j-1) + Dt*(b*xdet(j-1) - fdet(j-1))/tau;


%Stochastic integral
fsfsto(j) = ksf*(Deltasto(j)-xsto(j-1));
xsfsto(j) = fsfsto(j)/k;
xsto(j) = xsto(j-1) + Dt*(-k*xsto(j-1) + a*(xsto(j-1)-fsto(j-1)) - (xsto(j-1)-
fsto(j-1))^3 + Fc + Fext(j) + fsfsto(j)) + xNoiseSTD*xdW(j);
fsto(j) = fsto(j-1) + Dt*(b*xsto(j-1) - fsto(j-1))/tau + fNoiseSTD*fdW(j)/tau;

end


Xdet = zeros(2,length(tvec)-1);
Xsto = zeros(2,length(tvec)-1);

%Return vectors at tvecs specified by tvec.

Xdet(1,:) = xdet(1:Dtfac:N);
Xdet(2,:) = fdet(1:Dtfac:N);
Xsto(1,:) = xsto(1:Dtfac:N);
Xsto(2,:) = fsto(1:Dtfac:N);
```

SECTION II.3: *Peak Detection Algorithm*

```
function [P,T] = PTDetect(x, E)
% Peak detection in data x for a given threshold E
%
% [P,T] = PTDetect(x, E)
%
% Jacobson, ML. Auto-threshold peak detection in physiological signals,
% 2001.
%
% compiled: jsalvi@rockefeller.edu

P=[];T=[];a=1;b=1;i=0;d=0;
xL=length(x);

while (i ~= xL)
    i = i + 1;
    if (d == 0)
        if ( x(a) >= (x(i)+E) )
            d=2;
        elseif (x(i) >= (x(b)+E))
            d=1;
        end
        if (x(a)<= x(i))
            a = i;
        elseif (x(i) <= x(b))
            b = i;
        end
    elseif d==1
        if (x(a)<=x(i))
            a=i;
        elseif (x(a) >= (x(i)+E))
            P = [P a]; b=i; d=2;
        end
    elseif d==2
        if (x(i) <= x(b))
            b=i;
        elseif (x(i) >= (x(b)+E))
            T = [T b]; a = i; d=1;
        end
    end
end

end
```

SECTION II.4: *Vector Strength and Rayleigh Statistics*

```
function [VS, rayleigh_p] = vscalc2(x,y,rayleighyn)
% This function calculates the vector strength for two signals using
% each function's analytic signal.
%
%  [VS, rayleigh_p, rayleigh_stat] = vscalc(x,y,1)
%
%  VS : vector strength
%  rayleigh_stat : rayleigh statistic
%  x,y : input signals
%  rayleighyn : run rayleigh test? (1=yes)
%
% The function does not call angle() so that it may avoid wrapping
% artifacts when calculating the instantaneous phase.
%
% Joshua D Salvi, jsalvi@rockefeller.edu
%

% Calculate the analytic signal using the Hilbert transform.
xhilb = hilbert(x);
xhilb_eiphi = xhilb./abs(xhilb);    % normalize all lengths to 1
yhilb = hilbert(y);
yhilb_eiphi = yhilb./abs(yhilb);    % normalize all lengths to 1

% Calculate vector strength.
VS = abs(sum((xhilb_eiphi./yhilb_eiphi))/length(xhilb));

if rayleighyn == 1
    N = length(xhilb)*10/4;
    VS2_n = VS*N;
    rayleigh_p = exp(sqrt(1+4*N+4*(N^2-VS2_n^2))-(1+2*N));
end

end
```

SECTION II.5: *Mutual Information and Permutation Testing*

```
function [h p MIS I] = mutualinfostatkde(x,y,varargin)
% This function calculates a p-value for the mutual information value from
% two vectors. The function takes the vectors, reshuffles them "iter"
% times to calculate a probability distribution, and it then calculates a
% p-value based upon the input mutual information.
%
% [h p] = mutualinfostatkde(x,y,I,iter,alpha,bins,markovreps,maxorder,downsample)
%
%       I : mutual information input (if empty, will calculate it for you)
%       x : data set 1 (Mx1)
%       y : data set 2 (Mx1)
%       iter : number of iterations (default = 1E4)
%       alpha : alpha level for the statistical test (default=0.05)
%       bins : number of bins for meshgrid
%       markovreps : number of times to repeat the Markov process (default
%       = 100)
%       downsample : how much oversampling?  (e.g. Fs/nyquist) (default=5)
%       maxorder : maximum Markov order to be used (default = 2)
%       h : reject or accept the null hypothesis that the mutual
%       information comes from a random distribution as calculated here (1
%       = reject at alpha level, 0 = do not reject)
%       p : p-value associated with the statistical test
%
% [h p] = mutualinfostat(x,y,[],[],[],[],[]);
%
%
%   Joshua D. Salvi
%   jsalvi@rockefeller.edu

if isempty(varargin{2})
    iter = 1E4;
else
    iter = varargin{2};
end
if isempty(varargin{3})
    alpha = 0.05;
else
    alpha = varargin{3};
end
if isempty(varargin{4})
    bins = 2^4;
else
    bins = varargin{4};
end
if isempty(varargin{5})
    markovreps = 100;
else
    markovreps = varargin{5};
end
if isempty(varargin{6})
    maxorder = 2;
else
    maxorder = varargin{6};
end
if isempty(varargin{7})
    downsample = 5;
else
    downsample = varargin{7};
end
if iscolumn(x) == 0;x = x';end
if iscolumn(y) == 0;y = y';end
```

```
% Randomly shuffle the X and Y data and calculate MI - create surrogates
% Pethel et al, Entropy (2014) 16:2839-2849
% Determine the order of your Markov model, up to order 2
x=x(round(1:downsample:end));y=y(round(1:downsample:end));              %
Downsample
[px] = MarkovOrderTests(x,markovreps,maxorder);     % determine markov order
[py] = MarkovOrderTests(y,markovreps,maxorder);
rx=find(px>0.05);ry=find(py>0.05);
if isempty(rx) == 1     % if maximum markov order is not large enough, set to the
next highest order
    rx = maxorder+2;
end
if isempty(ry) == 1
    ry = maxorder+2;
end
rx=rx(1);ry=ry(1);    % select the smallest Markov order that was found from the
above algorithm

[fx, wx, ux, vx] = trans_count(x,rx-1);       % Nth order markov model
[fy, wy, uy, vy] = trans_count(y,ry-1);

for i = 1:iter
    clear z xn yn
    xn = whittle_surrogate(fx,wx,ux,vx);    % generate surrogates
    yn = whittle_surrogate(fy,wy,uy,vy);
    if length(xn) > length(yn)
        MIS(i) = rapidmi(xn(1:length(yn)),yn,bins);
    elseif length(xn) <= length(yn)
        MIS(i) = rapidmi(xn,yn(1:length(xn)),bins);
    end
end

minlength=min([length(xn),length(yn)]);
% Create a kernel density estimate
[a, b] = ksdensity(MIS,round(0:max(MIS)/10000:max(MIS)*2));
a=a./sum(a);
% Calculate mutual information if not an input
if isempty(varargin{1})
    I = rapidmi(x,y,bins);
else
    I = varargin{1};
end

% Find p-value for single-tailed test
p = sum(a(findnearest(b,I):end));
% Significant
if p < alpha
    h = 1;
else
    h = 0;
end
end
```

```
%%%%%%%%%%%%%%%%%%%%%%%%%%%%%%%%%%%%%%%%%%%%%%%%%%%%
%%%%%%%%%%%%%%%%%%%%%%%%%%%%%%%%%%%%%%%%%%%%%%%%%%%%
%%%%%%%%%%%%%%%%%%%%%%%%%%%%%%%%%%%%%%%%%%%%%%%%%%%%
function Ir = rapidmi(m,n,bins)

if iscolumn(m) == 0
    m = m';
end
if iscolumn(n) == 0
    n = n';
end

[bwmn,dmn,meshmnm,meshmnn]=kde2d([m n],bins);
dmn=abs(dmn);dmn = dmn./sum(sum(dmn));dmnlog = log2(dmn);
dmnlog(dmnlog==inf | dmnlog==-inf)=0;

Inh1 = log2(sum(dmn,1));Inh2 = log2(sum(dmn,2));
Inh1(Inh1==inf | Inh1==-inf)=0;Inh2(Inh2==inf | Inh2==-inf)=0;

Ir = sum(sum(dmn.*bsxfun(@minus,bsxfun(@minus,dmnlog,Inh1),Inh2)));

end
%%%%%%%%%%%%%%%%%%%%%%%%%%%%%%%%%%%%%%%%%%%%%%%%%%%%
%%%%%%%%%%%%%%%%%%%%%%%%%%%%%%%%%%%%%%%%%%%%%%%%%%%%
%%%%%%%%%%%%%%%%%%%%%%%%%%%%%%%%%%%%%%%%%%%%%%%%%%%%
```

APPENDIX III

Information-Theoretical Approach to Hair-Bundle Mechanics

Prior studies in hair-bundle mechanics focused on the mechanical resonance, phase locking, and sensitivity of sensory hair bundles in response to periodic stimuli. Each metric provides a unique tool to classify a bundle's behavior in response to changes to the values of one or more control parameters. Interestingly, hair bundles have been noted to phase lock to periodic stimuli with weak forcing, as measured with vector strength. As the stimulus force increases, a qualitative change in the hair bundle's pattern of oscillation emerges. Thus, there appear to be two functional regimes of bundle behavior at small and large stimulus amplitudes.

Although vector strength provides a simple yet powerful quantification of entrainment, it takes into account only the phase of an oscillator. Another nonlinear measure that can incorporate both the phase and amplitude of an oscillator, along with the possibility of quantifying other features, is mutual information. For two discrete random variables X and Y, mutual information is defined as

$$I(X;Y) = \sum_{i=1}^{M}\sum_{j=1}^{N} p(x_i, y_j)\log\left(\frac{p(x_i, y_j)}{p(x_i)p(y_j)}\right), \tag{III.1}$$

in which $p(x,y)$ is the joint probability distribution of X and Y with $x \in X$ and $y \in Y$, and $p(x)$ and $p(y)$ are the respective marginal probability distributions of X and Y. To estimate the probability distributions, we employed univariate and bivariate Gaussian kernel density estimators on a square grid of 4,096 points in the bivariate case and an

array of 64 points in the univariate case. Distributions incorporated either the position or the phase of the hair bundle and the position or phase of the stimulus.

To assess the significance of mutual information, we employed permutation testing. The time series of the bundle's position or phase was randomly shuffled 10^3 times and a value of mutual information calculated for each shuffled series. This generates a null distribution of mutual information values from the shuffled data. Comparing the experimental mutual information value with the null distribution yields a *p*-value for significance testing. Here we defined a significance level of $p < 0.001$.

A hair bundle from the bullfrog's sacculus was poised at three operating points and its behavior in the absence of stimulus characterized (Figure III.1). We then delivered periodic stimuli of increasing force at a frequency near the bundle's frequency of spontaneous oscillation. A region of phase locking can be defined as the range of forces over which the bundle's phase of motion matches that of its stimulus without a change in the bundle's shape of displacement. In other words, the region of phase locking is bounded by the minimal stimulus force required to entrain the bundle's motion to its stimulus and the smallest force at which the stimulus deforms the shape of the hair bundle's motion. To quantify this difference, we calculated the mutual information in both phase (Figure III.1a) and displacement (Figure III.1b) of the bundle's motion with respect to that of its stimulus. The bundle's phase distribution matched the phase distribution of the stimulus for stimulus forces of 3.1 pN, 2 pN, and 17.4 pN at load stiffnesses of respectively 150 $\mu N \cdot m^{-1}$, 217 $\mu N \cdot m^{-1}$, and 347 $\mu N \cdot m^{-1}$. As expected, the displacement distributions matched one another at larger forces of 7.9 pN, 10.9 pN, and

17.4 pN at the same load stiffnesses. This corresponds to a region of phase locking of 4.8 pN, 8.9 pN, and 0 pN at load stiffnesses of respectively 150 $\mu N \cdot m^{-1}$, 217 $\mu N \cdot m^{-1}$, and 347 $\mu N \cdot m^{-1}$. Thus, the phase-locked region as defined here achieves its maximum breadth at a load stiffness of 217 $\mu N \cdot m^{-1}$ for which the bundle's operating point was poised closest to a supercritical Hopf bifurcation. Interestingly, displacing the bundle's operating point far into the quiescent regime at a load stiffness of 347 $\mu N \cdot m^{-1}$ resulted in a disappearance of the phase-locked region. In other words, the bundle's motion did not entrain to the motion of its stimulus until the stimulus force was large enough to significantly distort the shape of the bundle's motion.

We also calculated the normalized difference between the mutual information in phase and the mutual information in displacement (Figure III.1c). Here a value of 1 indicates that all information in the bundle's response is contained in the phase, and a value of -1 corresponds to all information being transmitted in the bundle's displacement. For weak forcing, the bundle's information content in both phase and displacement were nearly equal at a load stiffness of 150 $\mu N \cdot m^{-1}$. When the value of load stiffness was increased to poise the bundle's operating point in the quiescent regime, nearly all information shared between the bundle's motion and that of its stimulus was contained in the displacement. For large forces, this relationship reversed, and a majority of the information content was contained in the bundle's phase of motion. This corresponds to the force at which the bundle began to phase lock to its stimulus. As expected, the maximum degree of phase locking occurred at a load stiffness of 217 $\mu N \cdot m^{-1}$.

In addition to measuring the range of phase locking across stimulus forces, mutual information can be applied as an alternative metric in the quantification of Arnol'd tongues (Figure III.2). To do so, we compared the phase distributions of the bundle's motion and that of its stimulus. As with vector strength, the bundle achieved maximum phase locking and the sharpness of the Arnol'd tongue increased with a rise in load stiffness.

Taken together, these preliminary analyses demonstrate the utility of nonlinear measures such as mutual information in the analysis of hair-bundle mechanics. Unlike quantities that are limited to a specific feature of a forced oscillator, information-theoretical approaches possess general applicability across a wide gamut of dimensions. Although the value of mutual information can at times be difficult to interpret, this challenge can be overcome with permutation testing or the normalization of mutual information across individual parameters with respect to the summed response.

Figure III.1. Phase and displacement of a forced hair bundle. (a) A hair bundle's motion was classified as oscillatory or quiescent at three values of load stiffness in the absence of stimulation. At each load stiffness, the bundle was sinusoidally driven with stimuli of increasing force near the bundle's frequency of spontaneous oscillation. The bundle's mutual information in phase with respect to its stimulus rose with increasing stimulus force, corresponding to an increase in the degree of phase locking. Arrows correspond to the force at which the bundle was classified as significantly entrained with $p < 0.001$. The hair bundle achieved significant entrainment for a stimulus force of 2 pN at a load stiffness of 217 $\mu N \cdot m^{-1}$ (yellow) but did not phase lock until the force exceeded 17.4 pN at a load stiffness of 347 $\mu N \cdot m^{-1}$ (cyan). (b) We next sought to quantify the shape of the bundle's displacement as the stimulus force was increased. To do so, the data from (a) were analyzed in order to measure the bundle's mutual information in displacement with respect to its stimulus. Here the shape of the bundle's response matched that of its stimulus for a force of 10.9 pN at a load stiffness of 217 $\mu N \cdot m^{-1}$ (yellow) but did not phase lock until the force exceeded 17.4 pN at a load stiffness of 347 $\mu N \cdot m^{-1}$ (cyan). The difference between the points marked by arrows in (a) and (b) corresponds to a region of phase locking without a change in the shape of the bundle's response. These differences were 4.8 pN (red), 8.9 pN (yellow), and 0 pN (cyan), indicating that the region of phase locking was broadest for a load stiffness of 217 $\mu N \cdot m^{-1}$ (yellow). (c) The normalized difference between mutual information in phase (MI_P) and displacement (MI_D) reveals the relative information between these two metrics. For weak forcing, the bundle exhibited nearly equal mutual information in phase and displacement at 150 $\mu N \cdot m^{-1}$ (red), whereas nearly all information was contained in the bundle's displacement at higher values of load stiffness. For larger forces, the bundle achieved maximum phase locking relative to changes in its displacement at a load stiffness of 217 $\mu N \cdot m^{-1}$ (yellow).

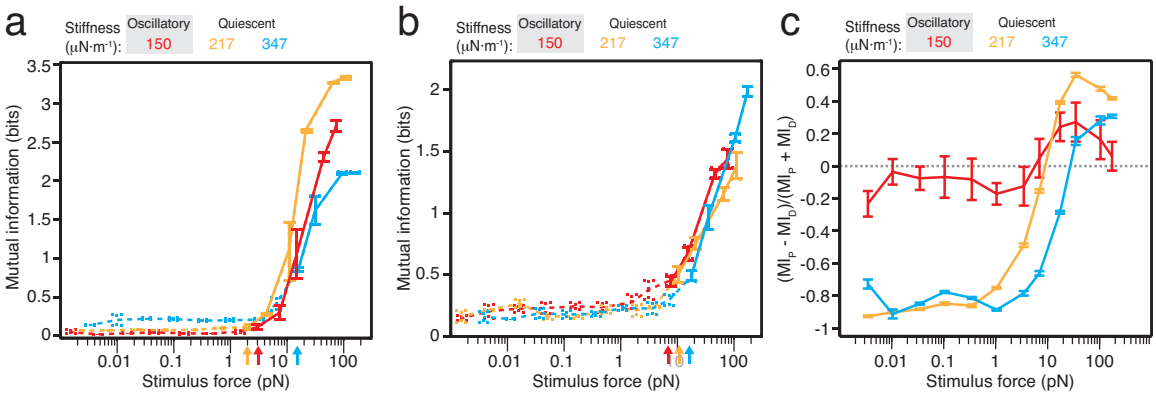
a
Stiffness (μN·m⁻¹):
Oscillatory
Quiescent
150
217
347
Mutual information (bits)
Stimulus force (pN)
b
Stiffness (μN·m⁻¹):
Oscillatory
Quiescent
150
217
347
Mutual information (bits)
Stimulus force (pN)
c
Stiffness (μN·m⁻¹):
Oscillatory
Quiescent
150
217
347
(MIP - MID)/(MIP + MID)
Stimulus force (pN)

Figure III.2. Entrainment of a hair bundle as measured by mutual information. A hair bundle oscillated spontaneously for three values of load stiffness. Stimuli of both increasing force and increasing frequency were delivered to the bundle and its degree of entrainment was measured from the mutual information in the phase distributions of the bundle's motion and that of its stimulus. As with vector strength, the hair bundle achieved greater phase locking and a sharper Arnol'd tongue as its load stiffness increased.

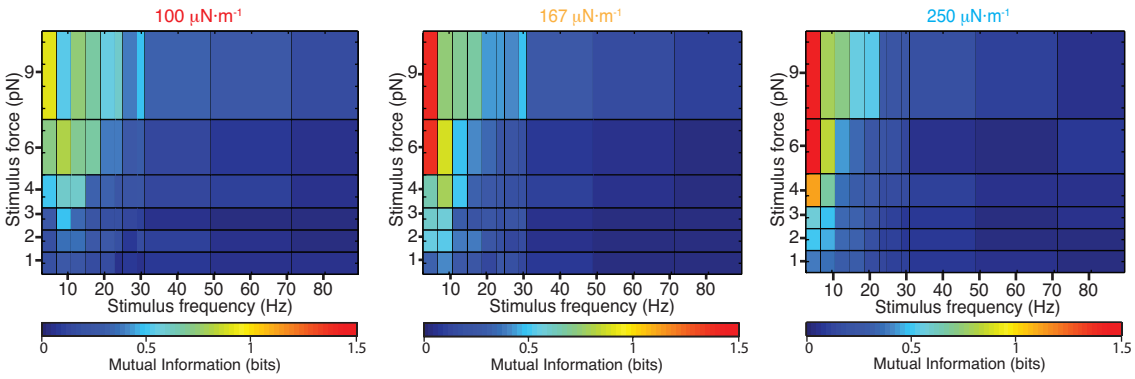
100 μN·m-1
167 μN·m-1
250 μN·m-1
Stimulus force (pN)
1
2
3
4
6
9
10 20 30 40 50 60 70 80
Stimulus frequency (Hz)
0 0.5 1 1.5
Mutual Information (bits)

REFERENCES

1. Fay RR (1988) *Hearing in Vertebrates: A Psychophysics Databook* (Hill-Fay Associates, Winnetka, Illinois).
2. Dallos P, Popper AN, & Fay RR (1996) *The Cochlea* (Springer, New York, NY).
3. Spiegel MF & Watson CS (1984) Performance on Frequency-Discrimination Tasks by Musicians and Nonmusicians. *Journal of the Acoustical Society of America* 76(6):1690-1695.
4. Zwicker E (1970) Masking and psychological excitation as consequences of the ear's frequency analysis. *Frequency Analysis and Periodicity Detection in Hearing*, eds R. P & G S (A.W. Sijthoff), pp 376-394.
5. Knudsen VO (1923) The sensibility of the ear to small differences of intensity and frequency. *Physics Review* 21(1):84-102.
6. Green DM & Huanping D (1991) Is human hearing limited by Brownian motion? *Journal of the Acoustical Society of America* 89(4B):1889.
7. Sellick PM, Patuzzi RB, & Johnston BM (1982) Measurement of the basilar membrane motion in the guinea-pig using the Mossbauer technique. *Journal of the Acoustical Society of America* 72:131-141.
8. Wiener FM & Ross DA (1946) The pressure distribution in the auditory canal in a progressive sound field. *Journal of the Acoustical Society of America* 78:2146-2148.
9. Teranishi R & Shaw EAG (1968) External-ear acoustic models with simple geometry. *Journal of the Acoustical Society of America* 33:257-263.

10. Dallos P (1973) *The Auditory Periphery: Biophysics and Physiology* (Academic Press, New York).

11. Dalhoff E, Turcanu D, Zenner H-P, & Gummer AW (2007) Distortion product otoacoustic emissions measured as vibration on the eardrum of human subjects. *Proceedings of the National Academy of Sciences USA* 104(5):1546-1551.

12. Kurokawa H & Goode RL (1995) Sound pressure gain produced by the human middle ear. *Otolaryngology — Head and Neck Surgery* 113(4):349-355.

13. Kandel ER, Schwartz JH, Jessell TM, Siegelbaum SA, & Hudspeth AJ (2012) *Principles of Neural Science* (McGraw-Hill Professional) 5th Ed.

14. Gilroy AM, MacPherson BR, & Ross LM (2008) *Atlas of Anatomy* (Thieme).

15. von Bekesy G (1960) *Experiments in hearing* (McGraw-Hill, New York).

16. Oghalai JS (2004) The cochlear amplifier: augmentation of the traveling wave within the inner ear. *Current Opinion in Otolaryngology & Head & Neck Surgery* 12(5):431-438.

17. Edge RM, *et al.* (1997) Morphology of the unfixed cochlea. *Hearing Research* 124:1-16.

18. Baker WF & Korista DS (2007) Burj Dubai: engineering the world's tallest building. *The Structural Design of Tall and Special Buildings* 16(4):361-375.

19. Purves D (2007) *Neuroscience* (Sinauer Associates, Inc.) 4th Ed.

20. Middlebrooks JC (2009) Auditory System: Central Pathways. *Encyclopedia of Neuroscience*, (Academic Press).

21. Hudspeth AJ (2013) SnapShot: Auditory transduction. *Neuron* 80(2):536.e531.

22. Gold T (1948) Hearing II: the physical basis of the action of the cochlea. *Proceedings of the Royal Society of London B: Biological Sciences* 135:482-491.

23. Davis H (1983) An active process in cochlear mechanics. *Hearing Research* 9:79-90.

24. Weiss TF (1982) Bidirectional transduction in vertebrate hair cells: a mechanism for coupling mechanical and electrical processes. *Hearing Research* 7:353-360.

25. Brownell WE, Bader CR, Betrand D, & de Ribaupierre Y (1985) Evokes mechanical responses of isolated cochlear outer hair cells. *Science* 227:194-196.

26. Zheng J, *et al.* (2000) Prestin is the motor protein of cochlear outer hair cells. *Nature* 405:149-155.

27. Robles L & Ruggero MA (2001) Mechanics of the mammalian cochlea. *Physiological Reviews* 81:1305-1352.

28. Fisher JAN, Nin F, Reichenbach T, Uthaiah RC, & Hudspeth AJ (2012) The spatial pattern of cochlear amplification. *Neuron* 76(5):989-997.

29. Manley GA (2000) Cochlear mechanisms from a phylogenetic viewpoint. *Proceedings of the National Academy of Sciences USA* 97:11736-11743.

30. Hudspeth AJ (2008) Making an effort to listen: mechanical amplification in the ear. *Neuron* 59:530-545.

31. Kemp DT (1978) Stimulated acoustic emissions from within the human auditory system. *Journal of the Acoustical Society of America* 64:1386-1391.

32. Kemp DT (2008) Otoacoustic emissions: concepts and origins. *Active Processes and Otoacoustic Emissions*, eds Manley GA, Fay RR, & Popper AN (Springer, New York), pp 1-38.

33. Manley GA (2001) Evidence for an Active Process and a Cochlear Amplifier in Nonmammals. *Journal of Neurophysiology* 86:541-549.

34. Hudspeth AJ (2014) Integrating the active process of hair cells with cochlear function. *Nature Reviews Neuroscience* 15:600-614.

35. Rhode WS (1971) Observations of the vibration of the basilar membrane in squirrel monkeys using the Mossbauer technique. *Journal of the Acoustical Society of America* 49:1218-1231.

36. Tan C-T, Moore BCJ, & Zacharov N (2003) The effect of nonlinear distortion on the perceived quality of music and speech signals. *Journal of the Audio Engineering Society* 51(11):1012-1031.

37. Kupfmuller K (1928) On the dynamics of automatic gain controllers. *Elektrische Nachrichtentechnik* 5(11):459-467.

38. King AB & Martin MC (1984) Is AGC beneficial in hearing aids? *British Juornal of Audiology* 18(1):31-38.

39. Eguiliz VM, Ospeck M, Choe Y, Hudspeth AJ, & Magnasco MO (2000) Essential nonlinearities in hearing. *Physics Review Letters* 84(22):5232-5235.

40. Tartini G (1754) Trattato di musica secondo la vera scienza dell'armonia. *PADOVA: Nella Stamperia del Seminario, Appresso Giovannia Manfre*.

41. Goldstein JL (1967) Auditory Nonlinearity. *Journal of the Acoustical Society of America* 41:676-689.

42. Chang KW & Norton SJ (1996) The effects of continuous versus interrupted noise exposures on distortion product otoacoustic emissions in guinea pigs. *Hearing Research* 96:1-12.

43. Chan DK (2005) Mechanical responses of the organ of Corti to acoustic and electrical stimulation in vitro. *Biophysical Journal* 89:4382-4395.

44. Dong W & Olson ES (2006) Middle ear forward and reverse transmission in gerbil. *Journal of Neurophysiology* 95:2951-2961.

45. Camalet S, Duke T, Julicher F, & Prost J (2000) Auditory sensitivity provided by self-tuned critical oscillations of hair cells. *Proceedings of the National Academy of Sciences USA* 97:3183-3188.

46. Beurg M, Tan X, & Fettiplace R (2013) A prestin motor in chicken auditory hair cells: active force generation in a nonmammalian species. *Neuron* 79(1):69-81.

47. Suga N, Neuweiler G, & Moller J (1976) Peripheral auditory tuning for fine frequency analysis by the CF-FM bat, Rhinolophus ferrumequinum. *Journal of Computational Physiology* 106(1):111-125.

48. Narins P & Lewis ER (1986) The vertebrate ear as an exquisite seismic sensor. *Journal of the Acoustical Society of America* 76:1384-1387.

49. Tilney L, Derosier D, & Mulroy M (1980) The organization of actin filamets in the stereocilia of cochlear hair cells. *Journal of Cell Biology* 86:244-259.

50. Pickles JO, *et al.* (1989) The organization of tip links and stereocilia on hair cells of bird and lizard papillae. *Hearing Research* 41:31-41.

51. Siemens J, Lillo C, Dumont RA, Reynolds A, & Williams DS (2004) Cadherin 23 is a component of the tip link in hair-cell stereocilia. *Nature* 428:950-955.

52. Sotomayor M, Weihofen WA, Gaudet R, & Corey DP (2012) Structure of a force-conveying cadherin bond essential for inner-ear mechanotransduction. *Nature* 492(7427):128-132.

53. Raphael Y & Altschuler RA (2003) Structure and innervation of the cochlea. *Brain Research Bulletin* 60(5-6):397-422.

54. Nagel G, Neugebauer D-C, Schmidt B, & Thurm U (1991) Structures transmitting stimulatory force to the sensory hairs of vestibular ampullae of fishes and frogs. *Cell and Tissue Research* 265:567-578.

55. Flock A, Flock B, & Murray E (1977) Studies on the sensory hairs of receptor cells in the inner ear. *Acta Otolaryngology* 83:85-91.

56. Hudspeth AJ (1983) The hair cells of the inner ear. *Scientific American* 248:54-64.

57. Howard J (2001) *Mechanics of Motor Proteins and the Cytoskeleton* (Sinauer Associates, Sunderland, MA).

58. Hudspeth AJ (1983) Mechanoelectrical transduction by hair cells in the acousticolateralis sensory system. *Annual Reviews of Neuroscience* 6:187-215.

59. Crawford AC, Evans MG, & Fettiplace R (1991) The actions of calcium on the mechanoelectrical transducer current of turtle hair cells. *Journal of Physiology* 434:369-398.

60. Ricci AJ, Crawford AC, & Fettiplace R (2003) Tonotopic variation in the conductance of the hair cell mechanotransducer channel. *Neuron* 40:983-990.

61. Holton T & Hudspeth AJ (1986) The transduction channel of hair cells from the bullfrog characterized by noise analysis. *Journal of Physiology* 375:195-227.

62. Crawford AC, Evans MG, & Fettiplace R (1989) Activation and adaptation of transducer currents in turtle hair cells. *Journal of Physiology* 419:405-434.

63. Corey DP & Hudspeth AJ (1983) Kinetics of the receptor current in bullfrog saccular hair cells. *Journal of Neuroscience* 3(5):962-976.

64. Crawford AC, Evans MG, & Fettiplace R (1991) The actions of calcium on the mechano-electrical transducer current of turtle hair cells. *Journal of Physiology* 434:369-398.

65. Geleoc GS, Lennan GW, Richardson GP, & Kros CJ (1997) A quantitative comparison of mechanoelectrical transduction in vestibular and auditory hair cells of neonatal mice. *Proceedings of Biological Sciences* 1381:611-621.

66. Corey DP & Hudspeth AJ (1979) Response latency of vertebrate hair cells. *Biophysical Journal* 26(3):499-506.

67. Martin P (2008) Active hair-bundle motility. *Active Processes and Otoacoustic Emissions,* Springer Handbook of Auditory Research, eds Manley GA, Fay RR, & Popper AN (Springer, New York).

68. Kennedy HJ, Evans MG, Crawford AC, & Fettiplace R (2003) Fast adaptation of mechanoelectrical transducer channels in mammalian cochlear hair cells. *Nature Neuroscience* 6(8):832-836.

69. Peng AW & Ricci AJ (2008) Somatic motility and hair bundle mechanics, are both necessary for cochlear amplification? *Hearing Research* 273(1-2):109-122.

70. Howard J & Hudspeth AJ (1987) Mechanical relaxation of the hair bundle mediates adaptation in mechanoelectrical transduction by the bullfrog's saccular hair cell. *Proceedings of the National Academy of Sciences USA* 84:3064-3068.

71. Jacobs RA & Hudspeth AJ (1990) Ultrastructural correlates of mechanoelectrical transduction in hair cells of the bullfrog's internal ear. *Cold Spring Harbor Symposium on Quantitative Biology* 55:547-561.

72. Hackney CM, Fettiplace R, & Furness DN (1993) The functional morphology of stereociliary bundles on turtle cochlear hair cells. *Hearing Research* 89(1-2):163-175.

73. Stauffer EA, *et al.* (2005) Fast adaptation in vestibular hair cells requires myosin-1c activity. *Neuron* 47(4):541-553.

74. Fettiplace R & Fuchs PA (1999) Mechanisms of hair cell tuning. *Annual Reviews of Physiology* 61:809-834.

75. Wu YC, Ricci AJ, & Fettiplace R (1999) Two components of transducer adaptation in auditory hair cells. *Journal of Neurophysiology* 82(5):2171-2181.

76. Hudspeth AJ (1992) Hair-Bundle Mechanics and a Model for Mechanoelectrical Transduction by Hair Cells. *Sensory Transduction: Society of General Physiologists 45th Annual Sympsoium*, eds Corey DP & Roper SD (The Rockefeller University Press, New York).

77. Ricci AJ, Kennedy HJ, Crawford AC, & Fettiplace R (2005) The transduction channel filter in auditory hair cells. *Journal of Neuroscience* 25(34):7831-7839.

78. Drummond HA, Price MP, Welsh MJ, & Abboud FM (1998) A molecular component of the arterial baroreceptor mechanotransducer. *Neuron* 21:1435-1441.

79. O'Hagan R, Chalfie M, & Goodman MB (2005) The MEC-4 DEG/ENaC channel of Caenorhabditis elegans touch receptor neurons transduces mechanical signals. *Nature Neuroscience* 8:43-50.

80. Hackney CM, Furness DN, Benos DJ, Woodley JF, & Barratt J (1992) Putative immunolocalization of the mechanoelectrical transducation channels in mammalian cochlear hair cells. *Proceedings of Biological Sciences* 248:215-221.

81. Benos DJ, Awayda MS, Ismailov II, & Johnson JP (1995) Structure and function of amiloride-sensitive Na+ channels. *Journal of Membrane Biology* 143:1-18.

82. Jorgenson F & Ohmori H (1988) Amiloride blocks the mechano-electrical transduction channel of hair cells of the chick. *Journal of Physiology* 403:577-588.

83. Kellenberger S & Schild L (2002) Epithelial sodium channel/degenerin family of ion channels: a variety of functions for a shared structure. *Physiological Reviews* 82:735-767.

84. Rusch A, Kros CJ, & Richardson GP (1994) Block by amiloride and its derivatives of mechano-electrical transduction in outer hair cells of mouse cochlear structures. *Journal of Physiology* 474:75-86.

85. Couloigner V, *et al.* (2001) Location and function of the epithelial Na channel in the cochlea. *American Journal of Physiology: Renal Physiology* 280:F214-F222.

86. Grunder U, Muller A, & Rupperberg JP (2001) Developmental and cellular expression pattern of epithelial sodium channel alpha, beta, and gamma subunits in the inner ear of the rat. *European Journal of Neuroscience* 13:641-648.

87. Reuter G, Gitter AH, Thurm U, & Zenner H-P (1992) High frequency radial movements of the reticular lamina induced by outer hair cell motility. *Hearing Research* 60:236-246.

88. Clapham DE, Runnels LW, & Strubing C (2001) The TRP ion channel family. *Nature Reviews Neuroscience* 2:387-396.

89. Nilius B & Voets T (2005) TRP channels: A TR(I)P through a world of multifunctional cation channels. *Pflugers Archives* 451:1-10.

90. Ramsey IS, Delling M, & Clapham DE (2006) An Introduction to TRP Channels. *Annual Reviews of Physiology* 68:619-647.

91. Walker RG, Willingham AT, & Zuker CS (2000) A Drosophila mechanosensory transduction channel. *Science* 287:2229-2234.

92. Shin JB, *et al.* (2005) Xenopus TRPN1 (NOMPC) localizes to microtubule-based cilia in epithelial cells, including inner-ear hair cells. *Proceedings of the National Academy of Sciences USA* 102:12572-12577.

93. Sidi S, Friedrich RW, & Nicolson T (2003) NompC TRP channel required for vertebrate sensory hair cell mechanotransduction. *Science* 301:96-99.

94. Corey DP (2003) New TRP channels in hearing and mechanosensation. *Neuron* 39:585-588.

95. Story GM, *et al.* (2003) ANKTM1, a TRP-like channel expressed in nociceptive neurons, is activated by cold temperatures. *Cell* 112:819-829.

96. Corey DP & Sotomayor M (2004) Hearing: Tightrope act. *Nature* 428:901-903.

97. Bautista DM, *et al.* (2006) TRPA1 mediates the inflammatory actions of environmental irritants and proalgesic agents. *Cell* 124:1269-1282.

98. Kawashima Y, *et al.* (2011) Mechanotransduction in mouse inner ear hair cells requires transmembrane channel-like genes. *Journal of Clinical Investigation* 121:4796-4809.

99. Pan B, *et al.* (2013) TMC1 and TMC2 are components of the mechanotransduction channel in hair cells of the mammalian inner ear. *Neuron* 79:504-515.

100. Beurg M, Kim KX, & Fettiplace R (2014) Conductance and block of hair-cell mechanotransducer channels in transmembrane channel-like protein mutants. *The Journal of General Physiology* 144(1):55-69.

101. Kim KX, *et al.* (2013) The role of transmembrane channel-like proteins in the operation of hair cell mechanotransducer channels. *Journal of General Physiology* 142:493-505.

102. LeMasurier M & Gillespie PG (2005) Hair-cell mechanotransduction and cochlear amplification. *Neuron* 48:403-415.

103. Assad JA & Corey DP (1992) An active motor model for adaptation by vertebrate hair cells. *Journal of Neuroscience* 12:3291-3309.

104. Eatock RA, Corey DP, & Hudspeth AJ (1987) Adaptation of mechanoelectrical transduction in hair cells of the bullfrog's sacculus. *Journal of Neuroscience* 7:2821-2836.

105. Gillespie PG & Cyr JL (2004) Myosin-1c, the hair cell's adaptation motor. *Annual Reviews of Physiology* 66:521-545.

106. Wu YC, Ricci AJ, & Fettiplace R (1999) Two components of transducer adaptation in auditory hair cells. *Journal of Neurophysiology* 82:2171-2181.

107. Benser ME, Marquis RE, & Hudspeth AJ (1996) Rapid, active hair bundle movements in hair cells from the bullfrog's sacculus. *Journal of Neuroscience* 16:5629-5643.

108. Howard J & Hudspeth AJ (1988) Compliance of the hair bundle associated with gating of mechanoelectrical transduction channels in the bullfrog's saccular hair cell. *Neuron* 1:189-199.

109. Martin P, Mehta AD, & Hudspeth AJ (2000) Negative hair-bundle stiffness betrays a mechanism for mechanical amplification by the hair cell. *Proceedings of the National Academy of Sciences USA* 97:12026-12031.

110. Ricci AJ, Crawford AC, & Fettiplace R (2000) Active hair bundle motion linked to fast transducer adaptation in auditory hair cells. *Journal of Neuroscience* 20:7131-7142.

111. Flock A & Strelioff D (1984) Graded and nonlinear mechanical properties of sensory hairs in the mammalian hearing organ. *Nature* 310:597-599.

112. Ricci AJ, Crawford AC, & Fettiplace R (2002) Mechanisms of active hair bundle motion in auditory hair cells. *Journal of Neuroscience* 22:44-52.

113. Russell IJ, Kossl M, & Richardson GP (1992) Nonlinear mechanical responses of mouse cochlear hair bundles. *Proceedings of the Royal Society of London B: Biological Sciences* 250:217-227.

114. Kennedy HJ, Crawford AC, & Fettiplace R (2005) Force generation by mammalian hair bundles supports a role in cochlear amplification. *Nature* 433:880-883.

115. Martin P, Bozovic D, Choe Y, & Hudspeth AJ (2003) Spontaneous oscillation by hair bundles of the bullfrog's sacculus. *Journal of Neuroscience* 23:4533-4548.

116. Iwasa KH & Ehrenstein G (2002) Cooperative interaction as the physical basis of the negative stiffness in hair cell stereocilia. *Journal of the Acoustical Society of America* 111:2208-2212.

117. Martin P & Hudspeth AJ (1999) Active hair-bundle movements can amplify a hair cell's response to oscillatory mechanical stimuli. *Proceedings of the National Academy of Sciences USA* 96(25):14306-14311.

118. Rusch A & Thurm U (1990) Spontaneous and electrically induced movements of ampullary kinocilia and stereovilli. *Hearing Research* 48:246-263.

119. Denk W & Webb WW (1992) Forward and reverse transduction at the limit of sensitivity studied by correlating electrical and mechanical fluctuations in frog saccular hair cells. *Hearing Research* 60:89-102.

120. Crawford AC & Fettiplace R (1985) The mechanical properties of cililary bundles of turtle cochlear hair cells. *Journal of Physiology* 364:359-379.

121. van Dijk P, Wit HP, & Segenhout JM (1989) Spontaneous otoacoustic emissions in the European edible frog. *Hearing Research* 42:273-282.

122. van Dijk P, Manley GA, Gallo L, & Pavusa A (1996) Statistical properties of spontaneous otoacoustic emissions in one bird and three lizard species. *Journal of the Acoustical Society of America* 100:2220-2227.

123. Bialek W & Wit HP (1984) Quantum limits to oscillator stability: theory and experiments on acoustic emissions from the human ear. *Physics Review Letters A* 104:173-178.

124. Martin P, Bozovic D, Choe Y, & Hudspeth AJ (2003) Spontaneous oscillation by hair bundles of the bullfrog's sacculus. *Journal of Neuroscience* 23(11):4533-4548.

125. Manley GA & Kirk DL (2002) The influence of injected AC and DC currents on spontaneous otoacoustic emissions in the bobtal lizards. *Journal of the Association for Reasearch in Otolaryngology* 3:200-208.

126. Manley GA, Sienknecht U, & Koppl C (2004) Calcium modulates the frequency and amplitude of spontaneous otoacoustic emissions in the bobtail skink. *Journal of Neurophysiology* 92:2685-2693.

127. Martin P, Mehta AD, & Hudspeth AJ (2000) Negative hair-bundle stiffness betrays a mechanism for mechanical amplification by the hair cell. *Proceedings of the National Academy of Sciences USA* 97(22):12026-12031.

128. Le Goff L, Bozovic D, & Hudspeth AJ (2005) Adaptive shift in the domain of negative stiffness during spontaneous oscillation by hair bundles from the internal ear. *Proceedings of the National Academy of Sciences USA* 102(47):16996-17001.

129. Martin P & Hudspeth AJ (2001) Compressive nonlinearity in the hair bundle's active response to mechanical stimulation. *Proceedings of the National Academy of Sciences USA* 98(25):14386-14391.

130. Fay RR & Coombs S (1983) Neural mechanisms in sound detection and temporal summation. *Hearing Research* 10:69-92.

131. Hillery CM & Narins P (1984) Neurophysiological evidence for a traveling wave in the amphibian inner ear. *Science* 225:1037-1039.

132. Gleich O & Narins P (1988) the phase response of primary auditory afferents in a songbird. *Hearing Research* 32:81-91.

133. Mhatre N & Robert D (2013) A Tympanal Insect Ear Exploits a Critical Oscillator for Active Amplification and Tuning. *Current Biology* 23(19):1952-1957.

134. Nin F, Reichenbach T, Fisher JAN, & Hudspeth AJ (2014) Contribution of active hair-bundle motility to nonlinear amplification in the mammalian cochlea. *Proceedings of the National Academy of Sciences USA* 109(51):21076-21080.

135. Martin P, Bozovic D, Choe Y, & Hudspeth AJ (2003) Spontaneous oscillation by hair bundles of the bullfrog's sacculus. *The Journal of Neuroscience* 23(11):4533-4548.

136. van Netten SM & Kroese ABA (1987) Laser interferometric measurements on the dynamic behavior of the cupula in the fish lateral line. *Hearing Research* 29:55-61.

137. Chiappe ME, Kozlov AS, & Hudspeth AJ (2007) The structural and function differentiation of hair cells in a lizard's basilar papilla suggests an operational principle of amniote cochleas. *Journal of Neuroscience* 27:11978-11985.

138. Tilney LG & Saunders JC (1983) Actin filaments, stereocilia, and hair cells of the bird cochlea I. Length, number, width, and distribution of stereocilia of each hair cell are related to the position of the hair cell on the cochlea. *Journal of Cell Biology* 96:807-821.

139. Eatock RA & Fay RR (2006) *Vertebrate Hair Cells*.

140. Lim DJ (1986) Functional structure of the organ of Corti: a review. *Hearing Research* 22:117-146.

141. Nam JH & Fettiplace R (2008) Theoretical conditions for high-frequency hair bundle oscillations in auditory hair cells. *Biophysical Journal* 95:4948-4962.

142. Esther J, Wiersinga-Post C, & van Netten SM (2000) Temperature dependency of cupular mechanics and hair cell frequency selectivity in the fish canal lateral line organ. *Jounral of Computational Physiology A* 186:949-956.

143. Beurg M, Nam JH, Crawford AC, & Fettiplace R (2008) The actions of calcium on hair bundle mechanics in mammalian cochlear hair cells. *Biophysical Journal* 94:2639-2653.

144. Benser ME, Issa NP, & Hudspeth AJ (1993) Hair-bundle stiffness dominates the elastic reactance to otolithic-membrane shear. *Hearing Research* 68(2):243-252.

145. Brownell WE (1990) Outer hair cell electromotility and otoacoustic emissions. *Ear Hearing* 11:82-92.

146. Hudspeth AJ, Julicher F, & Martin P (2010) A critique of the critical cochlea: Hopf—a bifurcation—is better than none. *Journal of Neurophysiology* 104(3):1219-1229.

147. Gopfert MC & Robert D (2003) Motion generation by Drosophila mechanosensory neurons. *Proceedings of the National Academy of Sciences USA* 100:5514-5519.

148. Kossl M, Mockel D, Weber M, & Seyfarth EA (2008) Otoacoustic emissions from insect ears: evidence of active hearing? *Jounral of Computational Physiology A* 194:597-609.

149. Field LH & Matheson T (1998) Chordotonal organs of insects. *Advances in Insect Physiology* 27:1-109.

150. Kindt KS, Finch G, & Nicolson T (2012) Kinocilia mediate mechanosensitivity in developing zebrafish hair cells. *Developmental Cell* 23(2):329-341.

151. Megela-Simmons A, Moss CF, & Daniel KM (1985) Behavioral audiograms of the bullfrog (Rana catesbeiana) and the green tree frog (Hyla cinerea). *Journal of the Acoustical Society of America* 78:1236-1244.

152. Koppl C, Forge A, & Manley GA (2004) Low density of membrane particles in auditory hair cells of lizards and birds suggests an absence of somatic motility. *Journal of Comparative Neurology* 479:149-155.

153. Mulroy MJ (1974) Cochlear anatomy of the alligator lizard. *Brain Behavior and Evolution* 10(1-3):69-87.

154. Gleich O & Manley GA (2000) The Hearing Organs of Birds and Crocodilia. *Comparative Hearing: Birds and Reptiles*, eds Dooling RJ, Fay RR, & Popper AN (Springer, New York), pp 70-138.

155. Jordan DW & Smith P (2007) *Nonlinear Ordinary Differential Equations* (Oxford University Press) 4th Ed.

156. Synge JL & Griffith BA (1949) *Principles of Mechanics* (McGraw-Hill) 2nd Ed.

157. Kuznetsov YA (2004) *Elements of Applied Bifurcation Theory* (Springer) 3rd Ed.

158. von Petersdorff T (2006) Critical Points of Autonomous Systems. *Differential Equations for Scientists and Engineers*, (University of Maryland).

159. Strogatz SH (1994) *Nonlinear Dynamics and Chaos* (Addison Wesley).

160. Guckenheimer J & Holmes P (1983) *Nonlinear Oscillations, Dynamical Systems, and Bifurcations of Vector Fields* (Springer).

161. Andronov AA, Leontovich EA, Gordon II, & Maier AG (1971) *Theory of Bifurcations of Dynamical Systems on a Plane* (Israel Program for Scientific Translations).

162. Marsden J & MacCracken M (1976) *Hopf Bifurcation and its Applications* (Springer).

163. Hudspeth AJ (2008) Making an effort to listen: mechanical amplification in the ear. *Neuron* 59(4):530-545.

164. Hudspeth AJ (2010) A critique of the critical cochlea: Hopf—a bifurcation—is better than none. *Journal of Neurophysiology* 104(3):1219-1229.

165. Izhikevich EM (2007) *Dynamical Systems in Neuroscience: The Geometry of Excitability and Bursting* (The MIT Press).

166. Izhikevich EM (2000) Neural excitability, spiking and bursting. *International Journal of Bifurcation and Chaos* 10(6):1171-1266.

167. Ó Maoiléidigh D, Nicola EM, & Hudspeth AJ (2012) The diverse effects of mechanical loading on active hair bundles. *Proceedings of the National Academy of Sciences USA* 109(6):1943-1948.

168. Ermentrout GB & Kopell N (1986) Parabolic bursting in an excitable system coupled with a slow oscillation. *SIAM-J.-Appl.Math.* 46:233-253.

169. Moudgil HK (2010) *Textbook of Physical Chemistry* (PHI Learning Private Limited).

170. Nadrowski B, Martin P, & Jülicher F (2004) Active hair-bundle motility harnesses noise to operate near an optimum of mechanosensitivity. *Proceedings of the National Academy of Sciences USA* 101(33):12195-12200.

171. Ginoux J-M & Letellier C (2012) Van der Pol and the history of relaxation oscillations: Toward the emergence of a concept. *Chaos* 22(023120):1-15.

172. van der Pol B (1920) A theory of the amplitude of free and forced triode vibrations. *Radio Review* 1:701-710.

173. van der Pol B (1926) On "relaxation-oscillations". *The London, Edinburgh, and Dublin Philosophical Magazine and Journal of Science* 7(2):978-992.

174. Graf RF (1999) *Modern Dictionary of Electronics* (Newnes).

175. van der Pol B & van der Mark J (1928) The heartbeat considered as a relaxation oscillation, and an electrical model of the heart. *Philosophical Magazine Series 7* 6(38):763-775.

176. Guantes R & Poyatos JF (2006) Dynamical principles of two-component genetic oscillators. *Plos Computational Biology* 2(3):e30.

177. Hodgkin AL & Huxley AF (1952) A quantitative description of membrane current and its application to conduction and excitation in nerve. *The Journal of Physiology* 117(4):500-544.

178. FitzHugh R (1955) Mathematical models of threshold phenomena in the nerve membrane. *Bulletin of Membrane Biophysics* 17:257-278.

179. FitzHugh R (1961) Impulses and physiological states in theoretical models of nerve membrane. *Biophysical Journal* 1:445-466.

180. Nagumo J, Arimoto S, & Yoshizawa S (1962) An active pulse transmission line simulating nerve axon. *Proceedings of the Institute of Radio Engineers* 50:2061-2070.

181. Equiluz VM, Ospeck M, Choe Y, Hudspeth AJ, & Magnasco MO (2000) Essential nonlinearities in hearing. *Physical Review Letters* 84(22):5232-5235.

182. Julicher F, Dierkes K, Lindner B, Prost J, & Martin P (2009) Spontaneous movements and linear response of a noisy oscillator. *The European Physical Journal E* 29:449-460.

183. Choe Y, Magnasco MO, & Hudspeth AJ (1998) A model for amplification of hair-bundle motion by cyclical binding of Ca2+ to mechanoelectrical-transduction channels. *Proceedings of the National Academy of Sciences USA* 95:15321-15326.

184. Hudspeth AJ & Lewis RS (1988) A model for electrical resonance and frequency tuning in saccular hair cells of the bull-frog, Rana catesbeiana. *Journal of Physiology* 400:275-297.

185. Ospeck M, Equiluz VM, & Magnasco MO (2001) Evidence of a Hopf bifurcation in frog hair cells. *Biophysical Journal* 80:2597-2607.

186. Barral J & Martin P (2012) Phantom tones and suppressive masking by active nonlinear oscillation of the hair-cell bundle. *Proceedings of the National Academy of Sciences USA* 109(21):E1344-1351.

187. Frederickson-Hemsing L, Ji S, Bruinsma R, & Bozovic D (2012) Mode-locking dynamics of hair cells of the inner ear. *Physical Review Letters E: Stat Nonlin Soft Matter Phys* 86(2-1):021915.

188. Hall J (1972) Auditory distortion products f2-f1 and 2f1-f2. *Journal of the Acoustical Society of America* 51:1863-1871.

189. Robles L, Ruggero MA, & Rich NC (1997) Two-tone distortion on the basilar membrane of the chinchilla cochlea. *Journal of Neurophysiology* 77:2385-2399.

190. Duke TAJ & Julicher F (2008) Critical oscillators as active elements in hearing. *Active Processes and Otoacoustic Emissions in Hearing*, eds Manley GA, Fay RR, & Popper AN (Springer Science and Business Media, New York), pp 63-92.

191. Ruggero MA, Rich NC, Recio A, Narayan SS, & Robles L (1997) Basilar-membrane responses to tones at the base of the chinchilla cochlea. *Journal of the Acoustical Society of America* 101:2151-2163.

192. Zweig G (1991) Finding the impedance of the organ of Corti. *Journal of the Acoustical Society of America* 89:1229-1254.

193. Duke T & Julicher F (2003) Active traveling wave in the cochlea. *Physical Review Letters* 90:158101.

194. Montgomery KA (2008) Multifrequency Forcing of a Hopf Oscillator Model of the Inner Ear. *Biophysical Journal* 95:1075-1079.

195. Vilfan A & Duke T (2003) Two Adaptation Processes in Auditory Hair Cells Together Can Provide an Active Amplifier. *Biophysical Journal* 85:191-203.

196. Tinevez J-Y, Julicher F, & Martin P (2007) Unifying the various incarnations of active hair-bundle motility by the vertebrate hair cell. *Biophysical Journal* 93:4053-4067.

197. Crawford AC & Fettiplace R (1985) The mechanical properties of ciliary bundles of the turtle cochlear hair cells. *Journal of Physiology* 364:359-379.

198. Jaramillo F & Hudspeth AJ (1993) Displacement-clamp measurement of the forces exerted by gating springs in the hair bundle. *Proceedings of the National Academy of Sciences USA* 90:1330-1334.

199. Barral J, Dierkes K, Lindner B, Julicher F, & Martin P (2010) Coupling a sensory hair-cell bundle to cyber clones enhances nonlinear amplification. *Proceedings of the National Academy of Sciences USA* 107(18):8079-8084.

200. Hartigan JA & Hartigan PM (1985) The dip test of unimodality. *Annals of Statistics* 13:70-84.

201. Cramer D (1997) *Basic Statistics for Social Research* (Routledge).

202. Hironori K, Lewis ER, Leverenz EL, & Baird RA (1982) Acute seismic sensitivity in the bullfrog ear. *Brain Research* 250:168-172.

203. Yu X, Lewis ER, & Feld D (1991) Seismic and auditory tuning curves from bullfrog saccular and amphibian papillar axons. *Journal of Comparative Physiology A*:241-248.

204. Shlomovitz R, *et al.* (2013) Low frequency entrainment of oscillatory bursts in hair cells. *Biophysical Journal* 104:1661-1669.

205. Roongthumskul Y, Frederickson-Hemsing L, Kao A, & Bozovic D (2011) Multiple-timescale dynamics underlying spontaneous oscillations of saccular hair bundles. *Biophysical Journal* 101:603-610.

206. Zhao X-Q (2003) *Dynamical Systems in Population Biology* (Springer Science & Business Media, New York).

207. Miermont A, Uhlendorf J, McClean M, & Hersen P (2011) The Dynamical Systems Properties of the HOG Signaling Cascade. *Journal of Signal Transduction* 2011:1-12.

208. Klipp E & Liebermeister W (2006) Mathematical modeling of intracellular signaling pathways. *BMC Neuroscience* 7(Suppl 1):S10.

209. Volterra V (1926) Variazioni e fluttuazioni del numero d'individui in specie animali conviventi. *Accademia dei Lincei* 2:31-113.

210. Lotka AJ (1910) Contribution to the Theory of Periodic Reaction. *Journal of Physical Chemistry* 14(3):271-274.

211. Hirono M, Denis CS, Richardson GP, & Gillespie PG (2004) Hair cells require phosphatidylinositol 4,5-bisphosphate for mechanical transduction and adaptation. *Neuron* 44(2):309-320.

212. Strimbu CE, Frederickson-Hemsing L, & Bozovic D (2012) Coupling and elastic loading affect the active response by the inner ear hair cell bundles. *PLoS ONE* 7:e33862.

213. Strimbu CE, Kao A, Tokuda J, Ramunno-Johnson D, & Bozovic D (2010) State and evoked motility in coupled hair bundles of the bullfrog sacculus. *Hearing Research* 265:38-45.

214. Fernandez C & Goldberg JM (1976) Physiology of peripheral neurons innervating otolith organs of the squirrel monkey. I. Response to static tilts and to long-duration centrifugal force. *Journal of Neurophysiology* 39(5):970-984.

215. Denk W, Webb WW, & Hudspeth AJ (1989) Mechanical properties of sensory hair bundles are reflected in their Brownian motion measured with a laser differential interferometer. *Proceedings of the National Academy of Sciences USA* 86:5371-5375.

216. Dinis L, Martin P, Barral J, Prost J, & Joanny JF (2012) Fluctuation-response theorem for the active noisy oscillator of the hair-cell bundle. *Physical Review Letters* 109(160602):1-5.

217. Yamoah EN, *et al.* (1998) Plasma Membrane Ca2+-ATPase Extrudes Ca2+ from Hair Cell Stereocilia. *The Journal of Neuroscience* 18(2):610-624.

218. Carafoli E (1994) Biogenesis: Plasma membrane calcium ATPase: 15 years of work on the purified enzyme. *The FASEB Journal* 8:993-1002.

219. Caroni P & Carafoli E (1981) The Ca2+ pumping ATPase of heart sarcolemma is activated by a phosphorylation-dephosphorylation process. *Journal of Biological Chemistry* 256:9371-9373.

220. James PH, Prushy M, Vorherr T, Penniston JT, & Carafoli E (1989) Primary structure of the cAMP-dependent phosphorylation site of the plasma membrane calcium pump. *Biochemistry* 28:4253-4258.

221. Smallwood JI, Gugi B, & Rasmussen H (1988) Modulation of erythrocyte Ca2+ pump activity by protein kinase C. *Journal of Biological Chemistry* 263:2195-2202.

222. Bormuth V, Barral J, Joanny JF, Julicher F, & Martin P (2014) Transduction channels' gating can control friction on vibrating hair-cell bundles in the ear. *Proceedings of the National Academy of Sciences USA* 111(20):7185-7190.

223. Liu J, *et al.* (1991) Calcineurin is a common target of cyclophilin-cyclosporin A and FKB-FK506 complexes. *Cell* 66(4):807-815.

224. Olson SD, Suarez SS, & Fauci LJ (2010) A model of CatSper channel mediated calcium dynamics in mammalian spermatozoa. *Bulletin of Mathematical Biology* 72:1925-1946.

225. Hong D, Jaron D, Buerk DG, & Barbee KA (2008) Transport-dependent calcium signaling in spatially segregated cellular caveolar domains. *American Journal of Physiology: Cell Physiology* 294:C856-C866.

226. Sneyd J, *et al.* (2003) A model of calcium waves in pancreatic and parotid acinar cells. *Biophysical Journal* 85:1392-1405.

227. Lumpkin EA & Hudspeth AJ (1998) Regulation of free Ca2+ concentration in hair-cell stereocilia. *Journal of Neuroscience* 18(16):6300-6318.

228. Kao A, Meenderink SWF, & Bozovic D (2013) Mechanical overstimulation of hair bundles: suppression and recovery of active motility. *PLoS ONE* 8(3):e58143.

229. Hodgkin AL (1948) The local electric changes associated with repetitive action in a non-medulated axon. *Journal of Physiology* 107:165-181.

230. FitzHugh R (1955) Mathematical models of threshold phenomena in the nerve membrane. *Bulletin of Mathematical Biophysics* 17:257-278.

231. Rinzel J & Ermentrout GB (1989) Analysis of neural excitability and oscillations. *Methods in Neuronal Modeling*, eds Koch C & Segev I (The MIT Press, Cambridge).

232. Ermentrout GB & Kopell N (1986) Subcellular oscillations and bursting. *Mathematical Biosciences* 78:265-291.

233. Ermentrout GB & Kopell N (1986) Parabolic bursting in an excitable system coupled with a slow oscillation. *SIAM Journal of Applied Mathematics* 46:233-253.

234. Ermentrout GB (1996) Type I membranes, phase resetting curves, and synchrony. *Neural Computation* 8:979-1001.

235. Izhikevich EM (2001) Resonate-and-fire neurons. *Neural Networks* 14:883-894.

236. Hansel D, Mato G, & Meunier C (1995) Synchrony in excitatory neural networks. *Neural Computation* 7:307-335.

237. Goldberg JM & Fernandez C (1971) Physiology of peripheral neurons innervating semicircular canals of the squirrel monkey. III. Variations among units in their discharge properties. *Journal of Neurophysiology* 34(4):676-684.

238. Kalluri R, Xue J, & Eatock RA (2010) Ion channels set spike timing regularity of mammalian vestibular afferent neurons. *Journal of Neurophysiology* 104:2034-2051.

239. Somps CJ, Schor RH, & Tomko DL (1994) Vestibular afferent responses to linear accelerations in the alert squirrel monkey in *NASA Technical Memorandum 4581*, ed Center NAR (Moffett Field, CA).

240. Ermentrout B, *et al.* (2008) Ermentrout-Kopell canonical model. ed Ermentrout B (Scholarpedia).

241. Jacobson ML (2001) Auto-threshold peak detection in physiological signals. in *Engineering in Medicine and Biology Society, 2001. Proceedings of the 23rd Annual International Conference of the IEEE*, eds Istefanopulos Y, Kearney R, Akay M, & Kahya Y (IEEE, Istanbul, Turkey).

242. Lindner B, Garcia-Ojalvo J, Neiman A, & Schimansky-Geier L (2004) Effects of noise in excitable systems. *Physics Reports* 392:321-424.

243. Roongthumskul Y & Bozovic D (2015) Mechanical amplification exhibited by quiescent saccular hair bundles. *Biophysical Journal* 108(1):53-61.

244. Shlomovitz R, Roongthumskul Y, Bozovic D, & Bruinsma R (2014) Phase-locked spiking of inner ear hair cells and the driven noisy Adler equation. *Interface Focus* 4(6):20140022.

245. Roongthumskul Y, Shlomovitz R, Bruinsma R, & Bozovic D (2013) Phase slips in oscillatory hair bundles. *Physical Review Letters* 110(14):148103.